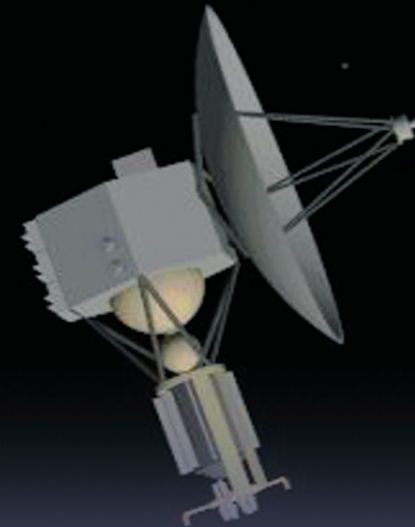


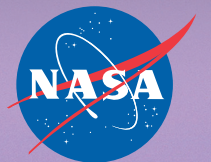
TDW'03

International Thermal Detectors Workshop
June 19-20, 2003



Proceedings

University of Maryland
Inn and Conference Center
3501 University Boulevard East
Adelphi, MD 20783



<http://www-lep.gsfc.nasa.gov/code693/tdw03/index.shtml>
TDW'03 info e-mail: info_tdw03@lepvox.gsfc.nasa.gov

The NASA STI Program Office ... in Profile

Since its founding, NASA has been dedicated to the advancement of aeronautics and space science. The NASA Scientific and Technical Information (STI) Program Office plays a key part in helping NASA maintain this important role.

The NASA STI Program Office is operated by Langley Research Center, the lead center for NASA's scientific and technical information. The NASA STI Program Office provides access to the NASA STI Database, the largest collection of aeronautical and space science STI in the world. The Program Office is also NASA's institutional mechanism for disseminating the results of its research and development activities. These results are published by NASA in the NASA STI Report Series, which includes the following report types:

- **TECHNICAL PUBLICATION.** Reports of completed research or a major significant phase of research that present the results of NASA programs and include extensive data or theoretical analysis. Includes compilations of significant scientific and technical data and information deemed to be of continuing reference value. NASA's counterpart of peer-reviewed formal professional papers but has less stringent limitations on manuscript length and extent of graphic presentations.
- **TECHNICAL MEMORANDUM.** Scientific and technical findings that are preliminary or of specialized interest, e.g., quick release reports, working papers, and bibliographies that contain minimal annotation. Does not contain extensive analysis.
- **CONTRACTOR REPORT.** Scientific and technical findings by NASA-sponsored contractors and grantees.
- **CONFERENCE PUBLICATION.** Collected papers from scientific and technical conferences, symposia, seminars, or other meetings sponsored or cosponsored by NASA.
- **SPECIAL PUBLICATION.** Scientific, technical, or historical information from NASA programs, projects, and mission, often concerned with subjects having substantial public interest.
- **TECHNICAL TRANSLATION.** English-language translations of foreign scientific and technical material pertinent to NASA's mission.

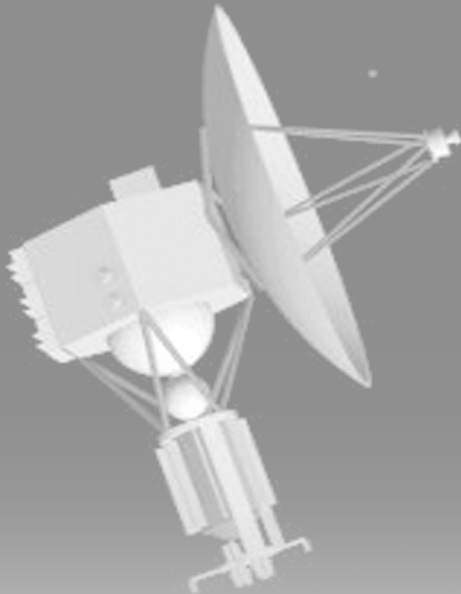
Specialized services that complement the STI Program Office's diverse offerings include creating custom thesauri, building customized databases, organizing and publishing research results . . . even providing videos.

For more information about the NASA STI Program Office, see the following:

- Access the NASA STI Program Home Page at <http://www.sti.nasa.gov/STI-homepage.html>
- E-mail your question via the Internet to help@sti.nasa.gov
- Fax your question to the NASA Access Help Desk at (301) 621-0134
- Telephone the NASA Access Help Desk at (301) 621-0390
- Write to:
NASA Access Help Desk
NASA Center for AeroSpace Information
7121 Standard Drive
Hanover, MD 21076-1320

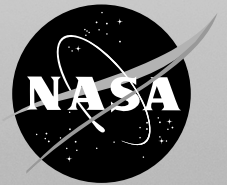
T D W ' 0 3

**International Thermal Detectors Workshop
June 19-20, 2003**



Proceedings

University of Maryland
Inn and Conference Center
3501 University Boulevard East
Adelphi, MD 20783



<http://www-lep.gsfc.nasa.gov/code693/tdw03/index.shtml>
TDW'03 info e-mail: info_tdw03@lepvax.gsfc.nasa.gov

NASA/CP-2004-212748

Available from:

NASA Center for AeroSpace Information
7121 Standard Drive
Hanover, MD 21076-1320
Price Code: A17

National Technical Information Service
5285 Port Royal Road
Springfield, VA 22161
Price Code: A10

Preface

NASA's future planetary and Earth Science missions will require ever more sensitive thermal detectors operating between 2K and 300 K.

It is in response to this need that the International Workshop on thermal detectors (TDW03) was held. It put together space borne IR/Sub-mm and heterodyne instrument scientists and astronomers, thermal detector developers, cryocooling technologists as well as bandpass and blocking filter experts. Their varied expertise and backgrounds allowed for a fertile discussion on outstanding issues and future detector developments. In this regard TDW03 was a great success.

We thank all the participants for making TDW03 a truly interesting forum for information exchange on the state of thermal detectors. Discussions are already underway to hold such Workshops in the future.

We also thank NASA's directors of funding programs (ACT, PIDDP, code SE and code R) for accepting our invitation to introduce their relative programs to the participants.

Sincerely,

The Editors: Brook Lakew, John Brasunas, Shahid Aslam,
Rainer Fettig, and Robert Boyle.

Workshop Scope

The aim of the Workshop is to bring together thermal detector developers and astronomers involved in space-based studies of the Sun and the Earth, as well as the inner and the outer planets of the solar system. Of particular interest will be thermal detectors operating at $2\text{ K} \leq T \leq 300\text{ K}$.

CONTENTS

Workshop Scope	v
Principal Authors	xiii
Organizing Committees	xiv

NASA Funding Programs

*** For more information on the following NASA funding programs, please see the TDW2003 CD included in the back of this publication.*

ACT, NASA Earth Science Technology funding program

Janice Buckner, Program Manager

PIDDP, NASA Solar System Exploration funding program

Susan Niebur, Program Manager

Code SE, NASA Solar System Exploration funding program

Ret. Colonel Lindley Johnson, Program Manager

Code R, NASA Aerospace Technology funding program

Chris Moore, Program Manager

Session 1—Upcoming and Proposed Missions (Planetary and Earth Science) Chairs: J. Brasunas, B. Lakew

1.1: Upcoming and Future Missions in the Area of Infrared Astronomy: Spacecraft and Ground-based Observations, Sittler, E. (invited paper).	1-1
1.2: Scripps-NISTAR—New Instrumentation for a Challenging Mission: Earth Radiation Budget Measurements from L-1, Lorentz, S.R., Rice, J.P., Valero, (invited paper).	1-11
1.3: In-flight Far-Infrared Performance of the CIRS Instrument on Cassini Nixon, C. et al.	1-12

Session 2—Far IR/Sub-mm Thermal Detectors—New Concepts and Materials

Session 2.1

Chairs: H. Moseley, S. Aslam

- 2.1.1: Superconducting TES Bolometers Above 1 K,**
Richards, P.L. (invited paper)2-1
- 2.1.2: Ultimate Sensitivity of Superconducting Single-photon
Detectors in the Visible to Infrared Range,**
Zhang, J., Pearlman, A., Slys, W., Verevkin, A., Sobolewski, R.,
Korneev, A., Kouminov, P., Okunev, O., Chulkova, G., Goltsman, G..... 2-6
- 2.1.3: Canadian Microbolometer Technology for Future Space Missions,**
Ngo Phong, L., Zheng, W. 2-10
- 2.1.4: Novel Electrically Substituted Optical Detectors,**
Rice, J., Lorentz, S., Houston, J. 2-14

Session 2.2

Chairs: D. Reuter, R. Boyle

- 2.2.1: Arrays of High Performance Thermal Detectors,**
Moseley, H. (invited paper)..... 2-15
- 2.2.2: Thermopile Detector Arrays for Space Science
Applications,**
Foote, M.C., Krueger, T. R., McCann, T.A., Chacon, R., Jones, E.W.,
Dickie, M.R., Schofield, J.T., McCleese, D.J., McCann, T.A., Jones E.W.,
Dickie, M.R. (invited paper). 2-16
- 2.2.3: The IR Detector System for the GERB Instrument,**
Nelms, N., Butcher, G., Whitford, C., Cole, R., Blake, O. 2-21
- 2.2.4: The Economical Microbolometer-Based Environmental
Radiometer Satellite (EMBERSat) Designed for Forest Fire
Detection and Monitoring,**
Lancaster, R., Beecken, B. 2-25
- 2.2.5: Thermal Emission Imaging System (THEMIS),**
Schueler, C., Silverman, S., Christensen, P. 2-29

2.2.6: Far IR and Sub-mm Filled Bolometer Arrays Performances at 300 mK and 2K,	
Rodriguez, L., Agnese, P., Reveret, V., Vigroux L.	2-33
2.2.7: Cold-Electron Bolometer with Strong Electrothermal Feedback,	
Kuzmin, L.	2-37

<p align="center">Session 3–High Temperature Superconducting (HTS) Bolometers Chairs: R. Ross, R. Fetting</p>
--

3.1: The Case for Moderately Cooled, Far-Infrared Thermal Detectors,	
Brasunas J.C. (invited paper).	3-1
3.2: Fabrication of Monolithic Sapphire Membranes for High T_c Bolometer Array Development,	
Pugel, D.E./ Lakew, B., Aslam S.	3-6
3.3: Perovskite Manganites: A New Family of Materials for Uncooled/Moderately Cooled IR Detector Applications,	
Rajeswari, M.R., Smolyaninova, V., Overby, M.	3-11
3.4: Bolometer Simulation Using SPICE	
Jones, H., Aslam, S., Lakew, B.	3-17

<p align="center">Session 4–Thin Films for Sensor Applications and Readout Electronics Chairs: S. Calcutt, S. Aslam</p>
--

4.1: High- and Mid-temperature Superconducting Sensors for Far IR/Sub-mm Applications in Space	
Lakew, B. (invited paper).	4-1
4.2: SQUID Multiplexers for Cryogenic Detector Arrays,	
Irwin, K., Beall, J., Deiker, S., Doriese, R., Duncan, W., Hilton, G., Moseley, S. H., Reintsema, C., Stahle, C., Ullom, J., Vale, L.	4-5
4.3: Epitaxial Superconducting MgB₂ Thin Films by HPCVD,	
Xi, Xiaoxing	4-6
4.4: Superconducting Digital Multiplexers for Sensor Arrays,	
Kadin, A.M.	4-7

4.5: Electrical Devices and Circuits for Low Temperature Space Applications, Patterson, R., Hammoud, A., Dickman, J., Gerber, S., Overton, E., Elbuluk, M.	4-11
--	------

<p align="center">Session 5: Bandpass and Blocking Filters Chairs: E. Sittler, J. Brasunas</p>

5.1: Far-infrared and Submillimeter Filters, Haynes, C.V., Ade, P.A.R., Lee, C., Tucker, C.E.	5-1
--	-----

5.2: Metal Mesh Filters for Infrared Applications, Sternberg, O., Stewart, K.P., Fettig, R., Moeller, K.D., Smith, H.A.	5-6
---	-----

<p align="center">Session 6: Cooling Systems Chairs: J. M. Lamarre, R. Boyle</p>

6.1: NASA Space Cryocooler Programs— A 2003 Overview, Ross, R.G. Jr., Boyle, R.F., Kittel, P. (invited paper).	6-1
---	-----

6.2: Sunpower Cooling Solutions, Keiter, D., Wilson, K.	6-8
--	-----

6.3: Integration of Oxford Class Cryocoolers with Thermal Detectors, Kirkconnell, C.	6-11
---	------

6.4: Space Cryocoolers, Tward, E.	6-16
--	------

6.5: On-Orbit Operating Experience with the NICMOS Cryocooler—First Year, Swift, W., Cheng, E., Zagarola, M., Dolan, F.	6-17
--	------

<p align="center">Session 7: Heterodyne Detection Chairs: W.J. Wiscombe, R. Fettig</p>

7.1: Heterodyne Spectroscopy in the Thermal Infrared Region, Kostiuk, T. (invited paper).	7-1
--	-----

7.2: THIS–Next Generation Tuneable Heterodyne Infrared Spectrometer for SOFIA, Sonnabend, G., Wirtz, D., Schieder, R.	7-8
7.3: Large Format Narrow-Band, Multi-Band, and Broad-Band LWIR QWIP Focal Planes for Space and Earth Science Applications, Gunapala, S., Bandara, S., Liu, J., Rafol, D., Jhabvala, M., Choi, K., Shott, C.	7-12
7.4: A Thermal Infrared Heterodyne Receiver with Applications to Astronomy, Hale, D.S.	7-16

POSTERS

P1: Superconducting Electronics for Detector Readouts, Luine, J., Durand, D., Eaton, L./TRW.	P1
P2: Development of a Submillimeter/Far-Infrared Radiometer for Cirrus Measurements, Hayton, D., Ade, P., Evans, F., Lee, C., Nolt, I., Vanek, M.	P1
P3: Thermoelectric Cooling Utilizing CeB₆ Single Crystal at Cryogenic Temperatures, Harutyunyan, S., *Vartanyan, V., Nikoghosyan, V., *Kuzanyan, A., Wood, K., **Gulian, A.	P2
P4: Anti-reflection Coatings for Far IR Filters, Tucker, C., Haynes, V., Ade, P.	P2
P5: In situ Pulsed Laser Deposition of C-Axis Oriented MgB₂ Films and Their Characterization, Shinde, S., Lakew, B., Ogale, S.B., Kulkarni V.N., Kale, S.N. Venkatesan, T.	P2
P6: Cryocoolers for Space, Kittel, P., Feller, J., Roach, P., Kashani, A., Helvensteijn, B.	P3
P7: High Aspect Ratio Hole Array Filters for a Wide Range of Wavelength, Fettig, R.K., Hein, H. Schulz, J.	P3

P8: Resonance Modes of Meshes with Rectangular and Hexagonal Structures,	
Sternberg, Oren, Shah, J., Moeller, K.D. Fettig, R.	P4
P9: Programmable 2-D Addressable Cryogenic Aperture Masks,	
Kutyrev, A.S., Moseley, S.H., Jhabvala, M., Li, M., Schwinger, D.S.,	
Silverberg, R.F., Wesenberg, R.P.	P4

Principal Authors

Name	E-mail Address	Affiliation
Brasunas, John	john.c.brasunas@nasa.gov	NASA Goddard Space Flight Center
Fettig, Rainer	rainer.fettig@imt.fzk.de	FZ-Karlsruhe
Foote, Marc C.	marc.c.foote@jpl.nasa.gov	Jet Propulsion Laboratory
Gaugue, Alain	alain.gaugue@lgep.supelec.fr	Supelec
Gunapala, Sarath	sarath.d.gunapala@jpl.nasa.gov	Jet Propulsion Laboratory
Hale, David D. Snyder	david@isi.mtwilson.edu	Univ. of California at Berkeley
Harutyunyan, Sergey	Sergey@ipr.sci.am	Institute for Physical Research
Haynes, V.C.	Vic.Haynes@astro.cf.ac.uk	University of Wales at Cardiff
Hayton, Darren	Darren.Hayton@astro.cf.ac.uk	University of Wales at Cardiff
Irwin, Kent D.	irwin@boulder.nist.gov	Natl. Inst. Standards & Technology
Jones, Hollis	holjones@pop500.gsfc.nasa.gov	NASA Goddard Space Flight Center
Kadin, Alan M.	kadin@hypres.com	HYPRES, Inc.
Karasik, Boris	boris.s.karasik@jpl.nasa.gov	Jet Propulsion Laboratory
Keiter, Doug	keiter@sunpower.com	Sunpower, Inc.
Kessler, Ernst	ernst.kessler@ipht-jena.de	Inst. for Physical High Technology
Kirkconnell, Carl	carl_s_kirkconnell@raytheon.com	Raytheon
Kittel, Peter	peter.kittel-1@nasa.gov	NASA Ames Research Center
Kostiuk, Theodor	Theodor.Kostiuk@gsfc.nasa.gov	NASA Goddard Space Flight Center
Kutyrev, Alexander S.	kutyrev@stars.gsfc.nasa.gov	NASA Goddard Space Flight Center
Kuzmin, Leonid	kuzmin@fy.chalmers.se	Chalmers University
Lakew, Brook	Brook.Lakew-1@nasa.gov	NASA Goddard Space Flight Center
Lancaster, Redgie	lancaster@virl.gsfc.nasa.gov	NASA Goddard Space Flight Center
Lorentz, Steven R.	lorentz@nist.gov	L-1 Standards and Technology Inc.
Luine, Jerome	jerome.luine@trw.com	TRW Space and Electronics
Maffei, Bruno	Bruno.maffei@astro.cf.ac.uk	University of Wales at Cardiff
Moseley, Harvey	moseley@stars.gsfc.nasa.gov	NASA Goddard Space Flight Center
Nelms, Nick	nin@star.le.ac.uk	University of Leicester
Ngo Phong, Linh	linh.ngo-phong@space.gc.ca	Canadian Space Agency
Nixon, Conor	conor.nixon@gsfc.nasa.gov	University of Maryland
Patterson, Richard	Richard.Patterson@grc.nasa.gov	NASA Glenn Research Center
Pugel, D.E.	bpugel@pop500.gsfc.nasa.gov	Raytheon Corporation
Rajeswari, M. Raj	mrageswari@towson.edu	Towson University
Rice, Joseph	joe.rice@nist.gov	Natl. Inst. Standards & Technology
Richards, Paul L.	richards@physics.berkeley.edu	Univ. of California Berkeley
Rodriguez, Louis	lrodriguez@cea.fr	CEA/DAPNIA/SAP
Ross, R.G. Jr.	Ronald.G.Ross-Jr@jpl.nasa.gov	Jet Propulsion Laboratory
Schueler, Carl	cfschueler@raytheon.com	Raytheon SBRS
Semenov, Alexei	Alexei.Semenov@dlr.de	German Aerospace Agency
Shinde, Sanjay	shinde@squid.umd.edu	University of Maryland
Sonnabend, Guido	samstag@ph1.uni-koeln.de	KOSMA/University of Cologne
Sternberg, Oren	oren.sternberg@nrl.navy.mil	Naval Research Laboratory
Swift, Walter	WLS@create.com	Create Inc.
Tucker, Carole	carole.tucker@astro.cf.ac.uk	Cardiff University
Tward, Emanuel	manny.tward@trw.com	Northrop Grumman Space Technology
Verevkin, Aleksandr	verevkin@ece.rochester.edu	University of Rochester
Xi, Xiaoxing	xxx4@psu.edu	Penn State University

Organizing Committees

Scientific Organizing Committee (SOC)

Harvey MOSELEY
Lab for Astronomy and Solar Physics
NASA Goddard Space Flight Center
USA

Ronald G. ROSS
Advanced Technology Group
Jet Propulsion Laboratory
USA

Simon CALCUTT
Dept. of Atmospheric Physics
Oxford University
UK

John C. BRASUNAS
Planetary Systems Branch
NASA Goddard Space Flight Center
USA

Dennis C. REUTER
Planetary Systems Branch
NASA Goddard Space Flight Center
USA

Brook LAKEW
Planetary Systems Branch
NASA Goddard Space Flight Center
USA

Warren J. WISCOMBE
Laboratory for Atmospheres
NASA Goddard Space Flight Center
USA

Clare LEE
Department of Physics and Astronomy
University of Wales at Cardiff
UK

Jean-Michel LAMARRE
LERMA/Observatoire de Paris, Paris
FRANCE

Edward C. SITTLER
Interplanetary Physics Branch
NASA Goddard Space Flight Center
USA

Local Organizing Committee (LOC)

Brook LAKEW (Chair)
NASA Goddard Space Flight Center
Code 693
e-mail: xr2bl@lepvax.gsfc.nasa.gov

John BRASUNAS
NASA Goddard Space Flight Center
Code 693
e-mail: Z1JCB@lepvax.gsfc.nasa.gov

Shahid ASLAM
Raytheon Corp.
e-mail: saslam@pop200.gsfc.nasa.gov

Robert BOYLE
NASA Goddard Space Flight Center
e-mail: Robert.F.Boyle.1@gsfc.nasa.gov

Rainer FETTIG
Institut f. Mikrostrukturtechnik (IMT)
Forschungszentrum Karlsruhe GmbH-
Germany)
e-mail: rainer.fettig@imt.fzk.de

UPCOMING AND FUTURE MISSIONS IN THE AREA OF INFRARED ASTRONOMY: SPACECRAFT AND GROUND BASED OBSERVATIONS

E. C. Sittler Jr.*

NASA Goddard Space Flight Center, Code 692, Greenbelt, MD 20771, USA

ABSTRACT

The IRIS instrument on the Voyager spacecrafts (Hanel et al., 1977) made major discoveries with regard to the giant planets, their moons and rings (Hanel et al., 1979a,b; Hanel et al., 1981, 1982; Hanel et al., 1986; Conrath et al., 1989) and paved the way for future infrared observations for planetary missions within our solar system. The CIRS instrument of Cassini with much greater spectral-spatial resolution and sensitivity than that provided by IRIS is now rapidly approaching the Saturnian system with orbit insertion on July 1, 2004, for which CIRS is expected to provide an order of magnitude advance beyond that provided by IRIS (Kunde et al., 2003). The Mars program is also presently dominated by infrared observations in the near to mid-infrared spectral bands for missions such as Mars Global Surveyor and its TES instrument and Odyssey with its THEMIS instrument. In the case of Earth science we have such missions as TIMED, which makes infrared observations of the thermosphere using the SABER instrument. With the newly formed New Frontiers Program we have the opportunity for \$650M missions such as Kuiper Belt-Pluto Explorer and Jupiter Polar Orbiter with Probes. Under the Flagship line, once per decade, we have the opportunity for \$1B missions for which Europa is presently being considered; for this mission infrared measurements could look for hot spots within the maze of cracks and faults on Europa's surface. On Kuiper Belt-Pluto there is an imaging near-IR spectrometer called LEISA. Another mission on the horizon is Titan Orbiter Aerover Mission (TOAM) for which there is planned a state-of-art version of CIRS called TIRS on the orbiter that will map out the atmospheric composition with unprecedented wavelength coverage and spectral-spatial resolution. This instrument will also provide temperature maps of the surface of Titan to look for hot spots where life may form. On the same mission there will be a descent imager on the Aerover (i.e., balloon) similar to that provided by LEISA on the Pluto mission to provide compositional-topographical maps of Titan's surface. Other future mission will also be discussed. Improved thermal detectors could have important applications in solar physics, specifically in the detection of far-IR synchrotron emission from energetic electrons in solar flares. For infrared astronomy we have missions like SIRTf and JWST, which will cover the spectral range from near-IR to far-IR in the search and probing of both new and old planetary systems in our galaxy and the measurement of the most distant galaxies of our universe. SIRTf is scheduled to be launched in August 2003, while JWST will be launched next decade. Another mission is TPF, which will use interferometer techniques at infrared wavelengths to search for planetary systems beyond 2010. With regard to ground based telescopes we have, for example, the twin 10 meter Keck telescopes and the IRTF telescope at Mauna Kea. The Keck telescopes are presently using interferometer techniques. Over the next several decades there are plans for 50 meter to 200 meter telescopes providing near-IR to far-IR measurements with the eventual plan to combine all telescopes using interferometer techniques to provide unprecedented spectral-spatial resolution and sensitivity.

* Contact information for E.C. Sittler- Email: edward.c.sittler@nasa.gov

SESSION 1- Upcoming and Proposed Missions (Planetary and Earth Sciences)

INTRODUCTION

We will review the future missions on the near horizon to those that will not occur until after 2013.

These missions will fall under four major categories or sub-headings: 1.) Astrophysics, 2.) Planetary Science, 3.) Earth Science and 4.) Sun Earth Connection (SEC) or Living with a Star (LWS). The list is very comprehensive in the first three categories. It will become clear that there is a very bright but challenging future in the area of infrared astronomy from NIR to FIR wavelengths to as high as microwave wavelengths. In the area of astrophysics the primary mission over the next decade is the James Webb Space Telescope (JWST), which will be looking for distant galaxies of very high red-shifts so that visible emissions will be shifted to FIR wavelengths. Also, up to 50% of the radiated energy in the universe is in the infrared (John Mathers, private communication 2003). In the area of planetary sciences we have the Jupiter Icy Moons Orbiter (JIMO) mission, which is also called Prometheus. This is a technology demonstration mission using a space fission reactor. This mission will provide ~ 500 kg total instrument payload mass with total instrument power in excess of 10 kwatts. This mission favors large high power instrument concepts with the potential for major scientific breakthroughs using measurements at infrared wavelengths. With this amount of mass and power one can design infrared spectrometers using large focal plane arrays for high spatial resolution and cryogenic refrigeration systems that will cool detector arrays to mK temperatures and thus high spectral and spatial resolution. Heterodyne techniques will also probably be used. Although JIMO could indicate a new paradigm in the area of spacecraft instrumentation, cost constraints will not go away and there will always be pressures to make instruments lighter, smaller in volume and lower in power. At an international level funding and facilities development in the area of nanotechnology is growing at leaps and bounds and major advances in this area are expected over the next decade. In this same arena we see significant progress in the field called MEMS, which stands for Micro Electro-Mechanical System. Both areas provide the potential for miniature low power infrared spectrometers, which could be flown on miniature spacecraft and landers for future planetary missions. In the area of Earth science the future in infrared astronomy is very bright. Over the next decade major advances in instrument capability are expected in the Earth science arena. This includes the next generation of Landsat missions and the NPOESS missions, which will start demonstration mission NPP and main phase beginning around 2009. Finally, we will discuss missions in the SEC/LWS sector and future developments in the area of ground based telescopic missions using interferometer techniques.

FUTURE MISSIONS USING INFRARED REMOTE SENSING INSTRUMENTS

Astrophysical Infrared Missions

In Table 1 we summarize future astrophysical infrared missions. As an example of these we show the JWST spacecraft in Figure 1, which will use a seven meter telescope with radiative cooling to achieve detector temperatures ~ 35°K, but could achieve 6°K temperatures or lower using a refrigeration system (see Stockman and Mather, 1999). The SIRTf 85 cm Beryllium telescope will operate at $T < 5^{\circ}\text{K}$, operate for wavelengths 3-180 μm and will study star formation, centers of galaxies, extrasolar planets and giant molecular clouds (see Gallagher et al., 2003). SOFIA will be the largest airborne observatory in the world using a Cassegrain System with 2.7 m telescope with wavelength coverage from 0.3 μm to 1.6 mm with main science goals of studying molecular clouds, infrared galaxies, low dust extinction and study formation of stars and galaxies (Becklin, 1997). ASTRO-F, built by the Japanese will have its telescope cooled to 6°K using superfluid liquid helium and Stirling-cycle coolers. It will search for primeval galaxies, infrared galaxies, protostars, brown dwarfs and protoplanetary disks. NGSS will look for IR galaxies, brown dwarfs near the Sun and detect ~ 500,000 asteroids using IR observations. The Astrobiology telescope will be cooled to $< 10^{\circ}\text{K}$ using cryogen solid hydrogen with InSb and SiAs detectors. Herschel will have a 3.5 m SiC telescope cooled to 70°K, SIRCE will combine radiative cooled shields and helium cooled telescope with ADR cooled TES bolometer arrays. The Japanese SPICA has 3.5 m actively cooled telescope at 4.5°K. SAFIR is a passively cooled 8 meter telescope that will build on JWST technology. The Terrestrial Planet Finder (TPF) mission will use a formation-flying interferometer of infrared telescopes that use large passively cooled optics, nulling interferometry, precision wavefront control, coronagraphs and cryocoolers. The SPIRIT mission uses a deployed linear array of telescopes using a common heat shield, while SPECS uses a separated spacecraft array similar to that used by TPF and the possible combined use of tethers and rotation (separation distances ~ 1 km. The missions SAFIR, TPF, SPIRIT and SPECS are all planned for launches after 2013.

SESSION 1- Upcoming and Proposed Missions (Planetary and Earth Sciences)

Planetary Infrared Missions

With regard to planetary missions (see Table 2) the first New Frontiers mission will be New Horizons, which will take images of Kuiper Belt objects and the Pluto-Charon system using an imaging NIR spectrometer called LEISA. This imaging spectrometer is also being considered for TOAM on the Aerover (i.e., powered balloon) for surface maps of Titan in the NIR, which is expected to provide surface compositional information. Regarding JIMO one of the main goals will be to provide high sensitivity, high spectral resolution and high spatial resolution measurements of icy moon surfaces to look for localized hot spots or hydrothermal vents where aqueous solutions may be extruding out from below due to tidal heating and radiogenic heating of their interiors where subsurface oceans may exist. For these measurements to be successful experimenters will have to shield against the large thermal radiators for the space fission reactor and provide active cryogenic cooling below 4°K so that large TES arrays can be constructed using SQUID switches at the focal plane. Heterodyne spectroscopy will also play an important role regarding icy moon exospheres. Here we note that the JIMO/Prometheus mission is setting a new paradigm in instrument development for which one can use instrumentation only reserved to ground based telescopes. The SPA-SR mission will take a sample of the moons surface at the South Pole-Aitken Basin where infrared measurements by Clementine showed permanently shadowed regions at the bottom of deep craters with temperatures less than 100°K and that frozen water lasting more than 10^9 years probably resides (Ingersoll et al., 1992). Bi-static radar measurements by Clementine gave further evidence for permanently frozen ice in these polar regions (Nozette et al., 1996). The Lunar Prospector Neutron Spectrometer measuring thermal and epithermal neutrons showed unequivocally evidence for water ice in these polar regions (Feldman et al., 1998). This was first predicted back in 1961 (Watson et al., 1961), though their stability is in question (Arnold, 1979). We expect an infrared imager to be part of the SPA-SR mission with regard to global surface temperature and composition measurements of these regions of permanently stored regions of water ice. Here, measurements in the NIR to MIR are recommended. For JPOP one of the primary objectives will be images of the polar aurora at Jupiter. In the past ground based observations have been made between 3-4 μm (Connerney et al., 1998, Satoh and Connerney, 1999) and most recently during the Cassini flyby the CIRS instrument measured emissions in the 7-14 μm range in the polar regions of Saturn at upper stratospheric depths and are believed to be associated with Jupiter's polar cusp (Flasar et al., 2003). Therefore, we expect these spectral regions to be covered by JPOP. In the case of CSSR the need for infrared observations of a comet at close quarters cannot be overstated considering the expected high abundance of water products and complicated organic chemistry. The recommended spectral range is 1-1000 μm . For MRO the CRISM instrument will provide high spatial and spectral resolution measurements over an extended wavelength range from 1.05-4.0 μm with a primary objective of detecting aqueous and/or hydrothermal activity regions on the surface of Mars and to map and characterize the composition, geology and stratigraphy of surface features (Murchie et al., 2003). This instrument uses doubly redundant cryogenic coolers and side-facing radiative cooler. For TOAM the orbiter will have a Titan Infrared Spectrometer (TIRS) covering the spectral range from 7 to 1000 μm (see Coustenis et al., 1993) and the LEISA instrument (1.0 – 3.5 μm) with both using passive radiative coolers for their detectors. A modified version of LEISA would also be used for the Aerover part of TOAM for which it would use the ambient cryogenically cold atmosphere to cool its detectors.

Earth Science Infrared Missions

For the Earth Science infrared missions we refer you to Table 3, which is not a complete list when one considers other international funded missions. There are also a large number of missions without infrared remote sensing instruments for which they instead do altimetry or radar observations of the Earth system. The Aura spacecraft makes measurements of the upper troposphere and lower stratosphere. It has two major remote sensing instruments, the High Resolution Dynamics Limb Sounder (HIRDLS) which has an infrared limb scanning radiometer to measure atmospheric temperature and concentration of various gases and aerosols and a Tropospheric Emission Spectrometer (TES) which is a high-resolution infrared imaging fourier spectrometer for both limb and nadir viewing in the spectral band from 3.2 to 15.4 μm . The SAGE III spacecraft makes stratospheric aerosol and gas measurements using the Sage-3 spectrometer, which makes measurements from 280 nm to 1040 nm and at 1550 nm with spectral resolution of 1-2 nm. It uses a combination of a CCD detector and photodetector. The NMP/EO-3 spacecraft has what is called a GIFTS Imager, which has a Fourier Transform Spectrometer with Michelson Interferometer. The sensor module is cryogenically cooled and makes measurements in the visible to infrared wavelengths. It uses a Large Area Format Focal Plane Detector Array (LFPA). One of its science objectives is to measure the greenhouse gases that may play an important role with regard to global warming. Landsat-7 is the next launch for the Landsat Data Continuity Mission (LDCM). It is a polar orbiting spacecraft with an imaging system called the Enhanced Thematic Sensor, which covers the wavelength range of 0.45 to 12.5 μm . It uses 8 spectral

SESSION 1- Upcoming and Proposed Missions (Planetary and Earth Sciences)

filters, a scan mirror assembly and radiative coolers. The detector technology is SiPD, InSb and HgCdTe. The spatial resolution is 30 to 1000 meters. The NPOESS spacecraft, for which NPP is a precursor, will make remote sensing images of the Earth system using wavelengths from the visible to infrared to microwave. The infrared measurements are provided by the Visible/Infrared Imager/Radiometer Suite (VIIRS) instrument and the Crosstrack Infrared Sounder (CrIS). Lastly, we have the DSCVR (Triana) spacecraft which uses the Scripps-NISTAR Imager. This imager covers the wavelength range from 0.2 to 100 μm and will make continuous global measurements of the Earth where the spacecraft is at the L-1 Lagrange point between the Earth and the Sun. The launch date is undetermined, since it was meant to be launched by the shuttle, but since the Columbia accident is in a holding state. For detectors they use heat sink receivers cooled to 40°K and SiPD photodiodes.

Solar Physics Infrared Missions

In the area of solar physics or SEC/LWS we have the recently proposed MIRAGES (France) mission proposed by Gerard Trottet and collaborators under the microsatellite programme of CNES. They propose to measure synchrotron emissions in the far infrared and γ -rays (bremsstrahlung) from relativistic 10 MeV electrons with $\tau \leq 1$ second time resolution during acceleration events such as solar flares.

Ground Based Infrared Missions

We now come to ground based observations. Here, most of the future efforts are being made to develop a very high tech interferometer capability using even larger telescopes than we have now. Sizes as big as 200 meter telescopes are being discussed. The science that is driving this capability falls under the heading of origins and the desire to detect terrestrial planets in other solar systems and ascertain whether such bodies can harbor life. Several technologies need to be developed to achieve this capability. We do not have the space to discuss such technologies other than to mention them. For example, the Palomar Testbed Interferometer's main purpose is to develop future fringe trackers, star trackers and active delay lines (Colavita et al., 1999). In most of these cases the measurements will be made at infrared wavelengths. To follow the Palomar effort we have the Keck Interferometer (Keck-I) on top of Mauna Kea, Hawaii, which is composed of two 10 Meter Keck Telescopes (see Figure 4) with four 1.8 meter outrigger telescopes. Here they want to develop planet detection, synthesis imaging, precision narrow-angle astrometry and detection of exozodiacal dust near stars. Will use cryogenic nulling interferometry, laser metrology (Gursel, 1993) and automation. Also, uses cascaded achromatic nulling interferometer to null central star. Alongside the Keck telescopes we have the University of Arizona's Large Binocular Telescope, which is made of two 8.4 meter mirrors on a beam. In the southern sky, the Very Large Telescope Array is being constructed by the Europeans in Chile and we have the U.S. version also based in Chile which is made of a pair of 6.5 meter telescopes. Using Heterodyne spectroscopy the Keck telescopes can also be used to measure winds on the Saturn moon Titan (Kostiuk et al., 2001).

Conclusions

In summary we can say there are a lot of missions in the next ten years that will use infrared detectors and that the field of Infrared Astronomy has a bright future and challenging future with applications in the area of astrophysics, planetary physics, Earth science and solar physics. The platforms for these various missions will be spacecraft, balloons, rovers, airplanes and ground based telescopes. Finally, the use of nanotechnology and MEMS technology will allow one to miniaturize future instrument concepts, while the Prometheus project could be a paradigm changing force toward the development of larger more power hungry instrument concepts with correspondingly greater spatial and spectral resolution, higher telemetry rate capabilities and order of magnitude advancements in science.

SESSION 1- Upcoming and Proposed Missions (Planetary and Earth Sciences)

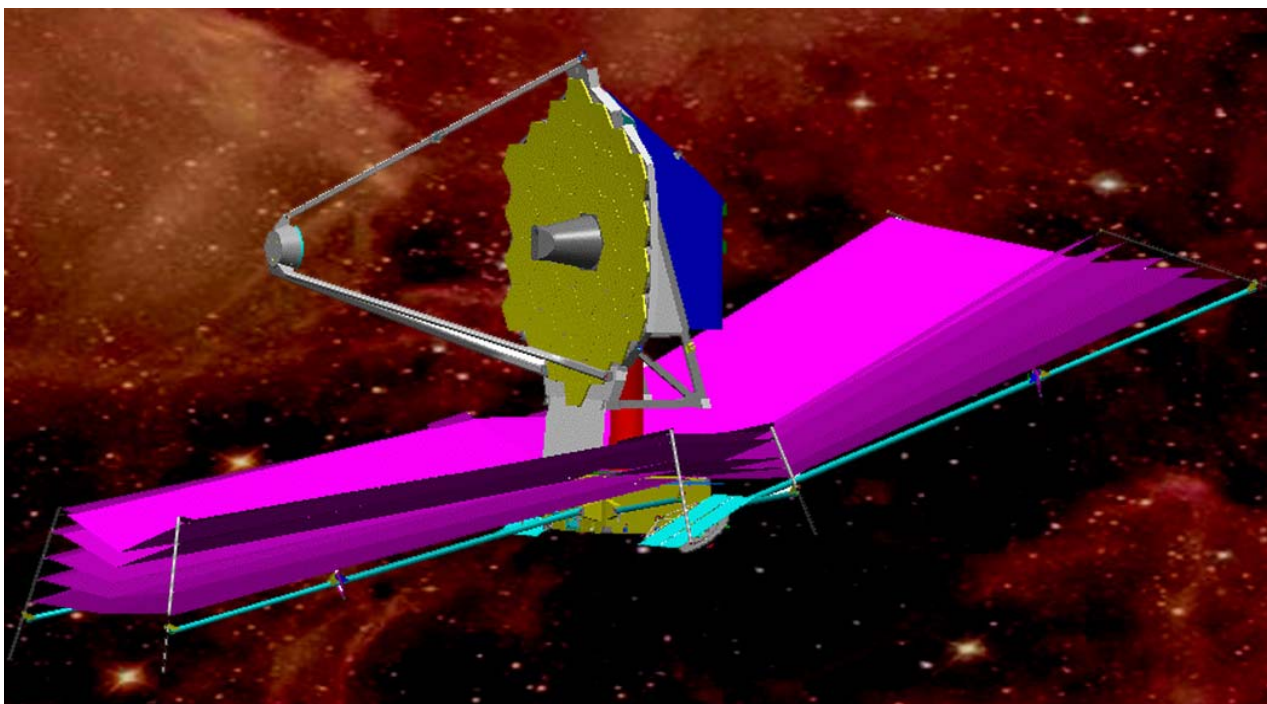


Figure 1. Artist rendition of James Webb Space Telescope showing heat shield to eliminate thermal input from Sun and Earth. Figure also shows 7 meter telescope composed of a network of smaller hexagonal mirrors.

SESSION 1- Upcoming and Proposed Missions (Planetary and Earth Sciences)



Figure 2. Artist rendition of the Jupiter Icy Moon Orbiter (JIMO) mission. The space fission reactor is at the tip far from the spacecraft body. Large radiators are used to dissipate excess heat. The ion engine clusters are shown.

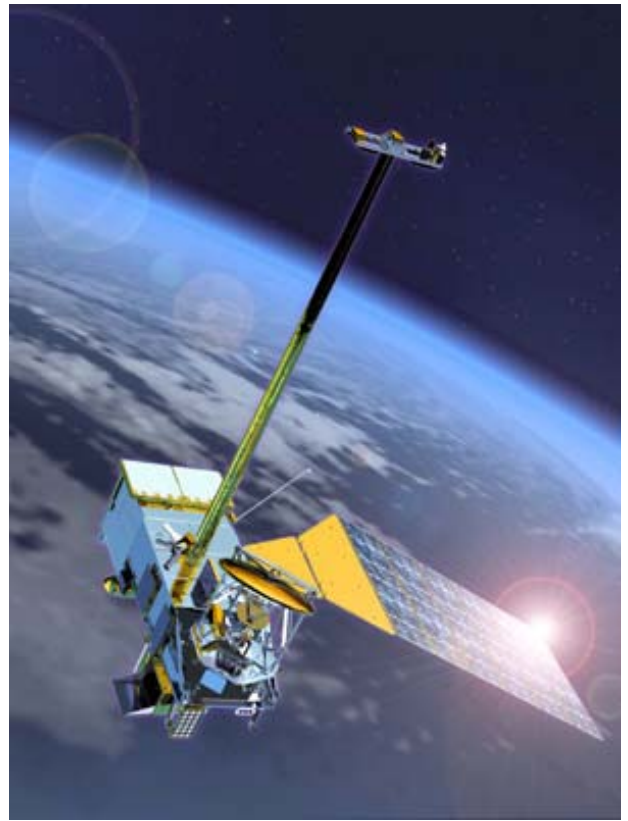


Figure 3. National Polar-Orbiting Operational Environmental System (NPOESS). Will use VIIRS = Visible / Infrared Imager / Radiometer Suite Instrument.

SESSION 1- Upcoming and Proposed Missions (Planetary and Earth Sciences)



Figure 4. The two 10 Meter Keck Telescopes on Mauna Kea, Hawaii.

SESSION 1- Upcoming and Proposed Missions (Planetary and Earth Sciences)

Table 1. ASTROPHYSICAL INFRARED MISSIONS

Launch Date	Mission Name	λ Coverage
2003	SIRTF = Space Infrared Telescope Facility	3-180 μm
2004	SOFIA = Stratospheric Observatory for Infrared Astronomy	5-20 μm
2004	IRIS – ASTRO-F (Japanese)	50-200 μm
2007	NGSS – Next Generation Sky Survey	3.5-23 μm
2007	ABE – Astrobiology Explorer	2.5-20 μm
2007	Planck – Measure the Microwave Background Radiation	300 μm – 1.2 cm
2007	Herschel = Far Infrared and Submillimeter Telescope	60-670 μm
2010	JWST = James Webb Space Telescope (was NGST)	1-27 μm
TBD	SIRCE – Survey of Infrared Cosmic Evolution	Not yet defined
2010	SPICA – Japanese proposed mission	5-200 μm
TBD	SAFIR – Single Aperture Far IR Observatory	Not yet defined
TBD	SPIRIT – Space Infrared Interferometric Telescope	Not yet defined
TBD	TPF – Terrestrial Planet Finder	7 – 20 μm
TBD	SPECS – Submm Probe of the Evolution of Cosmic Structure	Not yet defined

SESSION 1- Upcoming and Proposed Missions (Planetary and Earth Sciences)

Table 2. PLANETARY INFRARED MISSIONS

Launch Date	Mission Name	λ Coverage
2005	New Horizons (Kuiper Belt-Pluto Express)	1.25-3.5 μm
2006	DAWN (Vesta-Ceres)	1-5 μm
2008	South Pole-Aitken Basin Sample Return (SPA-SR)	1.25-2.5, 5-50 μm
2011	Jupiter Polar Orbiter with Probes (JPOP)	3-4, 7-14 μm
2014	Venus In Situ Explorer (VISE)	Not yet defined
2017	Comet Surface Sample Return (CSSR)	1-1000 μm
2012	Jupiter Icy Moons Orbiter (JIMO) or Prometheus	1-5, 5-50, 50-100 μm
2007	Mars Reconnaissance Orbiter (MRO)	1.05-40 μm
2009	Mars Smart Lander (MSL)	Not yet defined
2013	Titan Orbiter Aerover Mission (TOAM)	1.25-3.5, 7-1000 μm

Table 3. EARTH SCIENCE INFRARED MISSIONS

Launch Year	Mission Name	λ Coverage
2004	Aura – Upper Troposphere and Lower Stratosphere	3.2-15.4 μm
2005	ESSP/CALIPSO-Cloud Aerosol Lidar and Infrared Satellite Obs.	0.532-1.064, 8.7, 10.5, 12.0 μm
2005	Stratospheric Aerosol and Gas Experiment (SAGE-3)	0.28-1.04 μm , 1.55 μm
2005	New Millenium Program/Earth Observing-3 (NMP/EO-3)	NIR Lines
2007	Landsat Data Continuity Mission (LDCM)	0.45 – 12.5 μm
2006	NPOES Preparatory Project (NPP)	0.405 – 2.155 μm
TBD	DSCVR (Triana) – Global Earth Imaging	0.2 – 100 μm
2009	National Polar-Orbiting Operational Environmental Satellite System (NPOESS)	0.405 – 2.155 μm

SESSION 1- Upcoming and Proposed Missions (Planetary and Earth Sciences)

REFERENCES

- Arnold J.R., *Ice in the lunar polar regions*, J. Geophys. Res., **84**, 5659, 1979.
- E.E. Becklin, *Stratospheric Observatory for Infrared Astronomy (SOFIA)*, Proceedings of the ESA Symposium "The Far Infrared and Summillimetre Universe", 15-17 April 1997, Grenoble, France, ESA SP-401, 201, August 1997.
- M.M. Colavita et al., *The Palomar Testbed Interferometer*, ApJ, **510**, 1999.
- J.E.P. Connerney, M.H. Acuna, N.F. Ness and T. Satoh, *New models of Jupiter's magnetic field constrained by the Io flux tube footprint*, J. Geophys. Res., **103**, 11929, 1998.
- A. Coustenis, Th. Encrenaz, B. Bezard, G. Bjoraker, G. Graner, M. Dang-Nhu and E. Arie, *Modeling Titan's thermal infrared spectrum for high-resolution space observations*, Icarus, **102**, 240, 1993.
- Feldman et al., *Fluxes of fast and epithermal neutrons from Lunar Prospector: Evidence for water ice at the lunar poles*, Science, **281**, 1496, 1998.
- Flasar et al., *CIRS observations of polar hotspot in Jupiter's upper stratosphere*, Science, Manuscript in Preparation, 2003.
- D.B. Gallagher et al., *SIRTF Summary*, Proceedings of the SPIE, John Mather, Ed., **4850**, 17, 2003.
- Y. Gursel, *Laser metrology gauges for OSI*, Proceedings of SPIE conference on Spaceborne Interferometry, **1947**, 188, 1993.
- R. Hanel et al., *The Voyager Infrared Spectroscopy and Radiometry Investigation*, Space Sci. Rev., **21**, 129, 1977.
- R. Hanel et al., *Infrared observations of the Jovian System from Voyager 1*, Science, **204**, 32, 1979a.
- R. Hanel et al., *Infrared observations of the Jovian System from Voyager 2*, Science, **206**, 952, 1979b.
- R. Hanel et al., *Infrared observations of the Saturnian System from Voyager 1*, Science, **212**, 192, 1981.
- R. Hanel et al., *Infrared observations of the Saturnian System from Voyager 2*, Science, **215**, 544, 1982.
- R. Hanel et al., *Infrared observations of the Uranian System*, Science, **233**, 70, 1986.
- B. Conrath et al., *Infrared observations of the Neptunian System*, Science, **246**, 1454, 1989.
- Ingersoll et al., *Stability of polar frosts in spherical bowl-shaped craters on the Moon, Mercury and Mars*, Icarus, **100**, 40, 1992.
- T. Kostiuik et al., *Direct measurements of winds on Titan*, Geophys. Res. Lett., **28 (12)**, 2361, 2001.
- V. G. Kunde et al., *Exploring the Saturn System in the thermal infrared*, Space Sci. Rev., in press, 2003.
- Murchie et al., *CRISM: Compact reconnaissance imaging spectrometer for Mars on the Mars Reconnaissance Orbiter*, International Conference on Mars, 2003.
- Nozette et al., *The Clementine bistatic radar experiment*, Science, **274**, 1495, 1996.
- T. Satoh and J.E.P. Connerney, *Jupiter's H-3(+) emissions viewed in corrected jovimagnetic coordinates*, Icarus, **141 (2)**, 236, 1999.
- H.S Stockman. and J. Mather, *NGST: Seeing the first stars and galaxies form*, Galaxy Interactions at Low and High Redshift, IAU Symposia, **186**, 493, 1999.
- Watson et al., *The behavior of volatiles on the lunar surface*, J. Geophys. Res., **66**, 3033, 1961.

SESSION 1- Upcoming and Proposed Missions (Planetary and Earth Sciences)

PR32-INV4 *

Scripps-NISTAR–New Instrumentation for a Challenging Mission:
Earth Radiation Budget Measurements from L-1

Steven R. Lorentz (L-1 Standards and Technology, Inc.),

J.P. Rice (National Institute of Standards and Technology),

Francisco P.J. Valero (Scripps Institution of Oceanography, UCSD)

Space-based active cavity radiometers have traditionally been used to monitor solar irradiance, as in the ACRIM series of instruments and the VIRGO instrument on SOHO. They have also been used for Earth radiation budget experiments such as ERBE. Various improvements in radiometry at national standards laboratories such as NIST over the past few decades have opened up the possibility of making accurate total irradiance measurements from weaker sources such as the Earth through filtered channels, with higher accuracy than hitherto possible. The Scripps-NIST Advanced Radiometer (NISTAR) is an electrical-substitution radiometer that will fly aboard the Deep Space Climate Observatory mission. The role of NISTAR is to provide measurements of reflected solar and Earth thermal radiation as viewed from the Lagrange-1 point. Operation at L-1 affords the possibility of making simultaneous whole disk measurements, which is a new vantage point for Earth radiation budget measurements. This presentation will review the design and characterization of the Scripps-NISTAR instrument.

Keywords: Infrared, thermal, radiation, L-1, radiometer, cavity

IN-FLIGHT FAR-INFARED PERFORMANCE OF THE CIRS INSTRUMENT ON CASSINI

Conor A. Nixon¹, John C. Brasunas², Brook Lakew², Rainer Fetting³,
Donald E. Jennings², Ronald Carlson⁴, Virgil G. Kunde¹

¹ Department of Astronomy, University of Maryland, College Park, MD 20742

² NASA Goddard Space Flight Center, Code 693, Greenbelt, MD 20771

³ Institute für Mikrostrukturtechnik, Karlsruhe, Germany

⁴ S. S. A. I., 10210 Greenbelt Road, Suite 600, Lanham, MD 20706

ABSTRACT

The Composite Infrared Spectrometer (CIRS) on-board Cassini consists of two interferometers: a conventional Michelson for the mid-infrared; and a Martin-Puplett type in the far-infrared employing wire grid polarizers to split, recombine and analyze the radiation. The far-IR focal plane (FP1) assembly uses two thermopile detectors to measure the final transmitted and reflected beams at the polarizer-analyzer: if one fails, the interferometer can still operate, albeit with a lower efficiency. The combined effect is for good response from 10 to 300 cm^{-1} , and declining response to 600 cm^{-1} . This paper will examine in-flight performance of the far-IR interferometer, including NESR and response. Regular noise spikes, resulting from pickup from other electrical sub-systems has been found on the CIRS interferograms, and the removal of these effects is discussed. The radiometric calibration is described, and then we show how the calibration was applied to science data taken during the Jupiter flyby of December 2000. Finally, we discuss signal-to-noise on the calibrated spectra, emphasizing limitations of the current instrument and the potential for improvement in future missions.

INTRODUCTION

The CIRS instrument carried on-board the Cassini spacecraft mission to Saturn is the conceptual successor to the highly successful IRIS (Infrared Interferometer Spectrometer) instrument which flew on both Voyager spacecraft, although improved in almost every respect. CIRS was conceived and built by an international team including institutions in the USA, UK, France and Germany, and led by NASA Goddard Space Flight Center.

CIRS is a dual interferometer, and has been previously described in the literature^{1,2}. The Michelson mid-infrared interferometer and the Martin-Puplett type far-infrared interferometer both share a common mirror scan mechanism, reference laser and telescope assembly, although the beamsplitters and detectors are quite different. The telescope consists of a 50 cm F/6 paraboloidal primary mirror and 7.6 cm diameter hyperboloidal secondary mirror, both of beryllium. A field splitting mirror divides the radiation into the two interferometers. The far-IR radiation then passes through a solar-blocking filter, collimator and folding flat before reaching the polarizing beam splitter. The solar blocker rejects rays short-ward of 16.7 microns.

The input polarizer, beamsplitter and output analyzer are each 1 micron diameter photolithographic copper wires with a spacing of 2 micron, deposited on mylar. These give near 100% efficiency from 10 to 300 cm^{-1} , and good though declining efficiency from 300 to 600 cm^{-1} , the limit of the nominal range.

PRE-PROCESSING OF RAW INTERFEROGRAMS

CIRS interferograms (IFMs) suffer from several distinct types of noise interference. Firstly, there is a sine wave ripple on the IFM baseline, which was seen intermittently between launch and Jupiter flyby, with varying period and amplitude. Because of its transient nature, it has not been well characterized, although during the science phase of the Jupiter flyby its amplitude had diminished so that it did not significantly affect performance.

¹ Contact information for C.A. Nixon- Email: conor.nixon@gsfc.nasa.gov

SESSION 1- Upcoming and Proposed Missions (Planetary and Earth Sciences)

The second and third types are repetitive sequences of sharp spikes, or delta functions, which appear as a ‘comb’ on the IFMs. These have periods (frequencies) of 0.125 seconds (8 Hz) and 2.0 seconds (0.5 Hz) respectively. Both are caused by the CIRS Bus Interface Unit (BIU), which is queried 8 times a second by the spacecraft Command Data Subsystem (CDS), on the spacecraft clock signal pulses. Each query causes a small spike. Then, every 2 seconds data is transferred from CIRS to the CDS, which causes a larger spike.

Only the 0.5 Hz BIU interface spikes are large enough and repeatable enough to be treated by algorithmic methods at the present time. Fig. 1 (‘before’) shows a typical far-IR IFM before spike removal. CIRS IFMs are partially double-sided, consisting of a short scan at negative path difference and then a much longer scan at positive path difference after the zero path difference (ZPD) point, at sample 90. The first step in spike removal is to create a spike comb (shown offset above the IFM) having the correct period. This comb is then cross-correlated with the IFM to determine the best-fitting absolute offset.

Spikes may sometimes be offset by ± 1 sample from the expected position, due to the discretization process. To correct for this, a statistical technique is also used to hunt for spikes, defined as noise peaks above $2.5\text{-}\sigma$ in amplitude. If a $2.5\text{-}\sigma$ peak occurs immediately before or after a predicted spike position, then the comb spike is moved. Statistically detected positions are labeled below the IFM on Fig. 1.

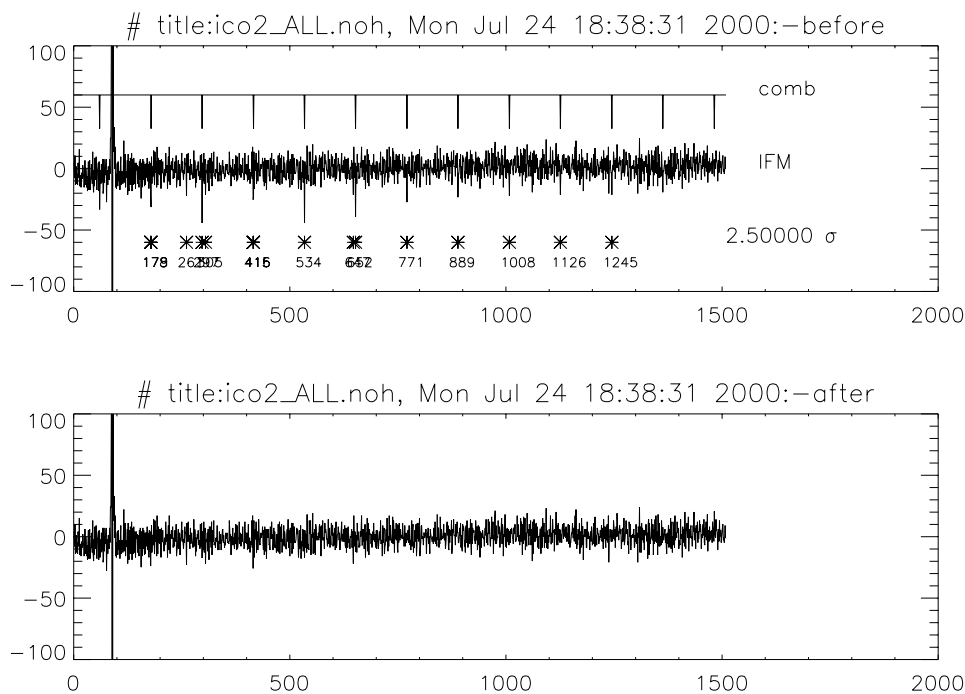


Figure 1: Example of removal of interference spikes by comb technique.

Finally, the comb amplitude is scaled to the mean value of the IFM at the predicted positions. The resulting comb is the best-guess model of the 0.5 Hz spike pattern inherent in the data. This comb is subtracted from the IFM, resulting in a ‘cleaned’ or ‘noise-filtered’ IFM, as shown in Fig. 1 (‘after’). Clearly, much of the regular spike pattern has been removed.

RADIANCE CALIBRATION

The most important calibration task concerns the absolute radiance, expressed by the spectral responsivity. In-flight calibration of the responsivity traditionally has been achieved by exposing the instrument to two well-known calibration sources. One is usually deep space, which for this purpose is assumed to be a perfect sink. The second source is often a blackbody of accurately known temperature. Perfect linearity and thermal stability of the instrument are required. An alternate approach, which was well demonstrated on Voyager, is to thermostat the

SESSION 1- Upcoming and Proposed Missions (Planetary and Earth Sciences)

instrument, the primary and the secondary mirror of the telescope at the same low temperature. Again, one calibration source is deep space while the other is replaced by a virtual blackbody at the instrument temperature. This method of calibration is directly applicable to the far infrared interferometer since all elements, including the detector, are precisely at the same temperature.

The spectral responsivity in the far-IR is simply the complex FFT power spectrum when looking at deep space, divided by the difference in Planck function radiance between space and the instrument (170 K):

$$r(\nu) = \frac{FFT(I_{cold})}{B_{cold}(\nu) - B_{instr}(\nu)} \dots (1)$$

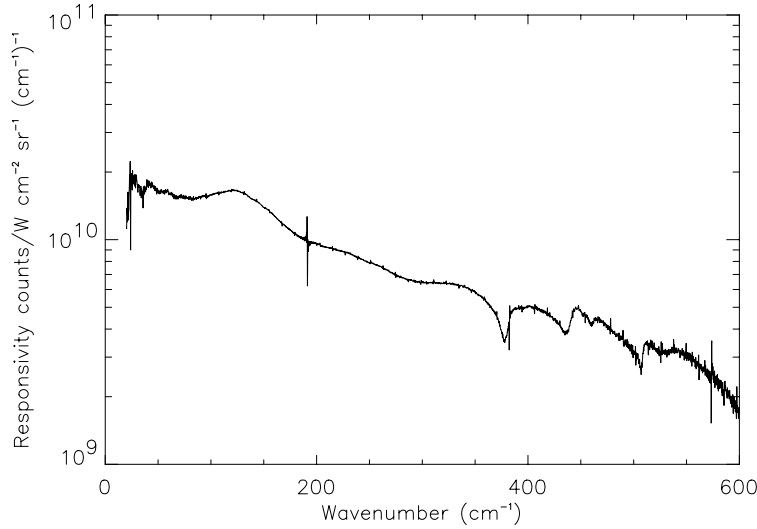


Figure 2: CIRS spectral responsivity.

Fig. 2 shows the CIRS responsivity in the far-IR. There are several important features. Firstly, the response declines by 1 order of magnitude from 20 cm⁻¹ to 600 cm⁻¹, as a combination of effects from the various optical elements, coatings and detectors; mainly the wire grid polarizer/analyzers, but also the digital filter beyond 500 cm⁻¹. Secondly, the deep, broad absorption features seen at 380, 440 and 510 cm⁻¹ arise from the mylar substrate on which the grids are deposited. Thirdly, the most prominent narrow features arise from the 8 Hz interference (191 cm⁻¹), along with its harmonics at 16 Hz (382 cm⁻¹) and 24 Hz (573 cm⁻¹). Finally, the pattern of smaller sharp lines above and below the continuum which become noticeable after 400 cm⁻¹ result from the 0.5 Hz interference, having a spacing of 11.9 cm⁻¹.

The responsivity, once determined, is used to calibrate science ('target') IFM scans as follows:

$$B_{target} = B_{cold} - \frac{FFT(I_{target} - I_{cold})}{r(\nu)} \dots (2)$$

EARLY RESULTS FROM JUPITER FLYBY

Fig. 3 shows a typical CIRS far-IR spectrum of Jupiter at 0.5 cm⁻¹ resolution. 100 spectra (each a 50-second scan) from January 2001 have been co-added to reduce random noise and emphasize features in the data. The very broad absorption feature from 250-500 cm⁻¹ is the S(0) collisionally-induced continuum of H₂; part of the S(1) absorption is visible from 500-600 cm⁻¹. To show other absorptions more clearly, a 25 cm⁻¹ smoothing kernel was applied to the data to create a rough continuum fit, which was then subtracted from the spectrum. The result is plotted as the discontinuous line in the middle of the figure, which shows the molecular absorption features more clearly.

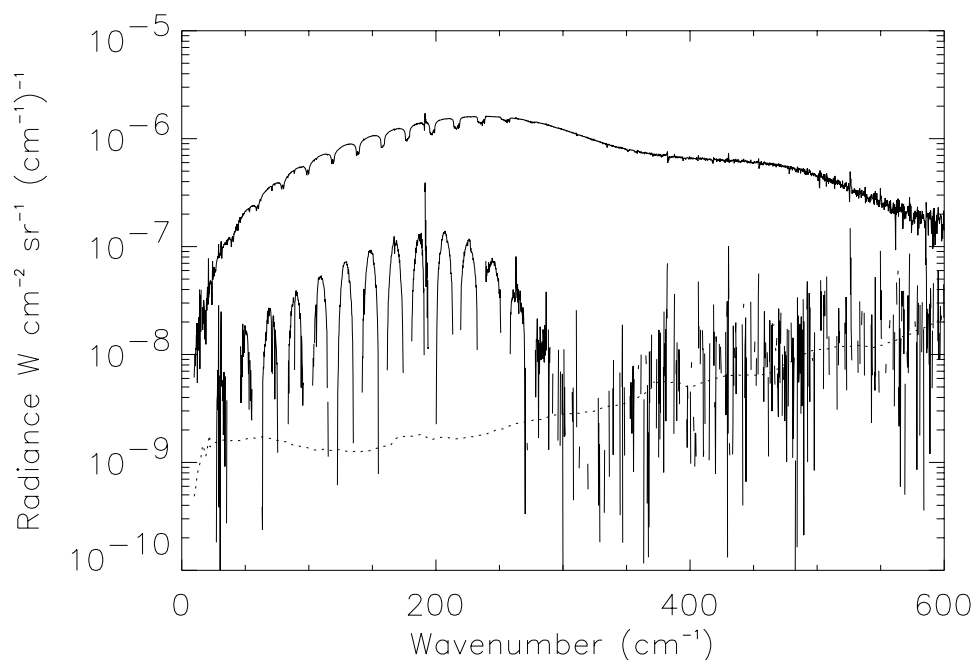


Figure 3: Far-infrared spectrum, and noise comparison.

For comparison, the 100-spectrum smoothed NESR is also plotted (dotted line). The NESR is the limit of detection of weak features. Clearly, the NH_3 and PH_3 absorption features ($20\text{--}250\text{ cm}^{-1}$) are well above the noise level. CIRS has also detected pure rotational lines of CH_4 in the $70\text{--}120\text{ cm}^{-1}$ region, for the first time on Jupiter. However, beyond 350 cm^{-1} the difference spectrum is equivalent to the noise, and no features are seen in this average. Co-adding up to 1300 spectra has enabled detections of HD lines at 89 and 265 cm^{-1} , at S/N of 8 to 10. Other HD and H_2 features are either masked by stronger bands or mingled with noise interference. Finally, ISO has seen emission lines of water³ at $100\text{--}250\text{ cm}^{-1}$, which are below the threshold of sensitivity achieved thus far with CIRS.

CONCLUSIONS

At Jupiter CIRS demonstrated that it will meet the requirements of the Cassini IR investigation and will achieve the science goals of its prime mission at Saturn. In the future, improvements in sensitivity for this type of far-IR FTS instrument will become possible with technology currently under development. These will be valuable in reducing the observation times (co-adding) required to detect weak lines in the $10\text{--}600\text{ cm}^{-1}$ spectral region on Jupiter and the other giant planets. Smaller averages will enable spatial mapping of D/H and gaseous abundances in the same time as present global detections. Greater sensitivity will arise from improvements in technology of the thermal detectors, and also optical components such as far-IR beamsplitters. We recommend that future instruments, before launch, carefully look for and eliminate the type of system-related interferences seen by CIRS, which add to the difficulty of reducing data.

REFERENCES

1. V. Kunde *et al.*, *Cassini Infrared Fourier Spectroscopic Investigation*, Proc. of Cassini/Huygens: A Mission to the Saturnian System, SPIE Proceedings, Vol. 2803, p162, 1996.
2. J.C. Brasunas and B. Lakew, *Long-term stability of the Cassini Fourier transform spectrometer en route to Saturn*, Recent Research Developments in Optics, Research Signpost, Kerala, India, 2003.
3. E. Lellouch *et al.*, *The Origin of Water Vapor and Carbon Dioxide in Jupiter's Stratosphere*, Icarus, Vol. 159, p112, 2002.

SUPERCONDUCTING TES BOLOMETERS ABOVE 1K

P.L. Richards¹

Department of Physics, University of California, Berkeley 94720, USA

ABSTRACT

The discovery of High T_c superconductivity led to the exploration of current-biased superconducting bolometers cooled with liquid nitrogen and optimized to view 300K backgrounds at wavelengths beyond $10\text{ }\mu\text{m}$. If such detectors reach the thermal fluctuation noise limit they would be a great improvement over room temperature pyroelectric detectors and thermopiles for many applications. The superconducting detectors fabricated in the 1990's had a number of operational problems, and were typically slow because of the large heat capacity of the materials used. However, voltage-biased (TES) superconducting bolometers operated at low temperatures now show superior operating characteristics and enhanced response speed due to electrothermal feedback. This approach may help higher temperature thermal detectors reach their theoretical potential. We have built and tested a Nb-based TES bolometer cooled with liquid helium at 4.2K. This device is optimized for the background power appropriate for far-infrared spectroscopy at frequencies below 100 cm^{-1} with a commercial rapid-scan Fourier transform spectrometer. The sensitivity of our TES detector is a factor ~ 10 better than that of a semiconducting bolometer optimized for the same operating temperature, linearity and speed of response.

Long wavelength infrared detectors are required for planetary missions which can achieve photon noise limited values of D^* when viewing background temperatures of a few hundred K in photometric bandwidths. Since the power, weight, and complexity required to cool infrared detectors increases rapidly with decreasing temperature, there is a need for moderately cooled long wavelength detectors for such missions. Detector arrays with good operating characteristics would significantly improve imaging and spectroscopy, especially of the cooler outer planets.

Infrared photon detectors for wavelengths $\lambda < 10\mu\text{m}$, such as photovoltaic and QWIP devices, function well when cooled to 77K. They are widely used for diffraction limited imaging of sources with $T \sim 300\text{K}$. They typically produce values of D^* close to the photon noise limit. Narrower band gaps are required for longer wavelengths. Thermal excitations at 77K then cause significant dark current and seriously degrade the performance of photon detectors. The extrinsic long wavelength photoconductors such as Si:As, Si:Sb, Ge:Ga and stressed Ge:Ga, which are used out to $200\mu\text{m}$ can be photon noise limited on much cooler sources, but require much lower operating temperatures. The far infrared detectors on SIRTf, for example, are operated from $1.5 < T < 20\text{K}$.

Bolometric detectors are used for astrophysical applications at longer wavelengths. They are typically cooled to temperatures of 0.3, or even 0.1K. Detectors such as room temperature pyroelectric detectors with $D^* \sim 3 \times 10^8\text{ cm Hz}^{1/2}\text{ W}^{-1}$ and thermopiles cooled to 170 K with $D^* \sim 3 \times 10^9\text{ cm Hz}^{1/2}\text{ W}^{-1}$ are widely used for $\lambda > 25\mu\text{m}$. These values of D^* are far below the values required for photon noise limited detection of 300K sources.

The discovery of high T_c superconductivity in YBCO with $T_c = 90\text{K}$, caused considerable excitement in the infrared detector community. Early reports of a novel photon detection mechanism sensitive at 77K proved illusory. There were many studies of a relatively insensitive response with a time constant of a few ns which was excited by pulsed lasers. This was later shown to be the time constant for the thermal response

¹ Contact information for P.L. Richards - Email: richards@physics.berkeley.edu

SESSION 2A- Far IR/Sub-mm Thermal Detectors—New Concepts and Materials

of the YBCO film relative to the substrate¹. The Berkeley group has actively developed superconducting bolometers for many years. This paper summarizes many of these developments. Conventional current-biased superconducting transition edge bolometers with a heat sink temperature of 77K were proposed by the author² and have been built by several groups. A review article by the author describes some of this early work³.

High film quality proved necessary for the narrow superconducting transitions that gave high responsivity, and especially for low noise. Since heat capacities of most materials at 90K are a substantial fraction of their full high-temperature limit, it is necessary to minimize the thickness of the YBCO film and of the substrate. However, most of the substrates on which high quality superconducting films can be grown are too fragile for thin bolometer substrates. It is difficult to produce high quality films on membranes of Si or low stress silicon oxy-nitride (LSN). Sapphire was frequently chosen as a compromise between strength and film quality. It has the advantage of good thermal conductivity at 90K.

Conventional composite bolometers were made using this technology, which gave significantly lower NEP in the far infrared than a 300K pyroelectric detector, but which had significant operational problems^{4,5}. Detectors with thermal conductance G optimized for viewing 300K, had long thermal time constants τ of 100 ms or more because of their high heat capacity. It proved difficult to increase the value of G without adding more heat capacity. The roll-off frequency was close to, or even below the knee of the $1/f$ noise spectrum. The relatively low impedances of a few hundred Ohms meant that amplified voltage noise was a problem. Antenna-coupled microbolometers were fabricated and tested.^{6,7} The thermal spreading resistance into the substrate from the small YBCO provided a time constant $\tau \sim 10^{-3}$ s.

These YBCO bolometers suffer from the weaknesses common to all current-biased superconducting transition edge bolometers. Because the resistance rises rapidly with T at the operating point on the transition, the power dissipated by the bias $P_B = I_B^2 R$ also increases with T . This is a positive electro-thermal feedback, which further increases the temperature. To keep the bolometer stable, the bias current I_B must be small enough that the effective loop gain of the feedback is less than unity. This requirement limits the detector responsivity and increases the combination of Johnson noise and amplifier noise to the NEP. Both the low T_C and high T_C versions of this detector require very precise regulations of the bath temperature and have a narrow dynamic range because their operating point (and thus the responsivity) are very sensitive to the level of incident background power. These fundamental features are largely responsible for the fact that current-biased superconducting transition edge bolometers have been rarely used since their introduction in 1942.

In 1995, K. Irwin pointed out that the sensitivity of current-biased TES calorimeters for detection of dark matter (or x-ray photons) could be improved if they were biased with a constant voltage. The electrothermal feedback is then negative. It keeps the sum of the infrared power P_{IR} plus the bias power $P_B = V_B^2/R$ fixed so that the operating point is stable. This idea was quickly applied to infrared bolometers. The review article on bolometers by the author³ suffers from the defect that it did not anticipate the importance of voltage-biased devices with large (negative) electrothermal feedback. In hindsight, it is possible to feel foolish. The article did contain the words “in principle, thermal runaway in a superconducting bolometer can be avoided by using a constant voltage bias and measuring the bolometer current.” There was also a discussion of SQUID readouts!

Electrothermal feedback in a bolometer can be described by the analogy to an operational amplifier with voltage gain A in parallel with a feedback link with voltage gain B . The loop gain \mathcal{L} of such a circuit is AB . The circuit gain, which describes the ratio of output to input is $(1+AB)^{-1}$. The current responsivity of a voltage biased TES bolometer, calculated using conservation of energy, can be written $S_I = \mathcal{L}/V_B (1 + \mathcal{L} + i\omega\tau_0)$, where the bare time constant $\tau_0 = C/G$ for a single node model of the bolometer. The quantity that plays the role of a loop gain is $\mathcal{L} = P_B \alpha/GT$, where $\alpha = TdR/RdT$ is a dimensionless measure of the steepness of the $R(T)$ curve at the bias point on the transition. The largest values of α and \mathcal{L} obtainable with a given film can be estimated as follows: If the $R(T)$ curve is fitted to a straight line at its steepest point and the intercepts of this line at $R=0$ and $R=R_N$ are separated by ΔT , then the maximum value of α is $\sim T_C/\Delta T$. Since about half of the temperature rise $T_C - T_S$ of a voltage biased TES is due to the bias, $P_B \sim G(T_C -$

SESSION 2A- Far IR/Sub-mm Thermal Detectors—New Concepts and Materials

$T_S)/2$, then $\mathcal{L} = G(T_C - T_S)/2\Delta T$. For a low T_C superconductor with a sharp transition, \mathcal{L} can vary from a few hundred to a few thousand. Smaller values are typical of high T_C films.

In the large gain limit, $\mathcal{L} \gg 1$, the current responsivity given by $S_I = -1/V_B$ is independent of changes in the infrared power loading and the heat sink temperature T_S . This responsivity rolls off when $\omega\tau_0 > \mathcal{L}$, so the single node time constant τ_0 is reduced by the loop gain giving an effective $\tau = \tau_0/\mathcal{L} = C/\mathcal{L}G$. However, the thermal feedback does not reduce the delay in the conduction of heat from the radiation absorber to the thermistor (called the internal thermal time constant). The voltage biased TES is fast, linear, and the responsivity is stable in the presence of changes in T_S or P_{IR} . The output of this detector is the current required to keep $P_B + P_{IR}$ fixed. It is read out with a SQUID ammeter which operates at the bolometer temperature, dissipates very little power, and has large noise margin. With collaborators at Stanford and NIST, the Berkeley Group reported the performance of the first voltage-biased TES bolometer,⁸ which was a hot electron device with $T_C \sim 100\text{mK}$, published the theory of TES bolometers,⁹ pointed out the possible usefulness of high T_C TES bolometers,¹⁰ made detailed comparisons between theory and the performance of a test device,⁹ fabricated and tested fully lithographed spider-web TES bolometers on LSN membranes,¹¹ designed and tested mesh absorber-coupled TES bolometers suitable for close packed arrays and fabricated 1024 element closed packed array structures,¹² gave a distributed thermal circuit explanation of apparent excess noise in suspended TES bolometers,¹³ and are working on dual-polarization antenna-coupled TES bolometers with strip-line band pass filters. Their early papers used the descriptive term VSB for the voltage-biased superconducting transition edge bolometer rather than the currently more popular term TES, which is ambiguous about both the bias mode and even the kind of device.

Application of TES bolometer to large arrays depends on the development of output multiplexers which allow a row of bolometers to be read out through a single SQUID ammeter. The NIST group¹⁴ has developed a time-domain multiplexer which uses a SQUID switch at each detector to sequentially switch the outputs of the detectors to the ammeter. The Berkeley group¹⁵ is working on a frequency-domain multiplexer which biases each detector in the row with a different frequency, adds the signals and amplifies them with a single SQUID ammeter. The signals are then separated with ambient temperature lock-in demodulators. One or both of these output multiplexers must work well for the TES technology to live up to its potential.

The Berkeley group has been funded by the NSF to build a 300 pixel array of horn-coupled TES bolometers for the new 12m APEX telescope in Chile and a 1000 pixel array of multiplexed horn-coupled bolometers for the new 7m South Pole Telescope. Both arrays will make unbiased searches for thousands of clusters of galaxies at 150GHz using the Sunyaev-Zeldovich effect. Once clusters are found and redshifts determined optically, the data will be used to deduce the expansion history of the universe and thus place limits on the equation of state of dark energy.

The Berkeley group is also developing an experiment called Polar Bear to measure the polarization anisotropy of the Cosmic Microwave Background using a dedicated $\sim 2.5\text{m}$ telescope. The Polar Bear focal plane will be developed in two stages, but will ultimately have ~ 900 pixels consisting of dual-polarization antenna-coupled TES bolometers with integrated strip-line band-pass filters. Other groups are also developing powerful receivers. The most spectacular is the SCUBA-II receiver with two 5,000 pixel arrays of close-packed multiplexed bolometers being developed by NIST and collaborators¹⁴.

The highest temperature voltage-biased TES bolometer made to date has a heat sink temperature $T_S = 4.2\text{K}$. It was developed by the Berkeley group for Fourier transform spectroscopy in the far infrared.¹⁶ Both the linearity and the speed of the TES device are important for this application. This bolometer is based on a Nb transition edge sensor with $T_C = 8.1\text{K}$. It will operate for absorbed infrared power up to $3 \times 10^{-6}\text{W}$ and has an absorber area of 7mm^2 . The response is inherently linear and the noise equivalent power, $\text{NEP} = 1.2 \times 10^{-13}\text{W Hz}^{-1/2}$ is dominated by thermal fluctuation noise. This NEP is at least a factor 10 better than that expected for a conventional 4.2K semiconductor bolometer which is optimized for far infrared Fourier Transform Spectroscopy in the far infrared with 1% saturation at the same infrared power. The optical response time $\tau = 1.2\text{ms}$ is dominated by the internal thermalization time. A smaller version of this

SESSION 2A- Far IR/Sub-mm Thermal Detectors—New Concepts and Materials

bolometer could be useful for diffraction-limited spectroscopy of small samples throughout the infrared, or even mid-infrared imaging. Estimates suggest that values of detectivity $D^* > 10^{11} \text{ cm in Hz}^{-1/2} \text{ W}^{-1}$ and time constants approaching 270 μs could be achieved.

The successful experience with low T_C voltage biased TES devices suggests that the time has come to seriously investigate high T_C voltage biased TES bolometers. The most promising superconductors for high quality films appears to be MgB_2 with $T_C = 40\text{K}$ and YBCO with $T_C = 90\text{K}$. The MgB_2 bolometer would be most sensitive with $T_S = 20\text{K}$ and the YBCO bolometer with $T_S = 45\text{K}$, though somewhat higher values of T_S would still be useful. The film quality must be high for large ℓ and low $1/f$ noise. The bolometer architecture should be designed to minimize the time delay in the transfer of heat from the absorber to the thermistor (internal time constant) for maximum speed. Feedback should be effective in reducing the external time constant

High T_C SQUID's exist with good enough performance to read out a high T_C TES bolometer. They are less available than low T_C SQUIDS and significant effort may be required to implement them. This is certainly true for a possible high T_C SQUID multiplexer. Such a development should not be undertaken until it is very clear that the properties of a high T_C voltage biased TES bolometers are favorable for important applications. Initially, the performance of the bolometers can be tested with a commercial Nb SQUID operated at 4.2K. One approach is to use planar lithographed flux transformer with a high T_C primary at temperature T_S separated by a small gap from a planar lithographed Nb secondary at 4.2K connected to the SQUID input. Since zero resistance is not required in these circuits, they need not be monolithic high T_C superconducting films.

REFERENCES

1. M. Nahum, S. Verghese, P.L. Richards, and K. Char, *Thermal Boundary Resistance for $\text{YBa}_2\text{Cu}_3\text{O}_{7-x}$ Films*, Seventh Int. Conf. on Phonon Scattering in Condensed Matter, digest of technical papers, p. 49 (1992).
2. P. L. Richards, J. Clarke, R. Leoni, Ph. Lerch, S. Verghese, M. R. Beasley, T. H. Geballe, R. H. Hammond, P. Rosenthal, and S. R. Spielman, *Feasibility of the High T_C Superconducting Bolometer*, Appl. Phys. Lett. **54**, 283 (1989).
3. P. L. Richards, *Bolometers for Infrared and Millimeter Waves*, J. Appl. Phys. **76**, 1 (1994).
4. S. Verghese, P.L. Richards, K. Char, and S.A. Sachtjen, *Fabrication of an Infrared Bolometer With a High T_C Superconducting Thermometer*, Applied Superconductivity Conf. Proc., IEEE Trans. Magn. **MAG-27**, 3077 (1991).
5. S. Verghese, P.L. Richards, S.A. Sachtjen, and K. Char, *Sensitive Bolometers Using High- T_C Superconducting Thermometers for Wavelengths 20-300 μm* , J. Appl. Phys. **74**, 4251 (1993).
6. Qing Hu and P. L. Richards, *Design Analysis of a High T_C Superconducting Microbolometer*, Appl. Phys. Lett. **55**, 2444 (1989).
7. M. Nahum, Qing Hu, P.L. Richards, S.A. Sachtjen, N. Newman, and B.F. Cole, *Fabrication and Measurement of High T_C Superconducting Microbolometers*, Applied Superconductivity Conf. Proc., IEEE Trans. Magn. **MAG-27**, 3081 (1991).
8. A.T. Lee, P.L. Richards, S.-W. Nam, B. Cabrera, and K.D. Irwin, *A Superconducting Bolometer with Strong Electrothermal Feedback*, Appl. Phys. Lett. **69**, 1801 (1996).
9. Shih-Fu Lee, Jan M. Gildemeister, Warren Holmes, Adrian T. Lee, and P.L. Richards, *A Voltage-Biased Superconducting Transition Edge Bolometer with Strong Electro Thermal Feedback Operated at 370 mK*, Applied Optics **37**, 3391 (1998).
10. A.T. Lee, J.M. Gildemeister, S.F. Lee, and P.L. Richards, *Voltage-Biased High- T_C Superconducting Infrared Bolometers with Strong Electro Thermal Feedback*, IEEE Trans. Appl. Superconductivity **7**, 2378 (1997).

SESSION 2A- Far IR/Sub-mm Thermal Detectors–New Concepts and Materials

11. J.M. Gildemeister, A.T. Lee, and P.L. Richards, *A Fully Lithographed Voltage-Biased Superconducting Spiderweb Bolometer*, Appl. Phys. Lett. 74, 868 (1999).
12. J.M. Gildemeister, A.T. Lee, P.L. Richards, *Monolithic Arrays of Absorber-Coupled Voltage-Biased Superconducting Bolometers*, Appl. Phys. Lett. 77, 4040 (2000).
13. J.M. Gildemeister, A.T. Lee, P.L. Richards, *A Model for Excess Noise in Voltage-Biased Superconducting Bolometers*, Appl. Optics-OT. 40, 6229 (2001).
14. K. Irwin et al: *Multiplexers for Cryogenic Detector Arrays*, Proc. International Workshop on Thermal Detectors –TDW03, Washington, DC, USA, in press.
15. H. Spieler, *Frequency Domain Multiplexing for Large-Scale Bolometer Arrays*, in *Proceedings Far-IR, Sub-mm & mm Detector Technology Workshop*, Wolf J., Farhoomand J. and McCreight C.R. (eds.), NASA/CP-211408, 2002.
16. J. T. Skidmore, J. Gildemeister, A. T. Lee, M. J. Myers, and P. L. Richards: Superconducting bolometer for far-infrared Fourier transform spectroscopy, Appl. Phys. Lett. 82, 469 (2003).

Ultimate sensitivity of superconducting single-photon detectors in the visible to infrared range

A. Verevkin¹, J. Zhang, A. Pearlman, W. Slysz, and Roman Sobolewski
University of Rochester, Rochester, NY 14627-0231, USA

A. Korneev, P. Kouminov, O. Okunev, G. Chulkova, and G. Gol'tsman
Moscow State Pedagogical University, Moscow 119435, Russia

ABSTRACT

We present our quantum efficiency (QE) and noise equivalent power (NEP) measurements of the meander-type ultrathin NbN superconducting single-photon detector in the visible to infrared radiation range. The nanostructured devices with 3.5-nm film thickness demonstrate QE up to $\sim 10\%$ at $1.3 - 1.55 \mu\text{m}$ wavelength, and up to 20% in the entire visible range. The detectors are sensitive to infrared radiation with the wavelengths down to $\sim 10 \mu\text{m}$. NEP of about $2 \times 10^{-18} \text{ W/Hz}^{1/2}$ was obtained at $1.3 \mu\text{m}$ wavelength. Such high sensitivity together with GHz-range counting speed, make NbN photon counters very promising for efficient, ultrafast quantum communications and another applications. We discuss the origin of dark counts in our devices and their ultimate sensitivity in terms of the resistive fluctuations in our superconducting nanostructured devices.

INTRODUCTION

Superconducting single-photon detectors (SSPDs) [1] based on ultrathin, submicron-width NbN superconducting meander lines have already found several practical applications [2-4], based on their picosecond-range response time, low jitter, and low dark counts. The SSPD ability to efficiently count single photons has been explained within a phenomenological hot-electron photoresponse model [1, 5]. This model describes formation and subsequent growth of a resistive hotspot in a very narrow, current-biased superconducting stripe upon the single-photon absorption event [6], [7]. The hotspot formation is followed by supercurrent redistribution, leading to a transient voltage response signal [8]. The NbN-based SSPDs are able to efficiently detect single photons in the wavelength range from ultra-violet to near infrared (IR) [4], [9] at a GHz-range counting speed [10]. They work at the 4-K temperature level, which allows a long-term, no-interruption work, when using modern closed-cycle refrigerators. Their fiber-optical coupling makes easy to perform room temperature photon-counting experiments.

The aim of this presentation is to demonstrate the performance of our new SSPDs, fabricated from 3.5-nm-thick NbN films. We found a significant (up to two orders of magnitude) increase of quantum efficiency (QE) in such detectors, as compared with the 10-nm-thick structures [4]. Our new 3.5-nm devices exhibit QE up to $\sim 10\%$ at near IR and above 15% in the visible range. We associate such an improvement of QE with the large increase of a hotspot size in thinner NbN films. We also present here the sensitivity performance of our detectors. Knowing the dark counting rate and its bias current dependence we were able to determine a noise equivalent power (NEP), which is widely regarded to be the best measure of the detector sensitivity. For our best devices the NEP reaches $2 \times 10^{-18} \text{ W/Hz}^{1/2}$ at $1.3 \mu\text{m}$ wavelength.

EXPERIMENTAL DETAILS

The devices used in our experiments were $10 \times 10\text{-}\mu\text{m}^2$ -area size NbN superconducting meander-type structures with the film thickness $d = 3.5 \text{ nm}$, the nominal stripe width $w \sim 200 \text{ nm}$, and the gap between the meander stripes of about 300 nm (filling factor ~ 0.4). The details of our fabrication process are described in [11]. Critical current density of devices varied within $5\text{-}8 \text{ MA/cm}^2$ range at 4.2 K and superconducting transition temperature T_c was about 10 K .

Contact information for A. Verevkin- Email: verevkin@ece.rochester.edu

SESSION 2A- Far IR/Sub-mm Thermal Detectors—New Concepts and Materials

The devices under study were wire-bonded to a 50- Ω microwave stripe line and mounted on a cold base plate maintained at 4.2 K in vacuum inside either a liquid-helium dewar or a two-stage cryocooler. Voltage pulses generated by the SSPD under illumination were amplified by 1-2 GHz bandwidth, room-temperature amplifier and fed to a photon counter. Radiation from different laser sources was delivered inside the cryostat through free space, or using a standard multimode 50- μm -core-diameter fiber, and focused by collimator on the device plane inside the cryostat. In *NEP* measurements the incoming 1.3- μm radiation from a luminescence diode was filtered inside cryostat with a cold (4.2 K) 0.9-1.6 μm bandpass filter to block long-wavelength thermal background as well as any parasitic visible light.

EXPERIMENTAL RESULTS

Our latest 3.5-nm-thick devices demonstrate significantly larger *QE*, as compared to the previous, 10-nm-thick devices [3]. The improvement is about two orders of magnitude in the visible range, and even larger for IR photons. Figure 1 presents *QE* versus wavelength for a $10 \times 10\text{-}\mu\text{m}^2$ area, 3.5-nm-thick NbN SSPD. We believe that in the visible range our latest SSPDs have already reached the limiting intrinsic *QE*, corresponding to counting of all photons incident upon the device's superconducting stripe. As the result, *QE* tends to be independent of radiation wavelength in the visible range. In addition, the entire spectral dependence shown in Fig. 1 is significantly flatter than the dependence characteristic for the 10-nm-thick devices [4]. The reason for such a significant improvement of *QE* in the thinner SSPDs is quite obvious – the normal resistance hotspot area in those devices is significantly larger, as it should be roughly inversely proportional to the film thickness [6].

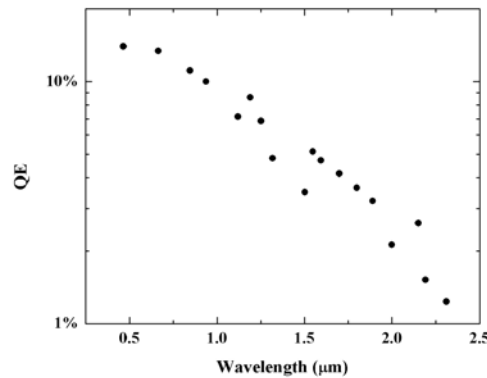


Fig. 1. Spectral dependence of *QE* for a typical $10 \times 10\text{-}\mu\text{m}^2$ area, 3.5-nm-thick NbN meander detector. Temperature is 4.2 K with the current bias is equal to $0.9I_c$.

The other parameter, besides *QE*, responsible for ultimate sensitivity of single-photon detectors is the dark counting rate *R*. *R*, together with *QE*, determines the *NEP* of single-photon detectors in the following manner:

$$NEP = \frac{h\nu}{QE} \sqrt{2R}. \quad (1)$$

The *R(I)* dependence, shown in Fig 2 (right vertical axis), demonstrates the activation law $R = a \times \exp(b \times I/I_c)$ in the whole biasing range used in our experiments ($0.98 > I/I_c > 0.85$), where *a* and *b* are constants, and *I_c* is the detector critical current. The activation-type behavior of *R(I)* can be observed within five orders of magnitudes range and is independent of the device size or the actual superconductor stripe width. Left vertical axis in Fig. 2 corresponds to *QE* dependence on the normalized current bias. As in the case of *R*, we observe an exponential decrease of *QE* with the *I/I_c* ratio decrease, but at least for bias currents close to *I_c*, the *QE* drop is relatively slow.

Figure 3 presents *NEP* versus *I/I_c*, obtained using Eq. (1) and the experimental results on both *QE* and *R* shown in Fig. 2 within the $0.98 > I/I_c > 0.85$ range (closed dots). We note that *NEP* of about $2 \times 10^{-18} \text{ W/Hz}^{1/2}$ has been achieved for *I/I_c* = 0.87. This is the best sensitivity in the near-IR range, ever reported for a single-photon detector operating at 4 K temperature level. As we can see in Fig. 3, the *NEP* rapidly decreases with the bias decrease, since close to *I_c*, *R* is a much stronger function of *I/I_c* than *QE*. Extrapolating the *R* data from Fig. 2 and extending the *NEP* plot into low bias using experimental *QE* points from Fig. 2, we can reach *NEP* below $10^{-20} \text{ W/Hz}^{1/2}$.

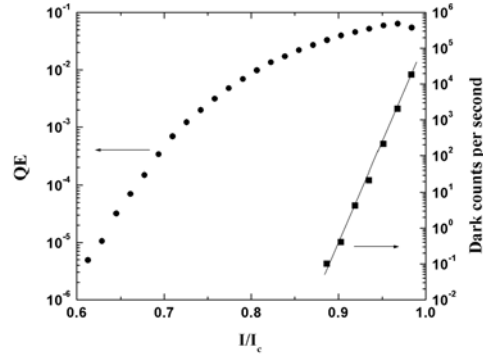


Fig. 2. QE and dark counting rate R versus the normalized bias current, measured for a 3.5-nm-thick, $10 \times 10\text{-}\mu\text{m}^2$ area SSPD at $1.3\text{-}\mu\text{m}$ wavelength. Solid line illustrates the activation-type law of the R dependence on the detector bias.

For low I/I_c values, the NEP saturates, due to the very fast drop of the QE curve at low current bias (Fig. 2). The physical meaning of this saturation phenomenon is quite simple – the detector becomes insensitive to incident radiation and the QE slope follows the R slope, as the supercurrent redistribution is too small to produce a voltage response at such low biases.

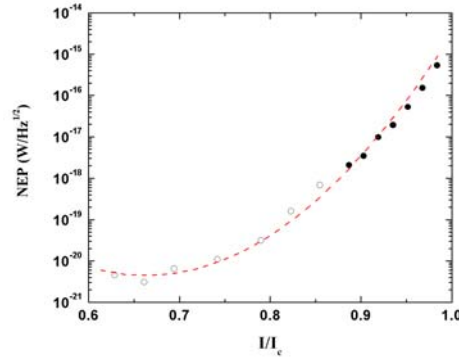


Fig. 3. NEP versus the normalized bias for a 3.5-nm-thick, $10 \times 10\text{-}\mu\text{m}^2$ area SSPD at $1.3\text{-}\mu\text{m}$ wavelength. Closed circles correspond to experimental data presented in Fig. 2, while open circles represent the extrapolated result based on the measured QE and the R (see Fig. 2) interpolated to the low bias currents. Dashed line is a guide to the eye.

DISCUSSION

Dark counts and their rate R play the basic role for the ultimate sensitivity of any single-photon detector, as we can see from Eq. (1). The origin of dark counts in our NbN SSPDs in absence of any incident photon flux or significant thermal background fluctuations represents an interesting physical problem. We believe that the observed dark counts are mainly due to resistive (or, equivalently, superconducting) fluctuations in our NbN superconducting stripes. Such fluctuations were observed in one-dimensional (1-D) superconducting stripes at low temperatures and have been discussed in terms of quantum phase slip centers (PSCs) [12-14]. We have already pointed out to the role of such fluctuations in the context of the experimentally measured, exponential spectral dependence of QE [4].

The 1-D picture is not fully adequate for our devices. The thickness d of the NbN superconducting stripe is indeed close to the BCS coherence length ξ , but the stripe width w is significantly larger than ξ . On the other hand, the 1-D approach seems to be productive to improve our understanding of the problem and for development of a quantitative model of dark counts in our NbN SSPDs. A significant extension of the 1-D phase slips formation process [15] towards the case of wider stripes ($w \gg \xi$) was obtained at low temperatures at the presence of bias currents close to I_c [16,17]. It was shown in [16] that the essential features of the PSC model are preserved, when compared with the 1-D case, including the quasiparticle diffusion length, and the drop of the pair chemical potential over the ξ distance. A general, theoretical investigation of the problem in the 2-D case

SESSION 2A- Far IR/Sub-mm Thermal Detectors—New Concepts and Materials

was proposed in [18], and it was recently used to study of PSC formation in Nb and YBCO bridges [19]. The main conclusion made in [19] was that the PSCs could occur in superconducting stripes more frequently than it is generally admitted by modern theories for uniform clean superconductors at temperatures well below T_c . Authors in [19] suggested that this latter observation could support the idea proposed in [18], namely that the PSCs are formed from microscopic normal-state hotspots existing in granular films.

We strongly believe that the above case applies to our NbN films. Detailed, atomic-force microscope and electron microscope studies did not show any evidence of nm-scale defects in our NbN films. However, our structures are characterized by a negative resistivity temperature coefficient within the 20-300 K temperature range, what is often associated with the existence of granular microstructure in thin NbN films [20]. Consequently, in agreement with the concept proposed in [18],[19], the origin dark counts in our structures is very likely to be associated with granularity of our NbN films. More detailed study on this subject will be presented elsewhere.

This work was funded by the US Air Force Office for Scientific Research grant F49620-01-1-0463 (Rochester) and by the RFBR grant 02-02-16774 (Moscow). Additional support was provided by the NPTest, San Jose, CA.

REFERENCES

1. G. N. Gol'tsman, O. Okunev, G. Chulkova, A. Lipatov, A. Semenov, K. Smirnov, B. Voronov, A. Dzardanov, C. Williams, and R. Sobolewski, *Appl. Phys. Lett.* **79**, 705 (2001).
2. S. Somani, S. Kasapi, K. Wilsher, W. Lo, R. Sobolewski and G. Gol'tsman, *J. Vac. Sci. Technol. B* **19**, 2766 (2001).
3. R. Sobolewski, A. Verevkin, G. N. Gol'tsman, A. Lipatov, and K. Wilsher, *IEEE Trans. Appl. Supercon.* (June 2003).
4. A. Verevkin, J. Zhang, R. Sobolewski, G. Chulkova, A. Korneev, A. Lipatov, O. Okunev, A. Semenov, and G. N. Gol'tsman, *Appl. Phys. Lett.* **80**, 4687 (2002).
5. A. D. Semenov, G. N. Gol'tsman, and A. A. Korneev, *Physica C* **351**, 349 (2001).
6. A. M. Kadin and M. W. Johnson, *Appl. Phys. Lett.* **69**, 3938 (1996).
7. K.S. Il'in, I. I. Milostnaya, A. A. Verevkin, G. N. Gol'tsman, E. M. Gershenzon, and R. Sobolewski, *Appl. Phys. Lett.* **73**, 3938 (1998).
8. J. Zhang, W. Slysz, A. Verevkin, R. Sobolewski, O. Okunev, and G. N. Gol'tsman, *Phys. Rev. B* **67**, 132508 (2003).
9. A. Lipatov, O. Okunev, K. Smirnov, G. Chulkova, A. Korneev, P. Kouminov, G. Gol'tsman, J. Zhang, W. Slysz, A. Verevkin, and R. Sobolewski, *Supercon. Sci. and Tech.* **15**, 1689 (2002).
10. J. Zhang, W. Slysz, A. Verevkin, O. Okunev, G. Chulkova, A. Korneev, A. Lipatov, G. N. Gol'tsman, and R. Sobolewski, *IEEE Trans. Appl. Supercon.* (June 2003).
11. G. N. Gol'tsman, K. Smirnov, P. Kouminov, B. Voronov, N. Kaurova, V. Drakinsky J. Zhang, A. Verevkin, and R. Sobolewski, *IEEE Trans. Appl. Supercon.* (June 2003).
12. C. N. Lau, N. Markovic, M. Bockrath, A. Bezryadin, and M. Tinkham, *Phys. Rev. Lett.* **87**, 217003 (2001).
13. M. Tinkham and C.N. Lau, *Appl. Phys. Lett.* **80**, 2946 (2002).
14. A. Bezryadin, C. N. Lau, and M. Tinkham, *Nature* **404**, 971 (2000).
15. W.J. Skocpol, M.R. Beasley, and M. Tinkham, *J. Low Temp. Phys.* **16**, 145 (1974).
16. V.G. Volotskaya, I.M. Dmitrenko, L.E. Musienko, and A.G. Sivakov, *Sov. J. Low Temp. Phys.* **7**, 188 (1981); *Sov. J. Low Temp. Phys.* **10**, 179 (1984).
17. A. Garzarella and C.J. Martoff, *J. Appl. Phys.* **79**, 2426 (1996).
18. A. Weber and L. Kramer, *J. Low. Temp. Phys.* **84**, 289 (1991).
19. J.-P. Maneval, F. Boyer, K. Harrabi, and F.-R. Ladan, *J. of Superconductivity* **14**, 347 (2001).
20. J.-H. Tyan, and J.T. Lue, *Journal of Appl. Physics* **75**, 325 (1994).

Canadian microbolometer technology for future space missions

Linh Ngo Phong* and Wanping Zheng
Canadian Space Agency, Saint-Hubert, QC J3Y 8Y9, Canada

ABSTRACT

This paper provides an overview of the microbolometer technology developed in Canada, including pixel engineering, readout electronics, and detector packaging. Design considerations are also presented for a two band LWIR radiometer intended for microsatellite-based demonstration of microbolometer technology.

INTRODUCTION

The use of uncooled microbolometers in space instruments such as infrared radiometers and earth sensors has received considerable attention in recent years. In Canada, the development of microbolometers started in 1995 under a collaborative agreement between the Canadian Space Agency, Defence R-D Canada, and INO. Driven by the requirements of space and defense applications, the technologies developed encompasses linear and focal plane arrays of resistive microbolometers, CMOS readout integrated circuits (ROIC), and detector packaging. This paper provides an overview of these technologies with emphasis on linear array technology for space applications. In addition, design considerations for a LWIR radiometer intended for microsatellite based demonstration of microbolometer technology will be presented.

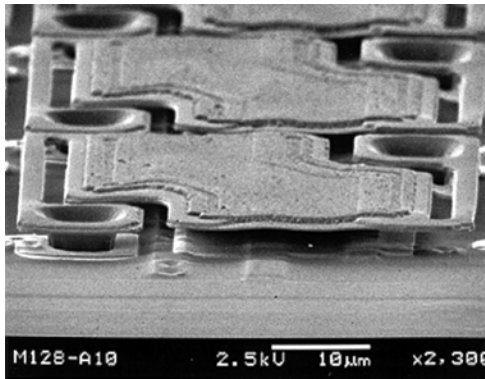
TECHNOLOGY OVERVIEW

To date, the main focus of the technology developed in Canada has been resistive microbolometers. These consist of room temperature VO_2 , VO_x , and YBaCuO semiconductors.^{1, 2} There was no major effort devoted to amorphous Si or capacitive microbolometers.

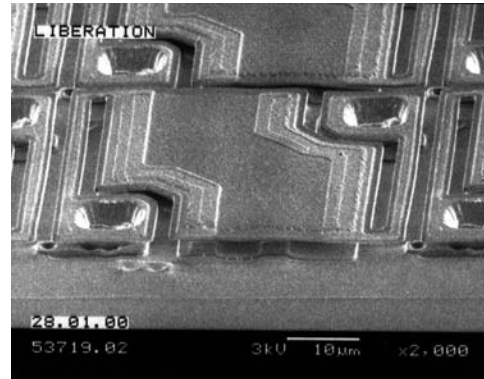
At the pixel level, bolometer films are sputter deposited onto free standing Si_3N_4 microbridges that serve as thermal isolation structures. The bridges are built monolithically on Si wafer with embedded ROIC using surface Si micromachining. The gap between the bridge and wafer is defined by the thickness of sacrificial polyimide layer. This process is fully compatible with 1.5 and 0.8 μm CMOS technologies. The resistance of via contacts between the microbolometers and ROIC is less than 5 Ω . Figure 1 shows examples of bridge structures tailored to different application requirements. The standard bridge (Fig. 1a), $50 \times 50 \mu\text{m}^2$, has a thermal conductance $\sim 4 \times 10^{-7}$ W/K and time constant ~ 5 ms. This type of bridge is found typically in 160×120 focal planes of FLIR cameras. As the bolometric responsivity improves with better thermal isolation, the length of the supporting hinges was increased. The bridge with elongated hinges, as shown in Fig. 1b, sees its thermal conductance reduced to $\sim 1.8 \times 10^{-7}$ W/K. However, because its thermal capacity is not reduced as much, the resulting time constant is about twice that of the previous bridge. Lately, smaller bridges have been designed so as to increase the number of linear array pixels. Figures 1c and 1d show the 39 μm and 25 μm bridges with thermal conductances $\sim 1.9 \times 10^{-7}$ and 4.4×10^{-7} W/K respectively. In particular the hinges of the 25 μm bridge are placed under the bridge, resulting in fill factors better than 80%. At room temperatures, the temperature coefficients of resistance (TCR) of VO_2 , VO_x , and YBaCuO microbolometers are respectively ~ 3 , 2.5 and 2 %. Although VO_2 exhibits the largest value of TCR, it is less immune to substrate temperature drifts due to the strong temperature dependence of its TCR near the transition. The 1/f noise is more dominant in VO_x pixel than in YBaCuO pixel. It is, for instance, equal to the Johnson noise at 280 Hz in the former and at 30 Hz in the latter. The typical D^* measured on $50 \times 50 \mu\text{m}^2$ pixel is $3 \times 10^9 \text{ cm.Hz}^{1/2}/\text{W}$ for 10 μA bias and 30 Hz modulation.

*Contact information for L. N. Phong – Email: linh.ngo-phong@space.gc.ca

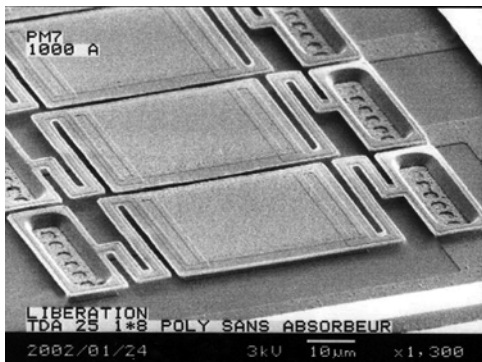
SESSION 2A- Far IR/Sub-mm Thermal Detectors–New Concepts and Materials



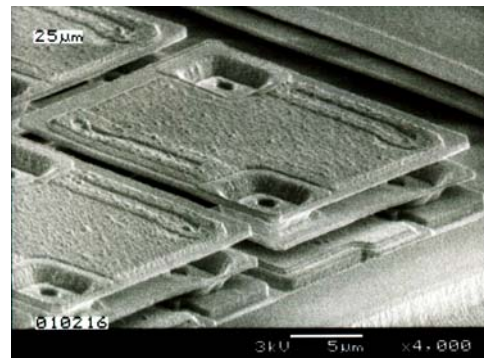
1a



1b



1c



1d

Figure 1: Examples of bridge structures for microbolometers: (a) standard 50 μm bridge; (b) bridge with elongated hinges for improved thermal isolation; (c) 39 μm bridge for high density linear array; (d) 25 μm bridge with underside hinges for large fill factor.

ROICs have been developed for three linear arrays, 256x2, 256x40, and 512 x3, all suited for pushbroom scanning mode. The last two arrays were custom developed for an earth sensor³ and a multispectral imager⁴, the latter being intended for ESA's Earthcare mission. The 256x2 array comprises an active 256x1 array plus a parallel reference array. The array pixel consists of 50x50 μm^2 microbolometer on 52 μm pitch. The reference pixel provides coarse offset correction and temperature drift compensation. The pixels are read out sequentially or in arbitrary sequences using either dc or pulsed bias. The 256x40 array is a quasi linear array of 256 pixels, each containing of a series of 20 pairs of microbolometers (Fig. 2). The size and pitch of the microbolometers are identical to those of the 256x2 array. The microbolometers of each pair are connected in parallel and can be excluded from the series by closing the transistor switch across each pair. The mismatches between pixels can further be corrected by inclusion or exclusion of four Si resistors in series with the microbolometers in each pixel. The 24 transistor switches are programmed such that the output signals of the pixels can be matched within 0.01% over a temperature range of several degrees.⁵ The pixels are addressed in random access mode and may be switched to either of two parallel output buses. These buses allow the array to be arranged in two parallel or sequential arrays or allow for differential measurement. The 512x3 array, currently under development, consists of three lines of 512 pixels with a 2 mm spacing. The signal in each line is integrated in parallel so that, when required, these lines would each collect radiation from a different spectral band. Because of the small interline spacing, the data for

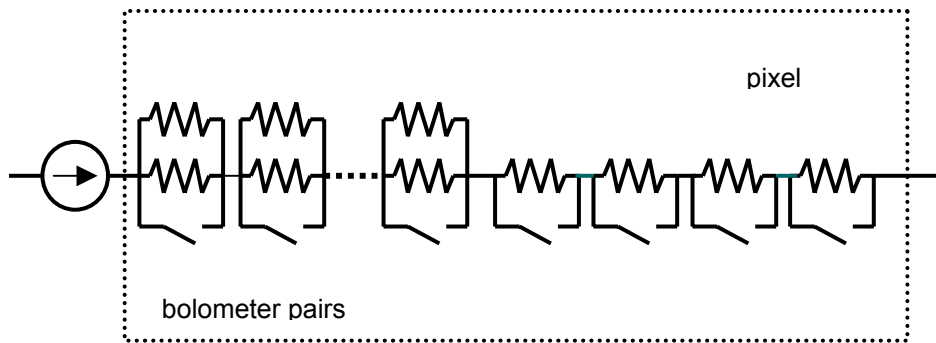


Figure 2: Arrangement of microbolometer pairs and Si resistors in a pixel of the 256x40 array

each spectral band may be obtained using a single broadband objective and dedicated filters for each band (in-field separation technique) without a large displacement of the field of view on the ground for each band. This reduces significantly the co-registration problem due to instability of satellite orientation. The ROIC of this array is implemented in an epitaxial process for increased immunity to radiation. The active, blind, and reference pixels, of 39 μm pitch, form the Wheatstone bridge circuit for offset correction and temperature drift compensation. The blind pixel incorporates a top mirror film so that it is thermally sensitive to Joule heating and substrate temperature change. The reference pixel consists of a bare microbridge (without bolometer) that is sensitive to substrate temperature change uniquely. Beside the linear arrays, a 160x120 focal plane array was also developed. The array pixel consists of 50x50 μm^2 microbolometer on 52 μm pitch. The pixel access can either be in sequential scanning or random access mode. In the latter mode the array may be used as a series of linear arrays by accessing certain rows only. This array, as the previous ones, contains also reference pixels for offset correction and temperature drift compensation.

In order to achieve good thermal isolation of the microbolometer, the devices are packaged in vacuum so as to minimize heat transfer from the bridge to heat sink. Typically, the diced device is mounted in a metal or ceramic leaded package using epoxy. Both packages are covered with transmissive infrared window made of Ge or ZnSe. The flat metal package has a footprint of 50x50 mm^2 and contains a side vacuum tube as a means to evacuate and seal off the package. The ceramic package has a footprint of 30x26 mm^2 . Access to the latter package consists of a small leaded opening in the back of the package. The package is evacuated in a vacuum chamber. When the desired pressure is reached in the chamber, a laser beam is used to thermally dissolve the lead in the opening, sealing it off. Hermeticity can be achieved for at least four years in these packages without the need for getter refiring. Tests of vibration, shock, and temperature cycling showed compliance with MIL-STD-810 and MIL-STD-883 specifications. Some of the devices were exposed to 60 MeV proton irradiation (dose $\sim 10^{12} \text{ cm}^{-2}$). The irradiated devices showed no measurable changes in resistance, responsivity, and noise.

RADIOMETER DESIGN

The Canadian Space Agency is currently planning a series of microsatellite based technology demonstration in view of providing Canadian industry with space heritage. The 512x3 array of microbolometers is among the candidates proposed for space experiments. To evaluate the performance of this device, its use for cloud temperature measurement from low earth orbits is being considered. The experiment will be performed in two spectral bands: 10.3-11.3 μm and 11.3-12.3 μm . The temperature difference between these bands can be used to discriminate ice cloud from water cloud on the basis of the

SESSION 2A- Far IR/Sub-mm Thermal Detectors—New Concepts and Materials

split window technique. Design considerations for a two-band instrument for this experiment are described in the following.

A radiometer with in-field separated bands appears to be the most compact instrument for the above purpose. The radiometer architecture implies the use of two lines of the 512x3 array behind a Ge optics, each with dedicated bandpass filter centered respectively at 10.8 and 11.8 μm . The third line is used as a reference for thermal drift compensation. The thickness of the filter substrate can be used as a parameter to correct the chromatic aberration of the optics. The device is operated in the pushbroom scanning mode. The spatial resolution that can be achieved in this mode is dictated by the data rate of the payload-to-computer interface. For instance, for direct data acquisition using the 300 kb/s RS-422 link, the resulting sampling interval for the 512x2 array of 15-bit pixels is 51.2 ms. Considering the equivalent ground speed ~ 6.8 km/s of the satellite, the spatial resolution and swath width would be respectively ~ 350 m and 180 km at nadir. The front size of the optics can roughly be estimated for this resolution. Assuming a low earth 600 km orbit, the required focal length (or diameter of F/1 optics) to image a 350 m ground pixel onto the 39 μm microbolometer is ~ 67 mm. The inherent field of view for the 180 km swath is ~ 8.5 deg.

The radiometric calibration is made by means of a mirror rotating between the external view (nadir), an on-board blackbody, and the cold space. The targeted accuracies of temperature measurement is 1 K for a 300 K scene and 2 K for a 200 K scene. The temperature stability of the array is achieved by means of an integrated thermoelectric cooler and precision temperature sensor with PID control. The required stability of the array is ~ 20 mK between calibrations. The thermoelectric cooler is connected to the radiator via a thermal strap. The radiation shield is thermally linked to the cooler so that its temperature remains as stable as the array temperature. The radiometer instrument is thermally decoupled from the platform with insulating washers and insulated with standard MLI. Distributed thermocouples will be used to further stabilize the temperature inside the instrument. Such stabilization is necessary to minimize the background fluctuation detected by the bolometers.

ACKNOWLEDGMENTS

We thank Hubert Jerominek and Timothy Pope of INO, Sainte-Foy, Canada, for helpful information and discussions.

REFERENCES

1. H. Jerominek, L. Ngo Phong and S. N. Qiu, in *Selected SPIE Papers, Vol. 1: Infrared Technology*, SPIE Press, Bellingham, 1998.
2. L. Ngo Phong and S. N. Qiu, *J. Vac. Sci. Technol. A* 18, 635, 2000.
3. P. J. Thomas *et al.*, *SPIE* 3439, 128, 1998.
4. ESA Report SP-1257 (1), 2001.
5. P. J. Thomas *et al.*, *SPIE* 3698, 826, 1999.

SESSION 2A- Far IR/Sub-mm Thermal Detectors—New Concepts and Materials

PR19 *

Novel Electrically Substituted Optical Detectors

Joseph Rice (National Institute of Standards and Technology),

Steven Lorentz (L-1 Standards and Technology, Inc.),

Jeanne Houston (National Institute of Standards and Technology)

Several new thermal-type optical detectors have been developed at NIST for various measurement applications over the past few years. These detectors share a common feature in that they incorporate a form of electrical substitution where chopper-synchronized electrical power, controlled by a servo loop, maintains the detector at a fixed operating temperature. This mode of operation increases temporal stability, improves time response, and provides a relatively straightforward basis for calibration. While related to operating modes utilizing electro-thermal feedback, electrical substitution is quite distinct, as will be shown.

We will present a general introduction to electrically substituted thermal-type optical detectors, and then provide specific details on up to four new examples: 1) An electrically substituted liquid helium cooled bolometer (ESB) that uses a gold-black coating for optical absorption and as the electrical substitution heater. This detector serves as a spectrally flat reference standard in a new calibration facility at NIST that measures the spectral responsivity of customer infrared detectors using tunable infrared lasers. 2) A liquid helium cooled active cavity radiometer that will serve as a next generation primary standard for optical detector responsivity measurements at NIST, the High Accuracy Cryogenic Radiometer 2 (HACR2). 3) The High-Tc Active Cavity Radiometer (High-Tc ACR), which uses YBCO thin-film sensors on the receiver cavity and only requires cooling to below about 85 K. It has been tested with the YBCO sensors operating both at the midpoint of the superconductive resistive transition (89 K, resistive-edge mode), and at slightly lower temperatures along the critical current versus temperature curve (85–89 K, critical current mode). One could imagine flying this with radiative cooling. 4) The Scripps-NIST Advanced Radiometer (Scripps-NISTAR), a spaceflight instrument that was developed with NASA and Scripps sponsorship for a flight to the Earth's L-1 point, where it will view the Earth and measure total Earth-emitted and solar-reflected irradiance for a better understanding of the Earth's radiative balance. The Scripps-NISTAR thermal detectors themselves are active cavity radiometers that operate at 40 degrees Celcius near the midpoint of the resistive transition in polycrystalline, doped BST (Barium Strontium Titanate) that is associated with the ferroelectric phase transition. These provide sensitivity that is adequate for accurate measurements of the total irradiance from the Earth at L-1, which is 4 or 5 orders of magnitude lower than the irradiance levels measured by existing spaceflight active cavity radiometers.

Keywords: Detectors, thermal, standards, optical, radiometry, superconductors, ferroelectrics

* A PowerPoint presentation is available on the CD version of the TDW '03 proceedings.

SESSION 2B- Far IR/Sub-mm Thermal Detectors—New Concepts and Materials

PR39-INV10 *

Arrays of High-Performance Thermal Detectors
Harvey Moseley, NASA Goddard Space Flight Center

Thermal detectors have historically been the sensors of choice for applications where photoconductive or photovoltaic detectors are unavailable. While they have the advantage of broad wavelength coverage, a primary disadvantage has been sensitivity; at a given operating temperature, bolometers are typically much less sensitive than photodetectors. The development of cryogenic bolometers has resulted in thermal detectors which can reach fundamental sensitivity limits. When operated at temperatures below 0.3 K these devices can provide background-limited sensitivity for cryogenic imaging and spectroscopy in space. The past decade has seen a rapid growth in sensitivity and array format in cryogenic bolometers. Micromachining technology, combined with advances in superconducting electronics, provides a strong technological base for future developments. I will describe the present state of development of low-temperature thermal detectors, and the possible extension of this technology to higher temperature operation.

* A PowerPoint presentation is available on the CD version of the TDW '03 proceedings.

THERMOPILE DETECTOR ARRAYS FOR SPACE SCIENCE APPLICATIONS

M. C. Foote*, M. Kenyon, T. R. Krueger, T.A. McCann, R. Chacon, E.W. Jones,
M.R. Dickie, J.T. Schofield and D.J. McCleese
Jet Propulsion Laboratory, California Institute of Technology
4800 Oak Grove Drive, Pasadena, CA 91109

S. Gaalema and W. Hu
Black Forest Engineering, 1879 Austin Bluffs Parkway, Colorado Springs, CO 80918

ABSTRACT

Thermopile detectors are widely used in uncooled applications where small numbers of detectors are required, particularly in low-cost commercial applications or applications requiring accurate radiometry. Arrays of thermopile detectors, however, have not been developed to the extent of uncooled bolometer and pyroelectric/ferroelectric arrays. Efforts at JPL seek to remedy this deficiency by developing high performance thin-film thermopile detectors in both linear and two-dimensional formats. The linear thermopile arrays are produced by bulk micromachining and wire bonded to separate CMOS readout electronic chips. Such arrays are currently being fabricated for the Mars Climate Sounder instrument, scheduled for launch in 2005. Progress is also described towards realizing a two-dimensional thermopile array built over CMOS readout circuitry in the substrate.

INTRODUCTION

Thermopile detectors have some desirable characteristics that make them better suited for certain applications than are uncooled bolometers and pyroelectric/ferroelectric detectors. They are passive devices, require no electrical bias, and generate a voltage output that is proportional to the input radiation signal. They are also typically uncooled and are insensitive to substrate temperature variations, making temperature stabilization unnecessary. They are highly linear, which combined with their insensitivity to substrate temperature, make them ideal for accurate radiometry. Finally, they require no optical chopper and they have negligible $1/f$ noise, provided the readout amplifier has high input impedance. These properties make them well suited for broadband and spectral radiometers for space science applications.

In spite of these properties, the development of thermopile arrays is much less mature than that of bolometers^{1,2} and pyroelectric³ detectors. Linear thermopile arrays with both metal⁴ and $(\text{Bi}_{1-x}\text{Sb}_x)_2(\text{Te}_{1-y}\text{Se}_y)_3$ alloy^{5,6} thermoelectric materials have been reported. Reports of two-dimensional (2D) thermopile arrays have been limited to CMOS materials,^{7,8} which are ideal for manufacturability but yield only moderate thermoelectric performance. The lack of maturity in thermopile detector array development is due in part to the fact that the thermoelectric materials with the highest figure of merit (ZT) are $(\text{Bi}_{1-x}\text{Sb}_x)_2(\text{Te}_{1-y}\text{Se}_y)_3$ alloys, which are not compatible with conventional semiconductor fabrication lines. More importantly, however, is the difficulty in implementing low-noise readout circuitry for thermopile arrays. While a bolometer array can be multiplexed by sequentially biasing pixels with large bias currents, each thermopile detector output signal must be continuously integrated to achieve the full detector signal-to-noise ratio. Thus, each pixel must have a dedicated low-noise amplifier and integrating circuit.

Here we report progress towards the realization of high-performance thermopile arrays with CMOS readout circuitry. Linear thermopile arrays, formed by bulk micromachining and wire bonded to adjacent readout chips, are currently being fabricated for the Mars Climate Sounder (MCS) instrument. MCS will fly on the Mars Reconnaissance Orbiter (MRO) scheduled to launch in 2005. Engineering models of these detector arrays, with readout, exhibit a specific detectivity D^* value of $8 \times 10^8 \text{ cmHz}^{1/2}/\text{W}$ in the frequency range

* Contact information for M.C. Foote- Email: marc.c.foote@jpl.nasa.gov; phone 818-354-9009; fax 818-393-4663; Mail Stop 302-231, Jet Propulsion Laboratory

SESSION 2B- Far IR/Sub-mm Thermal Detectors—New Concepts and Materials

0.03-0.25 Hz. Additionally, we report on an effort to build 2D arrays of thermopile detectors using surface micromachining to build thermally isolated detector structures over readout circuitry imbedded in the substrate. The 2D detectors and readout chips have been developed separately so far, but efforts will soon be under way to integrate the detectors on the readout chips.

THERMOPILE LINEAR ARRAYS

The JPL thermopile linear arrays have been described in detail previously.^{6,9} They consist of 0.5 micron thick silicon nitride membranes formed by backside etching of the underlying silicon substrate. On each membrane are a number of Bi-Te and Bi-Sb-Te thermocouples running along narrow legs between the substrate and membrane. The detectors are closely spaced, with slits through the membrane separating the detectors from each other and defining the detector legs. Typical detectors have D^* values in the range $1\text{-}2 \times 10^9 \text{ cmHz}^{1/2}/\text{W}$ and response times less than 100 ms.

Thermopile detector arrays are currently being fabricated at JPL for the Mars Climate Sounder (MCS) instrument. MCS is a limb-sounding radiometer to fly on the Mars Reconnaissance Orbiter (MRO) mission, scheduled to launch in 2005. MCS will measure temperature, pressure, water vapor, and the combination of dust and condensates as a function of altitude in Mars' atmosphere in addition to polar radiative balance. Nine 21-element linear arrays of thermopile detectors, distributed between two focal planes in twin telescopes, sit behind spectral bandpass filters spanning the wavelength range 0.3-45 microns. The requirements for the detector-readout subsystem are listed in Table 1. Note that D^* is specified in the 0.03-0.25 Hz range, corresponding to two-second integration times and a 30 second cycle between views of space. Thus, low 1/f noise in both the detectors and the readout circuitry is essential.

Table 1. Mars Climate Sounder detector requirements.

Parameter	Requirement
Detector Size	240 μm x 480 μm
Number of detectors per array	21
Arrays in Focal-Plane A	6
Arrays in Focal-Plane B	3
D^* (0.03-0.25 Hz, 0.3-45 μm)	$10^9 \text{ cmHz}^{1/2}/\text{W}$
Response Time	$\leq 100 \text{ ms}$
Pixel Crosstalk	$\leq 1\%$
Yield	100%
Dynamic Range for 2 sec Integration Time	13,000
Linearity	1%

Figure 1 shows an unblackened MCS thermopile detector pixel. Each pixel is 480 μm by 240 μm and has 12 Bi-Sb-Te / Bi-Te thermocouples connected in series to measure the temperature difference between the absorber and substrate. After detector fabrication, the chips are coated with gold black to provide high absorptivity and flat spectral response from 0.3 to 45 μm . During deposition, the gold black bridges the membrane slits, thermally shorting detectors to each other and to the substrate. These gold-black bridges are eliminated by laser ablation from the detector backside with 248 nm radiation, using the detector membrane as a mask. A detector array after gold black deposition and laser ablation is shown in Figure 2.

The MCS thermopile arrays are read out using a custom CMOS readout integrated circuit. The architecture of this circuit is shown in Figure 3. This readout chip is connected to the thermopile array with two wire bonds per detector. The roughly dc signal from each detector is modulated at 64 kHz by an electronic chopping circuit. The resulting ac signal is amplified, demodulated, and integrated. Because the amplification occurs at 64 kHz rather than near dc, the 1/f noise in the CMOS amplifier is dramatically reduced. Integrated signals from 64 channels are multiplexed into a single analog output stream. Thermopile detector noise is dominated by Johnson noise, which for the 80 k Ω MCS detectors is

SESSION 2B- Far IR/Sub-mm Thermal Detectors–New Concepts and Materials

36 nV/Hz^{1/2}. With a 80 kΩ source, the readout chip has an input-referred noise of 70 nV/Hz^{1/2} in the 0.03 to 0.25 Hz range. Thus, the readout chip is the dominant focal-plane noise source. Even with this excess readout noise, the MCS engineering model focal plane has demonstrated D^* values of 8×10^8 cmHz^{1/2}/W, close to the required 10^9 cmHz^{1/2}/W. Without readout, the detectors have D^* values of 1.7×10^9 cmHz^{1/2}/W.

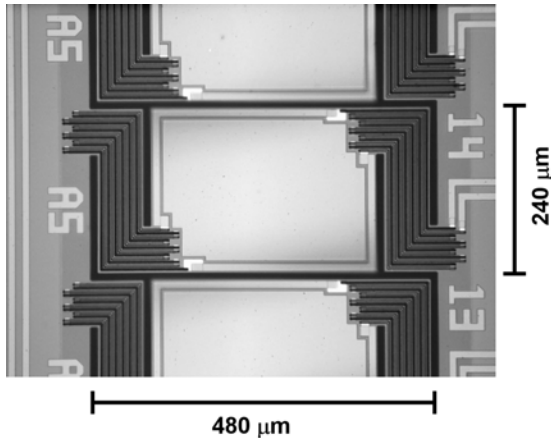


Figure 1. Unblackened MCS detector pixels.

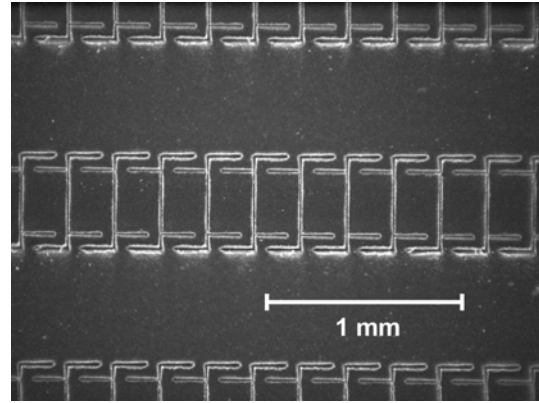


Figure 2. MCS detector array with gold black.

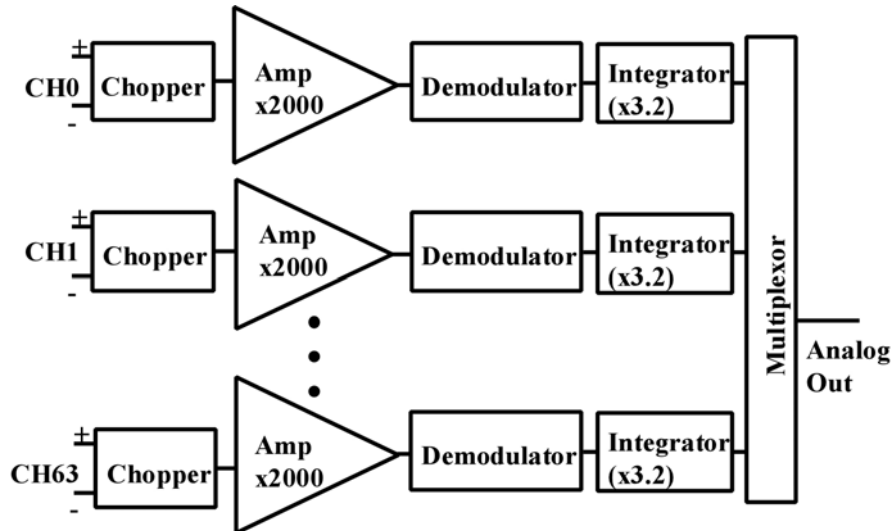


Figure 3. Architecture of MCS readout integrated circuit.

THERMOPILE 2D ARRAYS

In contrast to the linear thermopile arrays where membranes are formed by etching away the silicon substrate under the detectors, the 2D thermopile array effort at JPL involves using surface micromachining to build detectors over CMOS readout circuitry in the substrate. The design allows pixels to be arranged with a fill factor close to unity. To date, two parallel efforts have developed the detector pixels and the readout circuitry. Work will soon be underway to build detectors on readout chips.

A schematic diagram of a 2D thermopile detector pixel is shown in Figure 4. The pixel consists of three layers – a gold interconnect layer on the substrate surface, a middle layer consisting of the thermoelectric legs with a thin dielectric support structure, and a top absorbing layer. Two polyimide sacrificial layers present during detector fabrication are removed with a dry oxygen plasma etch in the final process step. The two thermoelectric layers are sputtered from targets with composition Bi_{0.4}Sb_{1.6}Te_{3.3} (p-type) and Bi_{1.6}Sb_{0.4}Te_{3.3} (n-type). Originally Bi₂Te₃ was used for the n-type thermoelectric, but it degraded in the

SESSION 2B- Far IR/Sub-mm Thermal Detectors–New Concepts and Materials

oxygen plasma polyimide etch step. N-type Bi-Sb-Te has been found to be more stable throughout the fabrication process.

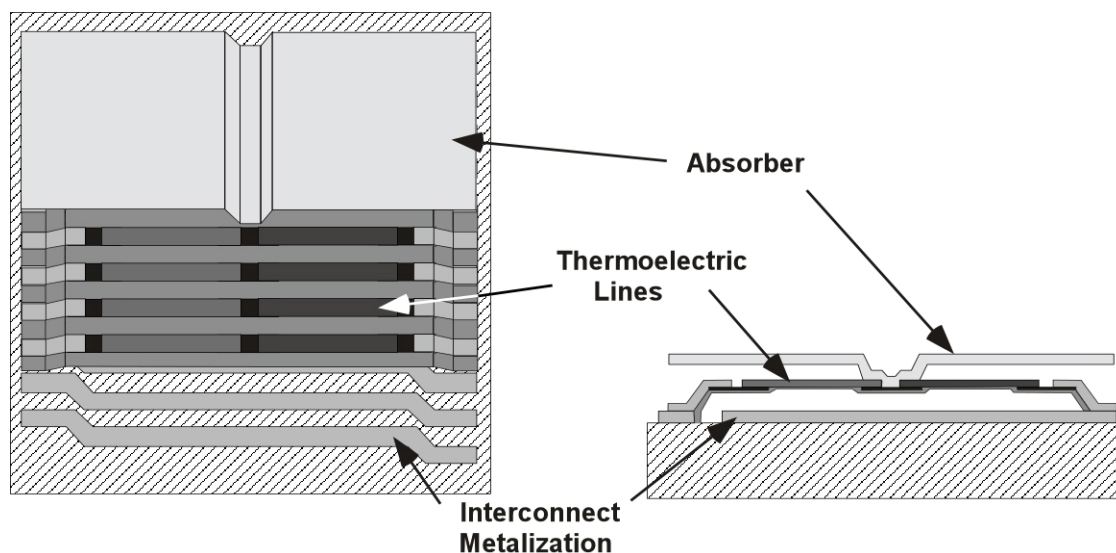


Figure 4. Schematic diagram of 2D thermopile pixel structure.

Figure 5 shows a scanning electron microscope picture of a single thermopile 2D detector. The holes through the absorbing structure allow the oxygen plasma to more quickly etch the polyimide film in the final fabrication step. The corrugation in the absorber is due to corrugation in the polyimide sacrificial layer below it, which in turn follows the contours of the thermoelectric lines underneath.

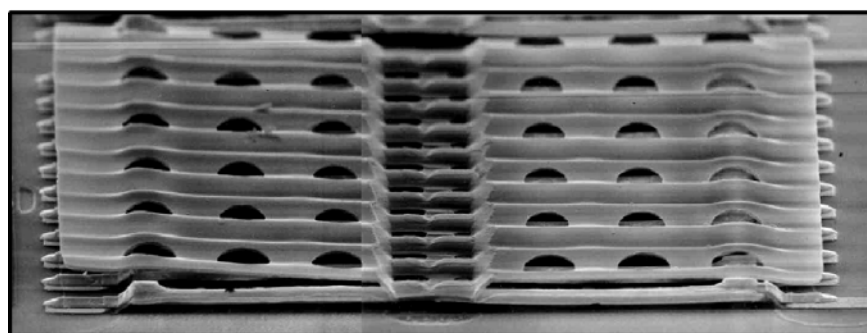


Figure 5. Scanning electron microscope picture of a thermopile detector in a 2D array.

Data from a 2D detector test chip are shown in Table 2. This chip consists of 21 detectors with a pixel size of 70 μm and 21 detectors with a pixel size of 100 μm . As Table 2 shows, D^* values for both pixel sizes thus far are only moderate. However, the response times of both the 70 μm and 100 μm pixel sized detectors are very fast. To increase D^* and improve the yield, we are currently building pixels with longer, narrower legs and reducing the number of thermoelectric legs per pixel.

Table 2. Measured characteristics for a 2D thermopile test chip. The resistance R , the infrared responsivity \mathcal{R} , and the specific detectivity D^* are shown with their respective standard deviations.

Pixel Size (μm)	Yield (%)	R ($\text{k}\Omega$)	\mathcal{R} (V W^{-1})	D^* ($\text{cm Hz}^{1/2} \text{W}^{-1}$)	Response Time (ms)
70	95	17.7 ± 3.5	726 ± 31	$3.1 \pm 0.3 \times 10^8$	2.1 ± 0.1
100	81	36.6 ± 3.6	1157 ± 25	$4.8 \pm 0.2 \times 10^8$	4.4 ± 0.3

SESSION 2B- Far IR/Sub-mm Thermal Detectors—New Concepts and Materials

CMOS readout chips have been fabricated, but not yet tested, for 32x32 arrays of 70 μm thermopile pixels. Under each pixel is a signal chain similar to that shown in Figure 3 for the linear arrays. The specification for these readout circuits is 60 $\text{nV}/\text{Hz}^{1/2}$ input referred noise for a 100 $\text{k}\Omega$ source resistance, and 1 μW power dissipation per pixel. Test chips with only the front end amplifier (expected to generate most of the noise and dissipated most of the power), exhibited 150 $\text{nV}/\text{Hz}^{1/2}$ input-referred noise and 0.6 μW power dissipation per pixel. The 32x32 array readout chips are expected to have lower noise due to an improved design and fabrication at a CMOS foundry with well-controlled 1/f noise.

CONCLUSIONS

The development of thermopile arrays has thus far lagged that of uncooled bolometers and pyroelectric/ferroelectric detector arrays. However, thermopiles have several advantages that make the pursuit of arrays worthwhile. In particular, their high linearity and insensitivity to substrate temperature variations make them ideal for radiometric applications. High performance linear arrays of thermopile detectors have been developed at JPL for space science applications. Linear arrays are currently being fabricated for the Mars Climate Sounder instrument. An additional effort, which seeks to develop 2D thermopile arrays, has resulted in pixel structures with moderate performance as well as readout integrated circuit chips. Future efforts will include integrating the current 2D detectors with readout circuitry, as well as optimizing the detector performance.

ACKNOWLEDGEMENTS

The research described in this paper was carried out at the Jet Propulsion Laboratory, California Institute of Technology, under a contract with the National Aeronautics and Space Administration.

REFERENCES

1. R.A. Wood, "Uncooled thermal imaging with monolithic silicon focal planes", Proc. SPIE 2020, Infrared Technology XIX, pp. 322-329, 1993.
2. D. Murphy, M. Ray, R. Wyles, J. Asbrock, N. Lum, A. Kennedy, J. Wyles, C. Hewitt, G. Graham, W. Radford, J. Anderson, D. Bradley, R. Chin, and T. Kostrzewa, "High Sensitivity (25 μm Pitch) Microbolometer FPAs and Application Development", Proc. SPIE 4369, Infrared Technology and Applications XXVII, pp. 222-234, 2001.
3. Charles Hanson, "Uncooled thermal imaging at Texas Instruments", Proc. SPIE 2020, Infrared Technology XIX, pp. 330-339, 1993.
4. R.A. Wood, T.M. Rezachek, P.W. Kruse and R.N. Schmidt, "IR SnapShot Camera", Proc. SPIE 2552, Infrared Technology XXI, pp. 654-660, 1995.
5. E. Kessler, U. Dillner, V. Baier, J. Müller, "A 256 pixel linear thermopile array using materials with high thermoelectric efficiency", Proc. of 16th Int. Conf. On Thermoelectrics, pp. 734-737, 1997.
6. M.C. Foote, E.W. Jones, and T. Caillat, "Uncooled Thermopile Infrared Detector Linear Arrays With Detectivity Greater Than $10^9 \text{ cmHz}^{1/2}/\text{W}$ ", IEEE Trans. on Elect. Devices, **45**, pp. 1896-1902, 1998.
7. T. Kanno, M. Saga, S. Matsumoto, M. Uchida, N. Tsukamoto, A. Tanaka, S. Itoh, A. Nakazato, T. Endoh, S. Tohyama, Y. Yamamoto, S. Murashima, N. Fujimoto, and N. Teranishi, "Uncooled infrared focal plane array having 128x128 thermopile detector elements", Proc. SPIE Vol. 2269, Infrared Technology XX, pp. 450-459, 1994.
8. A.D. Oliver, W.G. Baer, and K.D. Wise, "A Bulk-Micromachined 1024-Element Uncooled Infrared Imager", Proc. of the 8th Int. Conf. on Solid-State Sensors and Actuators (Transducers '95), and Eurosensors IX, pp. 636-639, 1995.
9. M.C. Foote and E.W. Jones, "High Performance Micromachined Thermopile Linear Arrays", Proc. SPIE 3379, Infrared Detectors and Focal Plane Arrays V, pp. 192-197, 1998.

THE IR DETECTOR SYSTEM FOR THE GERB INSTRUMENT

Nick Nelms¹, Gillian Butcher, Oliver Blake, Richard Cole, Chris Whitford, Andrew Holland

Space Research Group, Dept. Physics & Astronomy, University of Leicester, Leicester, LE1 7RH, UK.

ABSTRACT

The Geostationary Earth Radiation Budget (GERB) instrument is an Earth observing scientific payload launched on-board the European Space Agency Meteosat Second Generation (MSG) satellite in September 2002. The instrument measures reflected and emitted radiation in two wavebands, 0.3 – 4 μm and 4 – 30 μm . The detector system comprises the focal plane and supporting front-end electronics. The focal plane consists of a 256-element thermoelectric linear array operating at ~ 300 K and four application specific integrated circuits (ASIC) providing parallel amplification, filtering and digitisation. The front-end electronics are built around a digital signal processor, which performs integration and additional filtering of the ASIC product. This paper describes in detail the design, operation and performance of the GERB detector system.

INTRODUCTION

The aim of the GERB instrument¹ is to monitor the total radiation output (reflected and generated) from the Earth in the 0.3 to 30 μm range, over a period of several years, providing data for climate modelling and inter-calibration with other instruments. The MSG satellite will be placed into geostationary orbit at 0° latitude, 0° longitude (it is currently in a commissioning orbit at 0° lat, 10°W lon) from where GERB will view the whole Earth. The satellite rotates at 100 rpm and, to compensate for this, the instrument uses a de-spin mirror to stabilise the Earth view onto the detector for a period of ~ 40 ms, once per revolution of the spacecraft. During this time, the linear detector sees a complete slice of the whole Earth view in the North-South direction. Also, during each revolution, for calibration purposes, the detector views an internal warm blackbody and a solar diffuser. The motion of the de-spin mirror is adjusted during subsequent satellite rotations to scan the detector view forwards and backwards and in this way a full image of the Earth is obtained every 5 minutes.

DETECTOR SYSTEM DESCRIPTION

Overview

The detector system is divided into two parts, the focal plane assembly (FPA) and the associated front end electronics (FEE). Both units are contained within the instrument optical unit and are connected by a 0.75 m cable. Figure 1 is a simplified schematic of the detector system.

Focal Plane Assembly

The FPA components include detector, ASICs (4 off) and support electronics (voltage reference, decoupling and connector). Each of these sub-circuits is mounted on gold-plated ceramic circuit boards that include test structures. In addition the detector is mounted on a silicon substrate providing connection fan-out before mounting on the ceramic circuit board. Once operation of the sub-circuit is confirmed the test structures are removed. The individual sub-circuits are then mounted onto a molybdenum backplate and wire bonded together (figure 2). An aluminium plate covers the whole assembly with a single aperture for the detector.

¹ Contact information for N. Nelms - Email: nin@star.le.ac.uk, tel+44 (0) 116 252 2007

SESSION 2B- Far IR/Sub-mm Thermal Detectors–New Concepts and Materials

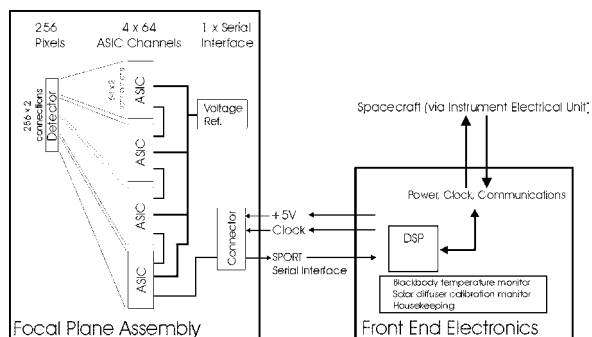


Figure 1: GERB detector system schematic.

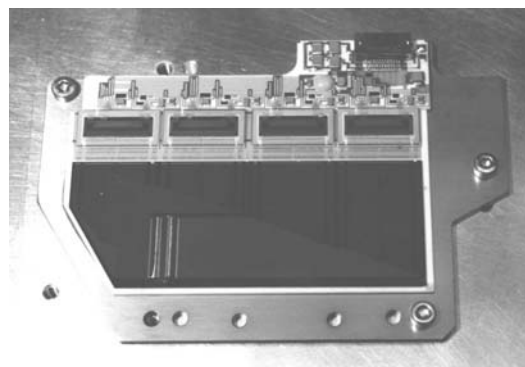


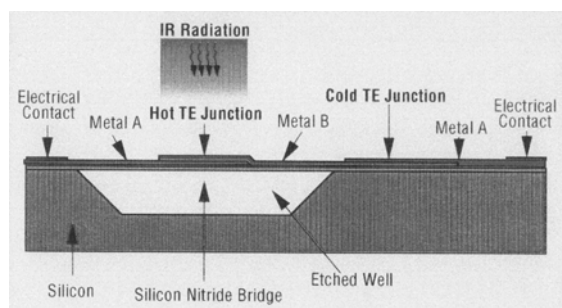
Figure 2: GERB focal plane assembly.

Detector

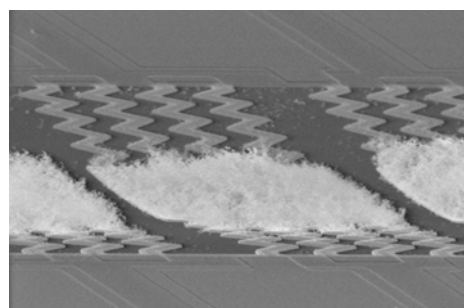
The detector is a custom thermoelectric linear array manufactured by Honeywell. It is a silicon micro-machined structure (figure 3a) with 256 pixels. Detector parameters are listed in table 1. The detector pixels also have a reticulated 20 μm thick goldblack coating (99% Au, 1% Cu) (figure 3b) to improve spectral response.

Table 1: Detector parameters

Number of pixels	256
Pixel size	45 μm x 55 μm
Pixel pitch	55 μm
Fill factor	82%
Impedance	$\sim 1200 \Omega$
Responsivity	300 V/W
Time constant	~ 4 ms
Noise source	Johnson noise of resistance



a)



b)

Figure 3: a) Pixel structure schematic and b) SEM micrograph of a single detector pixel showing goldblack coating.

ASICs

Each GERB ASIC² has 64 parallel signal processing channels allowing the full detector to be serviced using four devices. The ASIC is manufactured using the Mietec 0.7 μm CMOS process. Each channel comprises an input amplifier and a sigma-delta modulator to perform digitisation. To reduce the effect of $1/f$ noise introduced by the use of the CMOS process the input amplifier is chopped and then followed by a demodulator to return the signal to DC. This scheme has the disadvantage that the signal is sampled only for half the integration time whilst the noise is sampled over the whole period. To avoid this situation the amplifier input is chopped between the positive and negative outputs from a detector pixel, necessitating a differential connection. The output of the sigma-delta modulator feeds into a decimation filter to reduce the

SESSION 2B- Far IR/Sub-mm Thermal Detectors—New Concepts and Materials

data rate and outputs from the 64 decimated channels are shifted into a serial register for data output. The shift register also has a serial data input allowing up to four devices to be cascaded and is compatible with the SPORT interface of the Analog Devices ADSP21xx series of digital signal processors (DSP).

Timing is controlled by an external clock (in the case of GERB it uses the spacecraft clock at $2^{25}/9$ Hz ~ 3.73 MHz). The sigma-delta ADCs run at 1/64 of this rate. Two decimate by 128 filters operate in parallel, 180° out of phase and produce a new sample every 64 ADC clock cycles. The filters are shared by all 64 channels and hence are 64 times over-clocked. The maximum filter output is $64^2 = 4096$, which is represented as a 12-bit number (The ADC will not produce an all '1's data stream so the actual maximum is 4095). Frame count and parity bits are added to each sample, which is then fed into the serial register as a 16-bit word. The serial register is clocked continuously at the external clock rate which means that the entire 64 x 16 bits is shifted out in 1/4 of the output sample rate, in-line with the ability to cascade up to four ASICs. Operation from the GERB spacecraft clock results in a parallel (256 channels) sample time of 1.098 ms. The ASIC has an input signal range of ± 125 μ V and a dynamic range of >1600 . It operates from a single 5 V supply and dissipates 150 mW.

Front End Electronics

The FEE is built around an Analog Devices ADSP-2111 DSP which allows direct connection of the FPA (ASIC) serial output to the SPORT interface. The stable viewing period of the detector (Earth, blackbody or solar diffuser) is 40 ms (as determined by the rotation of the spacecraft and the de-scan mirror mechanism). The purpose of the FEE is to digitally integrate and process the output from the FPA during the 40 ms observation time. 36 samples are taken during this time ($36 \times 1.098 \sim 39.5$ ms) which are then convoluted with a filter optimised for the pixel time constant. A second filter provides a correction term for any changes in time constant during operation. The filtering provides high-frequency noise reduction and removal of detector memory effects, essential for an integration time of order only ten pixel time constants.

The FEE also monitors the warm blackbody temperature, solar diffuser calibration diodes and housekeeping parameters.

DETECTOR SYSTEM PERFORMANCE

Detector parameters evaluated include time constant, noise, linearity and spectral response. The time constant of each pixel was measured and the results are shown in figure 4. Linearity was measured using an Ar-Ion laser at a wavelength of 514 nm and the detector output normalised to a standard reference detector. Figure 5 shows the average linearity of the central 50 detector pixels. The error bars indicate the range within which 2-sigma of the pixels fall.

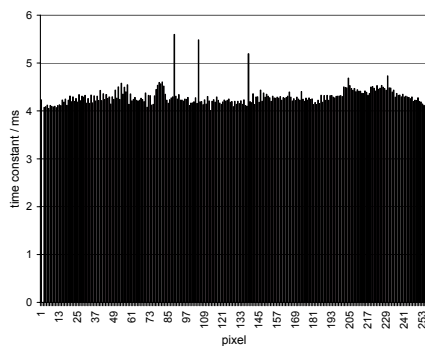


Figure 4: Detector pixel time constants.

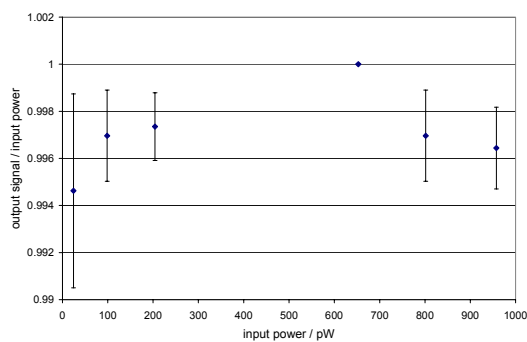


Figure 5: Average linearity of central 50 pixels.

The pixel noise (NEP) distribution (for a 40 ms integration time) is plotted in figure 6. The average NEP is ~ 135 pW which is equivalent to ~ 2.6 codes of a single 1.098 ms ASIC reading. During evaluation of the ASIC a common fault was detected in that channel 64 of all devices exhibited high noise. To compensate

SESSION 2B- Far IR/Sub-mm Thermal Detectors–New Concepts and Materials

for this the routing of detector pixels to ASIC input channels was arranged such that the two end pixels of the array were connected to channel 64 of an ASIC. This also meant that the end but-one pixels had to be left unconnected.

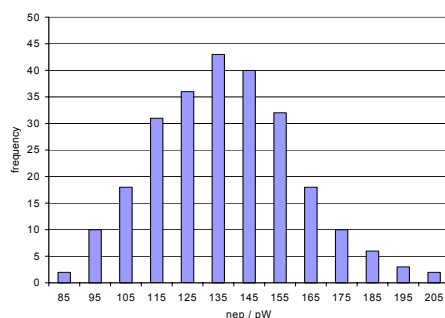


Figure 6: Pixel noise (NEP) distribution.

The system spectral response was measured over the range from 0.3 μm to 25 μm and then extrapolated out to 50 μm using data obtained from reflectance measurements of a goldblack sample substrate. The results are shown in figure 7.

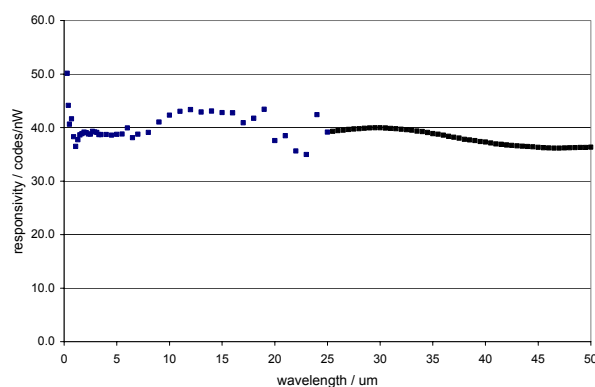


Figure 7: Absolute spectral response. (0.3 – 25 μm detector system, 25 – 50 μm goldblack sample).

FUTURE WORK

Three GERB instruments have been completed to date for launch on successive MSG satellites with a fourth in preparation. Together these instruments should provide continuous coverage of the Earth from geostationary orbit for a period of 15 – 20 years. For GERB-4 a new detector blacking program is underway with the construction of a new goldblack deposition facility at Leicester University.

ACKNOWLEDGEMENTS

Andrew Wood, Jeff Ridley and Bob Higashi were principally responsible for detector production and goldblack coating at Honeywell. The ASIC was designed by Richard Williams and Les Nuttall at Cambridge Consultants Ltd in the UK. The focal plane was assembled at Leicester University by Harold Chapman. Spectral calibration was performed at NPL with the help of Theo Theocarous and Nigel Fox.

REFERENCES

1. D.A. Bell: *A Geostationary Earth Radiation Budget Instrument*, Proc. SPIE 2209, 236, 1994.
2. N. Nelms, G. Butcher, C. Whitford, R.Cole, O.Blake, R. Williams, L. Nuttall: *Operation and performance of the ASIC for the GERB IR focal plane assembly*, Proc. SPIE 3759, 347, 1999.

THE ECONOMICAL MICROBOLOMETER-BASED ENVIRONMENTAL RADIOMETER SATELLITE (EMBERSAT) DESIGNED FOR FOREST FIRE DETECTION AND MONITORING

Redgie S. Lancaster¹, David R. Skillman, Wayne C. Welch, James D. Spinhirne, and
Katherine F. Manizade
NASA Goddard Space Flight Center, Greenbelt Maryland

Brian P. Beecken
Bethel College, St. Paul, Minnesota

ABSTRACT

Thermal infrared imagery from several satellite instruments, such as the NOAA AVHRR and the NASA MODIS, is presently used to detect and map forest fires. But while these radiometers can identify fires they are designed and optimized for cloud detection, providing relatively low spatial resolution and quickly saturating even for small fires. Efforts to detect and monitor forest fires from space would benefit from the development of single-sensor satellites designed specifically for this purpose. With the advent of uncooled thermal detectors, and thus the absence of aggressive cooling, the possibility of developing small satellites for the purpose of fire detection and monitoring becomes practical and cost-effective. Thus is the case with the Economical Microbolometer Based Environmental Radiometer Satellite (EMBERSat) program. The objective of this program is to develop a single, prototype satellite that will provide multi-band thermal imagery with a spatial resolution of 250m and a dynamic range of 300-1000K. The thermal imaging payload has flight heritage in the Infrared Spectral Imaging Radiometer that flew aboard mission STS-85 and the spacecraft is a variant of the SimpleSat bus launched from the shuttle Columbia as part of STS-105. The EMBERSat program is a technology demonstration initiative with the eventual goal of providing high-resolution thermal imagery to both the scientific community and the public.

INTRODUCTION

Satellite meteorology contributes a wealth of infrared imagery that is useful in identifying and monitoring forest fires from space. But while there is a niche for these data in fire detection their utility is limited by instrument design goals emphasizing the detection of clouds rather than fires. Clouds tend to be larger in extent and less bright in the infrared than fires and thus this imagery is of relatively coarse spatial resolution for fire detection and even small fires can saturate pixels. Further, the flight programs that provide these data do not have the flexibility to adopt changes that would make these measurements more useful for fire monitoring. The reasons being that these programs are costly and emphasize the provision of general-purpose meteorological data with a minimum of risk. As a result, the goal of achieving innovation in replacement payloads becomes secondary to the goal of providing data continuity and the security of past radiometer designs, which include HgCdTe detectors cooled to below 100K. Thus, in addition to not being optimally configured for fire detection these instruments also include the nontrivial costs and complexities associated with aggressive cooling. With the advent of uncooled IR detector technology new and exciting opportunities emerge to meet the challenges of remote fire detection using single-sensor, small satellites designed specifically for this measurement.

¹ Contact Information for R.S. Lancaster: Email: lancaster@virl.gsfc.nasa.gov, phone (310) 614-6284

SESSION 2B- Far IR/Sub-mm Thermal Detectors—New Concepts and Materials

In developing small satellites for infrared earth remote sensing the importance of eliminating aggressive cooling of the payload cannot be overstated. Such cooling typically consumes large amounts of electrical power, which is a precious commodity onboard a spacecraft. Further, the cooling subsystem adds cost, complexity and risk to the satellite development. Another important consideration in the development of small satellites is the presence of moving components often necessary to image in two dimensions. Uncooled detectors are available in large format arrays (480x640 pixels) and provide simultaneous imaging in two dimensions. The extended format of the array can also be used to improve the SNR of the measurement through the use of frame-averaging techniques such as Time Delay and Integration. By realizing these advantages the size and cost of IR imagers are reduced making them well suited for small spacecraft with limited power production capabilities.

The primary mission of the EMBERSat program is to demonstrate the utility of uncooled detector technology for identifying and monitoring forest fires from space using small, single-sensor spacecraft. The enabling technology is an uncooled microbolometer array detector (UMAD) built by BAE Systems. The EMBERSat project has its origins in two previous NASA flight projects that include the Infrared Spectral Imaging Radiometer (ISIR) and SimpleSat. The ISIR instrument was the first IR imaging radiometer payload to include a UMAD array and is shown on the left in Figure 1 (Lancaster et al., 2003). SimpleSat is a low-cost spacecraft bus designed for small payload applications and is shown on the right in Figure 1. Both were shuttle Hitchhiker projects.

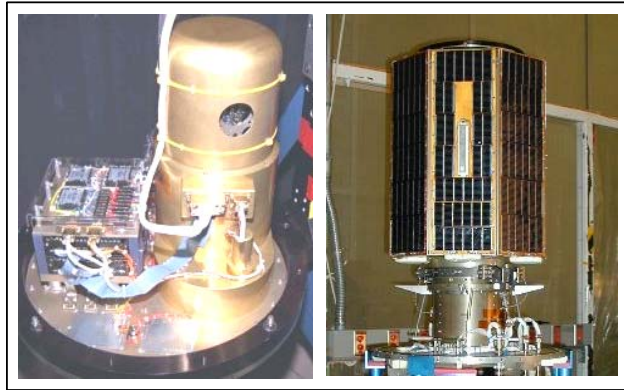


Figure 1: ISIR payload and SimpleSat spacecraft bus.

FIRE DETECTION METHODOLOGY

Forest fires appear bright in satellite imagery as a result of the enhanced blackbody emission they produce relative to cooler background regions. Thus to identify fires one searches the imagery for regions of anomalously high brightness temperature. The optimal portion of the infrared spectrum in which to conduct this search is the MWIR at a wavelength near 3.7 μ m. This wavelength corresponds to the color temperature of a fire at 800K and is centered within the atmospheric transmission window extending from 3.5 to 4 μ m. A channel near 11 μ m is used to provide context for what represents an anomalously high brightness temperature. This 11 μ m background channel is chosen based upon the color temperature of an object at 300K and the presence of an atmospheric transmission window. After calibration of the imagery a brightness temperature is calculated for each pixel in each of these spectral bands. The results of the background channel calculation are subtracted from those of the fire detection channel revealing pixels that contain the enhanced signature of a forest fire.

The level of spatial detail that is required to monitor forest fires from space depends upon the particular application. Data from existing meteorological satellites are currently utilized to assemble fire maps with a spatial resolution of about 1km. While this is sufficient for many applications there are others, such as potential operational uses, for which this spatial resolution is relatively coarse. Increasing the spatial resolution has associated costs, however, the primary ones being an increased data bandwidth or less frequent global coverage. Of these the latter is the most negotiable since two thirds of the earth is covered with water and not every fire needs to be viewed at the highest spatial resolution. Additionally, single-sensor spacecraft can be controlled for increased revisit times making higher spatial resolution practical.

The dynamic range of an imaging radiometer should be chosen so that saturation of the image is avoided. Current cloud radiometers typically saturate between 300-400K, which can occur even for small fires that do not fill the pixel field of view. To prevent saturation an upper limit of the dynamic range for a fire detection radiometer should be chosen around 1000K. The lower limit is selected to match typical background levels, which are at a temperature of about 300K. Historically, the choice of dynamic range

SESSION 2B- Far IR/Sub-mm Thermal Detectors—New Concepts and Materials

has also been restricted by the availability of digitizing hardware. Until recently imaging radiometers were limited to between 8 and 12-bit resolution requiring that a compromise be struck between the thermal resolution and dynamic range.

PAYLOAD DESCRIPTION

EMBERSat is a technology demonstration program that combines an UMAD-based infrared camera with the SimpleSat spacecraft bus for the purpose of remote fire detection and monitoring. Of these two technologies it is the uncooled detector array and the associated camera payload that serve as the focus of the current work. The EMBERSat camera payload builds upon the flight heritage of the Infrared Spectral Imaging Radiometer, which flew aboard the shuttle Columbia in 1997. This ISIR instrument was developed as a prototype compact imager for small satellite missions and has the unique distinction of being the first satellite meteorology payload to incorporate a UMAD.

The camera payload of EMBERSat is configured to provide measurements in spectral bands centered at 3.7 μ m and 11 μ m. The former channel has a passband of 0.5 μ m and the latter 1 μ m. The spatial resolution of the imagery is 250m when acquired from shuttle orbit. The dynamic range of the camera covers scene temperatures of 300 to 1000K and 14-bit thermal resolution is achieved.

Shown in Figure 2 are the telescope and detector electronics of the EMBERSat pushbroom imaging payload. This camera provides a cross track field of view of 15 degrees and 240x320-pixel imagery at a maximum rate of 60 frames per second. Channel selection is accomplished through the use of a spectral strip filter array assembled inside the UMAD package. The filter is oriented so that each portion of the ground track is sampled sequentially in the different spectral channels as the spacecraft advances in its orbit. This approach to spectral selection eliminates the need for a filter wheel, which would otherwise draw precious electrical power.

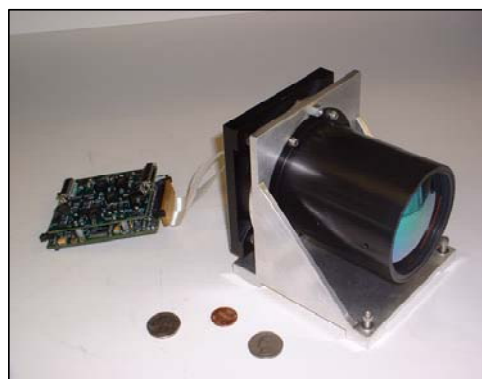


Figure 2. EMBERSat detector readout electronics and telescope

RADIOMETRIC PERFORMANCE

The EMBERSat payload is built upon the flight heritage of the ISIR shuttle experiment, from which a sample of data is shown in Figure 3. Also included for comparison in Figure 3 are measurements acquired during a coordinated under-flight by the MODIS Airborne Simulator (MAS). The Moderate Resolution Imaging Spectroradiometer (MODIS) payload currently supplies much of the imagery used in remote fire detection. The data displayed in Figure 3 are used to glean an NEDT estimate of 300mK (294K scene) for the 11 μ m channel of ISIR and a radiometric precision of approximately 100mK for the identical MAS channel. It is important to note, however, that current uncooled detectors offer an approximate threefold improvement in radiometric performance over these early ISIR measurements. This has been confirmed through measurements of the EMBERSat detector array. Hence, the thermal precision of the 11 μ m background channel of EMBERSat will rival that of the MODIS payload.

The fire detection channel of EMBERSat is less sensitive to low temperatures than the background channel for a variety of reasons. This does not pose a difficulty, however, since fires supply ample radiation due to their high temperatures. Measurements of the fire detection channel of EMBERSat reveal an achieved NEDT of 16K for a scene temperature of 300K. This is sufficient to detect a 4m² fire burning at an average temperature of 500K against a 300K background. Larger fires can be monitored with greater thermal resolution since the NEDT improves with increasing scene temperature. For example, the same fire would be measured with a precision better than 0.1K if it filled the entirety of the 250m pixel footprint. This thermal resolution matches the precision limit defined by the background measurement.

SESSION 2B- Far IR/Sub-mm Thermal Detectors—New Concepts and Materials

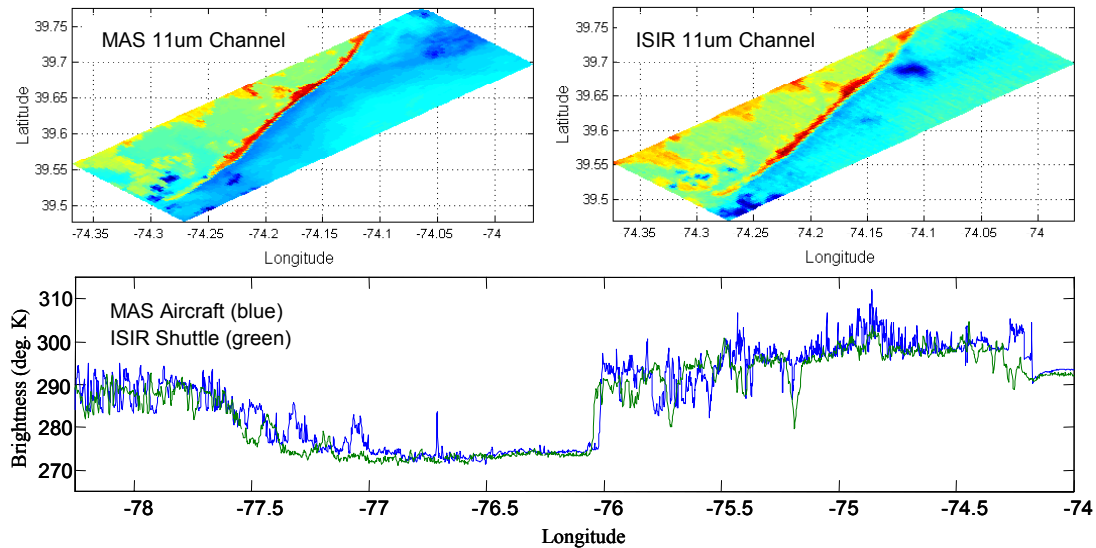


Figure 3: Comparison of imagery from the Infrared Spectral Imaging Radiometer that used an early prototype UMAD with MAS aircraft imagery commonly used in fire detection and monitoring.

DEVELOPMENT

The EMBERSat program operates under a development paradigm wherein undergraduate institutions build single-sensor satellites using the mature designs of previous NASA flight programs. The primary difficulty in developing satellites at the university level is that students and faculty typically have no experience doing so. The EMBERSat program fills this void by providing the flight designs, heritage and management experience required to make the program a success. University partners participate largely as technicians in this development. While unconventional this approach makes small satellite development accessible to even those institutions with no spaceflight infrastructure. All that is required on their part is a competence in science and engineering, an eagerness to accomplish something exciting and a willingness to follow instructions.

The EMBERSat program is designed for a budget of less than \$1M, which is much less than typical university-class satellites. There are several keys to achieving this budget. The first is to utilize existing flight designs. The second is to limit the program scope to one of technology demonstration requiring only a limited duration flight and providing for the exclusive use of commercial technologies. The third is to limit management to those engineers with direct experience developing either the spacecraft bus or the payload. By adopting these cost-saving measures widespread opportunity is created for educational institutions to participate in satellite development.

SUMMARY

With the advent of uncooled IR detector technology new and exciting opportunities emerge for the development of single-sensor satellites. EMBERSat is one such satellite designed to demonstrate the utility of using uncooled microbolometer array detectors for identifying and monitoring forest fires from space. The included UMAD technology is used to monitor fires with a spatial resolution of 250m, a dynamic range of 300-1000K and 14-bit thermal resolution. EMBERSat is being developed at the university level and provides undergraduate students with an opportunity be part of a satellite program that is both useful to the scientific community and capturing of the public's imagination.

REFERENCES

Lancaster, R.S., J.D. Spinhirne and K.F. Manizade, Combined infrared stereo and laser ranging cloud measurements from shuttle mission STS-85, J. Atmos. Ocean. Tech., 20, 67-78, 2003.

Thermal Emission Imaging System (THEMIS)

Carl F. Schueler¹ and Steven H. Silverman
Raytheon Santa Barbara Remote Sensing, Goleta, CA 93117

Philip R. Christensen
Department of Geological Sciences, Arizona State University, Tempe, AZ 85287-1404

ABSTRACT

The Thermal Emission Imaging System (THEMIS) is based on “bolt-together” pushbroom optics and uncooled silicon microbolometer focal plane array (FPA) technology. Sometimes dubbed “Mars Landsat,” THEMIS was launched in 2001 on Mars Odyssey, and provides guidance for future lander missions now in preparation for launch. Advanced materials and optical machining allow THEMIS low-scatter, reflective, wide field-of-view (WFOV) pushbroom optics for relatively long dwell-time compared to narrow FOV optics requiring cross-track scanning for equivalent spatial resolution. This allows uncooled silicon microbolometer FPAs, with less signal sensitivity than cryogenically cooled photo-diode FPAs, to meet the THEMIS sensitivity requirements.

INTRODUCTION

A major goal of the Mars Exploration Program is to help determine whether life ever existed on Mars via detailed *in situ* studies and surface sample return. It is essential to identify landing sites with the highest probability of containing samples indicative of early pre-biotic or biotic environments. Of particular interest are aqueous and/or hydrothermal environments in which life could have existed, or regions of current near-surface water or heat sources¹. The search requires detailed geologic mapping and accurate interpretations of site composition and history in a global context. THEMIS was designed to do this and builds upon a wealth of data from previous experiments.

Previous experiments include the Mariner 6/7 Mars Infrared Radiometer (MIR) and Infrared Spectrometer², the Mariner 9 Infrared Interferometer Spectrometer (IRIS)³, the Viking Infrared Thermal Mapper (IRTM)⁴, the Phobos Termoscan⁵, and the continuing Mars Global Surveyor (MGS) mission using the Mars Orbiter Camera (MOC)⁶ and MGS Thermal Emission Spectrometer (TES)⁷. TES has collected hyperspectral images (up to 286 spectral bands from 6-50 μm) of the entire martian surface, providing an initial global reconnaissance of mineralogy and thermophysical properties^{8,9}. By covering the key 6.3 to 15.0 μm region in both TES and THEMIS, it is possible to combine TES fine spectral resolution with THEMIS fine spatial resolution to achieve a global mineralogic inventory at the spatial scales necessary for detailed geologic studies within the Odyssey data resources.

Indeed, THEMIS is providing global maps of unique compositional units and the identification of key minerals and rock types with thermal infrared multi-spectral observations in nine wavelengths at 100-m resolution and 18-m visible imagery in up to five colors. The thermal-infrared spectral region was selected for mineral mapping because virtually all geologic materials, including carbonates, hydrothermal silica, sulfates, phosphates, hydroxides, and silicates have fundamental infrared absorption bands that are diagnostic of mineral composition. THEMIS visible imaging provides regional coverage (with global coverage a goal) at spatial scales that are intermediate between those of Viking and the detailed views from the MGS MOC⁶.

¹ Contact information for C. Schueler: Email: cfschueler@raytheon.com

THEMIS REQUIREMENTS AND DESIGN

THEMIS must identify minerals and morphology, i.e., compositional units. Mineral mapping has three thermal infrared requirements: (1) radiometric precision and accuracy to resolve the expected band depths for minerals present at 10% abundance; (2) spectral resolution to identify key minerals; and (3) 100 m spatial resolution to isolate small mineral deposits. The predicted performance for infrared noise equivalent temperatures (NEAT) range from 0.007 to 0.038 viewing Mars at surface temperatures of 245K to 270K. Most of the variation in SNR between bands is due to the variation in emitted energy for the 245 K reference temperature. As seen from these results, the THEMIS IR imager exceeds the proposed measurement requirements by a factor of two in most bands. The morphology objective yields a visible measurement requirement of 20 meters. Visible imager SNRs were computed for a low albedo (0.25), flat-lying surface viewed at an incidence angle of 67.5° under aphelion conditions. The SNR values for this case vary from 200 to 400.

THEMIS is shown in Figure 1 comprising two infrared and visible multi-spectral imagers that share optics and housing with independent power and data interfaces to the spacecraft for reliability, with a mass of 11.2 kg, dimensions of 29 x 37 x 55 cm, and 14 W orbital average power. The telescope is a three-mirror anastigmat with an f/1.6 12-cm effective aperture. A calibration flag, and the only moving part, provides thermal calibration and serves to protect the detectors from direct Sun. The electronics, on the left in the THEMIS artist concept, provide digital data collection and processing as well as instrument control and data to the spacecraft. An aluminum main frame provides the spacecraft mounting interface and supports the electronics and optics. Multi-layer insulation blankets and thermal control surfaces provide a stable thermal environment and a heatsink for the electronics and the thermal electric cooler (TEC) temperature controller on the focal plane arrays (FPAs).

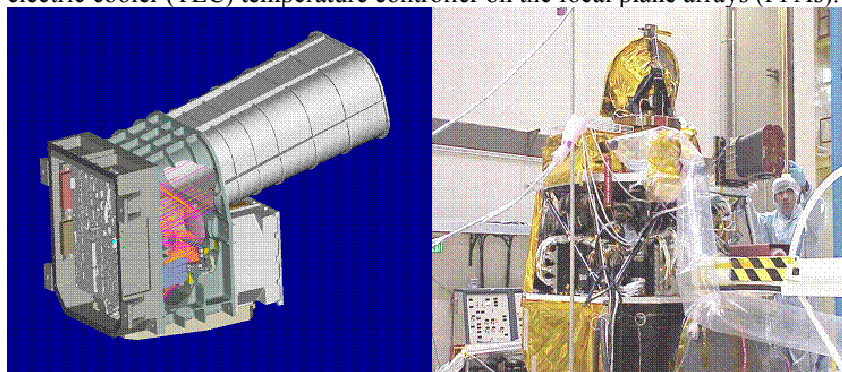


Figure 1: THEMIS artist concept and flight instrument being installed on the Mars Odyssey Spacecraft.

Diamond-turned, “bolt-together” telescope technology (Figure 2) was the first key to THEMIS affordability and success for a cost, mass, and volume constrained planetary science mission. Precision machining allowed the entire optical stage to be assembled without adjustments, yet with diffraction-limited performance in both the visible and infrared, with mounting surfaces machined to ± 5 μm tolerance. Optical surfaces were machined directly from high-order aspheric equations. Aluminum reduced cost, with nickel plating and automated post polishing to reduce surface scatter to levels unobtainable solely from diamond turning.

SESSION 2B- Far IR/Sub-mm Thermal Detectors—New Concepts and Materials

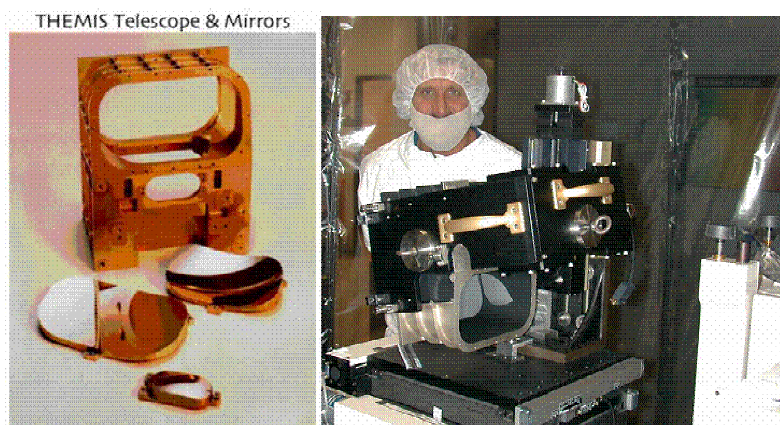


Figure 2. THEMIS diamond-turned “bolt-together” telescope components prior to and after assembly.

The second key to THEMIS success is the uncooled thermal IR microbolometer focal-plane array (FPA) operating at ambient temperature illustrated in Figure 3 to substantially reduced the complexity of fabrication, testing, spacecraft interfaces, and mission operations compared to what would have been necessary with cryogenically cooled photo-diode array technology. The array is 320 (cross-track) by 240 (along-track) with 50 μm unit cell dimension translating to 100 m geometric instantaneous field-of-view (GIFOV) and ~ 32 km swath width. A thermal electric cooler (TEC) stabilizes the IR FPA temperature to ± 1 mK. THEMIS uses microbolometer FPAs produced by Raytheon Vision Systems (RVS) under license from Honeywell, Inc., and the THEMIS IR FPA is derived from a Raytheon hand-held imager developed for rugged military use, which significantly reduced development cost compared to a custom design. The microbolometer arrays were grown directly on the surface of RVS Readout Integrated Circuits (ROIC).

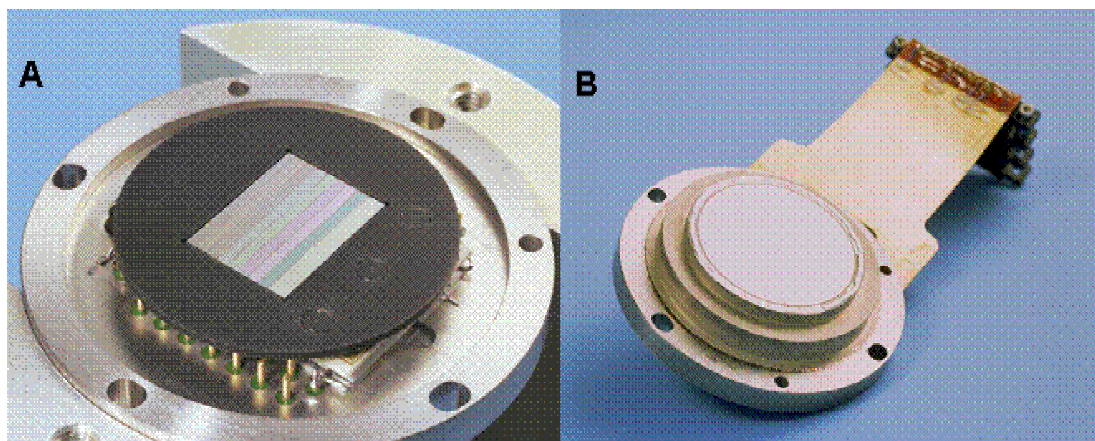


Figure 3: (a) THEMIS infrared focal-plane and stripe-filter layout. (b) Complete uncooled FPA package.

Figure 3 shows the stripe filters that produce $\sim 1\mu\text{m}$ wide bands at nine wavelengths from 6.78 to 14.88 μm graphed in Figure 4. These include eight surface-sensing wavelengths and one atmospheric wavelength. Each covers 16 lines along-track (320 detectors per line cross-track) in time-delay and integration (TDI) to build SNR, with an 8-line “dead-space” between filters. To maximize manufacturing yield and reduce costs, the stripe filters were fabricated separately and butted together. The calculated dwell time for a single pixel, at an orbit of 400 km and a 100-meter GIFOV is 29.9 msec, closely matching the 30 Hz microbolometer array frame rate. The visible imager is a derivative of the Malin Space Science Systems (MSSS) Mars Polar Lander (MPL) MARs Decent Imager (MARDI), with a 5-filter subset of the MSSS MARs Color Imager (MARCI) developed for the Mars Climate Orbiter (MCO). The visible imager has 1,024 cross-track pixels with an 18-m IFOV covering a 18.4-km swath bore-sighted with the IR imager through a beamsplitter and has five stripe filters centered from 0.425 to 0.86 μm .

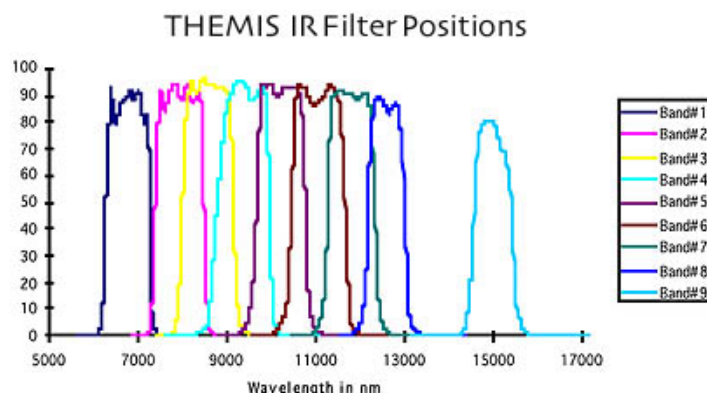


Figure 4: THEMIS IR spectral bandpasses from data collected at SBRS prior to instrument delivery.

ACKNOWLEDGEMENTS

We thank the THEMIS detailed design and implementation team at Raytheon SBRS and MSSS, and the software development team at ASU. Carl Kloss provided excellent management at JPL, and Tim Schofield provided the scientific interface with the MGS Project Office.

REFERENCES

1. *An exobiological Strategy for Mars Exploration*, Exobiology Working Group, NASA Headquarters, 1995.
2. G.C. Pimentel, P.B. Forney and K.C. Herr, *Evidence about hydrate and solid water in the Martian surface from the 1969 Mariner infrared spectrometer*, J. Geophys. Res., 79 (11), 1623-1634, 1974.
3. B. Conrath, R. Curran, R. Hanel, V. Kunde, W. Maguire, J. Pearl, J. Pirraglia and J. Walker, *Atmospheric and surface properties of Mars obtained by infrared spectroscopy on Mariner 9*, J. Geophys. Res., 78, 4267-4278, 1973.
4. H.H. Keiffer, T.Z. Martin, A.R. Peterfreund, B.M. Jakosky, E.D. Miner and F.D. Palluconi *Thermal and albedo mapping of Mars during the Viking primary mission*, J. Geophys. Res., 82, 4249-4292, 1977.
5. A.S. Selivanov, M.K. Naraeva, A.S. Panfilov, Y.M. Getkin, V.D. Kharlamov, A.V. Romanov, D.A. Formin and Y.Y. Miroshnichenko, *Thermal imaging of the surface of Mars*, Nature, 341, 593-595, 1989.
6. M.C. Malin and K.S. Edgett, *Mars Global Surveyor Mars Orbiter Camera: Interplanetary cruise through primary mission*, J. Geophys. Res., 106, 23,429-23,570, 2001.
7. P.R. Christensen, J.L. Bandfield, V.E. Hamilton, S.W. Ruff, H.H. Kieffer, T. Titus, M.C. Malin, R.V. Morris, M.D. Lane, R.N. Clark, B.M. Jakosky, M.T. Mellon, J.C. Pearl, B.J. Conrath, M.D. Smith, R.T. Clancy, R.O. Kuzmin, T. Roush, G.L. Mehall, N. Gorelick, K. Bender, K. Murray, S. Dason, E. Greene, S.H. Silverman, and M. Greenfield, *The Mars Global Surveyor Thermal Emission Spectrometer experiment: Investigation description and surface science results*, J. Geophys. Res., 106, 23,823-23,871, 2001a.
8. J.L. Banfield, *Global mineral distributions on Mars*, J. Geophys. Res., 107, 10.1029/2001JE001510, 2001.
9. S.W. Ruff, and P.R. Christensen, *Bright and dark regions on Mars: Particle size and mineralogical characteristics based on Thermal Emission Spectrometer data*, J. Geophys. Res., in press, 2002.

FAR IR AND SUBMILLIMETER FILLED BOLOMETER ARRAYS PERFORMANCES AT 300 mK AND 2K

Vincent Reveret, Louis Rodriguez^{*}, Laurent Vigroux
CEA/DSM/DAPNIA Service d'Astrophysique, CEA Saclay, 91191 Gif sur Yvette
Cedex, France

Patrick Agnese
LETI/CEA Grenoble, 17 avenue des Martyrs, 38054 Grenoble Cedex 9, France

ABSTRACT

CEA developed large (2048 pixels) filled bolometer arrays for the HERSCHEL PACS photometer in the 60-200 μm spectral band. We present the detector design and its performances at 300 mK. The PACS spectral band can easily be extended to longer wavelengths for future applications. Some details of the possible adaptation are given here. We also evaluate the expected performances when adapted and operated at higher temperature (2K). Calculations show that, in this condition, the expected NEP is close to $1.10^{-15} \text{ W/Hz}^{1/2}$ for a 100 pW/pixel flux.

INTRODUCTION

HERSCHEL, the future far infrared and submillimeter observatory, will include three instruments. Two of them, PACS¹ and SPIRE², are spectro-photometers and are designed for observations between 60 and 200 μm , and 200 and 600 μm respectively. CEA/LETI/DOPT/Laboratoire Infrarouge and CEA/DSM/DAPNIA/Service d'Astrophysique are developing new technology bolometer arrays optimized for the PACS photometer. The design was motivated by the need to provide very good image quality and fast mapping speed in high background conditions. These requirements have led to the following constraints:

- Optimal sampling of the PSF ($0.5 F\lambda$ pixel field of view)
- Large number of pixels (> 1000) to get large field of view
- Use of existing technologies to minimize development time and ensure a good production yield
- Integrated cold electronics including cold multiplexer
- Low operating temperature (300 mK) easily achievable by sorption coolers

The need for a manufacture based on existing technology has led to an all silicon design:

- Ionic implantation to obtain resistive thermometers
- Silicon micro-etching to realize suspended absorbing grids
- Flip-chip technology to assemble the different functions
- CMOS cold multiplexer and readout electronics

PACS photometer is divided in two bands :

- 60-130 μm devoted to the "blue" focal plane (32 x 64 pixels),
- 130-210 μm measured by the "red" focal plane 16 x32 pixels).

The first PACS focal plane was completed in January 2002.

^{*} *Contact information for L. Rodriguez - Email : louisrod@cea.fr*

DETECTOR DESIGN

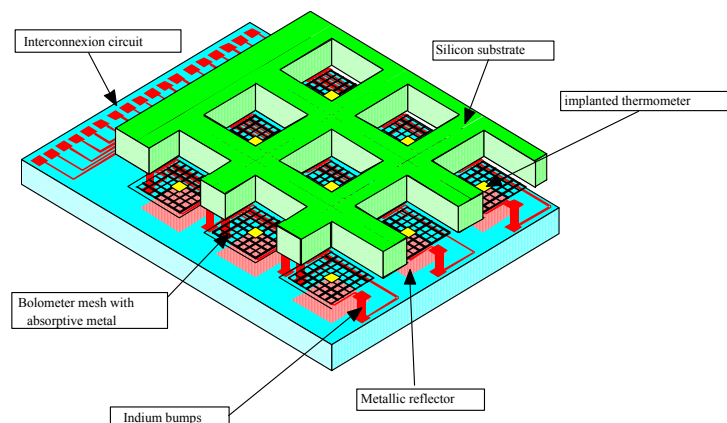


Figure 1: conceptual drawing of the Bolometer array developed for Herschel PACS.

Thermometer

The choice of CMOS cold electronics requires very high responsivity bolometers (10^{10} V/W or more). Such value is obtained by increasing the thermometers impedance to reach 1 to 10 G Ω . During the early phases of this project, we have demonstrated that it was possible to achieve such high resistance thermometers at 300 mK in the hopping conduction regime with phosphorus implantation and 50% Boron compensation. To ensure a good homogeneity of the implantation, we have developed a new process by ion implantation on a double silicon-on-insulator (SOI) substrate. The thermometer is implanted on the silicon, above the oxide; then the implantation is homogenized by thermal diffusion. Contact pads are implanted above the thermometer and micro-etching of the thermometric layer produces the thermometer at the required geometry.

Grids and metallic absorption layer

The absorption principle is based on resonant absorption by a metallic layer placed above a quarter wave resonant cavity. The high absorption efficiency profile can be extended beyond the vertical resonant cavity peak by suitable grid patterns, which create an “horizontal” resonance. The cavity is obtained, in our design, by two silicon layers. On the upper one, we have the suspended silicon grids with absorbing metal, beneath a gold reflector is deposited on the second silicon substrate, also used for the cold readout electronics. Indium bumps in between ensure the mechanical support of the grid layer and tune the cavity size. 20 and 25 μm bumps are used respectively for the blue and the red channels of PACS. The indium bumps also permit the electric contact with the thermometers, and ensure the thermal link of the bolometers with the 300 mK cryocooler tip.

Thermal design

The thermal decoupling between the absorbing grid and the silicon substrate is ensured by thin rods of silicon. The thermal impedance of these rods is $\sim 10^{11}$ K/W at 0.3 K for rods of 1 mm length and $2 \mu\text{m} \times 5 \mu\text{m}$ section. The passivation layer is silicon oxide, preferred to the “heavy” silicon nitride used previously. At 0.3 K the bulk silicon dominates the thermal impedance.

Signal processing

MOS transistors are implanted directly below each pixel and adapt the high impedance of the bolometers to the following amplifying stage at 2K. The possibility to commute between a reference voltage source and the bridge signal above the MOS readout allows double correlated sampling to remove the $1/f$ noise component of the MOS follower. This stage and the 16 to 1 multiplexer are implanted in the silicon plate below the absorbing grids. They are all working at 300 mK. A second stage of amplification is provided by

SESSION 2B- Far IR/Sub-mm Thermal Detectors–New Concepts and Materials

another PMOS preamplifier at 2 K. Two lines of blind pixels are implanted on the side of the 16x16 active pixel arrays. They are used to determine all the collective perturbations that affect the signal via differential measurements.

The following figure shows one of the assembled blue focal plane.

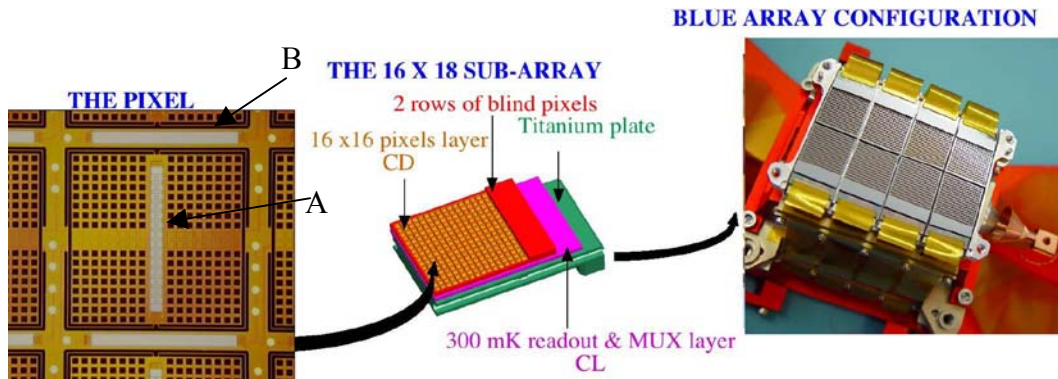


Figure 2: From left to right: a close view of the pixel grid (with the bolometric thermometer A in the center, and two reference thermometers B), a schematic drawing of the detector structure, and the complete blue focal plane with 8 sub-arrays.

RESULTS

Tests at 300 mK

The bolometer arrays have been successfully tested³ for vibration and shocks at 77 K.

The power budget available for bolometer operations is 14 μ W, which is compatible with the thermal dissipation of the 300 mK MOS followers.

All the operating modes of the control and readout electronics, multiplexer, double correlated sampling, differential mode with the blind pixels, have been tested and are functional.

We measured the noise spectral density to be $1 \mu\text{V}/\sqrt{\text{Hz}}$ at 10 Hz in the 40 Hz multiplexed mode. The infrared load per pixel was $\sim 1 \text{ pW}$, simulating the optical load inside the PACS instrument. In these conditions, we measured a response of $\sim 10^{10} \text{ V/W}$, using an internal 20 K black body and a temperature controlled cold chopper, leading to an NEP of $10^{-16} \text{ W}/\sqrt{\text{Hz}}$ which corresponds to the BLIP conditions.

The spectral response of the bolometers has been measured in a polarizing Fourier Transform Spectrometer. Early results show more than 85% of absorption in the two PACS bands. Uncertainty in the results is quite important for the highest frequencies because of problems with polarizing grids.

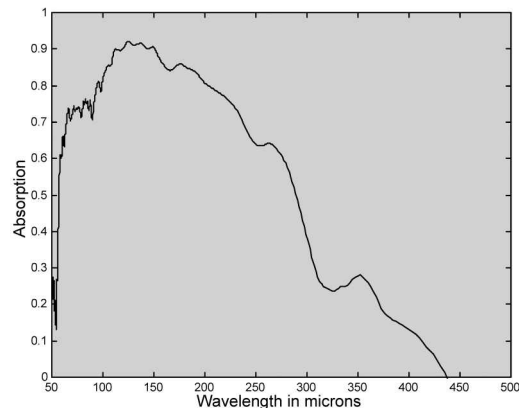


Figure 3: Absorption curves for the “Red” (--) array and “Blue” (-) array.

SESSION 2B- Far IR/Sub-mm Thermal Detectors—New Concepts and Materials

We are currently working on a system to increase the absorption in longer wavelengths (up to the 870 μm atmospheric band). The system will be made of simple dielectric materials deposited on the top of the bolometer and will act as an anti-reflecting layer (2002 CEA patent).

Simulations for the 2K case

The estimation of the performances at 2K is based on a numerical model that solves the bolometer differential equation with the specific parameters of the CEA bolometers. The optimum bias is estimated and leads to a total NEP of $10^{-15} \text{ W}/\sqrt{\text{Hz}}$ at 200 μm , for a 100 pW per pixel flux. This value is dominated by the MOS noise. The phonic noise is of the same order of magnitude as the photonic noise ($\sim 7 \cdot 10^{-16} \text{ W}/\sqrt{\text{Hz}}$).

CONCLUSION AND PROSPECTS

The results so far demonstrate the validity of the technical choices behind the design of these bolometer arrays. The noise performances and the optical absorption are good enough to achieve BLIP conditions in HERSCHEL PACS.

A simple solution has been found to adapt these bolometers to the detection of longer wavelengths (100 μm to 850 μm). In a near future, we envisage to develop other arrays at 450 and 865 μm for ground based or balloon instruments. In particular a balloon instrument, ELISA, is under evaluation by CNES, to be launched in 2005 – 2006 (PI: I. Ristorcelli, CESR, France).

REFERENCES

1. A. Potglitsch, C. Waelkens, N. Geis, *The Photodetector Array Camera and Spectrometer (PACS) for Herschel*: Proc. The Promise of the Herschel Space Observatory, 12-15 December 2000, Toledo, Spain, G.L. Pilbratt, J. Cernicharo, A.M. Heras, T. Prusti, R.A. Harris Edts. ESA publications, SP-460, page 29
2. M.J. Griffin, B.M. Swinyard, L. Vigroux: *The SPIRE instrument for Herschel*, Proc. The Promise of the Herschel Space Observatory, 12-15 December 2000, Toledo, Spain, G.L. Pilbratt, J. Cernicharo, A.M. Heras, T. Prusti, R.A. Harris Edts. ESA publications, SP-460, page 37
3. L. Rodriguez et al, Proc SPIE 4855, 108, 2003

COLD-ELECTRON BOLOMETER WITH STRONG ELECTROTHERMAL FEEDBACK

Leonid Kuzmin*

Chalmers University of Technology, Department of Microtechnology and Nanoscience
S-41296 Gothenburg, Sweden, kuzmin@fy.chalmers.se

ABSTRACT

A novel concept of the Cold-Electron Bolometer (CEB) based on strong *direct electron cooling* of the absorber has been proposed. This concept is purposed to overcome the unavoidable contradiction of supersensitive detectors between supersensitivity and supersaturation due to background power load. The effective electron cooling can be treated as strong electrothermal feedback (ETF) similar to TES (transition-edge sensor) in voltage-biased mode. However, in contrast to TES, an additional artificial dc heating for electrothermal feedback is replaced by deep electron cooling removing all incoming power from the absorber to the next stage and keeping minimum temperature (less than phonon temperature for small level of power). The CEB can be treated as "0-detector" in comparison with TES treated as "Tc-detector". Noise properties (NEP) are considerably improved by decreasing the electron temperature. It could mean principle breakthrough in realization of supersensitive detectors. All incoming power is removed from supersensitive absorber to the next stage of readout system – a SQUID with considerably higher dynamic range. As in TES, the strong ETF (up to 1000) decreases the response time of CEB from e-ph time ($\approx 10 \mu\text{s}$) to cooling (tunneling) time ($\approx 10 \text{ ns}$)

The estimations show that it is realistic to achieve NEP of the order of $10^{-19} \text{ W/Hz}^{1/2}$ with SQUID readout system at 100 mK and $10^{-18} \text{ W/Hz}^{1/2}$ at 300 mK. At 2 K the theoretical evaluations show that the expected NEP is of the order of $2 \times 10^{-16} \text{ W/Hz}^{1/2}$ and increases to the level of $8 \times 10^{-16} \text{ W/Hz}^{1/2}$ for background load of 100 pW.

INTRODUCTION

In the last decade superconducting detectors have become the most sensitive radiation detectors of Sub-mm, Infrared, and Optical radiation with an estimated ultimate sensitivity down to $10^{-20} \text{ W/Hz}^{1/2}$ [1]. A few modest imaging arrays for ground-based sub-mm observations are already operational and plans for building significant larger arrays are approved. Ultra-low-noise bolometers are required for space-based astronomical observations. The two proposed NASA missions, SPIRIT and SPECS, determine the highest level of requirements for bolometers for nearest future. The detector goal is to provide noise equivalent power less than $10^{-20} \text{ W/Hz}^{1/2}$ [2] over the 40 – 500 μm wavelength range in a 100x100 pixel detector array. No one existing technology could satisfy these requirements. The proposed CEB concept could be a good candidate to become a leading concept in this development.

* Contact information for L. Kuzmin-Email: kuzmin@fy.chalmers.se

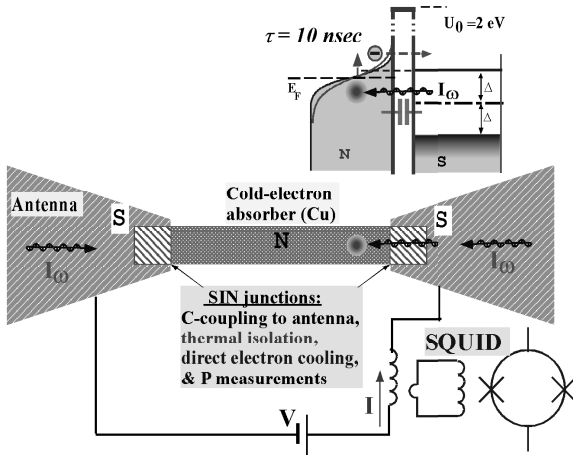


Fig. 1. Capacitively coupled Cold-Electron Bolometer (CEB) with SIN tunnel junctions for **direct electron cooling and power measurement**. The highest sensitivity (due to low T_e) is combined with fastest time response (around 10 ns) determined mainly by tunneling time

For the moment, the most developed superconducting bolometer is TES (transition-edge sensor) with strong electrothermal feedback [3]. However, the TES has some problems with excess noise, saturation, and the most drastic problem of artificial overheating by dc power for the feedback. This additional heating kills all efforts on deep

cooling and does not give good perspectives for realization of limit performance of the bolometer. In contrast to this overheating, the principle new concept of a “**Cold-Electron**” **Bolometer (CEB)** with direct electron cooling (Fig. 1) has been proposed by Kuzmin et al. [4,5]. The CEB is the only concept suggesting effective removing incoming background power from supersensitive region of absorber. This concept has good perspectives because it returns system to lowest temperature (noise) state with highest responsivity to the signal. All signal power is used for measurements (without lost to e-ph leakage). Time constant is determined by tunneling time that is at 2-3 orders of magnitude shorter than e-ph time and could be estimated as 10 ns [6]. This bolometer can be especially effective for operation in the presence of a real background power load. The optimal realization of this sensor proved to be a two junction **cold-electron bolometer with capacitive coupling** to the antenna [7]. Theoretical estimations and preliminary experiments show that it is possible to realize the necessary sensitivity of better than 10^{-18} W/Hz^{1/2} with antenna-coupled nanobolometers at a temperature ≤ 0.3 K. Additional advantages of such detectors are easy integration in arrays and the possibility of polarization measurements.

Comparison of CEB and TES

The operation of CEB can be analyzed using a heat balance equation [8]:

$$P_C(V, T_e, T_{ph}) + \Sigma \Lambda (T_e^5 - T_{ph}^5) + C_A \frac{dT}{dt} = P_0 + \delta P(t) \quad (1)$$

Here, $\Sigma \Lambda (T_e^5 - T_{ph}^5)$ is the heat flow from electron to the phonon subsystems in the normal metal, Σ is a material constant, Λ - a volume of the absorber, T_e and T_{ph} are, respectively, the electron and phonon temperatures of the absorber; $P_{cool}(V, T_e, T_{ph})$ is cooling power of the SIN tunnel junctions; $C_A = \gamma T_e$ is the specific heat capacity of the normal metal; and $P(t)$ is the incoming rf power. We can separate Eq. (1) into the time independent term, $\Sigma \Lambda (T_{e0}^5 - T_{ph}^5) + P_{cool0}(V, T_{e0}, T_{ph}) = P_0$, and the time dependent term,

$(\frac{\partial P_{cool}}{\partial T} + 5 \Sigma \Lambda T_e^4 + i \omega C_A) \delta T = \delta P$. The first term, $G_{cool} = \delta P_{cool} / \delta T$, is the cooling thermal conductance of the SIN junction that gives the negative electrothermal feedback (Fig. 2a), the second, $G_{e-ph} = 5 \Sigma \Lambda T_e^4$, is electron-phonon thermal conductance of the absorber.

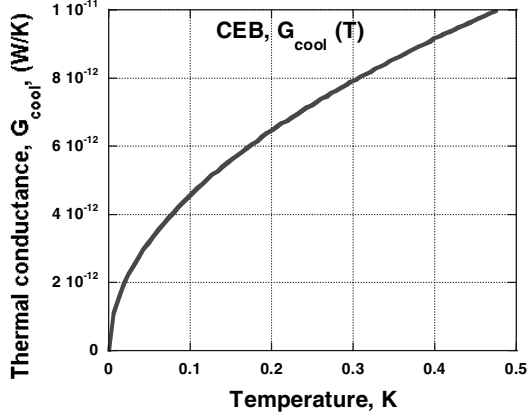


Fig. 2b: Cooling conductance of CEB for operation near “ $T=0$ ” (possible minimum T).

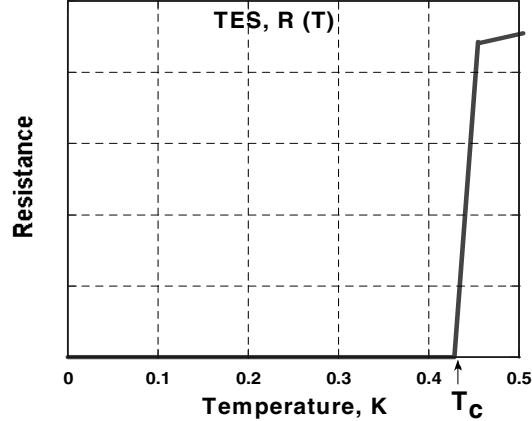


Fig. 2b: Nonlinear resistance of TES for operation near T_c

The current responsivity is given by

$$S_i = \frac{\partial I}{\partial P} = \frac{\partial I / \partial T}{G_{cool} + G_{e-ph} + i\omega C_A} = \frac{\partial I / \partial T}{G_{cool}} \frac{L}{(L+1)[1 + i\omega\tau]}, \quad (2)$$

where $L = G_{cool}/G_{e-ph} \gg 1$ is ETF gain, and $\tau = \tau_0/(L+1)$ is an effective time constant, $\tau_0 = C_A/G_{e-ph}$ ($\cong 10 \mu s$ at 100 mK). It is clear that the effective thermal conductance is increased by the effect of cooling (negative ETF) and time constant is proportionally decreased. These formulae for S_i are similar to TES ones with replacement of $(\partial I / \partial T)/G_{cool} (\cong e/kT)$ by $1/V_b$. We compare now the basic parameters of CEB and TES (Fig 2-4).

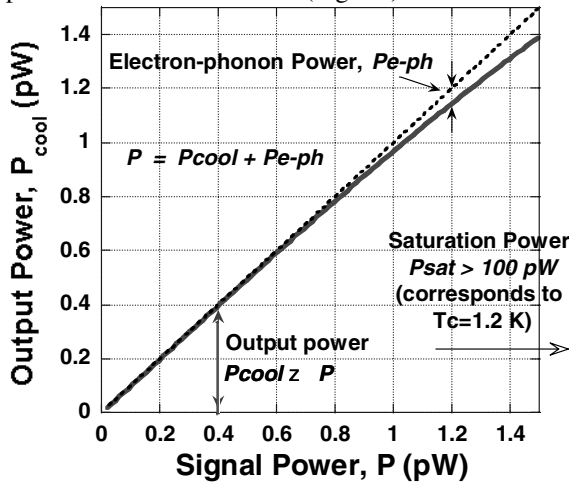


Fig. 3a: Output (cooling) power of CEB in dependence on Signal power (they are almost equal). There is no Saturation power at these level of signal and saturation can be achieved only after heating to T_c of Al electrode (P_{sat} around $100 \pm \text{pW}$).

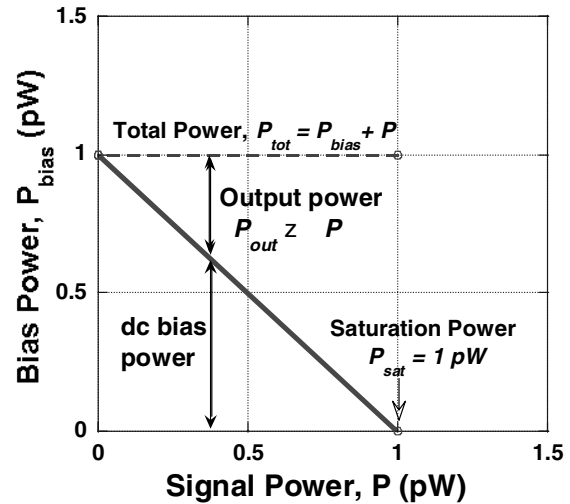


Fig. 3b: Bias power and Output power of TES in dependence on Signal power. Saturation power is equal to bias power without signal. To increase P_{sat} , the P_{bias} should be increased (but it leads to increase of T and NEP).

Due to strong ETF the output power is equal to signal power in both cases. The only difference is that for TES the P_{out} is decrease of dc bias power meanwhile for CEB the P_{out} is the directly removed power P_{cool} by cooling junctions.

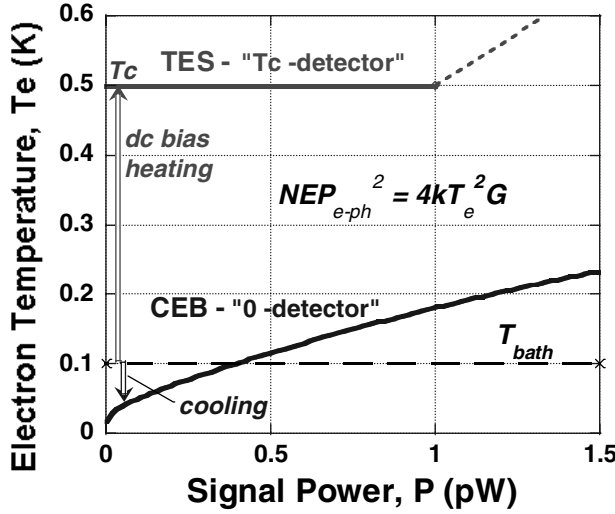


Fig. 4: Electron temperature as a function of signal power for $T_{bath}=100$ mK. For $P<0.4$ pW, the T_e of CEB is less than T_{bath} (real Cold-Electron Bolometer mode)

The Fig. 4 shows principle difference of TES and CEB: TES is working near T_c and supports this temperature decreasing dc heating by ETF proportionally to the received signal. On the contrary, CEB is working near zero temperature (possible available minimum of T_e) and removes incoming power from the absorber by tunnel junctions. As the result, all properties of CEB are determined by low temperature (NEP_{e-ph} is shown in Fig. 4) meanwhile for TES it is always T_c even for very small signals.

Noise properties of CEB are characterized by the noise equivalent power (NEP):

$$NEP_{total}^2 = NEP_{e-ph}^2 + NEP_{SIN}^2 + \frac{\delta I^2}{S_I^2}. \quad (3)$$

Here $NEP_{e-ph}^2 = 10k_B \Sigma \Lambda (T_e^6 + T_{ph}^6)$ is the noise associated with electron-phonon interaction; NEP_{NIS}^2 is the noise of the NIS tunnel junctions, and the last term, $\delta I^2/S_I^2$, is the noise of the amplifier (SQUID). The noise of the NIS tunnel junctions, NEP_{NIS}^2 , has three components: shot noise $2eI/S_I^2$, the fluctuations of the heat flow through the tunnel junctions and the correlation between these two processes

$$NEP_{SIN}^2 = \delta P_\omega^2 - 2 \frac{\delta P_\omega \delta I_\omega}{S_I} + \frac{\delta I_\omega^2}{S_I^2}. \quad \text{Due to this correlation the short noise is decreased at 30-50\%.$$

Similar correlation is in TES decreasing Johnson noise. The estimations for CEB show that it is realistic to achieve NEP of the order of 10^{-19} W/Hz^{1/2} at 100 mK and 10^{-18} W/Hz^{1/2} at 300 mK [7].

CEB at 2 K

The operation of CEB has been analyzed at 2K for typical parameters of the bolometer: $T_c = 9$ K (Nb), $\Lambda = 0.002$ μm^3 , $R = 1$ k Ω , $S_{\text{SQUID}} = 10$ fA/Hz^{1/2} (Fig. 5a). The change of NEP components in the presence of

background power load 100 pW is shown in Fig. 5a. Electron-phonon conductance $G_{e-ph} = 5 \Sigma \Lambda T_e^4$ is

replaced at this temperature by Kapitza resistance $R_K = K / T_{ph}^3$, where A is an area of the interface and K is material constant: for copper-plastic interface $K = 7.5 \times 10^{-4}$ K⁴m²/W [9]. Second term in Eq. 1 is

replaced by $K \Lambda (T_e^4 - T_{ph}^4)$.

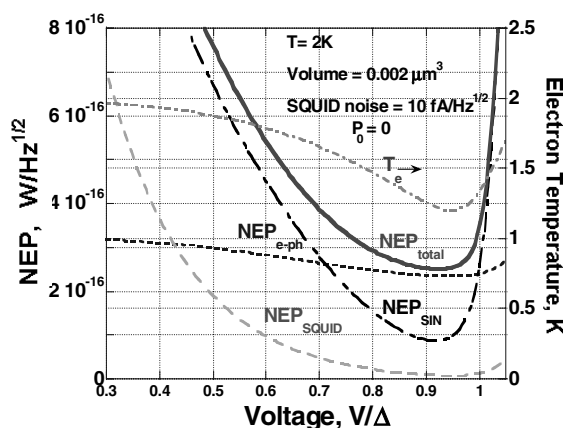


Fig. 5a. NEP components and electron temperature of the CEB in dependence on voltage for $\Lambda = 0.002 \mu\text{m}^3$, $R = 1 \text{ k}\Omega$, $S_{\text{SQUID}} = 10 \text{ fA/Hz}^{1/2}$, and bath temperature 2 K;

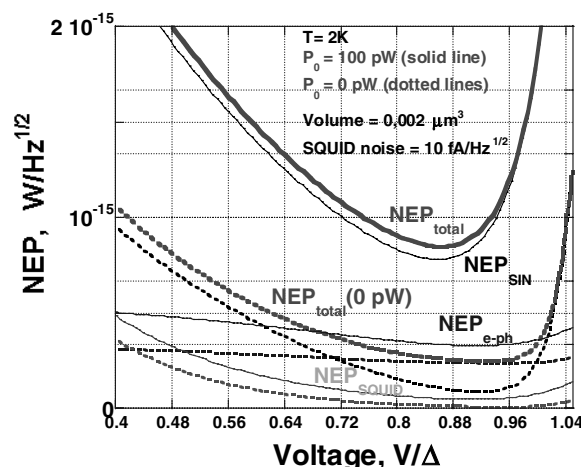


Fig. 5b. NEP of the CEB in presence of the background load 100 pW (solid line) and without it (dashed line) for the same bolometer parameters.

The theoretical evaluations show that the expected NEP is of the order of $2 \times 10^{-16} \text{ W/Hz}^{1/2}$ without load and increases to level of $8 \times 10^{-16} \text{ W/Hz}^{1/2}$ for background load of 100 pW. Cooling ability of CEB make it possible to keep relatively low NEP at $T = 2 \text{ K}$ with moderate decrease of T_e to 1.2 K.

The author would like to thank Paul Richards for stimulating discussions. The work was supported by VR and STINT agencies.

REFERENCES

1. A. Bitterman, *Superconductor & Cryoelectronics*, Vol. 12, No. 2, (1999) 17.
2. D. Leisawitz et al., "Scientific motivation and technology requirements for the SPIRIT and SPECS far-infrared/submillimeter space interferometers", SPIE 2000.
3. A. Lee, P. Richards, S. Nam, B. Cabrera, K. Irwin, *Applied Physics Letters*, **69**, (1996) 1801.
4. L. Kuzmin, I. Devyatov, and D. Golubev. "Cold-electron" bolometer with electronic microrefrigeration". Proceeding of SPIE, v. 3465, pp. 193-199 (1998).
5. L. Kuzmin, "On the Concept of a Hot-Electron Microbolometer with Capacitive Coupling to the Antenna" *Physica B: Condensed Matter*, **284-288**, (2000) 2129.
6. D.-V. Anghel, and L. Kuzmin. *Applied Physics Letter*, **82**, N2, 293-295 (2003).
7. L. Kuzmin and D. Golubev. *Physica C* **372-376**, pp 378-382 (2002).
8. D. Golubev and L. Kuzmin. *Journal of Applied Physics*. **89**, 6464-6472 (2001).
9. R. Bayrle and O. Weis. *J. Low Temp. Phys.*, **76**, 129 (1989).

THE CASE FOR MODERATELY-COOLED, FAR- INFRARED THERMAL DETECTORS

John C. Brasunas¹, Brook Lakew

Code 693, NASA Goddard Space Flight Center, Greenbelt, MD 20771 USA

ABSTRACT

There are moderately-cooled (around 77K) infrared detectors, for instance InSb (around 5 microns wavelength) and HgCdTe (around 15 to 20 microns wavelength). However for longer wavelengths there are either uncooled thermal-type detectors or highly cooled (about 4K and lower) quantum and thermal detectors, with the notable exception of high T_c superconductor detectors.

We will describe certain long-wavelength applications in space where only moderate cooling is feasible, and where better sensitivity is required than possible with uncooled detectors. These requirements could be met with high T_c bolometers, but it may also be prudent to develop other technologies. Additionally, over the past 16 years a marketplace has not developed for the commercial production of high T_c bolometers, indicating their production may be a natural endeavor for government laboratories.

GENERAL OVERVIEW OF AVAILABLE DETECTOR TECHNOLOGY

Infrared (IR) detectors (direct detection only will be discussed here) are generally available in two modes, thermal and quantum, and for a range of operating temperatures. Colder detectors are generally faster, more sensitive, and usable to longer wavelengths. Uncooled (~300K) detectors are very broadly available, both in thermal mode (throughout the IR spectrum from a few microns to 1000 μ m or so) and in quantum mode (generally in the near infrared, a few microns). Highly cooled (~4K and below) detectors are available throughout the IR spectrum, in both thermal and quantum modes. Moderately cooled detectors (~77K) are available as quantum detectors to 5 μ m (InSb), about 15-20 μ m (HgCdTe, varies with doping), but generally not as thermal detectors or for the far-infrared (FIR, from about 25 μ m to 1000 μ m). The major exception, of course, is the high T_c superconductor bolometer.

There is a huge difference between the performance of thermal-mode, room-temperature detectors (detectivity $D^* \sim 10^8$ to 10^9 cmHz^{1/2}/W, where D^* is an area-normalized measure of S/N, higher D^* being better) and 4K detectors ($D^* \sim 10^{13}$). When the detector operating temperature is lowered, the phonon noise decreases; also, the minimum possible thermal conductance G (radiative) decreases. Furthermore, the heat capacity C declines as phonon modes freeze out (this happens sooner rather than later for high Debye temperatures). The theoretically possible D^* , assuming the minimum thermal conductance and assuming all other noise sources are small compared with thermal fluctuation noise (phonon noise), scales as $T^{-5/2}$.

Table 1: Theoretical D^* , limited by phonon noise

Temperature	limiting D^*
300K	1.8×10^{10}
90K	3.6×10^{11}
40K	2.7×10^{12}

This limit in general is not reached when looking at a target much hotter than the detector (due to photon noise) or for frequencies much higher than $\omega\tau = 1$ (τ is the time constant, C/G), since then the Johnson or electronics noise will begin to dominate the phonon noise. Low enough frequencies are also hobbled by $1/f$

¹ Contact information for J.C. Brasunas- Email: john.c.brasunas@nasa.gov

SESSION 3- High Temperature Superconducting (HTS) Bolometers

noise. Thus at best the limiting D^* can only be reached for a fairly small range of frequencies, falling away at lower and higher frequencies.

RESOURCE LIMITATIONS FOR PLANETARY MISSIONS

Planetary missions, particularly those to the outer planets (the gas giants, Jupiter and beyond) are in general highly resources constrained. It is difficult to send heavy instruments to the outer planets, or to provide large amounts of electrical power. Thus cooling options are generally limited to passive coolers or single-stage mechanical coolers, with a lower limit around 60K. This poses a problem for FIR observations. In general (with one exception to be noted below) it does not appear feasible to launch 4K detectors to the outer planets. As has been noted above, this then restricts science instruments to the relatively insensitive, 300K thermal detectors. Moderately cooled FIR detectors with intermediate D^* could greatly benefit outer planet missions.

The relative ease of moderate cooling can be appreciated by referring to the following table of planetary temperatures.

Table 2: *Range of Planetary Temperatures¹*

Planet	T _{surface}	T _{sphere}
Mercury	100-700K	445K
Venus	740	325
Earth	288-293	277
Mars	140-300	225
Jupiter	165	123
Saturn	134	90
Uranus	76	63
Neptune	72	50
Pluto	40	44

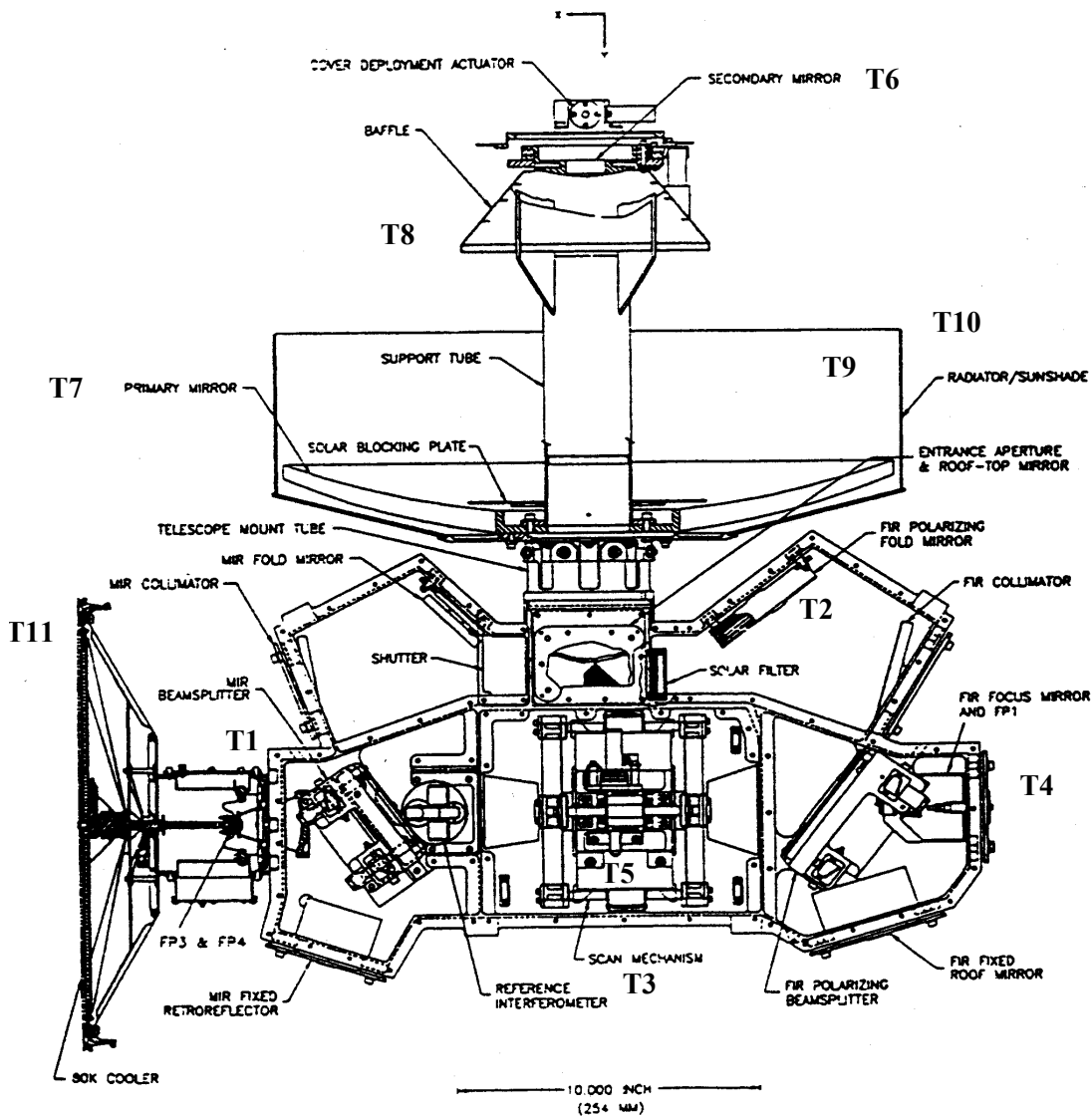
T_{sphere} is the temperature of a black sphere in equilibrium with the Sun; a flat plate facing the Sun would have a temperature higher by $\sqrt{2}$. Except for the Earth and Venus, the temperature in space is not room temperature. Rather than call a 300K detector “uncooled”, one might call a 90K detector at Saturn “unheated”. In any case, the potential sensitivity benefit of moderate cooling combined with the ease of reaching the 77K neighborhood in the outer solar system makes a strong case for developing and using moderately cooled FIR detectors on outer planet missions. On the other hand, considering the relatively high target temperatures (for instance, Jupiter at 1 bar is 165K), there is in general no need for the coldest and most sensitive detectors (sub-Kelvin).

MODERATELY-COOLED FIR DETECTOR PERFORMANCE AVAILABLE NOW AND IN THE NEAR TERM

COTS (commercial off the shelf) 300K pyroelectric detectors have D^* 's around 10^8 to $1-2 \times 10^9$. The Cassini CIRS Fourier transform spectrometer (FTS) (launched in 1997; Jupiter flyby in 2000/2001/ Saturn arrival in 2004) has a FIR channel, focal plane 1 (FP1) with a BiTe thermoelectric detector operating at 170K. The FP1 D^* is about 4×10^9 near the low frequency end of a 0.4 to 30 Hz band pass (10 to about 670 cm^{-1}). As a self-biasing device, it is nearly free of $1/f$ noise. The CIRS instrument is shown in Figure 1, and an example of a FP1 spectrum of Jupiter is shown in Figure 2 (the regularly spaced sharp features above about 400 cm^{-1} are due to electrical interference). Interestingly enough, such a spectrum has never been taken of the Earth, so that in this sense Jupiter is better characterized than Earth (the FIR spectrum). Beyond about $50 \mu\text{m}$ (lower than 200 cm^{-1}), the Earth has only been characterized by broad-band, radiometric observations.

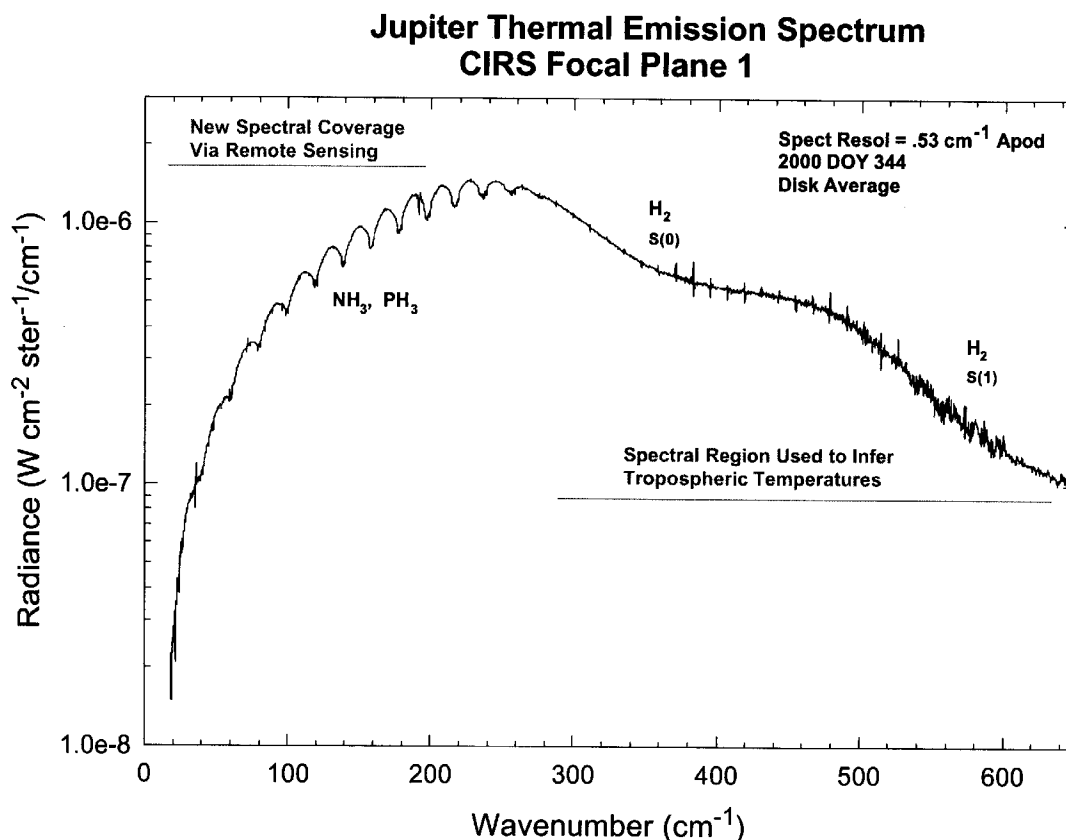
SESSION 3- High Temperature Superconducting (HTS) Bolometers

Figure 1. The Cassini CIRS FTS



SESSION 3- High Temperature Superconducting (HTS) Bolometers

Figure 2. Cassini CIRS Jupiter Spectrum in the FIR



Due to the nature of the Planck function, the radiance is rapidly falling as one approaches 10 cm^{-1} . It is remarkable that such a fairly high resolution spectrum can be recorded of a fairly cold target with such an insensitive detector, not much more sensitive than the best COTS uncooled detectors. The drawback of course is the long integration time that may be required, easily hours for weak spectral features towards the longest wavelengths. The Cassini CIRS instrument, like the Voyager IRIS FTS before it, could very much benefit from improved sensitivity IR detectors consistent with the resources constraints of an outer planet mission. In fact, NASA Goddard has produced high T_c bolometers of increasing D^* , culminating² in a D^* of 1.2×10^{10} . This has been further improved to 2×10^{10} @ 2Hz, using GdBaCuO instead of YBCO on a $5 \mu\text{m}$ thick sapphire substrate. This detector exceeds the performance of the Cassini CIRS detector over the entire FP1 frequency range, by about a factor of 5.

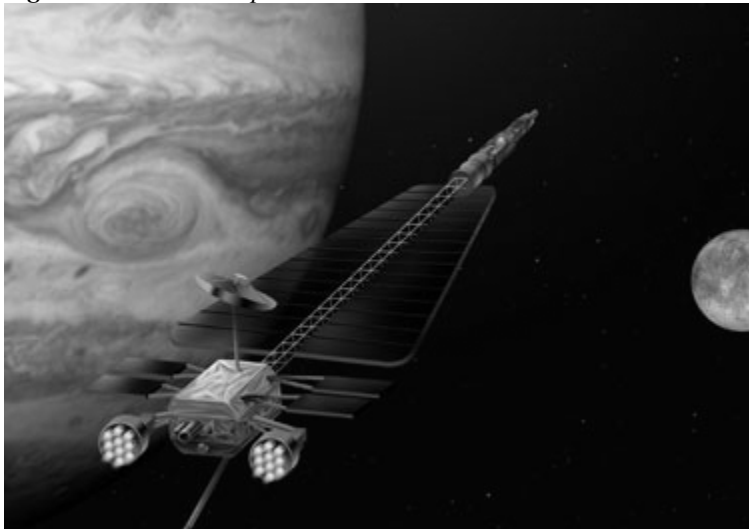
NASA Goddard has also funded numerous small companies through the SBIR program. The following companies were funded through both Phase I and Phase II: Advanced Technology Materials, Talantic, Excel Superconductor, Neocera, Conductus, and Energy Science Laboratories. There was a range of technical readiness at the completion of Phase II; in particular, Conductus came closest to having a device³, producing array-compatible pixels for IR camera applications. However a commercial market never developed for high T_c IR detectors, and industry instead moved to provide products for wireless telecommunications such as passive RF filters for cell-phone base stations. Given the lack of a commercial market and yet the clear advantage of high T_c bolometers for outer planet missions, the production of high T_c bolometers may be a logical niche market for government laboratories. Meanwhile the academic and industrial sectors continue to play a key role in the discovery and development of high T_c materials, substrates, deposition techniques, and biasing techniques.

SESSION 3- High Temperature Superconducting (HTS) Bolometers

ONE EXCEPTIONAL OPPORTUNITY FOR THE FUTURE

Till now, much has been made of the resource-starved nature of outer planet missions. There is an exception being contemplated, a once-per-decade opportunity for a quite large mission within the Prometheus program. The Prometheus program advocates sending nuclear reactors into space, producing 100 kW of electrical power and 600 kW of waste heat; by way of comparison, less than 1 kW of electrical power is available from the Cassini radioisotope thermoelectric generators. In the proposed first mission, JIMO (Jupiter Icy Moons Orbiter), the copious electrical power is used to power an ion drive for transit to Jupiter.

Figure 3: *JIMO concept*



Prometheus encourages high power, high data rate instruments, with perhaps 500 kg for the total of the science instruments. Under these conditions a 200-300 W, ~45 kg multi-stage cooler can be flown, capable of reaching ~4K, instead of a 4 or 5 kg, single-stage mechanical cooler capable of reaching ~65K. This opens up the utilization of FIR detectors much more sensitive than the high T_c detectors. Still, for every such Prometheus mission there will be 10-20 regular missions with the usual constraint to moderate cooling.

REFERENCES

1. *The Planetary Scientist's Companion*, K. Lodders and B. Fegley, Oxford, 1998.
2. *High T_c superconducting bolometer on chemically-etched 7 μm thick sapphire*, B. Lakew, J.C. Brasunas, A. Pique, R. Fetting, B. Mott, S. Babu and G.M. Cushman, *Physica C* **329** (2000), 69-74.
3. *Low noise high-temperature superconducting bolometers for infrared imaging*, S.J. Berkowitz, A.S. Hirahara, K. Char and E.N. Grossman, *Appl. Phys. Lett.* **69**(14) (1996), 2125-2127.

Contact information for J.C. Brasunas: Email: john.c.brasunas@nasa.gov

Fabrication of Monolithic Sapphire Membranes for High T_c Bolometer Array Development

D.E. Pugel¹, B. Lakew², S. Aslam¹, L. Wang³

¹ Raytheon Corporation, Lanham, MD 20706

² NASA Goddard Space Flight Center, Greenbelt, MD 20771

³ Swales Aerospace, Beltsville, MD 20705

ABSTRACT

This paper examines the effectiveness of Pt/Cr thin film masks for the architecture of monolithic membrane structures in r -plane single crystal sapphire. The development of a pinhole-free Pt/Cr composite mask that is resistant to boiling $H_2SO_4:H_3PO_4$ etchant will lead to the fabrication of smooth sapphire membranes whose surfaces are well-suited for the growth of low-noise high T_c films. In particular, the relationship of thermal annealing conditions on the Pt/Cr composite mask system to (i) changes in the surface morphology (ii) elemental concentration of the Pt/Cr thin film layers and (iii) etch pit formation on the sapphire surface will be presented.

INTRODUCTION

The primary motivation for this work is to develop a highly sensitive micro-machined transition-edge bolometer array on sapphire membranes for thermal imaging applications in the spectral wavelength range 20-100 μ m. Sapphire has several advantages over silicon as a substrate material for the development of high T_c bolometers, in particular, better high T_c film epitaxy resulting in sharper transitions, lower specific heat capacity and higher thermal conductivity at the temperature of operation. However, unlike silicon, sapphire is extremely hard to thin because of its chemical inertness. It would be extremely useful to develop a technique for micromachining sapphire that can be used in conjunction with existing standard photolithographic techniques, for architecturing small area bolometer arrays where each bolometer has an optimized thermal time constant, $\tau = C/G$ where C is the total heat capacity and G is the thermal conductance to a heat sink at temperature T_s . Smaller bolometer areas will result in smaller thermal time constants giving rise to higher temperature excursions in the bolometer film.

Recently, Lakew *et al.*¹ reported on a composite 1mm² single pixel YBCO bolometer fabricated by thinning a sapphire substrate from 25 μ m to 7 μ m in thickness suspended with Kevlar fibers for thermal isolation. This device gave a thermal time constant of 100 ms and a detectivity of 1.2×10^{-10} cm Hz^{1/2}/W at 4 Hz. In order to alleviate the need for epoxied Kevlar fibers and eliminate unknowns in contributions to the total heat capacity, it would be advantageous to fabricate monolithic thin membrane structures in thick sapphire frames. This approach will not only result in further bolometer performance improvements (higher sensitivity and faster response time) but will also lead to the long term goal of producing linear arrays while maintaining ease of handling, hybridization and packaging. A notable challenge in the production of bolometers with such an architecture is the design and construction of a pinhole-free mask capable of withstanding boiling $H_2SO_4:H_3PO_4$ used for bulk sapphire etching^{2,3}. Such harsh etch conditions place strict requirements on the materials and methods utilized in the fabrication of an etch mask. An attractive strategy is to use a corrosion-resistant metal such as Pt with a thin, underlying adhesion-promoting layer such as Cr. Subsequent annealing of the Pt/Cr layers should further promote the adhesive

¹ Contact information for D.E. Pugel – Email: bpugel@pop500.gsfc.nasa.gov

SESSION 3- High Temperature Superconducting (HTS) Bolometers

integrity of the Pt/Cr thin film mask through the formation of a Pt-Cr solid solution^{4,5}. This work investigates the effects of thermal annealing on the morphology and structural integrity of Pt/Cr thin film masks. Scanning electron microscopy (SEM), electron dispersive x-ray spectroscopy (EDS) and optical microscopy were used to probe for changes in surface morphology and elemental concentration under different annealing conditions. Implications of the effectiveness of such masks for use in bulk sapphire etching are discussed.

EXPERIMENTAL PROCEDURE

Substrates used in this study were 2" (1-102) sapphire wafers obtained from Kyocera Corporation. Prior to metal film deposition, samples were cleaned and degreased in successive ultrasonic baths of semiconductor grade acetone, methanol and deionized water. Substrates were blown dry with N₂ gas and baked at 120°C for approximately 2 hours.

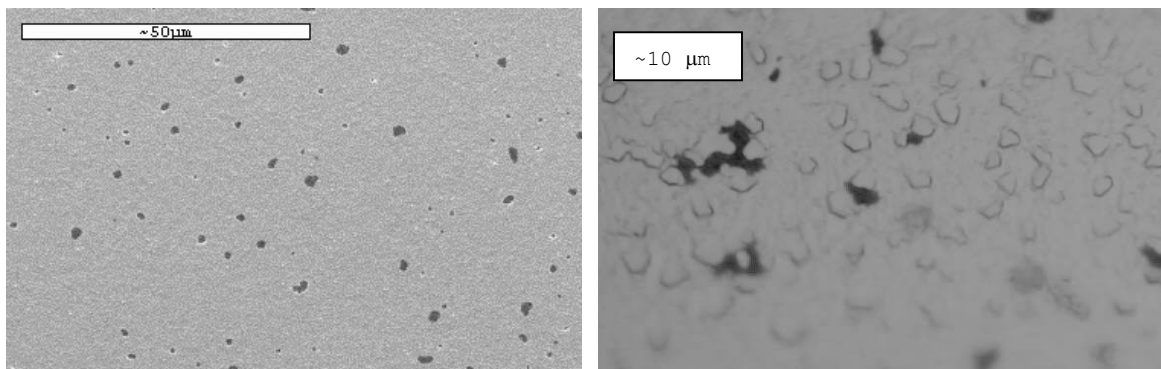
Pt/Cr layers were deposited using on-axis dc magnetron sputtering from 2" high-purity metal targets mounted in a high-vacuum system. The deposition system was initially evacuated to a base pressure of $\sim 2 \times 10^{-6}$ Torr. Deposition occurred near room temperature in an Ar atmosphere. 50 nm of dc magnetron-sputtered Cr was deposited, followed by a cooling period and subsequent deposition of 250 nm of Pt. Thicknesses were measured using a standard Dektak profilometer.

Prior to annealing, samples were examined using optical microscopy, SEM, EDS and atomic force microscopy (AFM). Film surfaces had mirror finishes and were featureless. No defects were found on the surface. The films were shown to be elementally pure and the thicknesses agreed with profilometry results. AFM measurements of the rms roughness of the unannealed Pt/Cr layer = 2.52 nm. The blank substrate had an rms roughness = 0.42 nm.

Samples were annealed *ex situ* in an oxygen atmosphere (flow rate = 10 sccm, scaled to N₂) at atmospheric pressure. Annealing temperatures were selected between 500 - 1000°C. Annealing times were 5, 30 or 60 minutes. Test samples were inserted into an annealing oven pre-heated to 500°C. The furnace temperature setting was increased and the samples were advanced on a quartz sled at until the center was reached. The insertion occurred as the temperature of the furnace was increasing towards the desired setting. Once the sample reached the oven center and the furnace setting stabilized, timing began. The samples cooled to room temperature in an oxygen atmosphere.

RESULTS

Two main types of surface structures were found: blisters and holes (*Figure 1*). SEM and optical microscopy showed that the density and continuity of these structures is dependent upon annealing conditions. Most specifically, the duration of annealing influenced the density of the surface structures, particularly the number of holes. There was no apparent influence of the annealing conditions on the size of either the blisters or holes that were found on the annealed surfaces.



SESSION 3- High Temperature Superconducting (HTS) Bolometers

Figure 1: Scanning electron micrographs of Pt/Cr surface after annealing at 1000°C, 60 minutes for (a) 100 x 100 μm^2 square region & (b) 50 x 50 μm^2 region. Note the blisters (outlined regions) and holes (solid regions).

Samples annealed at 1000 °C exhibited an extensive amount of blistering and holes (Figure 1). The holes found on these samples were likely created by some of the blisters being popped open and exposing the underlying substrate. The holes that appeared on the sample surface had no apparent size limit and a broad range of diameters, indicating that there was no exact critical radius for the blisters to burst open. EDS examination of the regions on the sapphire substrate, beneath the burst blisters showed an insignificant concentration of Cr.

Samples annealed at lower temperatures and/or shorter time (for example, 500 °C for 30 minutes) exhibited a very limited amount of blistering (Figure 2). EDS detected a small amount of Cr beneath burst blisters found on these samples.

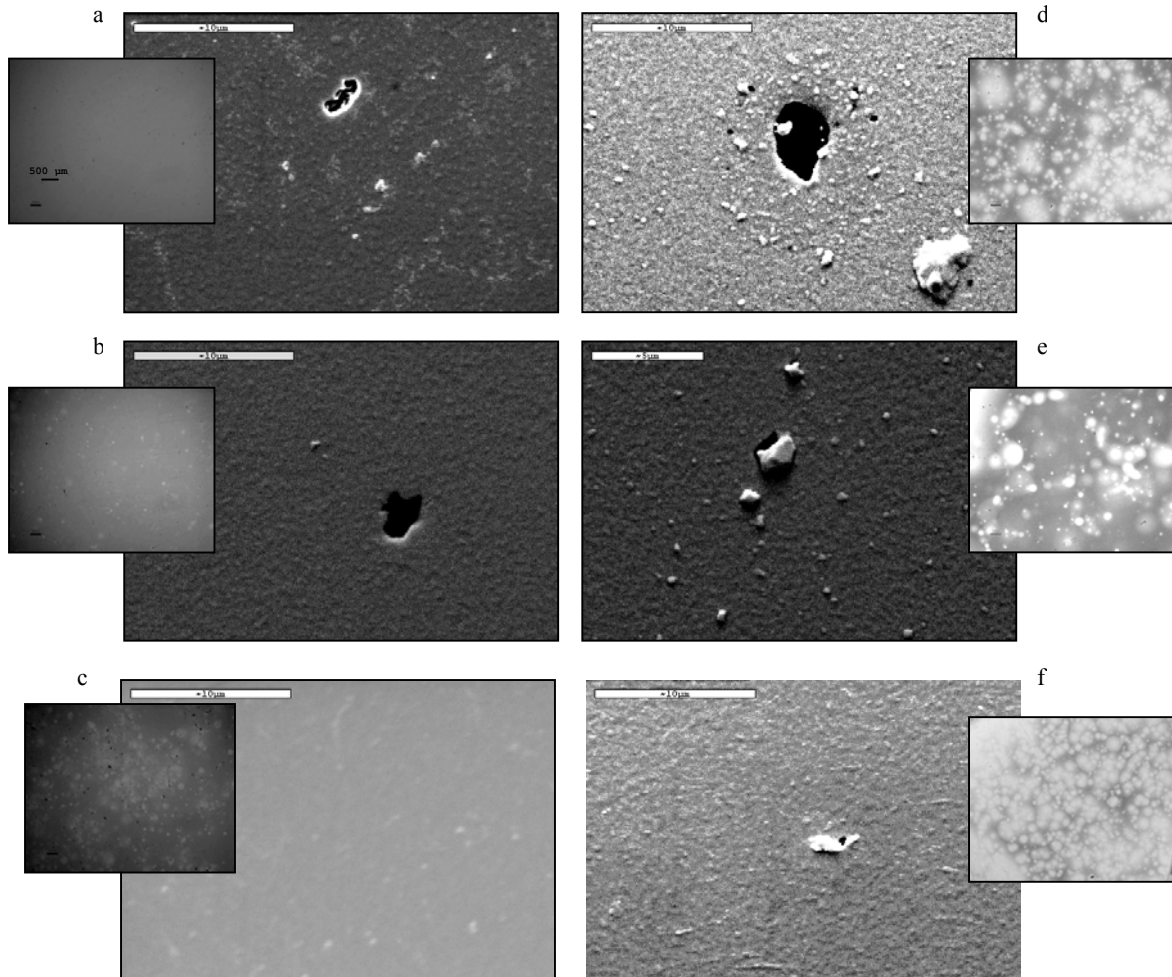


Figure 2 Scanning electron micrographs of Pt/Cr surfaces, illustrating the temperature and time dependence matrix utilized in this study. Each small inset is an optical micrograph taken for the same annealing condition (scale bar= 400 μm). Left-side column: samples annealed at 500°C for (a) 5 min, (b) 30 min, (c) 60 min. Right-side column: (d) & (e) samples annealed at 1000°C for 5 min and 30 min, respectively; (f) Unannealed sample. Compare with 1000°C, 60 min micrograph shown in Figure 1(a).

SESSION 3- High Temperature Superconducting (HTS) Bolometers

Away from the blistered regions, EDS showed an increase in surface concentration of Cr with increasing annealing temperature (*Figure 3*). Some of the chromium (Cr) appeared to have diffused into the platinum (Pt) layer during the annealing and accumulated on the sample surface.

Optical microscope inspection showed increased surface discoloration of the samples with increasing annealing temperature or time (*Figure 2, insets*). This is likely due to oxidation of the Cr that has diffused onto the surface, as supported by EDS surface data (*Figure 3*).

DISCUSSION

All samples annealed at 1000°C for 5, 30 and 60 minutes and annealed at 500°C for 60 minutes were blistered. Burst or intact, such features produce a mask which directly permits the entry of corrosives. An intact blister strains the overlying film and may possess fractures at the blister's base. Such fractures may permit corrosive entry. Burst blisters and holes produced by other means provide a direct path of entry for corrosives. Thus, a blistered mask is ineffective for the production of a pit-free sapphire surface.

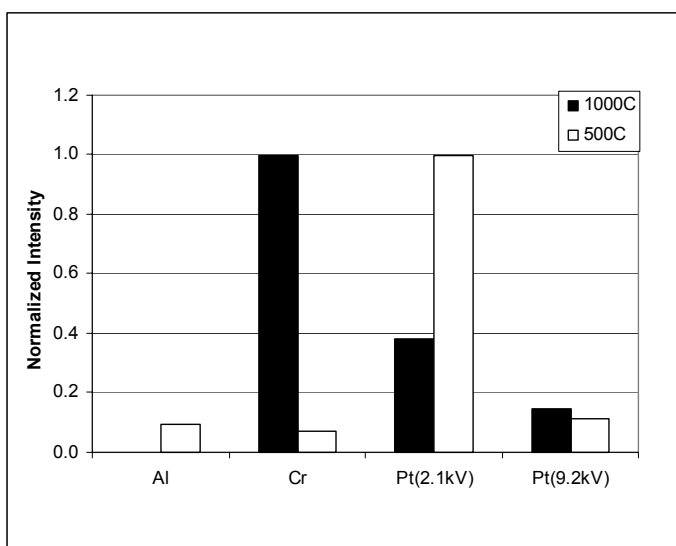


Figure 3: Comparison of elemental EDS lines for 1000°C and 500°C anneals. Duration of anneal = 60 min. The beam was directed away from blistered regions and holes. Data has been normalized with respect to the full scale counts per second setting for a given measurement.

Annealing as-deposited films composed of a Pt-Cr solid solution results in preferential Cr segregation and oxidation at the films surface. Since Cr is readily attacked by corrosives commonly used in the sapphire etch process, a mask with excessive Cr surface concentration may lose its continuity under standard sapphire etch conditions.

We have determined that surface morphology and composition of the Pt/Cr etch mask significantly influence a mask's effectiveness in sapphire wet etch process. Controlling processing conditions of this etch mask controls the degree to which a mask may be vulnerable or even have its integrity compromised during the etch process. High temperature anneals or anneals above 500°C for times greater than 30 minutes produce a mask that is not pinhole-free, leaving the underlying sapphire vulnerable to pitting by the etchant.

REFERENCES

1. B. Lakew, J.C. Brasunas, A. Piqué, R. Fettig, B. Mott, S. Babu, G.M. Cushman, *Physica C* **329**, 69 (2000).
2. R.G. Vardiman, *J. Electrochem. Soc.* **118**, 1804 (1971).
3. A. Reisman, M. Berkenbilt, J. Cuomo, and S.A. Chan, *J. Electrochem. Soc.* **118**, 1653 (1971).
4. J.E.E. Baglin and F. M.d'Heurle, *J. Electrochem. Soc.* **126**, 277 (1979).
5. A. Reisman, M. Berkenbilt, J. Cuomo, S.A. Chan, *J. Electrochem. Soc.* **126**, 1004 (1979).

PEROVSKITE MANGANITES: A NEW FAMILY OF MATERIALS FOR UNCOOLED/ MODERATELY COOLED IR DETECTOR APPLICATIONS

M. Rajeswari¹, V. Smolyaninova and M. Overby
Department of Physics, Astronomy and Geosciences,
Towson University,
Towson, MD 21252, USA

ABSTRACT

Alkaline earth doped perovskite manganites have been a focus of research during the past several years on account of the phenomenon of colossal magneto-resistance (CMR) and its application in magnetic information storage technology. Somewhat less known is the potential of these materials for use as bolometric infrared detectors. The bolometric sensor functionality is based on the steep temperature dependence of resistance in the vicinity of the insulator-metal transition. The insulator-metal transition temperature can be tuned by manipulating the chemistry, which makes it feasible to tailor these materials for sensor operation over a wide temperature range anywhere from well over room temperature down to liquid nitrogen and lower temperatures. Figure of merit calculations based on the best currently demonstrated values of the temperature-coefficient of resistance and 1/f noise indicate good potential for development of state-of-the-art IR detectors based on manganites.

INTRODUCTION

Perovskite rare earth manganites, also popularly known as “colossal magnetoresistive (CMR) oxides, have recently been a focus of materials research^{1,2}. From the applications perspective, interest in these materials arose initially from their unusually large magnetoresistance. However, recently it has been realized that CMR manganites have promising potential for bolometric infrared detection in a wide range of temperatures from room temperature down to liquid nitrogen temperatures^{3,4}. The operating temperatures can be tuned over a wide range by simple variations in chemistry.

The bolometric application of CMR manganites is based on the steep drop in resistivity with temperature accompanying an insulator-metal transition. The CMR Manganites are derived from rare earth manganese oxides such as (La, Nd or Pr) MnO₃ which are antiferromagnetic insulators. The insulator-metal transition is brought about by the partial substitution of the trivalent rare earth site by divalent alkaline earth elements, thereby driving manganese ions into a mixture of two valence states, Mn (3+) and Mn (4+). The electron transport between these two types of Mn ions is coupled to the alignment of the core Mn spins via Hund's coupling. To put it very simply, based on the concentration of Mn (4+) ions (determined by the amount of alkaline earth substitution) along with several structural factors (partly related to the average ionic radius of the rare earth site), ferromagnetic ordering accompanied by metallic electron transport becomes energetically favorable over the antiferromagnetic insulating state below a certain temperature. This results in the insulator-metal (I-M) transition which is the phenomenon relevant to the bolometric application. The temperature at which slope of the resistance vs temperature is steepest (i.e. the optimal operating point of the bolometer) occurs typically about 10 –15 K below the I-M transition. Fig.1 shows the insulator-metal transition and the associated bolometric optical response of a

¹ Contact information for M.R. Rajeswari - Email: mrjewari@towson.edu

SESSION 3- High Temperature Superconducting (HTS) Bolometers

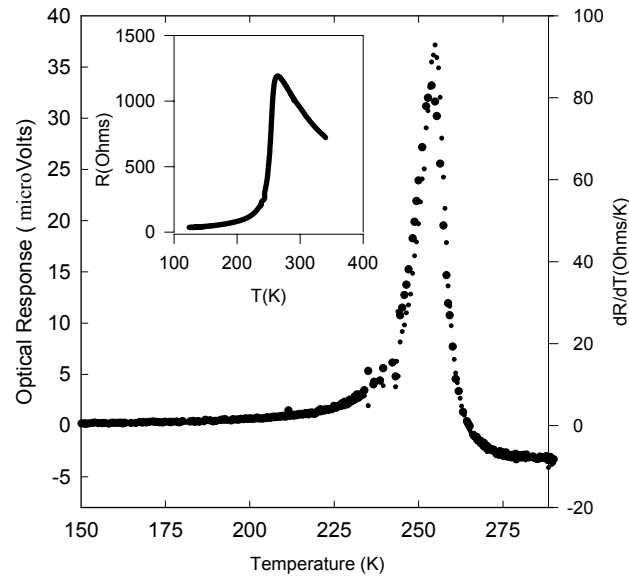


Fig.1 : Bolometric optical response and dR/dT of a $\text{La}_{0.67}\text{Ca}_{0.33}\text{MnO}_3$ thin film. Inset shows the insulator-metal transition (Ref. 3) .

of a manganite thin film ³ .The I-M transition temperature in turn depends on the choice of the rare earth and alkaline earth elements and the amount of alkaline earth substitution. The material composition can therefore be tailored for the desired operating point of the bolometer depending on the application. The range of such tunability is quite broad, spanning a temperatures range from several tens of degrees above room temperature down to liquid nitrogen temperatures, including uncooled operation at room temperature.

Table-1: A partial list of manganite materials for uncooled/moderately cooled bolometer application.

Materials Composition	Peak Temperature (K)	TCR (%/K)	Peak Resistivity ($\text{m}\Omega\text{-cm}$)
$\text{La}_{0.7}\text{Ba}_{0.3}\text{MnO}_3$	330	4	17.5
$\text{La}_{0.7}\text{Sr}_{0.3}\text{MnO}_3$	380	2.5	0.5
Ag-doped $\text{La}_{0.7}\text{Ca}_{0.3}\text{MnO}_3$	285	18	8.0
$\text{Nd}_{0.7}\text{Sr}_{0.3}\text{MnO}_3$	235	32	40.0
$\text{Pr}_{0.7}\text{Sr}_{0.3}\text{MnO}_3$	320	11	8.0
$\text{La}_{0.9}\text{Sr}_{0.1}\text{MnO}_3$	277	5	14.0
$\text{La}_{0.37}\text{Pr}_{0.30}\text{Ca}_{0.33}\text{MnO}_3$	230	58	200
$\text{La}_{0.8}\text{Ca}_{0.2}\text{MnO}_3$	298	8	12.0
$\text{Nd}_{0.6}\text{Sr}_{0.4}\text{MnO}_3$	215	7	60.5

RELEVANT MATERIAL PROPERTIES

Several CMR material compositions have been investigated and shown to be potential candidates for bolometric application. The data presented here are on epitaxial thin films grown by the Pulsed Laser Deposition (PLD) technique which has been established as the technique of choice for the growth of the best quality manganite films. The following is a summary of the current status of materials properties that are relevant to the IR detector application.

Temperature Coefficient of Resistance (TCR)

One of the key figures of merit for the bolometric application is the temperature-coefficient of resistance (TCR, defined as $1/R \, dR/dT$). Several CMR materials have been shown to have insulator-metal transitions and remarkably high values of TCR in the temperature range 200 K – 300 K (see table-1). TCR values as high as 8 % at room temperature which is significantly higher compared to $< 3\%/K$ of Vanadium Oxide and 3-4%/K for semiconducting YBCO. CMR manganites hold even better promise for applications that are compatible with lower temperatures of operation. TCR as high as 18%/K has been demonstrated at 270 K and 58%/K at 200 K. The manganite family also offers the potential for development of detectors for operation at lower temperatures below 100 K by tuning the chemistry to achieve lower insulator-metal transition temperatures . Comparison of different manganite materials indicates that TCR increases as the insulator-metal transition temperature shifts to lower temperatures⁵. Highest values of TCR are observed in materials which show percolative insulator-metal transitions accompanying phase separation (e.g. $\text{La}_{0.37}\text{Pr}_{0.33}\text{Ca}_{0.33}\text{MnO}_3$ in table-1). However, percolative transitions are characterized by thermal hysteresis and larger noise values which are not desirable for bolometric applications. (Note that except for $\text{La}_{0.37}\text{Pr}_{0.33}\text{Ca}_{0.33}\text{MnO}_3$, none of other materials listed in table-1 show thermal hysteresis, which is another advantage over vanadium oxide which exhibits hysteresis at room temperature).

Electrical Noise

Another key materials property of interest from the perspective of bolometric applications is the electrical noise, which includes Johnson noise, and $1/f$ resistance noise. Since the resistivity of these materials is rather low , Johnson noise is not expected to be a concern. A major concern in the initial phase of our research was the anomalously large magnitudes of $1/f$ noise, which these materials were shown to exhibit^{5,6}. However, continued efforts at improving the materials quality have resulted in significant reduction of $1/f$ -noise magnitudes by several orders of magnitudes⁷. Fig.2 shows the normalized noise power spectral density κ evaluated according to the Hooge model as

$$\kappa = S_v f^{1/2} v / V_{dc}^2$$

where S_v is the noise power spectral density, f is the frequency, v is the sample volume and V_{dc} is the dc voltage.

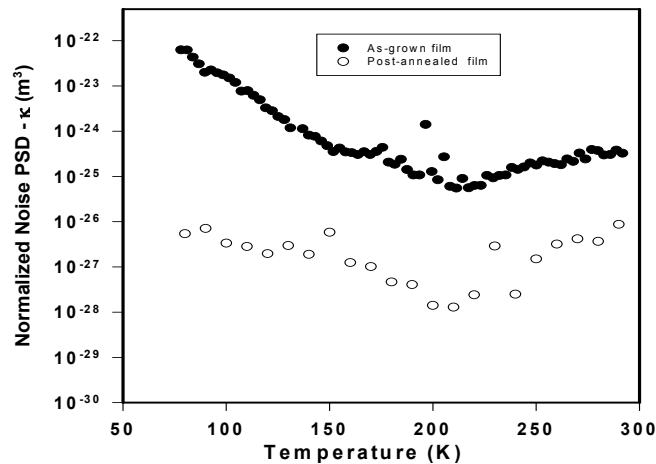


Fig.2 : Normalized noise power spectral density of an as-grown and post-annealed $\text{La}_{0.67}\text{Ca}_{0.33}\text{MnO}_3$ film as a function of temperature (Ref.7).

SESSION 3- High Temperature Superconducting (HTS) Bolometers

Oxygen stoichiometry has been identified to be a key parameter that influences the noise magnitudes and novel materials modification schemes to promote enhanced oxygenation have been developed. One such scheme involves the addition of a small amount of Ag⁸ (5-10 weight %) which has been shown to increase the I-M transition temperature via enhanced oxidation. Recently it has been demonstrated that noise values at room temperature are only marginally higher than that of Vanadium Oxide⁹. Thus 1/f noise is no longer considered to be an insurmountable hurdle for the bolometric application of manganite thin films.

Growth of epitaxial manganite thin films on Si

In addition to possessing the materials properties relevant to the figures of merit for the bolometric application, it is also necessary that the candidate material be compatible with growth of high quality thin films on substrates such as Si for the fabrication and demonstration of actual bolometric detectors. Si is a preferred substrate for thermal IR detectors on account of its thermal properties (low heat capacity and high thermal conductivity), micro-machinability (facilitating detector fabrication on micro-machined membranes in air-bridge structure, thus reducing the device thermal mass and providing enhance thermal isolation) as well as the potential for integration of the detector with measurement or read-out electronics on a single chip. However, Si is chemically reactive with the manganites at high temperatures and also has the disadvantage of large thermal expansion coefficient mismatch (as in the case of YBCO). This calls for lattice-engineering schemes employing buffer and template layer growth for the integration of CMR Manganite films with Si. Ytria stabilized Zirconia (YSZ) is used as the buffer layer to avoid the chemical reaction with the Si substrate. YSZ however has a large lattice mismatch with the manganites which necessitates the growth of a lattice-matched template layer over the YSZ layer to ensure good crystallinity of the manganite film. Bi₃Ti₄O₁₂ (BTO) has been shown to be an effective template layer facilitating the growth of high quality manganite films on Si^{10,11}.

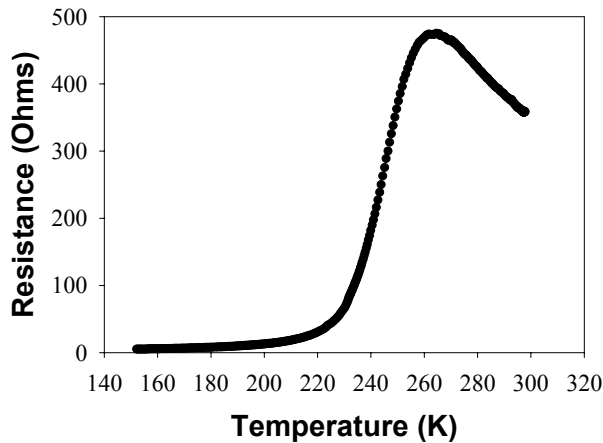


Fig.3 : Metal-insulator transition in a $Pr_{0.67}Sr_{0.33}MnO_3$ thin film grown on Si.

TCR and noise values of manganite thin films grown on Si employing the above mentioned schemes are comparable to the best-demonstrated values on other substrates. A typical result showing the resistivity and TCR of $La_{0.7}Pb_{0.3}MnO_3$ thin film on Si is shown in Fig.3.

Figure of merit calculations

We have calculated the achievable figure of merits for manganite bolometers based on the best demonstrated values of TCR and noise in epitaxial thin films. Table 2 shows the results of our calculations of the noise equivalent power (NEP) and detectivity D^* . The calculations are for a device patterned into a meander line on 1 μ m micro-machined Si membrane with state-of-the-art thermal isolation of the transducer element. We assume device area = 1 mm², bias Current = 1 μ A, operating Frequency = 30 Hz, thermal conductance $G = 6 \times 10^{-8}$ W/K and heat capacity $C = 7 \times 10^{-10}$ J/K. Note that the only noise sources

SESSION 3- High Temperature Superconducting (HTS) Bolometers

considered are Johnson noise and 1/f noise of the sensor material. We have not take into account noise sources from the electronics in these estimates which therefore do not represent practically achievable values. In other words, the figures-of-merit in table-2 serve mainly to indicate the limitations based on material properties alone. The projected NEP and D* values of the manganite detectors compare well with those of the state-of-the-art bolometric detectors operating close to room temperature.

Table-2: Figure of merit calculations based on best TCR and noise values currently demonstrated

Operating Temperature	Material	TCR or β (dlnR/dT)	Device Resistance (Ohms)	Responsivity (V/W)	NEP W/ $\sqrt{\text{Hz}}$	Effective Detectivity D*(cm $\sqrt{\text{Hz/W}}$)
295 K	Pb-doped LaCaMnO ₃	.07	60,000	3.2×10^3	9.9×10^{-12}	2.6×10^9
270 K	Ag-doped LaCaMnO ₃	0.18	60,000	8.2×10^3	3.7×10^{-12}	7×10^9
220 K	NdSrMnO ₃	0.4	300,000	9.1×10^4	6.8×10^{-13}	3.8×10^{10}
240 K	LaCaMnO ₃	0.22	60,000	1×10^4	2.9×10^{-12}	8.9×10^9

SUMMARY

The results presented above clearly show that the family of CMR manganites offer several candidate materials for the development of bolometric IR detectors in the temperature range from room temperature to below 200 K. The temperature range can be extended to lower temperatures below a 100K by tuning the chemical composition. The temperature coefficient of resistance close to room temperature is superior to that of materials like vanadium oxide and semiconducting YBCO which are currently being actively pursued for uncooled IR detector applications. High quality manganite films have been demonstrated on Si employing buffer and template layer growth schemes. The figure of merit calculations based on the best values of TCR and 1/f noise currently achieved indicate the potential for achieving manganite based detectors with state-of-the-art performance. Manganites are stable and robust materials. An added advantage offered by the manganites is the feasibility of developing a generic materials technology for IR detectors for a wide operating temperature range thus catering to a wide spectrum of users.

Acknowledgements: This work is presently supported by the NSF MRI grant (Grant # DMR 0116619) and faculty development research grant (Summer 2003) at Towson University. MR acknowledges past support from the DARPA/Rockwell Grant (1998-2000) and NSF MRSEC (DMR 96-32521) at the University of Maryland, College Park and collaborations with T. Venkatesan R. L. Greene, A. Goyal, M. Downes and D.J. Kang at the Center for Superconductivity Research, University of Maryland, College Park.

SESSION 3- High Temperature Superconducting (HTS) Bolometers

REFERENCES

1. S. Jin et al, Science 264 413 (1994).
2. T. Venkatesan et al, Phil. Trans. Roy. Soc. London A356 p1661 (1998).
3. M. Rajeswari et al, Appl. Phys. Lett. 68 3555 (1996).
4. A. Goyal et al, Appl. Phys. Lett. 71 2535 (1997).
5. M. Rajeswari et al, Appl. Phys. Lett. 69 851(1996).
6. G.B. Alers et al Appl. Phys. Lett. 68 3644 (1996).
7. M. Rajeswari et al, Appl. Phys. Lett. 73 2672(1998).
8. R. Shreekala et al, Appl. Phys. Lett. 74 2857(1999).
9. I. Gergis, Rockwell Science Center (Private Communication).
10. Z .Trajanovic et al, Appl. Phys. Lett. 69 1005(1996).
11. M. Rajeswari et al (to be published)

BOLOMETER SIMULATION USING SPICE

Hollis H. Jones¹

NASA Goddard Space Flight Center, Greenbelt, MD 20771, USA

Shahid Aslam

RITSS, 4400 Forbes Blvd, Lanham, MD 20706, USA

Brook Lakew

NASA Goddard Space Flight Center, Greenbelt, MD 20771, USA

ABSTRACT

A general model is presented that assimilates the thermal and electrical properties of the bolometer—this block model demonstrates the Electro-Thermal Feedback (ETF) effect on the bolometers performance. This methodology is used to construct a SPICE model that by way of analogy combines the thermal and electrical phenomena into one simulation session. The resulting circuit diagram is presented and discussed.

BOLOMETER SIMULATION

General steady-state bolometer model

A general model describing the bolometer operation is presented here. The model can be utilized for normal state and transition edge (TE) types of operation and is not exclusively driven by any particular mathematical expression for the bolometer resistance $R(\Delta T)$, where ΔT is the temperature difference between the bolometer mass and the heatsink. Moreover, the model expounds easy-to-visualize mechanisms and yields simple mathematical statements. The static-state model as shown in Figure 1 is constructed in the usual system form—that is, with the plant, feedback, and summation blocks.

The following briefly describes the process of Figure 1. The input is the optical power Φ into which the electrical or self-heating power P_e is summed. This summation is divided by the thermal conductance G making it the temperature argument for $R(\Delta T)$. The result is then multiplied by the bias current I to produce the output of the plant—in this case, the readout voltage V . The output voltage is in turn multiplied by feedback block I to form P_e , thus demonstrating regenerative feedback. Under proper conditions, an equilibrium point is reached—otherwise, one obtains thermal runaway. In other terms, this model demonstrates the Electro-Thermal Feedback (ETF) effect explicitly.

The configuration of Figure 1 provides two additional features: 1) If no optical power is present, i.e., $\Phi=0$, P_e can bypass the summation block and V gives the equilibrium voltage offset V_e ; and 2) the model depicts a constant current configuration, by substituting V for I (and vice-versa) and reciprocating $R(\Delta T)$, a model is derived that responds to a constant voltage bias operation. With this setup, the load that reads the current, such as a SQUID, must be included.

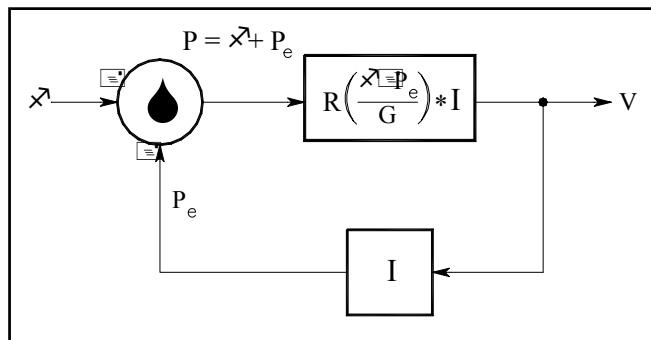


Figure 1. General static-state bolometer model

¹ Contact information for H. H. Jones: Email: holjones@pop500.gsfc.nasa.gov, phone 301-286-5755

SESSION 3- High Temperature Superconducting (HTS) Bolometers

To demonstrate the utility of the model, using a normal state expression, $R(\Delta T) = m \cdot \Delta T + R_a$, where m is the slope or the invariant $\alpha_0 R_0$ and R_a is the intercept or resistance at $\Delta T = 0$, one can easily extract a simple output expression from the model such that ΔT is eliminated. The output, assuming constant current, can be shown as, $V = V_\phi + V_e$, where,

$$V_\phi = \frac{\phi}{G} \cdot m \cdot \frac{I_b}{(1-a)}, \quad V_e = R_a \cdot \frac{I_b}{(1-a)} \quad \text{and} \quad a = \frac{m \cdot I_b^2}{G} \quad (1)$$

In Eq. (1), V_ϕ is that part of the output voltage due to the applied optical signal—the responsivity—and V_e is that part due to the offset voltage at ETF equilibrium.

PSPICE model

The Simulation Program with Integrated Circuit Emphasis (SPICE) program has the ability to simulate both thermal and electrical properties—these authors use PSPICE. By way of analogy, current and voltage represent heat flow Q and temperature differences ΔT respectively. Other authors have revealed this technique. For example, Yvon and Sushkov¹ and Shie, *et. al.*², used SPICE models to emulate normal state bolometer circuits.

The model realized here relies on an otherwise unknown $R(\Delta T)$ as shown in Figure 1, but note that PSPICE does not allow passive devices to be varied during a simulation session. They can be changed via a *.step* command for each session run, but this is a very tedious activity. However, as Figure 2 shows, any resistor can be modeled as a Voltage Controlled Voltage Source (VCVS) or a Voltage Controlled Current Source (VCCS) for a constant current or a constant voltage bias-mode operation, respectively. Using the VALUE option in the statement allows one to use a mathematical expression that can contain voltage nodes or currents through other devices.

Focusing only on the VCVS, by analogy, $R(VT1 - VT2)$ is a $R(\Delta T)$ equation where $VT1$ and $VT2$ represent the temperatures developed at the bolometer mass and the heatsink, respectively. Note that in Figure 2, the statement $R(VT1 - VT2)$ is not a valid PSPICE construct, it represents the function that will describe the actual $R(\Delta T)$. This function is multiplied by the current flowing through the source rendering a voltage drop across the VCVS device.

Figure 3 gives a simple PSPICE circuit for a constant current-mode normal state bolometer circuit in which the VCVS from Figure 2 has been inserted. On the left side is the thermal loop with its device analogues

whereas on the right side is the electrical loop with its components. Examining Figure 3 left-to-right, the independent current source **Iphi** symbolizes the optical signal power—the current represents this power. In parallel with this, the VCCS, **Getf**, emulates the ETF effect by injecting current into the junction. This current is determined by the statement $V(10) \cdot I(Vbo)$, where $V(10)$ is the bolometer element voltage drop and $I(Vbo)$ is the current into the element. The resistor device **RG** acts as the thermal conductance G . Its value is the reciprocal of G . The voltage across **RG** emulates the

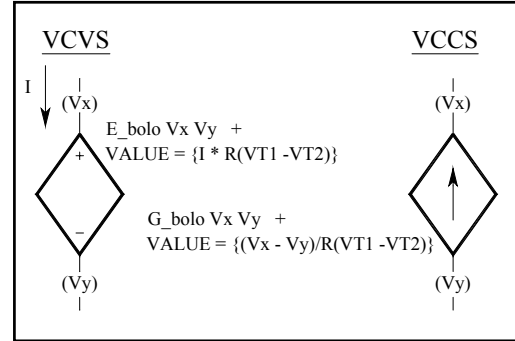


Figure 2. SPICE resistance emulation devices

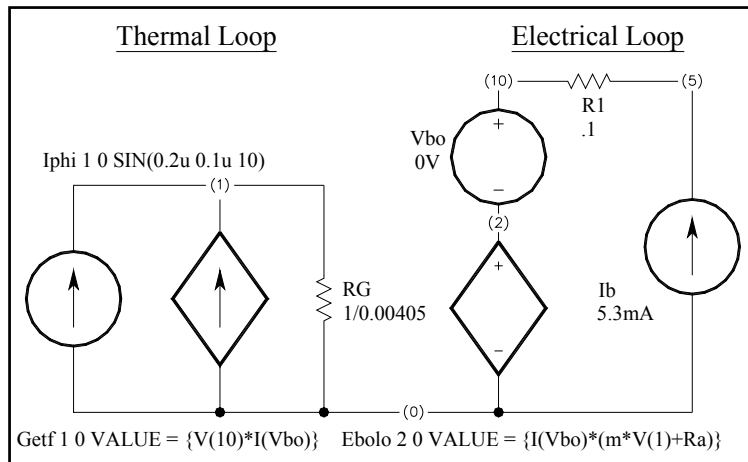


Figure 3. Static-state SPICE diagram for bolometer circuit in constant current mode

SESSION 3- High Temperature Superconducting (HTS) Bolometers

temperature difference ΔT and controls **Ebolo**. In series is **Vbo**, a 0-volt source used to measure the current through **Ebolo**. The placement of resistor **R1** not only serves as a topology resistance but also can be increased in value to yield a voltage divider scheme in the circuit. The independent current source **Ib** provides the necessary constant bias current. The output voltage is determined, for the values shown in Figure 3 or for a voltage divider scheme, by the nodes on either end of the VCVS **Ebolo**—that is, at nodes 10 and 0.

Noise voltage and current sources can be inserted for complete sensor/readout simulation, but these are not options in PSpice—that is, the package does not contain random generators. It does allow one to obtain thermal noise spectral density for every resistor and/or calculate shot and $1/f$ spectral densities for every semiconductor device. In both cases, when the `.noise` statement included in the circuit file, the results are presented only in the frequency domain. Motchenbacher and Connelly³ and Fish⁴ dedicate entire chapters to methods in which noise voltage and current source of various categories can be constructed in SPICE, such as $1/f$ noise, excess, and amplifier noise. In addition, post-processing measurement techniques for spectral densities noise bandwidths are covered.

Figure 4 depicts an example voltage noise source (shot noise) containing a $1/f$ component that can be constructed and inserted into Figure 3 as a subcircuit. The amplitude and order can be modified by adjusting the current source **In** and the parameters of the `.model` statement for the diode **Dn**. Parameter **KF** is the $1/f$ noise coefficient in amps and parameter **AF** is the $1/f$ exponent. Other subcircuits can be constructed that produce Johnson or resistor excess noise also containing $1/f$ spectral noise.

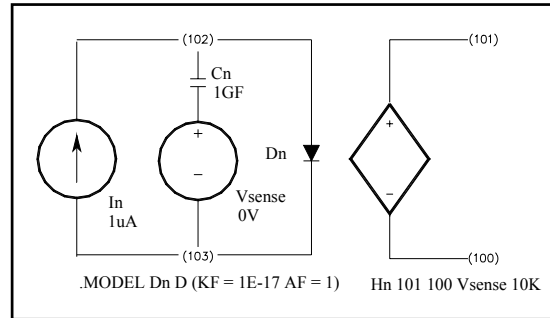


Figure 4. SPICE noise source with $1/f$ component

Simulation test

To test the simulation, Figure 3 is modified to reflect an actual measurement setup so that the effective thermal conductance as well as the actual static thermal conductance can be extracted. Figure 5 shows the

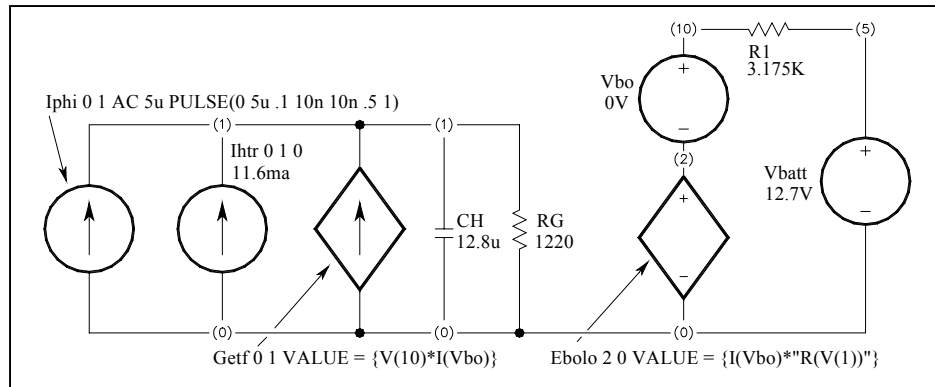


Figure 5. Simulation diagram of measurement setup

modified diagram with the constant current source replaced with a 12.7V battery (**Vbatt**) and **R1** increased to 3.175K Ω in order to present a nearly constant current of 4.0mA to the bolometer element. A closed-form functional equation⁵ is used in **Ebolo**. A thermal capacity⁶ **CH** of 12.8 μ J/K as well as the current source **Ithr** to represent heater energy to maintain the operating point is inserted into the thermal loop. Thermal resistance **RG** was iteratively adjusted until the effective time constant of the output was at 90ms. A value of 1220 Ω was found that represents a thermal conductance of ~ 0.820 mW/K. An effective conductance of 0.142mW/K was derived from the time constant. **Iphi** is configured to produce a square wave optical signal of 5 μ W peak-to-peak. This produces the resulting exponential waveform at the voltage output node 10 as depicted by Figure 6. Larger values of optical signal eventually distort the waveform as the resistance slope

SESSION 3- High Temperature Superconducting (HTS) Bolometers

at the TE region becomes less a straight-line slope and more an exponential shape. A frequency spectrum result is shown in Figure 7. A sinusoid optical signal is swept from 1mHz to 100Hz at 5 μ W rms. The result not only demonstrates the high responsivity acquired (> 1000) in the TE region but also confirms the time constant value due to the half-power point of ~ 1.7 Hz.

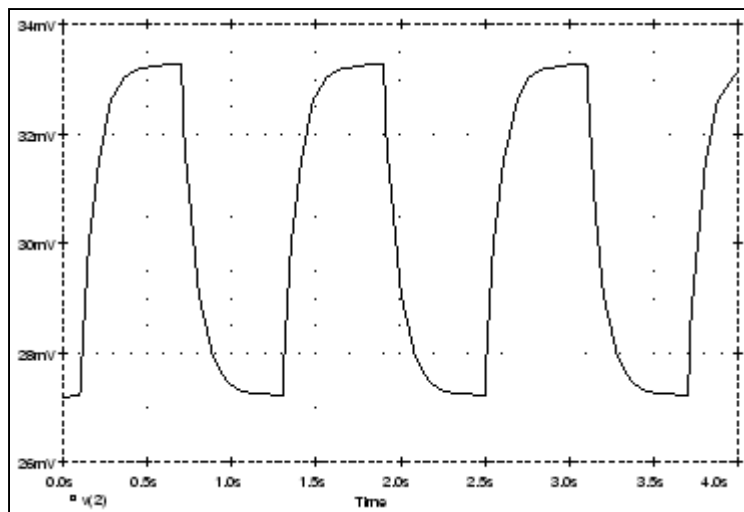


Figure 6. Simulated bolometer output voltage

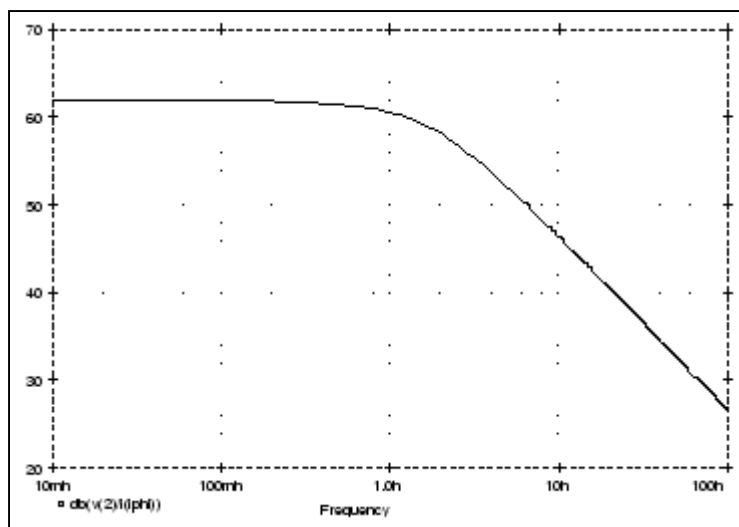


Figure 7. Simulated bolometer frequency response

CONCLUSION

A general model is demonstrated that portrays the thermal and electrical properties of the bolometer. The model is one that can be used for all steady state configurations—current or voltage bias modes. A PSPICE simulation model for steady state configurations was considered with a brief examination of a dynamic state modeling. Furthermore, information about noise modeling was disseminated. Amplifier components, such as opamps and transformers, can also be inserted into Figures 3 or 5 for complete readout/sensor simulation. Moreover, by replacing the VCVS (*Ebolo*) with a VCCS (*Gbolo*) and *Ib* with an independent voltage source, simulation models of Figures 3 and 5 can be rearranged to perform as a constant voltage-bias bolometer circuit.

SESSION 3- High Temperature Superconducting (HTS) Bolometers

REFERENCES

1. D. Yvon, V. Sushkov, *Low Noise Cryogenic Electronics: Preamplifier Configurations with Feedback on the Bolometer*, IEEE Transactions on Nuclear Science, Vol. 47, No. 2, April 2000.
2. J. Shie, Y. Chen, *et. al.*, *Characterization and Modeling of Metal-Film Microbolometer*, Journal of Micromechanical Systems, Vol. 5, No. 4, December 1996.
3. C.D. Motchenbacher, J.A. Connelly, Low Noise Electronic System Design, John Wiley and Sons, New York, NY, 1993.
4. P. J. Fish, Electronic Noise and Low Noise Design, McGraw-Hill, New York, NY, 1994.
5. H.H. Jones and S. Aslam, private communication, May, 2003.
6. J. Brasunas, private communication, March, 2000.

High and Mid Temperature Superconducting Sensors for far IR/Sub-mm applications in space.

Brook lakew*, J. C. Brasunas
NASA- Goddard Space Flight Center, Greenbelt, MD 20771

ABSTRACT

In this review paper an overview of the potential applications of high Tc (~90 K) superconductors (HTS) and mid-Tc (~ 39 K) superconductors (MTS) thin films in far IR/Sub-mm thermal detectors is presented. HTSs (YBCO, GdBCO etc.) were discovered in the late 80s while superconductivity in MgB₂, an MTS, was discovered in 2001. The sharp transition in transport properties of HTS has allowed the fabrication of composite infrared thermal detectors (bolometers) with better figures of merit than thermopile detectors - thermopiles are currently on board the CIRS instrument on the Cassini mission to Saturn. The potential for developing even more sensitive sensors for IR/Sub-mm applications using MgB₂ thin films is assessed. Current MgB₂ thin film deposition techniques and film quality are reviewed.

INTRODUCTION

YBCO and GdBCO

HTS materials were discovered almost 15 years ago. Two of the most known among them are Y₁B₂Cu₃O_{7-x} (YBCO) and Gd₁B₂Cu₃O_{7-x} (GdBCO). The potential uses of these materials especially HTSs have been enumerated in many papers. Just to list a few applications: SQUID readouts, far IR bolometers, lossless power transmission cables, energy storage devices, filters for the mobile phone communications etc. The early euphoria has subsided and the mechanism by which these materials superconduct is yet to be explained. However the interest in HTS superconductors has remained constant in the planetary exploration arena.

Bolometers using HTS materials can be particularly suited for far IR instruments on planetary missions. These missions typically take many years (7 years for the Cassini mission to Saturn)¹ and have stringent mass and power budgets limitation thus making it impossible to carry heavy cryogenics or use high power cryocoolers.

MgB₂

Since early 2001, yet another material, MgB₂ has been found to be superconducting. MgB₂ is simpler than HTSs and superconducts² at 39 K. It is a simple binary intermetallic compound and a common reagent in the chemical reactions in which compounds exchange partners³. MgB₂'s lower Tc in conjunction with the strong cryocoolers development effort at NASA⁴ could yield more sensitive bolometers for application in planetary and Earth sciences.

1. Bolometers:

Bolometers are composite IR detectors consisting of a substrate that has a thermistor on one side, a radiation absorber on the other and coupled to a heat sink via a thermal conductance G. The temperature coefficient of resistance β of the thermistor = $1/R(dR/dT)$. And if the total heat capacity of the bolometer is C, the thermal time constant $\tau = C/G$.

* Contact information for B. Lakew- Email: brook.lakew-1@nasa.gov

SESSION 4- Thin Films for Sensor Applications and Readout Electronics

Responsivity, NEP and specific detectivity D:*

When the HTS thin film is current biased, the voltage across it is

$V = IR$ and if the effect of thermal feedback neglected then the responsivity is commonly expressed as:

$$S = V\beta / G (1 + i2\pi f\tau)$$

where f is the chopping frequency of the incoming radiation

The sensitivity of the bolometer is usually expressed as the noise equivalent power (NEP). It is defined as the input signal power such that the signal-to-noise ratio at the output is 1 (in a 1 Hz bandwidth). It is usually obtained by summing the squares of statistically independent contributions to the noise. The Noise Equivalent Power (NEP)² is the sum of the squares of statistically independent contributions. Thus:

$$NEP = \left(\frac{4k_B^5 T_B^5 A \Omega}{c^2 h^3} \int_0^{x_c} \frac{t^4 e^t dt}{(e^t - 1)^2} + 4k_B T_c^2 G + \frac{4k_B T_c R}{|S|^2} + \frac{AV}{f|S|^2} + \frac{4k_B T_N R}{|S|^2} \right)^{1/2} \quad (1)$$

Of particular interest are the two dominant terms of equation 1: the second term (phonon noise) and third term (Johnson noise in the HTS)⁵.

The specific detectivity D^* is a normalized figure of merit that is widely used. For a detector of area A it is expressed as:

$$D^* = \frac{\sqrt{Area}}{NEP} \quad (\text{cm.Hz}^{1/2}.\text{W}^{-1})$$

The lower the NEP the higher the D^* .

2. YBCO and GdBCO based TES bolometers

In HTS bolometers the thermistor is a superconducting thin film operated near the mid-point of its transition. The substrate is typically either Al_2O_3 , YSZ, MgO or SrTiO_3 . The thermistor is an HTS thin film: YBCuO, GdBCuO etc. (typically 1000 to 1500 Å thick). It is either current or voltage biased.

A selection of the most sensitive ones is put in table 1.

Authors	Sensing element	Substrate	Time constant (ms)	NEP ($\text{W/Hz}^{1/2}$)	D^* ($\text{cmHz}^{1/2}\text{W}^{-1}$)	IR Source
Takehi et al	$25\mu\text{m}^2$	Thick MgO	NG	2.1×10^{-14}	2.5×10^{11}	0.830 μm laser
Lakew et al	GdBCO $1 \times 1 \text{ mm}^2$	Al_2O_3 (7 μm) + absorber	100	8×10^{-12}	2×10^{10} at 3.8 Hz*	Black Body
Li H et al	GdBCO 0.7 mm^2	YSZ (50 μm)	1-5	3.8×10^{-12}	1.7×10^{10}	Black Body
de Nivelles et al	GdBCO 0.9 mm^2	SiN 0.62 μm +buffer	115	5.5×10^{-12}	1.8×10^{10}	Black Body

Table 1. A selection of the most sensitive HTS bolometers on thick, thin and ultrathin substrates. Kreisler and Gague have compiled an excellent list of 34 HTS bolometers⁶.

SESSION 4- Thin Films for Sensor Applications and Readout Electronics

3. HTS bolometers and other thermal detectors:

The NASA/Goddard HTS bolometer is compared to other uncooled or moderately cooled thermal detectors in Table 2.

Detector	Sensing element	Operating temp (K)	Time constant (ms)	D* (cmHz ^{1/2} W ⁻¹)
Thermopile	BiTe	140 – 300	25	3.9 x 10 ⁹
Pyroelectrics	LiTaO3	>240	0.3	2 to 3 x 10 ⁸
NASA/Goddard HTS	GdBCO	90	100	2 x 10 ¹⁰
Optimal HTS bolometer	YBCO	90	56	~7 x 10 ^{10*}

Table 2. Performance of NASA/GSFC's HTS bolometers vs other thermal detectors. Note: *Calculated using $G \sim 1 \mu\text{W/K}$ and $C \sim 0.1 \mu\text{J/K}$ for current biased bolometer⁵. For higher G values the time constant of the ideal bolometer can be made smaller but with a smaller D^* as a consequence.

4. MTS bolometers- the case of MgB₂

MgB₂'s crystal structure consists of hexagonal honeycombed planes of boron atoms separated by planes of magnesium atoms, with the magnesium atoms along the c axis in the hexagonal lattice².

It is believed that MgB₂ forms by diffusion of Mg into Boron grains⁷. Unlike HTS, MgB₂ grain boundaries are not weak and can carry large currents⁸. Experiments by Bud'ko *et al* have shown that lower mass isotopes of B increase T_c indicating that phonons play an important role in the superconducting interaction⁹.

Advantage of MgB₂ thin films as thermistors:

Assuming that thermal noise and Johnson noise dominate in Equation 1 then $\text{NEP} \sim (4k_B T_c^2 G + 4k_B T_c R / S^2)^{1/2}$. Everything else being equal, including thin film quality, the noise will be smaller when T_c is smaller. Thus the promise of more sensitive bolometers with MgB₂ thin films as thermistors.

MgB₂ thin films growing methods:

- Hybrid Physical-Chemical Vapor Deposition (HPCVD): a combination of Physical Vapor Deposition (PVD) and Chemical Vapor Deposition (CVD)– at ~750 °C, film grows epitaxially on (0001) sapphire and (0001) 4H-SiC substrates¹⁰.
- Molecular beam epitaxy (MBE) – Pure metal sources are evaporated via electron beam evaporators in vacuum chamber (1×10^{-9} Torr)¹¹.
- Sintering (the Ames Method) – A stoichiometric mixture of Mg and B are sealed⁷ in Ta tube and heated to 950 °C.
- Pulsed Laser Deposition (PLD): *ex situ* or *in situ* :
Ex situ : (PLD and Ames method): Boron deposited via PLD on SITiO₃ (100) and (111) at 800 °C, then reacted with Boron in a sealed Ta tube.
In situ : (1) PLD from sintered MgB₂ target; (2) PLD of multilayers of MgB₂ and Mg followed by *in situ* anneal at high temperature, (3) PLD of multilayers of B and Mg followed by *in situ* anneal at high temperature. Better T_c obtained with *ex situ* anneal¹².

Summary

SESSION 4- Thin Films for Sensor Applications and Readout Electronics

Method	Growth temp (° C)	Transition Temp (K)	Substrate	Application
HPCVD	650	40	SiC/ sapphire (0001)	IR Sensors
MBE	150-350	36	SrTiO ₃ (001), Sapphire R & C, Si (001)	Junctions& multilayers
Sintering (Ames method)	950	39.2* 40.2**	Mostly wires and pellets	Transport properties/ Research
Pulsed Laser Deposition	900	22 (<i>in situ anneal</i>) 40 –(<i>ex situ anneal</i>)	R plane sapphire	Single& multilayers

Table 3. Summary of current MgB₂ thin films growing methods. * Isotope Mg¹¹ ; **Mg¹⁰

Film Quality:

The main obstacle to obtaining good quality films is the high volatility of Magnesium^{11,13}. Degradation of MgB₂ due to exposure to water on film quality has also been noticed¹⁴.

5. Conclusion

For space borne IR instruments that have moderately cooled focal planes, HTS and MTS bolometers remain, to date, the sensors with the highest signal to noise (S/N). MgB₂ with a T_c at 39 K promises even better S/N. Improvements in the fabrication methods will hopefully improve the quality and stability of MgB₂ thin films.

REFERENCES

1. V. Kunde et al., Vol. 2803, SPIE, Vol. 2803, Denver, CO, 1996.
2. J. Nagamatsu, N. Nakagawa, T. Muranaka, Y. Zenitani, and J. Akimitsu, Nature 410, p. 63, 2001.
3. R.J. Cava, Nature 410, p. 23, 2001.
4. R.G. Ross, Jr., R.F Boyle, P.Kittel, *NASA's space cooler program – A 2003 overview*, TDW03 Workshop on Thermal Detectors in press, 2003.
5. P. L. Richards et al, Appl. Phys Lett., 54, p 283, 1989.
6. A. Kreisler, A. Gaugue, Supercond. Sci. Technol., 13, , 1235-1245, 2000.
7. P.C. Canfield, et al., Phys. Rev. Lett., 86(11):2423-6, 2001.
8. D.K. Finnmore, J.E. Ostenson, S.L. Bud'ko, G. Lapertot and P.C. Canfield , Phys rev Letters, 86, p 2420, 2001.
9. S.L. Bud'ko, G. Lapertot, C. Petrovic, C. Cunningham, N. Anderson and P.C. Canfield, Phys. Rev Lett., 86, 1877, 2001.
10. X. Zeng et al, Nat. Mater., 1, 35-38, 2002.
11. Ueda et al, Appl. Phys. Letters, vol 79, 2001.
12. S.R. Shinde, S.B. Ogale, R.L. Greene, T. Venkatesan, P.C. Canfield, S.L. Bud'ko, G. Lapertot and C. Petrovic, Appl Phys. Letters, vol 79, No 2, p 227, 2001.
13. Zhai et al, Supercond. Sci. Technol., 14, 425-428, 2001.

SESSION 4- Thin Films for Sensor Applications and Readout Electronics

PR38-INV9*

SQUID Multiplexers for Cryogenic Detector Arrays

Kent Irwin, James Beall, Steve Deiker, Randy Doriese
(National Institute of Standards and Technology),

William Duncan (UK ATC),

Gene Hilton (National Institute of Standards and Technology),

S. Harvey Moseley, (NASA Goddard Space Flight Center),

Carl Reintsema (National Institute of Standards and Technology),

Caroline Stahle (NASA Goddard Space Flight Center),

Joel Ullom, Leila Vale (National Institute of Standards and Technology)

SQUID multiplexers make it possible to build arrays of thousands of cryogenic detectors with a manageable number of readout channels. We are developing time-division SQUID multiplexers based on Nb trilayer SQUIDs to read arrays of superconducting transition-edge sensors. Our first-generation, 8-channel SQUID multiplexer was used in FIBRE, a one-dimensional TES array for submillimeter astronomy. Our second-generation 32-pixel multiplexer, based on an improved architecture, has been developed for instruments including Constellation-X, SCUBA-2, and solar x-ray astronomy missions. SCUBA-2, which is being developed for the James Clerk Maxwell Telescope, will have more than 10,000 pixels. We are now developing a third-generation architecture based on superconducting hot-electron switches. The use of SQUID multiplexers in instruments operating at above 2 K will also be discussed.

* A PowerPoint presentation is available on the CD version of the TDW '03 proceedings.

SESSION 4- Thin Films for Sensor Applications and Readout Electronics

PR15*

Epitaxial Superconducting MgB_2 Thin Films by HPCVD
Xiaoxing Xi (Penn State University)

The recently discovered superconductor MgB_2 with T_c at 39 K has great potential in superconducting electronics. In this paper, we present results of in situ epitaxial MgB_2 thin films grown by Hybrid Physical-Chemical Vapor Deposition (HPCVD) technique which successfully achieves a high Mg pressure necessary for in situ growth of MgB_2 thin films. Excellent superconducting properties have been obtained in these films.

Keywords: Superconductor, thin films, chemical vapor deposition

* A PowerPoint presentation is available on the CD version of the TDW '03 proceedings.

SUPERCONDUCTING DIGITAL MULTIPLEXERS FOR SENSOR ARRAYS

Alan M. Kadin^{*}, Darren K. Brock, and Deepnarayan Gupta
HYPRES, Inc., 175 Clearbrook Road, Elmsford, NY 10523, USA

ABSTRACT

Arrays of cryogenic microbolometers and other cryogenic detectors are being developed for infrared imaging. If the signal from each sensor is amplified, multiplexed, and digitized using superconducting electronics, then this data can be efficiently read out to ambient temperature with a minimum of noise and thermal load. HYPRES is developing an integrated system based on SQUID amplifiers, a high-resolution analog-to-digital converter (ADC) based on RSFQ (rapid single flux quantum) logic, and a clocked RSFQ multiplexer. The ADC and SQUIDS have already been demonstrated for other projects, so this paper will focus on new results of a digital multiplexer. Several test circuits have been fabricated using Nb Josephson technology and are about to be tested at $T = 4.2$ K, with a more complete prototype in preparation.

INTRODUCTION

Arrays of superconducting and other low-temperature detectors are widely being developed for imaging across the electromagnetic spectrum, from microwaves through gamma radiation. These include microbolometers for infrared and microcalorimeters for x-ray single-photon detection. One type of detector is the transition-edge superconducting sensor (TES)¹; another is the superconducting tunnel-junction detector (STJ)². Both require cooling to very low (sub-K) temperatures for maximum sensitivity. In this context, large numbers of leads for control and readout of the array elements are impractical, since they conduct too much heat into the cryogenic environment. One approach is to multiplex multiple sensors onto the same output lines, using a matrix of switches lying close to the sensors at low temperatures.

Furthermore, the sensor signals must be amplified and transmitted to warm electronic circuits for further signal processing. In particular, SQUID amplifiers are well matched to TES sensors, providing low noise and isolation with sufficient gain to drive room-temperature circuitry. Several groups have demonstrated approaches to multiplexing multiple SQUID amplifiers, in either the time-domain³ or the frequency domain.⁴

We have made use of SQUID amplifiers in a somewhat different mode. A SQUID in the voltage state actually produces a time-series of single-flux-quantum pulses (also known as SFQ pulses or fluxons) at a rate proportional to the voltage, as given by the Josephson voltage-frequency ratio $f = V/\Phi_0$, where $\Phi_0 = h/2e = 2.07$ mV-ps is the magnetic flux quantum. These SFQ pulses (with pulsewidth ~ 2 ps and pulse height ~ 1 mV) form the basis for a superconducting logic family known as RSFQ, for rapid-single-flux-quantum.^{5,6} The pulse rate can be counted in a binary counter, effectively providing a digital measurement of the voltage. An analog-to-digital converter (ADC) based on these principles was recently fabricated in a monolithic superconducting integrated circuit based on Nb Josephson junctions,⁷ and demonstrated in liquid helium at a temperature of 4.2 K.⁸ In the present work, we describe how a set of digital switches can adapt this ADC to become a digital time-domain multiplexer (see Fig. 1). At any given time, the switch for only one sensor is open, permitting the SFQ pulses for that sensor to pass through to the counter. By proper sequencing of the switches for the SQUIDS and triggers for the counter, a properly multiplexed digital output signal can be obtained. This will be discussed in more detail below.

There are a number of general advantages of carrying out this digitization in the cryogenic environment close to the sensors. Most important among these is noise resistance; once a signal is in digital format, it is

^{*} Contact information for A.M. Kadin: Email: kadin@hypres.com, phone (914) 592-1190.

SESSION 4- Thin Films for Sensor Applications and Readout Electronics

virtually immune to the effects of low-level noise. This is also true for any subsequent amplification of the signal; unlike the case for amplification of a weak analog signal, any weak nonlinearity or added analog noise should not affect the content of a digital signal, provided that it is not above the threshold level needed to produce bit errors. Furthermore, digital signals can be easily averaged to increase resolution and reduce noise, and can be conveniently calibrated for non-ideal sensors (e.g., with gain and offset corrections). Furthermore, a system of digital signals has great flexibility in scaling to large arrays and in interfacing with general-purpose computers, for further processing of digital images.

Finally, superconducting digital electronics is notable for operating at very low power levels, typically ~ 1 mW or less for a complex digital circuit. This level is compatible with monolithic integration with cryogenic sensors, without excessive heating. Conventional semiconductor digital systems generally dissipate orders of magnitude more power, and cannot effectively be integrated close to cryogenic sensors.

DIGITAL READOUT DESIGN AND SIMULATION

The digital multiplexing scheme is shown in Fig. 1. Here the output signals from a row of sensor elements are currents, each of which is inductively coupled to a SQUID loop. Each SQUID generates a pulse sequence at a rate proportional to the SQUID voltage (which in turn is linear in the signal current). Each pulse is shaped and propagated toward an RSFQ digital switch S using a Josephson transmission line (JTL). If the switch is closed, the pulse train is coupled to the line that goes to the fluxon counter. The counter generates a binary number (with, e.g., 16 bits), which can be serialized in a parallel-to-serial converter (PSC) so as to reduce the number of output leads. In practice, this is followed by a high-voltage output driver consisting of a series array of SQUIDs, so as to raise the voltage (and increase the pulsewidth) to levels more appropriate for access by standard room-temperature electronics. The layout of a 5-mm x 5mm

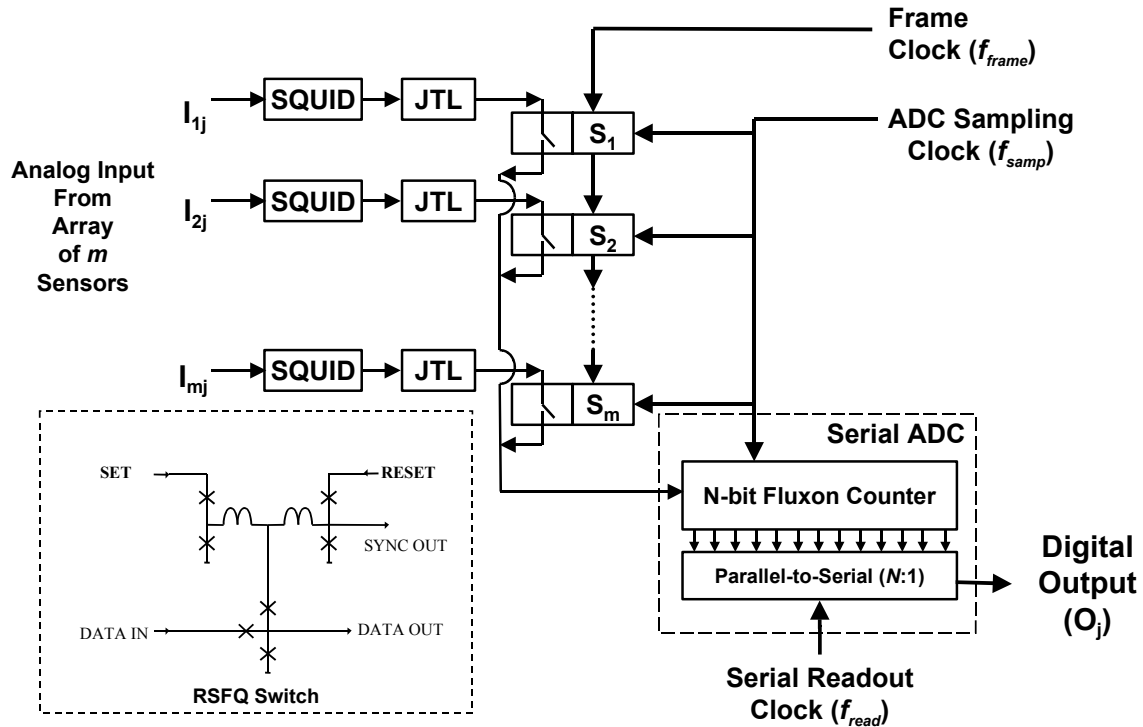


Figure 1: Superconducting digital multiplexing scheme for readout from array of TES sensors. Each SQUID amplifier generates a sequence of SFQ pulses at a rate which is linear with the sensor current. All of the switches S are initially closed, but are opened one-at-a-time to permit the pulse sequence from a particular sensor to pass through to the fluxon counter. The multi-bit binary output from the counter is periodically serialized and read out to room-temperature electronics. The inset in the bottom left shows the detailed circuit diagram of the digital switches, where \times represents a Josephson junction.

SESSION 4- Thin Films for Sensor Applications and Readout Electronics

superconducting integrated circuit with these components (but only a single switch) is shown in Fig. 2a (left). The chip on the right is an array of 3 switches configured for testing of proper timing sequences. These chips are currently being fabricated by HYPRES in Nb Josephson technology based on junctions with a critical current density $J_c = 1 \text{ kA/cm}^2$ and 3- μm linewidths, and will be tested soon at 4 K.

Several clock signals are needed to synchronize the proper operation of this system. The sampling clock opens all switches and resets the counter, transferring the contents to the PSC for subsequent readout. The frame clock closes one switch, moving sequentially down the column after each sampling period. The serial readout clock reads out the contents of the PSC, so that the counter can then be reset to zero. A circuit simulation that illustrates the operation of these switches is shown in Fig. 3, for three input signals, at three different pulse rates. The switches and counters have been found in simulation to operate with acceptable margins up to pulse rates of at least 30 GHz.

DISCUSSION AND CONCLUSIONS

Let us project a digital multiplexer such as we have described as the readout electronics for a sensor array. Consider, for example, an array of 100 TES sensors, each with a characteristic response time $\sim 100 \mu\text{s}$. If the integration time is $\sim 1 \mu\text{s}$ for each sensor, this corresponds to a total count of 30,000 for a 30 GHz pulse rate. This is compatible with a 16-bit counter, which we have already demonstrated, although the system may be limited by analog noise in the sensors or input SQUIDs. With optimum layout, it should be possible to include all 100 channels on a single 1-cm x 1-cm superconducting chip. Such a chip would normally operate at $T=4.2 \text{ K}$, although it should operate equally well at the reduced temperatures typical of TES sensors. Since the total power dissipation should be less than 1 mW, it might even be possible to fabricate a complete monolithic IC that incorporates both the microbolometer focal plane array and the readout electronics.

In conclusion, we have designed and laid out preliminary superconducting circuits for a combined digitizer-multiplexer for an array of sensors such as TES microbolometers, which will be tested in the near future.

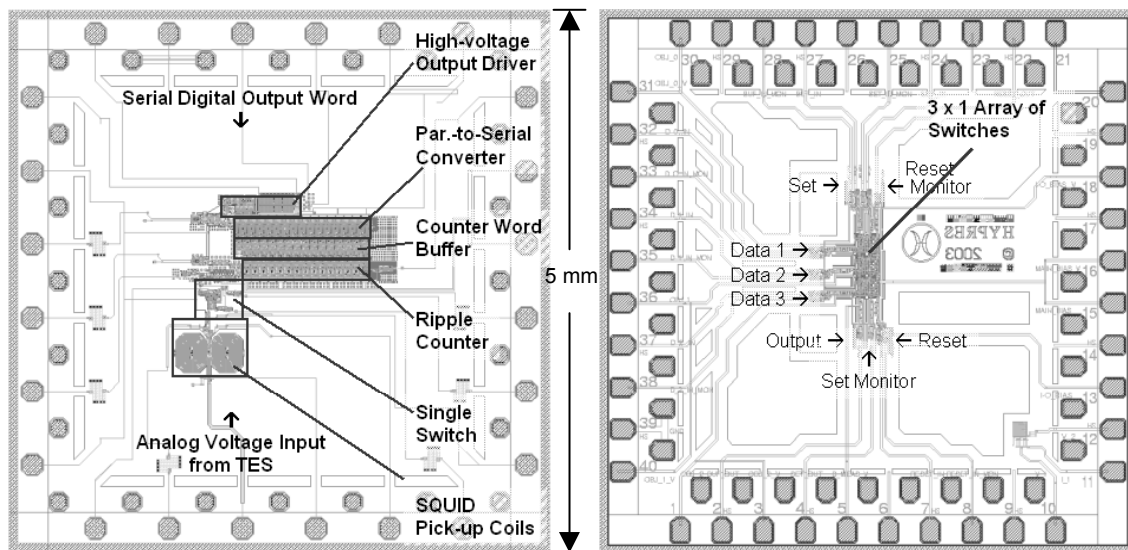


Figure 2: Circuit layouts for two superconducting Nb test chips, each 5 mm x 5 mm. (a - left) Serial ADC, with single inductive input to SQUID pickup coils, followed by a digital counter and parallel-to-serial converter and SQUID array output driver for sending digital data to room temperature. (b - right) Multiplexer test chip, with array of 3 RSFQ switches permitting sequential streaming of three independent data inputs. Following testing and analysis at 4 K, a complete digital multiplexing chip with perhaps 16 input channels and a serial ADC will be designed and tested with simulated sensor data.

SESSION 4- Thin Films for Sensor Applications and Readout Electronics

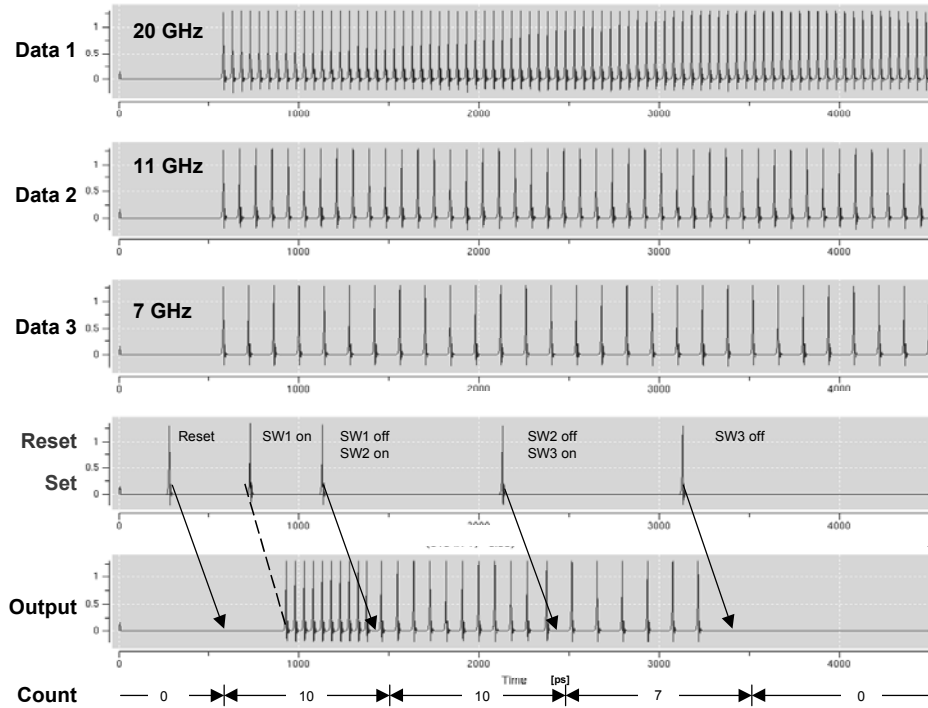


Figure 3: Circuit-level simulation of switching circuit in Fig. 2b. The 3 inputs with different pulse stream rates represent three different sensor signals. The output starts with all switches open, followed by switches 1, 2, and 3 being closed in sequence, one-at-a-time.

Digitizing the signal in the cryogenic environment offers significant advantages in terms of reduced noise and increased flexibility, particularly as the arrays become larger. Pending availability of future funding, we intend to continue toward the development of a complete integrated prototype system that generates a serialized digital output for an array of up to 100 sensors. Full integration of the readout electronics with the sensors themselves may also be feasible.

ACKNOWLEDGMENT

Research supported in part by NASA Small Business Research Project #NAS3-03044, managed by Jet Propulsion Laboratory.

REFERENCES

1. S. Deiker, J. Chervenak, G.C. Hilton, K.D. Irwin, J.M. Martinis, S. Nam, and D.A. Wollman, *Transition Edge Sensor Development*, IEEE Trans. Appl. Supercond. 11, 469, 2001.
2. P. Verhoeve, N. Rando, A. Peacock, D. Martin, and R. den Hartog, *Superconducting tunnel junctions as photon-counting imaging spectrometers from optical to the x-ray band*, Opt. Eng. 41, 1170, 2002.
3. K.D. Irwin, *SQUID multiplexers for transition-edge sensors*, Physica C 368, 203, 2002.
4. J. Yoon, J. Clarke, J.M. Gildenmeister, A.T. Lee, M.J. Myers, P.L. Richards, and J.T. Skidmore, *Single SQUID multiplexer for arrays of low-temperature sensors*, Appl. Phys. Lett. 78, 371, 2001.
5. K.K. Likharev and V.K. Semenov, *RSFQ Logic Family: A New Josephson Technology for Sub-THz Digital Systems*, IEEE Trans. Appl. Supercond. 1, 3, 1991.
6. D.K. Brock, *RSFQ Technology: Circuits & Systems*, Int. J. High Speed Electron. Syst. 11, 307, 2001.
7. M. Radparvar, *Superconducting Nb and NbN processes for medium-scale integration processes*, Cryogenics 35, 535, 1995; see also HYPRES Nb foundry design rules at <http://www.hypres.com>.
8. S. Sarwana, D. Gupta, A.F. Kirichenko, et al., *High-sensitivity, high-resolution dual-function signal and time digitizer*, Appl. Phys. Lett. 80, 2023, 2002.

ELECTRICAL DEVICES AND CIRCUITS FOR LOW TEMPERATURE SPACE APPLICATIONS

R.L. Patterson¹, A. Hammoud², J.E. Dickman¹, S. Gerber³, M.E. Elbuluk⁴, & E. Overton¹

¹NASA Glenn Research Center, Cleveland, Ohio 44135, USA

²QSS Group, Inc., NASA Glenn Research Center, Cleveland, Ohio 44135, USA

³ZIN Technologies, Inc., NASA Glenn Research Center, Cleveland, Ohio 44135, USA

⁴University of Akron, Department of Electrical Engineering, Akron, OH 44325, USA

ABSTRACT

The environmental temperature in many NASA missions, such as deep space probes and outer planetary exploration, is significantly below the range for which conventional commercial-off-the-shelf electronics is designed. Presently, spacecraft operating in the cold environment of such deep space missions carry a large number of radioisotope or other heating units in order to maintain the surrounding temperature of the on-board electronics at approximately 20 °C. Electronic devices and circuits capable of operation at cryogenic temperatures will not only tolerate the harsh environment of deep space but also will reduce system size and weight by eliminating or reducing the heating units and their associate structures; thereby reducing system development cost as well as launch costs. In addition, power electronic circuits designed for operation at low temperatures are expected to result in more efficient systems than those at room temperature. This improvement results from better behavior in the electrical and thermal properties of some semiconductor and dielectric materials at low temperatures. An on-going research and development program on low temperature electronics at the NASA Glenn Research Center focuses on the development of efficient electrical systems and circuits capable of surviving and exploiting the advantages of low temperature environments. An overview of the program will be presented in this paper. A description of the low temperature test facilities along with selected data obtained from in-house component testing will also be discussed. On-going research activities that are being performed in collaboration with various organizations will also be presented.

INTRODUCTION

Electronics capable of low temperature operation are required for many future NASA space missions where it is desirable to have smaller, lighter, and cheaper (unheated) spacecraft. These include Mars orbiters, landers, and rovers; Europa oceanic exploratory probes and instrumentation; and outer planetary exploration and deep space probes. Table 1 shows operational temperatures for unheated spacecraft in the environments of the outer planets. For example, an inter-planetary probe launched to explore the rings of Saturn would experience a temperature near Saturn of about -183 °C. In addition to surviving the space hostile environments, electronics capable of low temperature operation would contribute to improving circuit performance, increasing system efficiency, and reducing development and launch costs.

Presently, spacecraft operating in the cold environment of deep space carry on-board a large number of radioisotope heating units (RHUs) to maintain an operating temperature for the electronics at approximately 20 °C. This is not an ideal solution because the radioisotope heating units are always producing heat, even when the spacecraft may already be too hot, thus requiring an active thermal control system for the spacecraft¹. In addition, RHUs add cost and require elaborate containment structures. Electronics capable of operation at cryogenic temperatures will not only tolerate the hostile environment of deep space but also reduce system size and weight by eliminating radioisotope heating units and associated

Table 1: Typical operational temperatures for unheated spacecraft

Mission	Temperature °C
Mars	-20 to -120
Jupiter	-151
Saturn	-183
Uranus	-209
Neptune	-222
Pluto	-229

¹ Contact information for R.L. Patterson-Email: Richard.patterson@grc.nasa.gov

SESSION 4- Thin Films for Sensor Applications and Readout Electronics

structures; thereby reducing system development and launch costs, improving reliability and lifetime, and increasing energy densities.

In addition to deep space applications, low temperature electronics have potential uses in terrestrial applications that include magnetic levitation transportation systems, medical diagnostics, cryogenic instrumentation, and super-conducting magnetic energy storage systems. The utilization of power electronics designed for and operated at low temperature is expected to result in more efficient systems than room temperature systems. This improvement results from better electronic, electrical, and thermal properties of certain materials at low temperatures^{2,3}. In particular, the performance of certain semiconductor devices improves with decreasing temperature down to liquid nitrogen temperature (-196 °C). At low temperatures, majority carrier devices demonstrate reduced leakage current and reduced latch-up susceptibility^{3,4}. In addition, these devices show higher speed resulting from increased carrier mobility and saturation velocity³⁻⁵. An example is the power MOSFET which has lower conduction losses at low temperature due to the reduction in the drain-to-source resistance $R_{DS(on)}$ resulting from increased carrier mobility^{4,6,7}.

NASA GRC LOW TEMPERATURE ELECTRONICS PROGRAM

The Low Temperature Electronics Program at the NASA Glenn Research Center (GRC) focuses on research and development of electrical components and systems suitable for applications in deep space missions. Research is being conducted on devices and circuits for use down to cryogenic temperature (-196 °C). The goal of the low temperature electronics program is to develop and demonstrate reliable, efficient, power systems capable of surviving and exploiting the advantages of low temperature environments. The targeted systems are mission-driven and include converters, inverters, controls, digital circuits, and special-purpose circuits. Initial development efforts have produced the successful demonstration of low temperature operation and cold-restart of several DC/DC converters (with outputs from 5 to 1000 Watts) utilizing different design topologies^{1,4,7}. Some of these circuits employed superconducting inductors.

In support of system development, device and component research and development efforts are underway in critical areas of passive and active components, and energy generation and storage. Initially, commercial-off-the-shelf (COTS) devices and components are characterized in terms of their performance at low-temperatures. When viable commercial devices fail to meet mission requirements, efforts are then undertaken to develop advanced components.

In addition to the development efforts to fill the technology gaps in low temperature power electronics, thermal issues relating to packaging, integration, and cycling are being explored.

GRC LOW TEMPERATURE FACILITIES

At NASA Glenn Research Center, facilities exist for the testing of power and control circuits operating from DC to several Megahertz over a wide temperature range. These facilities consist of several liquid nitrogen cooled environmental chambers in which a circuit can be operated with controlled temperature in the range of 300 °C to -196 °C. The chambers have built-in controllers that allow selecting the desired temperature rate of change as well as soak times. Computer-controlled instrumentation is interfaced with the environmental chambers via IEEE 488 GPIB for data acquisition. Measurement equipment include a digital signal analyzer, pattern generators, precision digital RLC meters, high speed storage oscilloscopes, precision temperature controller and recorder, various electronic loads, and resistive loads from mW's to kW's in power.

Another unique computerized control system is used in conjunction with a cryopumped vacuum chamber containing a cryocooled sample holder for the characterization of commercial and developmental semiconductor devices and components. This facility is capable of *in-situ* I-V and C-V characterization of semiconductor devices from 23 °C to -248 °C.

GRC has designed computer-controlled facilities for low-temperature long term thermal cycling and characterization of electrical and physical properties of dielectrics and capacitors. In addition, facilities exist for reliability studies and life testing of passive and active devices in space-like environments under

SESSION 4- Thin Films for Sensor Applications and Readout Electronics

multi-stress conditions. Typical studies that can be carried out using these facilities include dielectric material characterization, DC and AC breakdown voltages, resistivity measurements, switching characteristics, and electronic system overall performance such as regulation and efficiency.

Other on-site supporting research facilities include physical, chemical, and mechanical test chambers and diagnosis stations. Characterization of materials and evaluation of systems and components under space-like environment, such as vacuum, plasma, ultraviolet radiation, and atomic oxygen, can be achieved in multi-stress aging test rigs and facilities.

LOW TEMPERATURE R&D ACTIVITIES

Some of the components that are being characterized include semiconductor switching devices, capacitors, batteries, temperature transducers, and A/D converters, to name a few. Figure 1 shows the change in capacitance for three types of capacitors in the temperature range of 25 °C to -190 °C at a frequency of 20 kHz. It can be seen clearly that while the mica capacitor exhibits excellent stability with temperature, the electrolytic tantalum capacitor undergoes significant decrease in capacitance when the test temperature goes below -25 °C. In fact, at temperatures below -80°C the capacitance drops to zero. Unlike its electrolytic counterpart, the solid tantalum capacitor exhibits only a slight decrease in capacitance as temperature is decreased. This reduction in capacitance amounts to only about 10% even down to -190 °C.

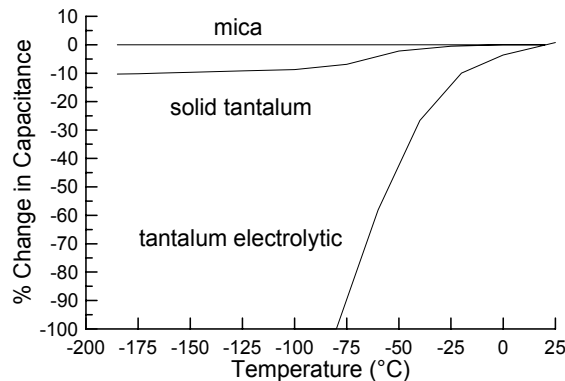


Table 2: *Converted output voltage at various temperatures.*

Input (V)	Output (V) @ 25 °C	Output (V) @ -100 °C	Output (V) @ -190 °C
0	0.007	0.010	0.010
0.5	0.505	0.498	0.508
1	1.004	1.006	1.004
2	2.000	2.002	1.993
5	4.994	4.994	5.001
7.25	7.241	7.228	7.226
10	9.983	9.963	9.963
10.1	10.000	10.000	10.000

Figure1: *Capacitance change with temperature for various types of capacitors.*

A commercial off-the-shelf 12-bit serial CMOS analog-to-digital converter, which was rated for operation between -40 °C and +85 °C, was evaluated from room temperature to -190 °C in a liquid nitrogen cooled chamber. Parameters investigated included voltage conversion and control signal timing at a switching frequency of 100 kHz. Although the device had a built-in internal voltage reference, tests were also carried out using an external voltage reference. In either case, the device was able to provide the voltage conversions throughout the entire test temperature range down to -190 °C. The converted output obtained using an external voltage reference, however, was more accurate than those obtained with an internal voltage reference. Results obtained at three different temperatures with an external reference are shown in Table 2.

Commercially available DC/DC converter modules were investigated for potential use at low temperatures. For example, the output voltage of a commercial DC/DC converter at various load levels is shown as a function of temperature in Figure 2. It can be seen that the output voltage of this particular module tended to be steady only between +20 °C and -20 °C. A slight reduction occurred in voltage regulation as temperature was further decreased to -80 °C. Below that temperature, the converter tended to become unstable in terms of voltage regulation. This behavior occurred regardless of the levels of the applied input voltage and connected output load. Another commercial DC/DC module included in this investigation fared relatively well in terms of its output regulation with temperature. The output voltage of this converter is depicted in Figure 3 as a function of temperature at various load levels.

SESSION 4- Thin Films for Sensor Applications and Readout Electronics

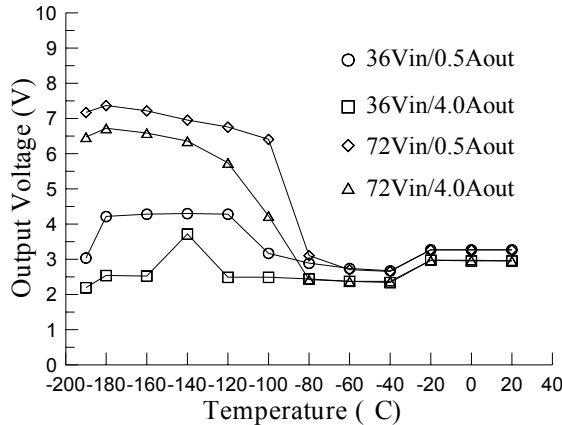


Figure 2: Poor performance of one commercial dc/dc converter module.

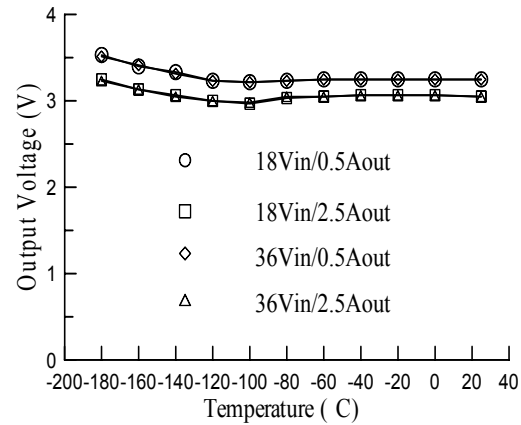


Figure 3: Superior performance of another commercial dc/dc converter.

Current-mode and voltage-mode pulse width modulation controllers were evaluated extensively for low temperature operation. The performance of one of those commercial grade pulse width modulation controller chips was evaluated between 25 °C and -190 °C. The device displayed acceptable performance throughout the entire test temperature range. Waveforms of the device reference voltage, oscillator, and output switching voltage, which were recorded at a control voltage (VC) of 1.5V, are shown in Figures 4a and 4b at test temperature of 25 °C and -190 °C, respectively. It can be seen clearly that all investigated properties did not undergo much change with temperature, as evident from the similarity of the waveforms shown for both extreme temperature, i.e. 25 °C and -190 °C.

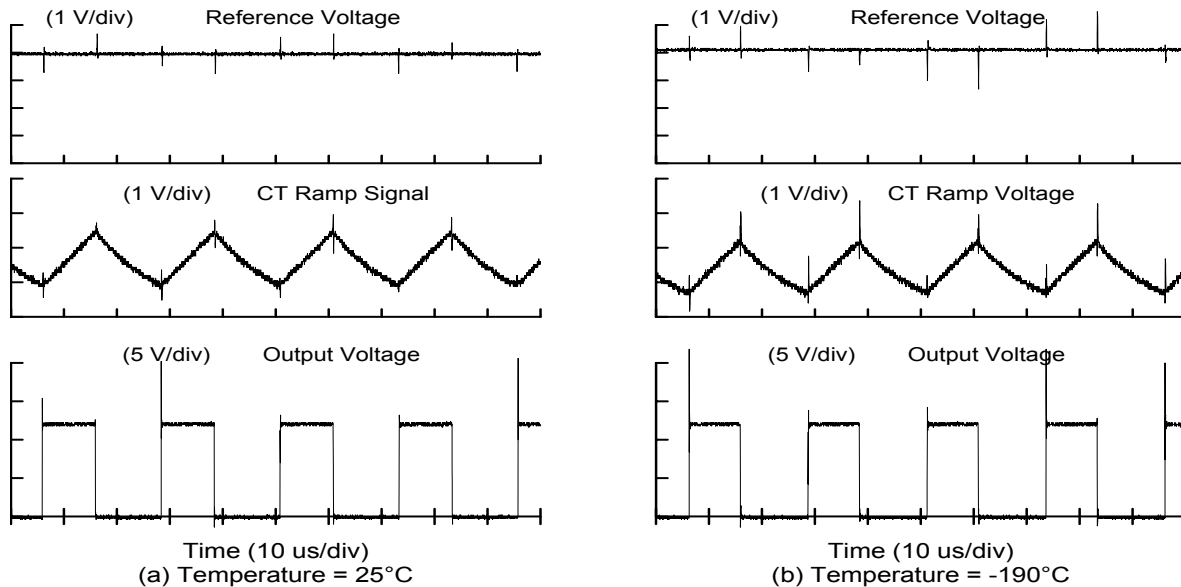


Figure 4: Waveforms of PWM controller at (a) 25 °C and (b) -190 °C.

The performance of three precision oscillators was investigated at low temperatures. One uncompensated oscillator was able to function to -196 °C. A second uncompensated oscillator was built to operate at ultra-low temperatures, and it operated down to -263 °C. A third oscillator, which was temperature compensated and modified for low temperature use, operated within 0.3 ppm in frequency down to -160 °C. The normalized output frequencies of the three oscillators are shown as a function of temperature in Figure 5.

Figure 6 shows the drain-to-source on-state resistance ($R_{DS(on)}$) versus temperature for two types of MOSFET devices. It can be seen that the standard as well as the silicon-on-insulator devices show similar behavior in their R_{DS} with temperature. The on-state resistance of either device seemed to decrease with

SESSION 4- Thin Films for Sensor Applications and Readout Electronics

decrease in temperature till about -170°C . This trend, however, was reversed as the test temperature was decreased further as reflected by the slight increase in the on-state resistance of both devices. At any temperature, the SOI device exhibited a slightly higher on-state resistance than its standard counterpart.

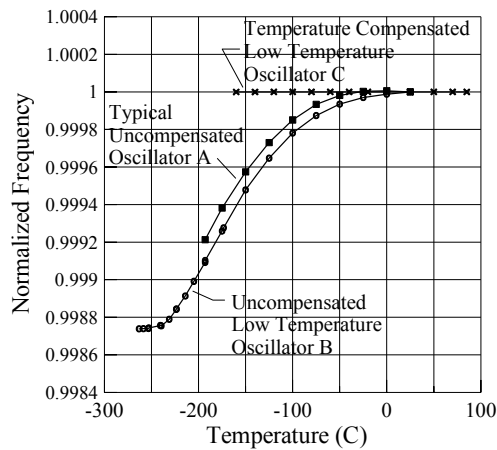


Figure 5: Normalized frequency output for three types of oscillators.

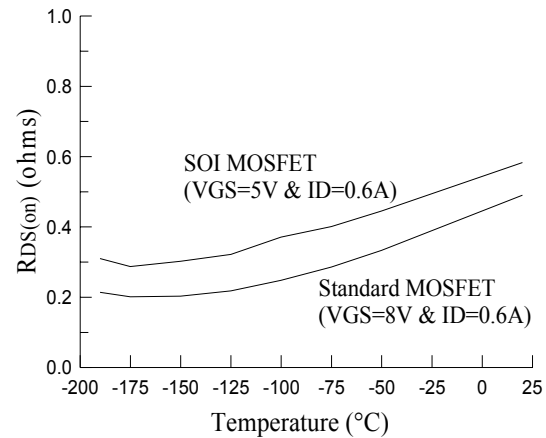


Figure 6: Drain-to-source on-resistance for SOI and standard MOSFET devices versus temperature.

CONCLUSION

An overview of the Low Temperature Electronics Program at NASA Glenn Research Center was given. The research efforts are focused on developing selected, mission-driven, power systems and supporting technologies for low temperature operation. The on-going activities include dielectric and insulating material research and evaluation, development and testing of low temperature power components, and electronic system integration and demonstration. Other supporting research investigations comprise long term reliability assessment of power devices and integrated circuits and the effects of low temperature exposure on device interconnect and packaging. These research and development efforts are performed in collaboration with other agencies, academia, and the aerospace industry in order to meet the needs of future space power and other electrical systems.

REFERENCES

1. S.S. Gerber, R.L. Patterson, B. Ray and C. Stell, *Performance of a spacecraft DC/DC converter breadboard modified for low temperature operation*, IECEC 96, 1, 592-598, 1996.
2. R.K. Kirschman, *Low temperature electronic device operation*, Symposium of Electrochemical Society, 14, 1991.
3. M. Dean, D. Foty, N. Saks, S. Raider, and G. Oleszel, *Low temperature microelectronics: opportunities and challenges*, Proc. Symposium on Low Temperature Electronic Device Operation, Electrochemical Society, 91,14, 25-37, 1991.
4. B. Ray, S. S. Gerber, R. L. Patterson and I. T. Myers, *Power control electronics for cryogenic instrumentation*, Advances in Inst. and Control, 50, 1, Int. Soc. for Measurement and Control, 131-139, 1995.
5. R. K. Krishman, *Cold electronics: an overview*, Cryogenics, 25, 3, 115-122, 1985.
6. O. Mueller, *On-resistance, thermal resistance and reverse recovery time of power MOSFETs at 77K*, Cryogenics, 29, 1006-1014, 1989.
7. B. Ray, S. S. Gerber, R.L. Patterson and I. T. Myers, *77K Operation of a multi-resonant power converter*, IEEE PESC'95 Record, 1, 55-60, 1995.

FAR-INFRARED AND SUBMILLIMETER FILTERS

C. V. Haynes*, P. A. R. Ade, J. Budd, C. Lee, C. E. Tucker
University of Wales, Cardiff, U.K.

ABSTRACT

Filters are critical for thermal detector systems, which are responsive to a wide frequency range. Without spectral limitation the detectors respond to frequencies outside those of interest with the consequence of increased photon noise and detector loading. For cooled systems it is also important to filter out high frequency radiation, minimising the thermal load and cooling power necessary. At Cardiff University we are developing far-infrared and submillimeter bandpass, high-pass, and low-pass blocking filters using a metal mesh technology. We have been able to maintain high in-band transmission with good out of band rejection to UV wavelengths. This technology is space qualified and has been used in a number of Astronomical and Earth Observation projects. Here we present our latest advancements.

INTRODUCTION

Polymer film supported air-gap metal mesh filters have been under development in this group for more than 25 years and are in use in many instruments and observatories for frequency selection and thermal control. These devices show good rejection outside the pass band with high transmission in band. Their performance is not subject to drift after regular cryogenic cycling and they are able to withstand vibration at 30g while cold, so achieving space qualification. High-pass, low-pass, broad and narrow band-pass and band stop characteristics can be all achieved.

These devices however have some drawbacks, which could be improved. They are sensitive to poor handling, solvents and are easily damaged beyond recovery. The steel mounting rings can limit the packing density of a detector array and increase the load on the cooling system. The U.V. resistance could be better. Though never noted as a problem, the grids are free to vibrate independently and possibly introduce microphonic pickup especially with closed cycle coolers. They have significantly varying characteristics dependent on beam angle and should ideally be only used with nearly collimated beams. They require individual assembly making closely matched sets difficult to achieve.

These problems have been solved by using a solid polymer self-supporting filter without cavities. The filters are extremely durable and immune to all normal solvents. No mounting rings are required so array packing density is limited by the packing of cone and detector blocks. The thermal load of the devices is also considerably reduced. The U.V. sensitivity of the air-gap filters is due to the use of 1.5 μ m P.E.T. as the grid support medium whereas the solid polymer devices involve greater thickness of polymer. In this solid assembly, vibrations will cause all the grids to move in step and will not affect the filter characteristic. The use of a solid polymer will cause refraction of the beam towards the normal and reduce spectral problems caused by highly off-axis rays. These filters are made as a sheet of material with good uniformity across the sheet. The sheet can then be cut up to give a batch of closely matched devices or be used as a single large filter for an entire array. These filters now replace the air-gap models in most applications.

* Contact information for C.V. Haynes: Email: vic.haynes@astro.cf.ac.uk

SESSION 5- Bandpass and Blocking Filters

MANUFACTURE

The solid polymer filters are assembled as a stack of polypropylene sheets of accurately known thickness, some of which have photolithographically formed thin copper grids on them. This stack is placed in a precision platen press and is heated in a vacuum oven until equilibrium is reached. The vacuum oven is required to prevent entrapment of air and degradation of the polymer. The assembly is allowed to cool and then the filter is removed ready for a wide range of machining according to the application. The same general designs of grids as for air-gap filters are used though the actual recipes have to be changed due to the change of the refractive index between the grids. The tolerance of the grid spacing can be controlled to of the order of $0.1\mu\text{m}$, this is confirmed by the agreement between the model and the manufactured device. Filters can be made by this method with edges within better than 1% of the design. Reliable manufacture requires very close control of parameters.

PERFORMANCE MEASUREMENT

All devices are characterised using an evacuated Martin Puplett Fourier transform spectrometer. The instrument has a spectral resolution of 0.0625 cm^{-1} but the sampling beam is converging rapidly at $F/3$ so the observed sharpness of filter edges may be reduced. Figure 1 shows the typical characteristics for an edge filter.

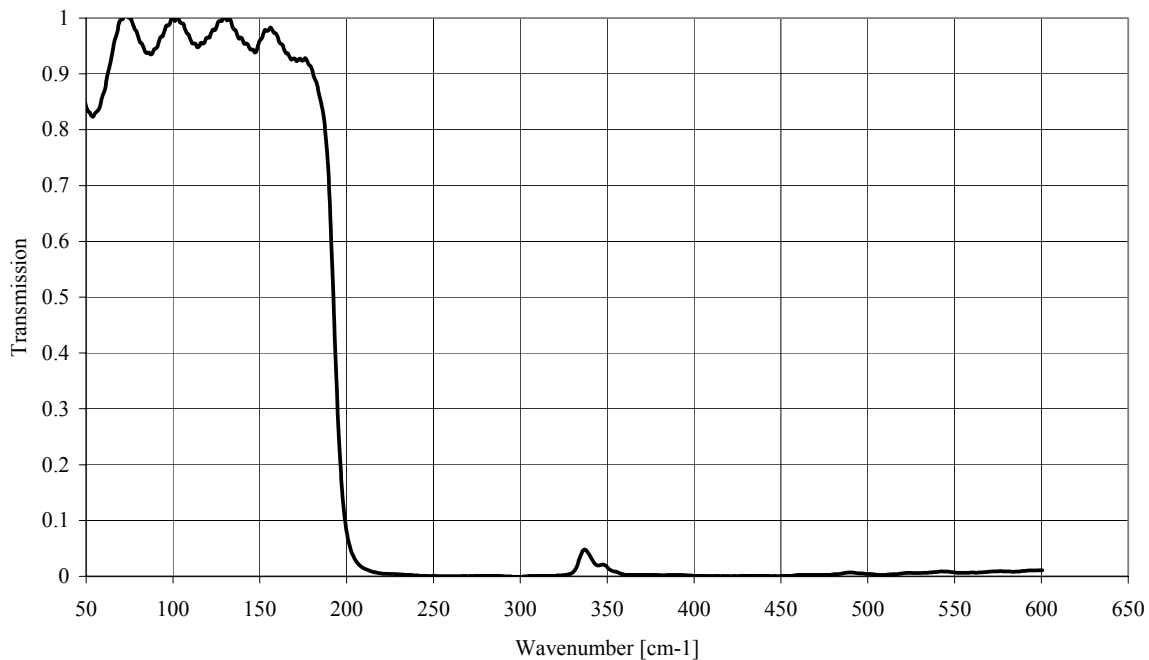


Figure 1: Transmission spectrum of 50 cm^{-1} solid polymer edge filter.

SESSION 5- Bandpass and Blocking Filters

Detector systems usually employ several filters in succession in order to manage thermal loading. Harmonic leaks at multiples of an edge frequency are characteristic of grid filters and are removed by ensuring that the leaks in successive filters do not coincide.

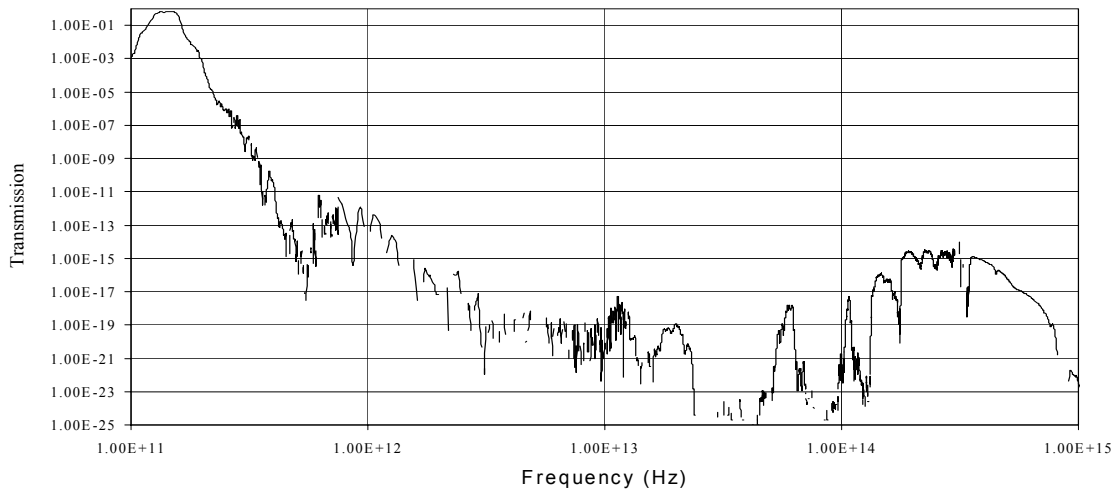


Figure 2: Transmission spectrum of a series of solid polymer edge filters with one bandpass filter.

THEORETICAL COMPARISON

All designs are produced by computer model, which can accurately predict the behaviour of the filters prior to manufacture. The computer program is based on a model⁽¹⁾⁽²⁾ where the grids correspond to lumped discrete electrical elements spaced on a transmission line. The discrete element values depend on the metallic grid geometric factors, which are modified by the optical properties of the polymer matrix. The distribution on the transmission line corresponds to the optical spacing between the grids. The polymer and metal may also modify the transmission due to absorption especially if they are in a resonant field. This model has been found to predict useful designs between 3cm^{-1} and 675cm^{-1} .

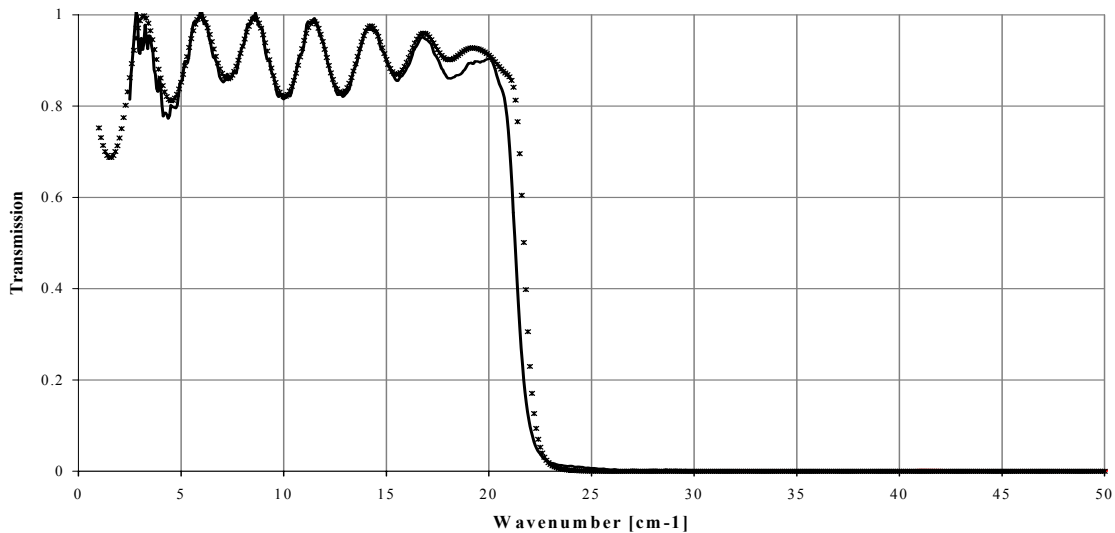


Figure 3: Transmission spectrum of 22 cm^{-1} solid polymer edge filter and model.

SOLID DIELECTRIC AND AIR-GAP FILTER COMPARISON

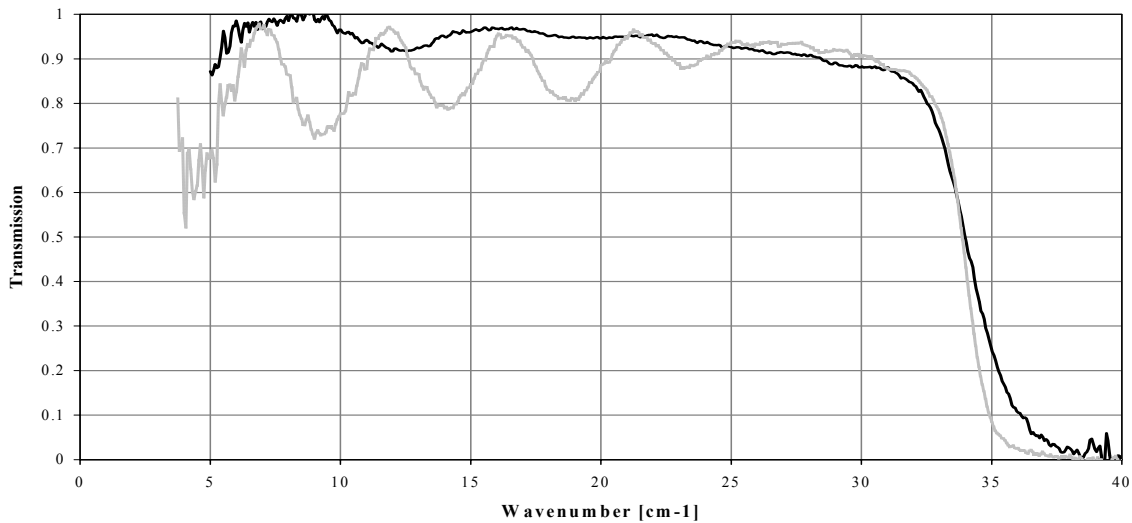


Figure 4: Transmission spectrum of 34 cm^{-1} solid polymer edge filter and air-gap filter.

Figure 4 shows that while the transmission band for the air gap filter reaches almost 100% that for the solid polymer is degraded by thickness fringing. This is not a problem for narrow band systems as design changes can move a fringe peak to coincide with the band. For broader band systems at wavelengths greater than $200\mu\text{m}$, a quarter wavelength 50% porosity P.T.F.E. ($R.I.=1.2$) layer has been found to be a suitable antireflection coating. This can be bonded to both surfaces of a filter using a similar technique to the filter manufacture. This coating has however been found to absorb short wavelength radiation and warm the filter leading to thermal emission. This problem was solved by producing an additional very thin thermal blocking solid grid filter which prevented the heating without reintroducing thickness fringing.

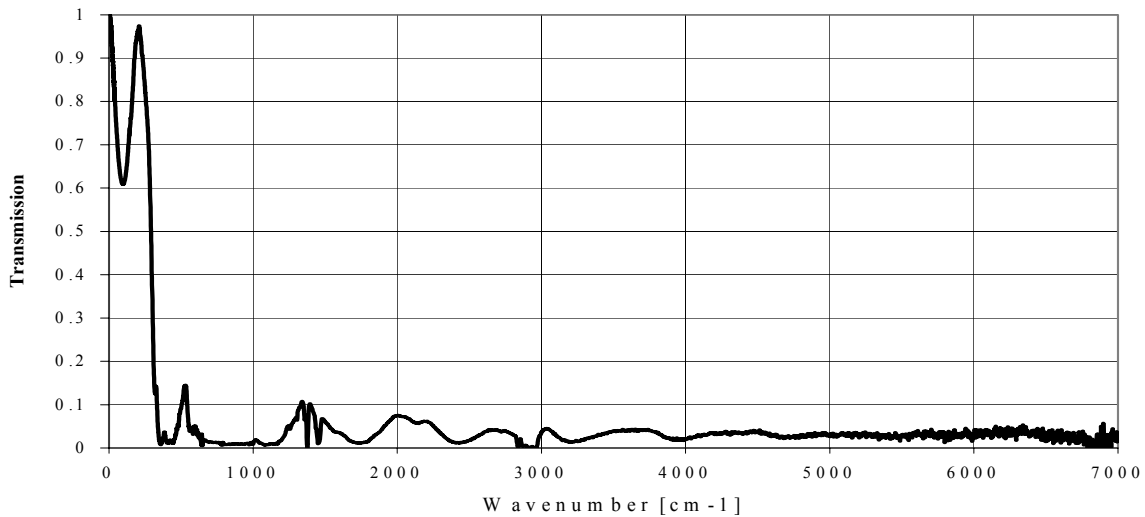


Figure 5: High frequency transmission spectrum of thermal blocking solid polymer grid filter.

SESSION 5- Bandpass and Blocking Filters

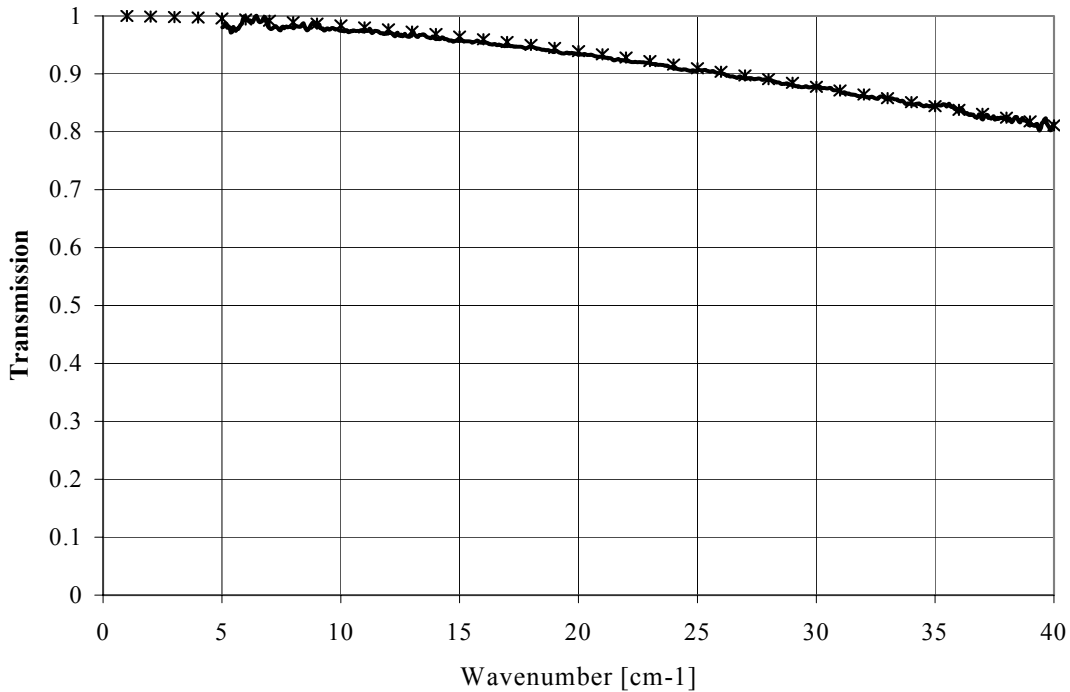


Figure 6: Low frequency transmission spectrum of thermal blocking solid polymer grid filter.

CONCLUSIONS

Grids embedded in solid polymer as filters can rival the performance of cavity spaced versions. The model program is sufficiently general to be able to model the solid filters. The advantages of the solid versions have led to them now replacing the cavity versions in most applications. Progress is being made towards larger diameters in order to fulfil the future needs of array detection systems. The lower frequency limit of this technology is probably set by the increasing device size in that limit though 1cm^{-1} may be achievable. To extend the upper frequency limit may require a change of matrix in order to avoid absorptions in the polymer, also the scale of the lithography will become submicron and require a change of technique.

REFERENCES

1. R. Ulrich: *Infrared Physics*, vol. 7, pp. 65-74, Pergamon Press Ltd. 1967.
2. N. Marcuvitz: *Waveguide Handbook*, Radiation Laboratory Series, McGraw-Hill Book Company, USA, 1951.

METAL MESH FILTERS FOR INFRARED APPLICATIONS

Oren Sternberg*, Jacqueline Fischer, Kenneth P. Stewart, Milton L. Rebbert
Naval Research Laboratory, Washington DC

Karl D. Möller, Haim Grebel
Electronic Imaging Center, New Jersey Institute of Technology, Newark, NJ

Howard Smith
Center for Astrophysics, Harvard Smithsonian, Cambridge, MA

Rainer Fetting
Institut f. Mikrostrukturtechnik, Forschungszentrum Karlsruhe, Germany

ABSTRACT

The transmittance peaks of inductive and capacitive metal meshes have been assigned to a number of modes and their interaction. Single thin meshes show resonance modes depending on the periodic structure of the mesh and slab modes when in touch with dielectric layers. Two and four meshes show stacking modes depending on separation similar to photonic crystals.

INTRODUCTION

Infrared filters play an integral role on every infrared astronomy airborne and/or space mission. They isolate the desired infrared signal from more energetic short wavelength radiation, allow color temperature measurements, provide order sorting for grating spectrometers, and improve the signal-to-noise for Fourier transform spectrometers. The need for such devices is critical now, as space astronomy in particular begins to emphasize far infrared research programs in the new millennium. At the same time, only in the past few years has the technology been available to design and fabricate these nanotechnology filters: the new computer codes, which have been used, are able to calculate precise electromagnetic solutions for filter designs, while modern nano-technology facilities are available for fabrication.

Metal mesh filters work on fundamentally different principles than multi-layer dielectric filters, and suffer none of the problems of dielectric coatings. By understanding the resonance behavior of metal-dielectric meshes as well as the various near field effects, one can further develop the design theory for these components and fabricate better and new devices. Among these are bandpass and low (or high) pass filters and dichroic or polarizing beamsplitters.

Metal Meshes

Inductive cross shaped metal meshes are made of thin metal foils with cross shaped openings. The inverse structure is called capacitive mesh. Babinet's principle in vector formulation states that complementary screens have complementary transmittance. This is shown in Figure 1 for inductive and capacitive free standing mesh. One observes a maximum for the inductive mesh and a minimum for capacitive mesh. The incident light excites a standing wave on the surface of the mesh, and transfers the incident energy into reflected and transmitted light¹.

* Contact information for Oren Sternberg Email: Oren.Sternberg@nrl.navy.mil , phone: 202-767-0043

SESSION 5- Bandpass and Blocking Filters

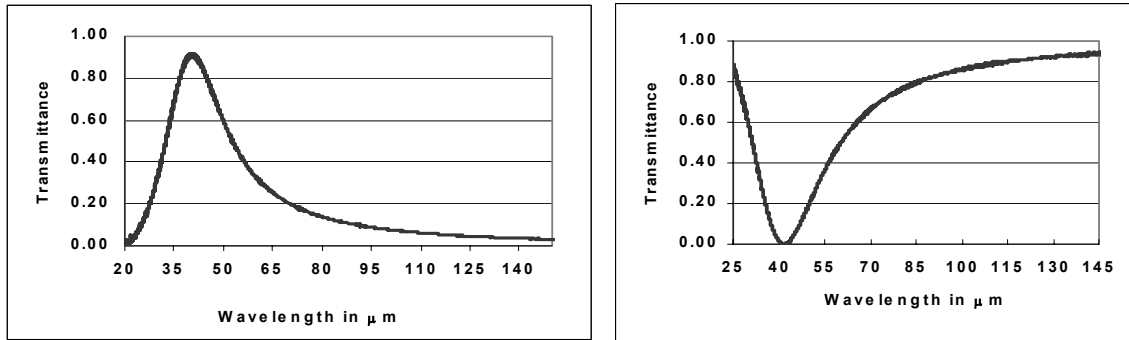


Figure 1: Transmittance through inductive (left) and capacitive (right) metal meshes (periodicity constant of $20\mu\text{m}$). The resonance wavelength is the same for thin complementary inductive and capacitive meshes

Resonance and Stacking Modes of Two Meshes at a Separation S

In Figure 2 we show two meshes at a separation S . The incident light excites resonance modes of wavelength λ_R . When changing the separation of the meshes from $S=0$ to larger values, a new mode shows up with wavelength λ_S . This “stacking mode” will also appear when more than two meshes are stacked up and have the same separation S . Depending on the separation S , the resonance mode and the stacking mode will interact in the same manner two oscillators do. Figure 3 shows that the “non crossing rule” is obeyed when the wavelength λ_S approaches the value of λ_R .²

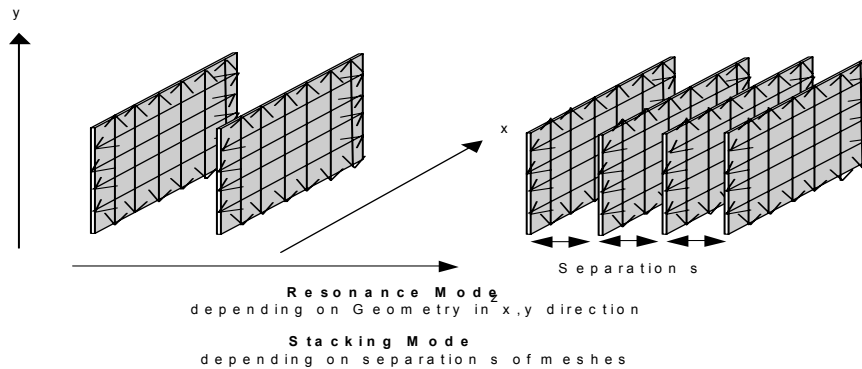


Figure 2: Two and four metal meshes at same separation S . There is the resonance mode of the single mesh and the Stacking Mode depending on the separation. Both modes interact when the stacking mode approaches the resonance mode

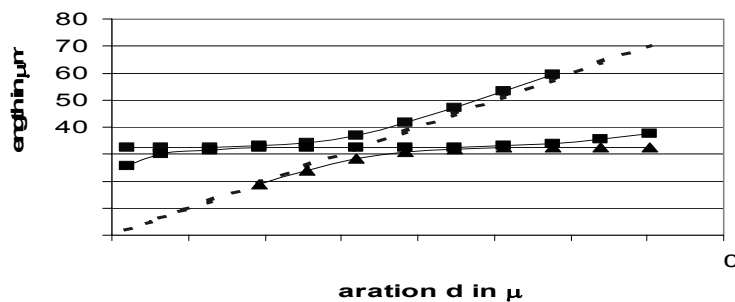


Figure 3: Interaction of resonance (squares) and Stacking Modes (triangles) for two meshes depending on separation S . The “non crossing rule” applies at about $\frac{1}{2}$ of the resonance wavelength

SESSION 5- Bandpass and Blocking Filters

Aligned Meshes and Photonic Crystals

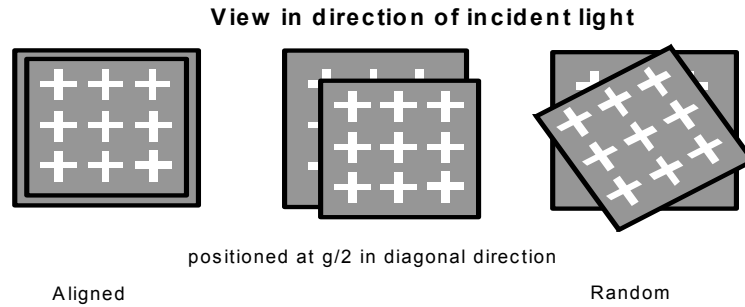


Figure 4: Schematics of positioning of two meshes: “aligned”, “non aligned/shifted”, and “random”

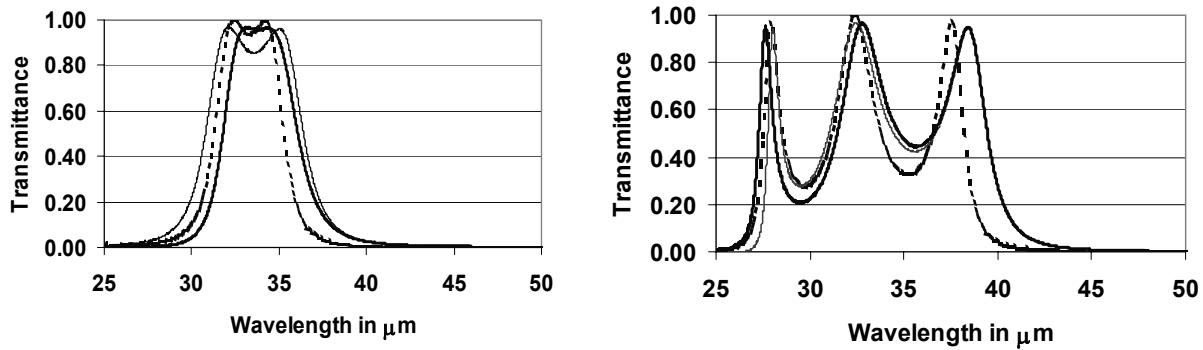


Figure.6: Two metal meshes at separation s . Single mesh: Resonance wavelength at $32.4\mu\text{m}$. Geometrical parameters: $g = 24\mu\text{m}$, $2a = 9.6\mu\text{m}$, $2b = 3.6\mu\text{m}$. Thickness $0.2\mu\text{m}$. Two meshes :Bold solid line: aligned. Solid line: shifted. Broken line: Random.

b) Separation at $1/4$ of resonance wavelength, Minimum interaction of resonance and stacking mode, only resonance modes are shown..

c) Separation at $1/2$ of resonance wavelength, Maximum interaction of resonance and stacking mode, resonance modes at longer and stacking mode at shortest wavelength.

Experimental and simulated results of metal mesh with dielectrics

The experimental results of metal meshes with dielectrics agree very well with simulated results, as seen in Figure 7. When a metal mesh is on top of a thick dielectric substrate the resonance peak length will shift by a factor ⁶ expressed below

$$0.5(n_1^2 + n_2^2)^{0.5} \quad (1)$$

However, when the thickness of the substrate is decreased the shift will be reduced. In Figure 7(a) we show a cross shaped mesh with a thin layer of polyimide. In Figure 7(b) we show a “hybrid” type metal mesh filter with a stucture of a few layers of inductive and capacitive meshes.³⁻⁶

SESSION 5- Bandpass and Blocking Filters

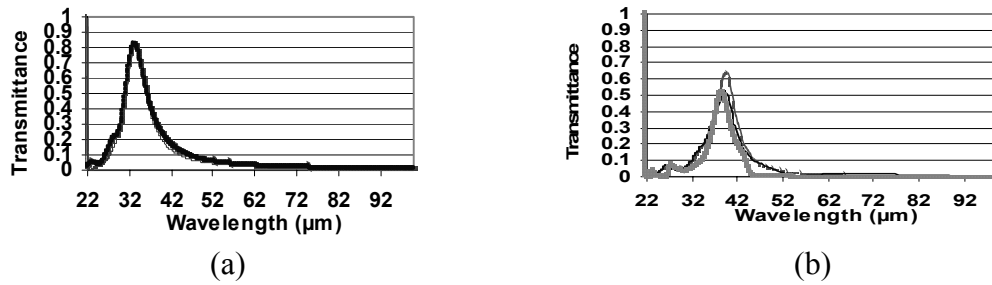


Figure 7: Metal mesh with dielectric. (a) cross shaped metal mesh with thin dielectric measurement bold line, simulated thin line. (b) 38μm filter mesh gray simulated, dark line 298K, light gray cold 5K. simulated.

Summary

The transmittance of two cross shaped metal mesh filters can be described by the interaction of resonance and stacking modes, with a near field effect apparent for small distances. At a spacing of $\lambda_R/4$, as expected from oscillator theory, two meshed filters show just one peak, indicating minimum interaction of the modes. Four layers of aligned meshes (photonic crystals) show a more square like shape of transmittance. The resonance wavelength and bandwidth of a single mesh in contact with dielectric layers, calculated with electromagnetic theory, shows a wavelength shift of the resonance to longer wavelength. The interpretation, using the oscillator model, is in simple terms: the incident light excites a compound mode of mesh and dielectric. This excited mode is composed of a standing wave with wave vector $k = 0$ and transfers the energy to the reflected and transmitted light. The stacking modes depend on the separation of the oscillators and have a wave vector parallel to the incident light. Simulations using electromagnetic theory, verified by experimental observations, show that filters with a width of 10-20% and 80-90% transmittance can be made in the Mid and Far IR wavelength region.

Acknowledgements

The research has been sponsored by the remote sensing division of Naval Research Laboratory. Some of this research has been performed while the O. Sternberg held a National Research Council Research associateship award at Naval Research Laboratory.

REFERENCES

1. O. Sternberg *Resonances of Periodic Metal-Dielectric Structures in the Infrared Wavelength Region*, Thesis Advisor: Dr. K.D Möller, 2002.
2. K. D. Möller, Oren Sternberg, Haim Grebel, and Kenneth P. Stewart, *Near-field effects in multilayer inductive metal meshes*, *Applied Optics*, 41, 1942-1948, 2002.
3. K. D. Möller, Oren Sternberg, Haim Grebel, and Kenneth P. Stewart *Inductive cross-shaped metal meshes and dielectrics*, *Applied Optics*, 41, 3919, 2002.
4. O. Sternberg, K.D. Möller, H. Grebel, K.P. Stewart, R.M. Henry, *Inductive Cross-Shaped Metal Meshes on Silicon Substrate*, *Journal of Infrared Physics*, 44, 17-25, 2003.
5. H. Smith, M. Rebbert, and O. Sternberg, *Designer infrared filters using stacked metal lattices*, *Applied Physics Letters*, 82, 21 3605-3607, 2003.
6. T. Timusk and P. L. Richards, *Near_Millimeter wave band-pass filters*, *Applied Optics*, 20, 1355-1360, 1981.
7. R. Ulrich, K.F. Renk, and L. Genzel, *Tunable submillimeter interferometers of the Fabry-Perot type*, *IEEE Trans. Micro-wave Theory Tech*, MTT-11, 363-371, 1963.
8. Micro-Stripes Program Ver 6.0, [Computer Software], (2002), Southborough, Massachusetts: Flomerics

NASA SPACE CRYOCOOLER PROGRAMS: A 2003 OVERVIEW

R.G. Ross, Jr.*

Jet Propulsion Laboratory, California Institute of Technology, Pasadena, CA 91109

R.F. Boyle

NASA Goddard Space Flight Center, Greenbelt, MD 20771

P. Kittel

NASA Ames Research Center, Moffett Field, CA 94035

ABSTRACT

Mechanical cryocoolers represent a significant enabling technology for NASA's Earth and Space Science missions. An overview is presented of ongoing cryocooler activities within NASA in support of current flight projects, near-term flight instruments, and long-term technology development. NASA programs in Earth and space science observe a wide range of phenomena, from crop dynamics to stellar birth. Many of the instruments require cryogenic refrigeration to improve dynamic range, extend wavelength coverage, and enable the use of advanced detectors. Although, the largest utilization of coolers over the last decade has been for instruments operating at medium to high cryogenic temperatures (55 to 150 K), reflecting the relative maturity of the technology at these temperatures, important new developments are now focusing at the lower temperature range from 4 to 20 K in support of studies of the origin of the universe and the search for planets around distant stars. NASA's development of a 20K cryocooler for the European Planck spacecraft and its new Advanced Cryocooler Technology Development Program (ACTDP) for 6-18 K coolers are examples of the thrust to provide low temperature cooling for this class of missions.

COOLERS ON NEAR-TERM EARTH AND SPACE SCIENCE MISSIONS

In spring 2002 three new cryocooler systems were launched into space to support NASA missions. Two of the three were based at least partially on the Oxford cooler technology that first flew on the Improved Stratospheric and Mesospheric Sounder (ISAMS) instrument in 1991; this type of cooler has demonstrated multi-year lifetime in orbit, and has been adopted by many long-life instruments to enable new and improved science. The third cooler, the NICMOS cooler, was the first space application of a long-life turbo-Brayton cooler.

These recently launched coolers, which are reviewed below, have each now achieved over a year of successful operation in space, adding to the growing number of long-life space coolers enabling the acquisition of important new space-science data. These recent applications build upon the coolers of earlier NASA missions, such as those on the MOPITT, ASTER and Hyperion instruments that have achieved over two years of space operation at this point.² Additional coolers, such as the Northrup Grumman (TRW) pulse tube coolers on the TES instrument and the Ball Aerospace Stirling cooler on the HIRDLS instrument, are in the queue for launch aboard NASA missions in early 2004 and are also described below.

RHESSI Gamma-Ray Spectrometer

Launched in February 2002, the Ramaty High-Energy Solar Spectroscopic Imager (RHESSI) uses an array of nine large germanium gamma-ray detectors to observe solar flares from 3 keV to 25 GeV. The detector

* Contact information for R. G. Ross Jr. – Email: Ronald.G.Ross-Jr@jpl.nasa.gov

SESSION 6- Cooling Systems



Figure 1: Sunpower M77B Stirling cryocooler mounted on RHessi cutaway radiator structure.



Figure 2: The flight NICMOS Cooling System mounted on temporary structure during buildup.

array is cooled to 75 K by a Sunpower M77B Stirling cooler (Fig. 1) running at 65 K.^{3,4} This mission represents the first application of a low-cost commercial cooler to achieve multi-year operation in space.

Additionally, the cooler uses a heat intercept strap clamped to the Stirling coldfinger to provide simultaneous cooling to the instrument's higher temperature radiation shields at 155 K. This technique thus provides the capability of a two-stage cooler with an off-the-shelf single-stage cooler. Since launch, the cooler has maintained the gamma-ray detectors at their required 75K temperature, with a goal of up to two years on orbit.⁵

NICMOS Cooling System

The Creare NICMOS Cooling System (NCS) was designed to cool the Near Infrared Camera and Multi-Object Spectrometer (NICMOS) instrument of the Hubble Space Telescope. It was successfully launched and integrated into the Hubble Space Telescope during the HST's fourth servicing mission (SM3B) in March 2002.⁶ This followed an earlier flight test of the entire cooling system aboard a week-long Shuttle mission in October 1998.⁷ The NCS, shown in Fig. 2, is a large turbo-Brayton cooler with a nominal cooling capacity of 7 W at 80 K with 400 W input power. The NICMOS instrument was originally launched in 1997 using a solid Nitrogen dewar to cool its sensitive infrared focal plane. However, after a dewar failure led to a shorter than expected on-orbit life, the NCS was identified as a way to extend the mission and recover the original science objectives. Thus, the NCS was developed to be retrofitted to the NICMOS instrument during a subsequent HST servicing mission in space.

The NCS is designed to maintain the instrument's detectors in the range of 75-85K by circulating refrigerated neon gas through the NICMOS dewar's existing liquid helium freeze lines. The very large (7 W at 80 K) heat load is associated with the inefficiencies of using existing in-space Bayonet couplings on the NICMOS dewar to connect with the gas lines.

To date, the system has performed flawlessly and the NICMOS instrument has been returned to its job of gathering infrared images of the far reaches of space.

Atmospheric Infrared Sounder (AIRS) instrument

JPL's Atmospheric Infrared Sounder (AIRS) instrument was launched in May 2002 on NASA's Earth Observing System Aqua platform. Its mission is to measure the atmospheric air temperature using a HgCdTe focal plane cooled to 58 K by a redundant pair of 55 K TRW pulse tube coolers.^{8,9} The instrument was designed and built under JPL contract by Lockheed Martin Infrared Imaging Systems, Inc. (now BAE Systems IR Imaging Systems) of Lexington, MA.

Initiated in 1994, the cryocooler development effort was the first space application to select a pulse tube cryocooler. The highly collaborative development effort, involving cryocooler development at TRW and extensive cryocooler testing at JPL and Lockheed Martin, has served as the pathfinder for much of the pulse tube development to date. The AIRS flight pulse tube coolers, shown in Fig. 3, were originally

SESSION 6- Cooling Systems

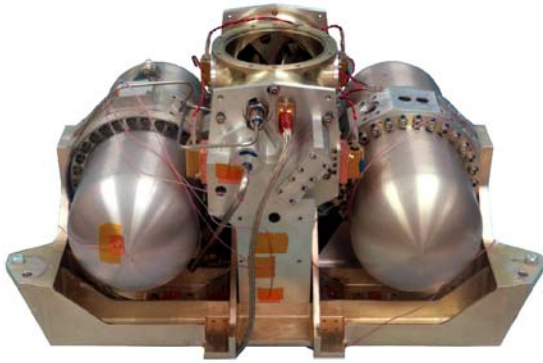


Figure 3: AIRS cooler system.



Figure 4: TES cooler system.

delivered to JPL for testing in October 1997, and completed spacecraft-level testing in September 2001. Since being launched in May 2002 the coolers have been performing flawlessly.¹⁰

TES Cooler Development

The EOS Tropospheric Emission Spectrometer (TES) instrument is the next large JPL cryogenic instrument. TES is an infrared instrument designed to measure the state of the earth's troposphere. It is scheduled for launch into polar orbit aboard NASA's third earth observing systems spacecraft (EOS-Aura) early in 2004.

TES uses two 57 K coolers to cool two separate focal planes to 62 K. The two coolers are identical and are a variant of the TRW AIRS pulse tube cooler, but configured with the pulse tube hard mounted to the compressor.^{11,12} The coolers were fabricated by NGST (formerly TRW) under contract to JPL, and have recently completed system-level testing on the Aura spacecraft in preparation for launch.

HIRDLS Cooler Development

On the same spacecraft as the TES instrument, the High Resolution Dynamics Limb Sounder (HIRDLS) instrument uses a single-stage Stirling cryocooler manufactured by Ball Aerospace under contract to Lockheed Martin. The HIRDLS cooler, which provides 720 mW at 55 K for an infrared array covering 21 bands between 6-17 μ m, uses technology developed under a number of NASA and DoD contracts.¹³ It incorporates radial position sensors for establishing and monitoring the clearance seals in the cooler, prior to closeout of the housing. It is similar in design to a two-stage 30 K cooler delivered to GSFC in 1997, and life tested to 13,000 hours.

AMS-2 Charged-Particle Spectrometer

A set of four Sunpower M87 coolers has been baselined to fly on the Alpha Magnetic Spectrometer-2 (AMS-2) mission in October 2004. The instrument, mounted on the International Space Station, will use a large superconducting magnet assembly in a search for antimatter nuclei from cosmic sources. The coolers will be used to intercept heat at the outer thermal shield on a 2500 liter helium tank. With a mass of over 2000 kg for the superconducting magnets and helium tank, it is extremely challenging to provide enough thermal isolation to allow a 3-year lifetime, even with the coolers operating at nominal power. The four coolers, each capable of 6-7 W of heat lift at 77 K, will be run at reduced power to provide a total of 20-25 W of cooling on the shield at 77 K. The coolers, operating in the stray field of the magnet system, will be specially qualified for operation in a magnetic field of 750-1000 gauss.

Planck Cooler Development

As a precursor to the US low-temperature cryocooler missions, JPL is presently working on the development of a 1 W at 18-20 K hydrogen sorption cryocooler for the Planck mission of the European Space Agency. The objective of the Planck mission is to produce very high resolution mapping of temperature anisotropy in the cosmic microwave background (CMB) radiation. Planck's Low Frequency Instrument (LFI) will have an array of tuned radio receivers to detect radiation in the range 30-100 GHz. These receivers will be operated at a temperature of about 20 K. The High Frequency Instrument (HFI) will use bolometers operated at 0.1 K for frequencies from 100 GHz to 900 GHz.

SESSION 6- Cooling Systems

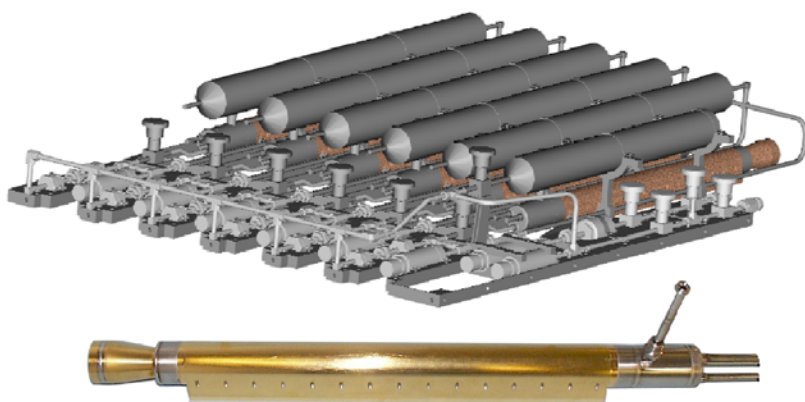


Figure 5: 20K Planck sorption compressor system (top) and fabricated compressor element (bottom).

The redundant hydrogen sorption cryocoolers are being designed to cool the LFI detectors to 18 - 20 K and to precool the Rutherford Appleton Lab (RAL) 4 K helium J-T that cools the 0.1 K dilution refrigerators in the HFI cooling system. A successful test of the breadboard Planck sorption cooler was conducted in February 2002,¹⁴ following significant development of the refrigerators compressor elements.¹⁵ The flight coolers are currently in fabrication, with the first qualification/flight unit scheduled for delivery and instrument integration in early 2004, followed by the second flight unit a year later.

Other Applications

Another NASA application for space cryocoolers is in propulsion systems. NASA's Glenn Research Center and Ames Research Center are studying the use of cryocoolers to enable zero-boiloff storage of cryogenic propellants in space flight systems.^{16,17} At the Johnson Space Center, the Variable Specific Impulse Magnetoplasma Rocket (VASIMR) project is designing a system that will use high-temperature superconducting coils for plasma containment and acceleration.¹⁸

CRYOCOOLER DEVELOPMENT FOR FUTURE NASA MISSIONS

Over the years, NASA has collaborated with the US Air Force to develop new cryocooler technologies for future space missions. Recent achievements include the NCS, AIRS, TES and HIRDLS cryocoolers described previously, and new smaller pulse tube coolers at NGST/TRW¹⁹⁻²¹ and Lockheed Martin.^{22,23} The largest technology push within NASA right now is in the temperature range of 4-10 K. Missions such as the James Webb Space Telescope (JWST) and Terrestrial Planet Finder (TPF) plan to use infrared detectors operating between 6-8 K, typically arsenic-doped silicon arrays, with telescopes of greater than 5 m diameter. Other missions use bolometers and X-ray microcalorimeters operating as low as 50 mK.

Advanced Cryocooler Technology Development Program

To develop the needed cryocooler technology for this mission set NASA initiated the Advanced Cryocooler Technology Development Program (ACTDP) in 2002 under the leadership of JPL and in collaboration with the NASA Goddard Space Flight Center.²⁴ In 2002, four contractors conducted initial study-phase contracts to develop preliminary cryocooler designs capable of providing cooling in the 6-20 K temperature range. Following the study phase, three of the cooler concepts were selected to proceed into Engineering model development. The three contractors include Ball Aerospace & Technologies Corp., Lockheed Martin ATC, and Northrup Grumman Space Technology. The three concepts being pursued by these contractors are illustrated in Fig. 6 and summarized below:

Ball ACTDP Cryocooler Concept. Ball Aerospace's ACTDP cryocooler concept utilizes a multistage Stirling refrigerator to precool a J-T loop powered by a linear-motion Oxford-style compressor. The J-T loop provides remote cooling of the 6 K and 18 K loads and isolates the loads from compressor-generated vibration and EMI; the compressor elements are easily separated by over 10 meters from the cryogenic

SESSION 6- Cooling Systems

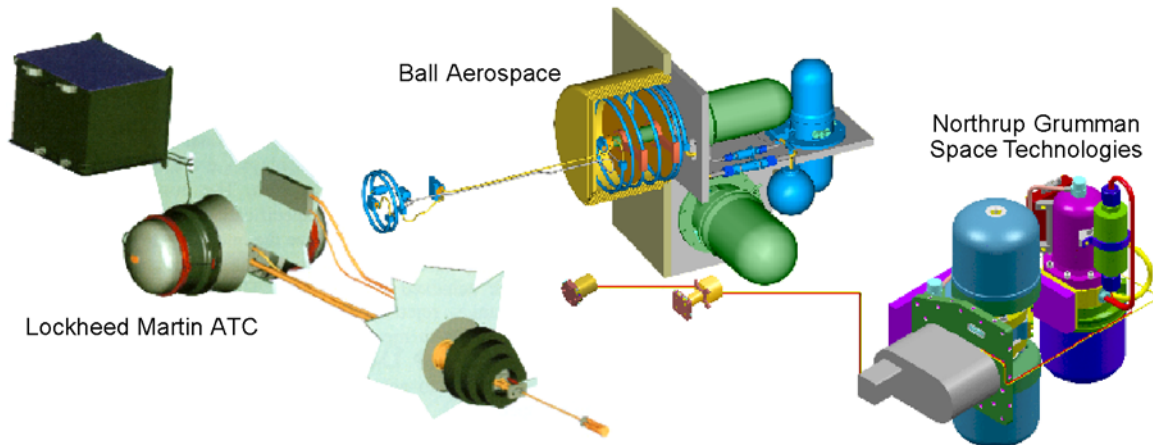


Figure 6. ACTDP Cryocooler Concepts.

loads. The multistage refrigerator is based on leveraging existing Ball flight-quality Stirling compressors, J-T cold-end technology, and drive electronics; these technologies are configured and adapted to meet the specific needs of the ACTDP mission requirements.

NGST ACTDP Cryocooler Concept. The Northrup Grumman Space Technology (NGST) concept is similar to the Ball Aerospace ACTDP concept in that it uses a combined 6K/18K J-T loop to provide the remote cooling of the 6 K and 18 K loads, thus isolating the loads from any compressor-generated vibration and EMI. However, the NGST concept utilizes a multistage pulse tube refrigerator for precooling the J-T loop. The multistage refrigerator is powered by linear-motion Oxford-style compressors and is based on leveraging existing NGST/TRW flight-quality pulse tube compressors and drive electronics, and developmental J-T cold-end technology. These components are configured and adapted to meet the specific needs of the ACTDP cooler requirements.

Lockheed Martin ACTDP Cryocooler Concept. Lockheed Martin's ACTDP cryocooler concept utilizes a multistage all-pulse-tube refrigerator to directly cool the 6 K and 18 K loads. Though not compatible with highly remote coldloads, this concept has the potential for improved reliability with fewer drive motors and less complex electronics. The single-unit multistage refrigerator leverages existing Lockheed flight-quality pulse-tube compressors, cold heads, and drive electronics, and laboratory pulse tube technology²⁵ that has demonstrated direct cooling down to ~5K; these are being configured and adapted to meet the specific needs of the ACTDP mission requirements.

Basic Research in Support of Low Temperature Refrigeration

To support the development work on 4-20 K cryocoolers, NASA ARC is exploring new rare earth alloys that hold the promise of significantly improving cryocooler efficiency. For example, modeling of a pulse tube cooler using either Er_3Ni or layers of some new materials shows that using random wires of the new materials results in a 2.8x higher efficiency than Er_3Ni powders. Similarly, substituting a new material for lead spheres in the second stage predicts an additional 1.37x improvement. Thus, a cooler making use of the new materials would require 4x less power from the spacecraft and would reject 1/4 of the heat. The newer materials also offer advantages in terms of cost, manufacturability, and long-term reliability. In particular, the new materials neither fracture, as Er_3Ni does, nor flow, as Pb does, under the repeated pressure and temperature oscillations that occur within cryocooler regenerators. In a cooler operating at 40 Hz, the pressure gradient in the regenerator reverses 4×10^8 times over a 10-year period.

SUMMARY

Cryocoolers are increasingly being adopted for usage in NASA science instruments, with a total of 10 cryocoolers launched into orbit over the past 10 years, and several more scheduled for the next few years. With flight cryocoolers widely available for the 30 K to 150 K temperature range, NASA-funded

SESSION 6- Cooling Systems

technology development is now focusing primarily on coolers in the 4-20 K temperature range, and on coolers for special applications such as storage of cryogenic propellants in space.

ACKNOWLEDGMENT

The work described in this paper was carried out by NASA Centers and contractors including the Jet Propulsion Laboratory, California Institute of Technology, NASA Goddard Space Flight Center; and NASA Ames Research Center; it was sponsored by the National Aeronautics and Space Administration.

REFERENCES

1. R.G. Ross, Jr., *JPL Cryocooler Development and Test Program: A 10-year Overview*, Proceedings of the 1999 IEEE Aerospace Conference, Snowmass, Colorado, Cat. No. 99TH8403C, ISBN 0-7803-5427-3, IEEE, New York, pp. 115-124, 1999.
2. R. Boyle and R.G. Ross, Jr., *Overview of NASA Space Cryocooler Programs*, Adv. in Cryogenic Engin., Vol 47B, Amer. Inst. of Physics, New York, pp. 1037-1044, 2002.
3. R. Boyle, S. Banks, P. Cleveland and P. Turin, *Design and Performance of the HESSI Cryostat*, Cryogenics 39 (12), pp. 969-973, 1999.
4. R. Boyle et al., *Cryocoolers for the HESSI Spectrometer: Final Report of the Cryocooler Tiger Team*, Internal Document, Goddard Space Flight Center, 2001.
5. R. Boyle, S. Banks and K. Shirey, *Final Qualification and Early On-Orbit Performance of the RHESSI Cryocooler*, Cryocoolers 12, Kluwer Academic/Plenum Publishers, New York, 2003.
6. W.L. Swift, F.X. Dolan and J.J. Breedlove, *Initial Operation of the NICMOS Cryocooler on the Hubble Space Telescope*, Cryocoolers 12, Kluwer Academic/Plenum Publishers, New York, 2003.
7. W.L. Swift et al., *Flight Test Results for the NICMOS Cryocooler*, Adv. in Cryogenic Engineering, Vol 45A, Kluwer Academic/Plenum Publishers, NY, pp. 481-488, 2000.
8. R.G. Ross, Jr. and K. Green, *AIRS Cryocooler System Design and Development*, Cryocoolers 9, Plenum Publishing Corp., New York, pp. 885-894, 1997.
9. R.G. Ross, Jr. et al., *AIRS PFM Pulse Tube Cooler System-level Performance*, Cryocoolers 10, Plenum Publishing Corp., New York, pp. 119-128, 1999.
10. R.G. Ross, Jr., *AIRS Pulse Tube Cooler System Level Performance and In-Space Performance Comparison*, Cryocoolers 12, Kluwer Academic/Plenum Publishers, New York pp. 747-754, 2003.
11. J. Raab et al., *TES FPC Flight Pulse Tube Cooler System*, Cryocoolers 11, Kluwer Academic/Plenum Publishers, New York, pp. 131-138, 2001.
12. S.A. Collins, J.I. Rodriguez and R.G. Ross, Jr., *TES Cryocooler System Design and Development*, Adv. in Cryogenic Engin., Vol 47B, Amer. Inst. of Physics, New York, pp. 1053-1060, 2002.
13. W.C. Kiehl et al., *HIRDLS Instrument Flight Cryocooler Subsystem Integration and Acceptance Testing*, Cryocoolers 11, Kluwer Academic/Plenum Publishers, New York, pp. 769-774, 2001.
14. D. Pearson et al., *Test Performance of a Closed Cycle Continuous Hydrogen Sorption Cryocooler*, Cryocoolers 12, Kluwer Academic/Plenum Publishers, New York, 2003.
15. R.C. Bowman, Jr. et al., *Evaluation of Hydride Compressor Elements for the Planck Sorption Cryocooler*, Cryocoolers 12, Kluwer Academic/Plenum Publishers, New York, 2003.
16. L. Hastings et al., *An Overview of NASA Efforts on Zero Boil-off Storage of Cryogenic Propellants*, to be presented at 2001 Space Cryogenics Workshop, Milwaukee, WI, 2001.
17. A. Hedayat et al., *Large Scale Demonstration of Liquid Hydrogen Storage with Zero Boiloff*, Adv. in Cryogenic Engin., Vol. 47B, Amer. Institute of Physics, Melville, NY, pp. 1276-1283, 2002.
18. F. R. Chang Díaz, *Research Status of The Variable Specific Impulse Magnetoplasma Rocket*, Fusion Technology 35, 1999, pp. 87-93.
19. C.K. Chan, R.G. Ross, Jr. et al., *IMAS Pulse Tube Cooler Development and Testing*, Cryocoolers 10, Plenum Publishing Corp., New York, pp. 139-147, 1999.
20. J. Raab et al., *Jami Flight Pulse Tube Cooler System*, Cryocoolers 12, Kluwer Academic/Plenum Publishers, New York, pp. 191-197, 2003.

SESSION 6- Cooling Systems

21. L.J. Salerno et al., *Performance Testing of a Lightweight, High Efficiency Cooler*, Cryocoolers 12, Kluwer Academic/Plenum Publishers, New York, pp. 199-204, 2003.
22. R.G. Ross Jr. et al., *Gamma-Ray Pulse Tube Cooler Development and Testing*, Cryocoolers 11, Kluwer Academic/Plenum Publishers, New York, pp. 155-162, 2001.
23. T.C. Nast et al., *Miniature Pulse Tube Cryocooler for Space Applications*, Cryocoolers 11, Kluwer Academic/Plenum Publishers, New York, pp. 145-154, 2001.
24. R.G. Ross Jr., R.F. Boyle, R.W. Key and D.R. Coulter, *NASA Advanced Cryocooler Technology Development Program*, Proceedings of the International Society of Optical Engineering (SPIE) Conference, Waikoloa, Hawaii, August 22-28, 2002.
25. J. Olson, T. Nast and B. Evtimov, *Development of a 10 K Pulse Tube Cryocooler for Space Applications*, Cryocoolers 12, Kluwer Academic/Plenum Publishers, New York, pp. 241-246, 2003.

SESSION 6- Cooling Systems

Sunpower Cooling Solutions

Douglas E. Keiter¹
Sunpower, Inc., Athens, OH 45701, USA

Kyle B. Wilson
Sunpower, Inc., Athens, OH 45701, USA

ABSTRACT

Sunpower specializes in free-piston Stirling engines and cryocoolers, pulse tube cryocoolers, and free-piston linear compressors. Sunpower offers four different Stirling cryocoolers to meet varying performance, environmental and cost targets. All of Sunpower's cryocoolers are hermetically sealed, contain no HCFC's, and are designed for high performance with maintenance-free, long-life operation. Sunpower is also developing pulse tube cryocoolers as another option for cooling solutions. Single and multi-stage pulse tube cryocoolers are currently at the laboratory prototype level. Figure 1 shows the thermodynamic performance of each cryocooler discussed in this paper.

M77

The M77 is the first cryocooler designed and built by Sunpower. The first M77 was delivered to a commercial customer in 1992. At a price of approximately \$40,000, the M77 is a low-cost cryocooler for clients such as NASA and other government and university laboratories. Sunpower has delivered about 100 M77s since 1992, and one M77 at Sunpower has run continuously over 18,000 hours.

The M77, not designed for mass production, is assembled in small quantities and is designed to lift 4W at 77K with 100W of input power. The M77 was space qualified by NASA and is currently flying on the RHESSI solar flare mission. The original schedule called for the Sunpower M77 to remain in space for less than six months. As of June 2003, RHESSI has been operational for 16 months.

M87

A company specializing in medical products approached Sunpower for the design and production of a long-life, commercially-priced cryocooler. The result, the M87, was an M77 offshoot redesigned for cost-reduction and manufacturability. In parallel to the development of the M87, Sunpower established a modern production facility currently capable of producing 500 cryocoolers per month, extendable to 2,000/month with modest additional investment. This facility is also capable of producing each of the models discussed here.

The M87 is designed for use in climate-controlled environments, providing 7.5W of cooling at 77K with 150W of input power. Sunpower has built approximately 180 M87s since 2000. One hundred of the current version of the design have accumulated 330,000 hours of run time since January 2001.

CryoTel^{CT}

At the end of 2000, Sunpower and linear compressor development partner LG Electronics identified a potential need in the telecommunications industry for a small, efficient, low-cost cryocooler. The two companies formed a strategic alliance with the primary goal of developing this product. The strategic alliance planned to capitalize on Sunpower's history of free piston Stirling cryocooler research and development and LGE's experience in large scale manufacturing of low-cost white goods. The outcome of the strategic alliance was the CryoTel^{CT}, which is based on the M87 but can provide 10W of cooling at 77K with 155W of input power.

¹ Contact information for D.E. Keiter: Email: keiter@sunpower.com

SESSION 6- Cooling Systems

The environmental operating range of the CryoTel^{CT} was extended to meet the needs of the telecommunications industry and can operate in ambient temperatures between -40°C and +60°C. The CryoTel^{CT} was also designed to be able to operate in any physical orientation without affecting cooling performance or reliability.

Sunpower has built more than 100 CryoTel^{CT} units since 2002. The design is ready for pilot production in the Sunpower manufacturing facility. The CryoTel^{CT} is designed to have a minimum operating life of five years. The next focus will be to implement an accelerated life test to establish the Mean Time To Failure (MTTF) and uncover any potential reliability issues with the CryoTel^{CT}. Due to the increased performance and low cost, the CryoTel^{CT} may eventually replace both the M77 and the M87.

CryoTel^{MT}

The CryoTel^{MT}, a smaller version of the CryoTel^{CT}, is the newest cryocooler model from Sunpower. The CryoTel^{MT} can operate across the same range of ambient temperatures as the CryoTel^{CT} and can lift 6W at 77K with 100W of input power. A manufacturing test run of the CryoTel^{MT} is currently underway and will be completed during the summer of 2003. The CryoTel^{MT} has the same efficiency and reliability expectations as the CryoTel^{CT}.

Pulse Tube

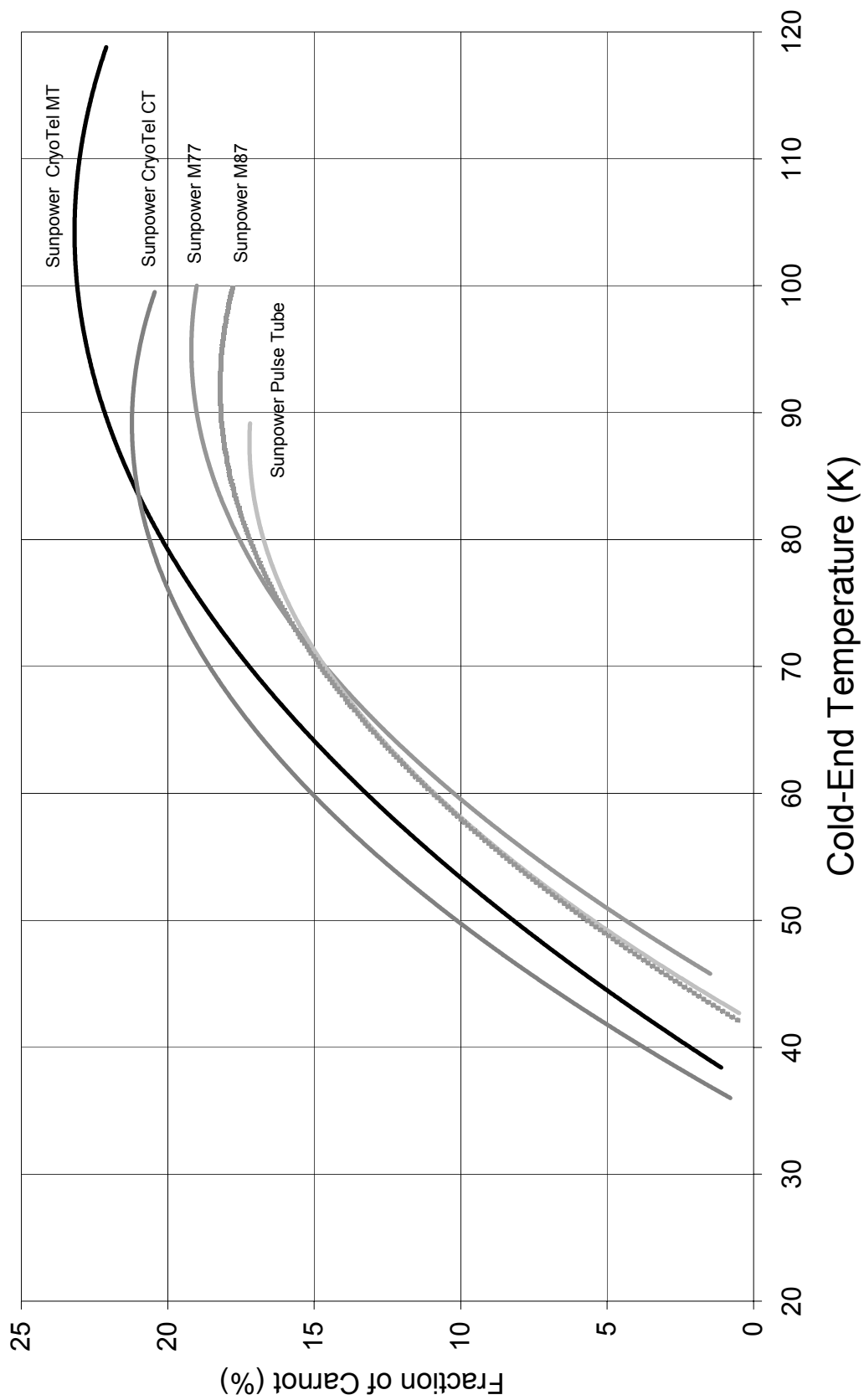
In addition to the line of Stirling coolers produced by Sunpower, single and multi-stage pulse tube cryocoolers (PTCs) are also under development as potential Sunpower products. The funding for PTC development came largely from Small Business Innovative Research (SBIR) funding from NASA Goddard Space Flight Center. In pursuit of this work, Sunpower partnered with David Gedeon of Gedeon Associates for his expertise in modeling and analysis of PTCs. Gedeon is the author of the commercial modeling software Sage and Sunpower is an industry leader in the design and production, including manufacture, of linear compressors. This combination of expertise in linear compressors and PTC analysis led to the successful development of one single-stage PTC prototype and one two-stage PTC prototype.

Sunpower constructed both inline and u-tube configurations of the single-stage PTC. The u-tube configuration allows for more convenient packaging of the cooler and easier addition of multiple stages. The inline cooler was integrated, meaning the cold head was attached directly to the compressor. In the u-tube and two-stage configurations, the cold head was separated from the compressor by a connecting tube. These design features are flexible depending on the requirements of the customer. Acoustic tuning in all configurations was accomplished by an inertance assembly rather than an orifice or double inlet PTC. As part of the development program, a cost study of the single-stage u-tube configuration was performed. This study showed that the cost of the components was very similar to the cost of components in the Sunpower M87 Stirling cooler. Depending on the cost of assembly and processing, this information suggests that the single-stage PTC should be cost competitive with Sunpower's line of Stirling coolers in production volumes.

Technical advancements under internal funding from Sunpower have actually boosted the performance achieved at the end of the SBIR development program by 25%. The single-stage inline PTC is currently capable of 6W of lift at 77K with 100W input power. The two-stage prototype achieved 260 mW of cooling at 30K, with 100W input power and the first stage unloaded at 80K. The single and two-stage pulse tube technologies at Sunpower are ready to take the next step toward commercial development. Sunpower is currently seeking funding for such development.

Currently, under additional NASA Phase II SBIR funding Sunpower is building a prototype three-stage PTC for cooling below 10K. The program will end in January 2004. Initial performance of the three-stage PTC will be presented at the CEC/ICMC conference to be held in Anchorage, Alaska in September 2003. The three-stage PTC also promises potential for a commercial product at Sunpower.

SESSION 6- Cooling Systems



INTEGRATION OF OXFORD CLASS CRYOCOOLERS WITH THERMAL DETECTORS

Carl S. Kirkconnell* and Kenneth D. Price
Raytheon Company, PO Box 902, MS E1/D102, El Segundo, CA 90245, USA

ABSTRACT

Mechanical cryocoolers are generally preferable to stored cryogen dewar systems for space applications because they are more than an order of magnitude smaller in size and lighter in weight. Successful flight qualification, endurance testing, and on orbit performance of mechanical cryocoolers over the past ten years have made the use of cryocoolers viable from a lifetime and system reliability perspective. However, the size and weight advantage is partially offset by the introduction of operational vibrations, the possibility of temperature fluctuations at the cooler mounting interface and cold tip, and power draw on the spacecraft bus. The first two can directly affect detector performance. These inherent technical challenges are met through the combination of cryocooler-level and system-level design features and accommodation. For example, adaptive feed forward (AFF) active vibration control provided by the cryocooler control electronics significantly reduces vibration output at the cold tip. Using a flexible thermal strap to connect the detector to the cold tip further attenuates vibrations transmitted from cold tip to detector. Unfortunately, thermal strap efficiency and mechanical strap compliance react in opposite directions with respect to strap cross-sectional area, so a system-level design optimum must be found. Lower cryocooler vibration output and/or higher cryocooler efficiency facilitate the identification of an optimum strap design that meets the detector thermal and jitter requirements. The pages that follow discuss these and other examples of system-level issues that arise in the integration of Stirling-cycle, Oxford-class cryocoolers, and more importantly, how those challenges can be overcome.

INTRODUCTION

The common design objectives of virtually any space cryocooler include long life, high reliability, and high efficiency. Long life and high reliability are essential because, in general, on-orbit service and replacement of deployed systems is not possible. Efficiency is important because cryocooler power consumption adversely impacts multiple spacecraft subsystems. First, the requirements on the spacecraft power system (batteries and solar panels) increase as cryocooler efficiency decreases. Second, all of the input power to the cryocooler must eventually be rejected from the spacecraft radiatively to space. Thus the spacecraft radiator size and weight increase as cryocooler input power increases.

The so-called "Oxford class" cryocooler has emerged as a widely applicable solution to these lifetime, reliability, and efficiency requirements¹. The Oxford class cryocooler is characterized by the following:

- Separate expander and compressor modules;
- Linear drive motors;
- Flexure suspended pistons;
- Non-contacting clearance seals;
- Hermetically sealed housings.

Later improvements to the basic Oxford class cryocooler have been incorporated to minimize the vibration output of the machines²:

- Piston position control systems;
- Drive axis vibration control systems.

* Contact information for C. S. Kirkconnell- Email: carl_s_kirkconnell@raytheon.com

SESSION 6- Cooling Systems

Though the original Oxford cryocooler was a Stirling, the term “Oxford-class” is nowadays commonly taken to include both Stirling and pulse tube cryocoolers that utilize the flexure suspended, non-contacting pistons for the moving mechanisms, which in the case of the pulse tube includes only the compressor.

The stated design objectives of high reliability and long life have been demonstrated through life testing by the space cryocooler industry in collaboration with various government agencies. A brief summary of Raytheon Oxford-class cryocooler life test results/status is provided in Table 1. Life test results such as these at Raytheon and elsewhere have largely convinced the customer community that space cryocooler technology is sufficiently mature to baseline for real on-orbit systems. The inherently smaller size and lower mass of the active cryocoolers provide distinct advantages over the incumbent dewar and cryoradiator passive cooling technology, but the mechanical cryocoolers introduce new system integration challenges that must be met. This paper describes those challenges and how they are overcome both through the design of the cryocooler and at the system integration level.

Table 1. Life test history of Raytheon Oxford-class cryocoolers; >120,000 hours without failure.

Cryocooler	Date	Location	TTL Hours	Operating Point	Status
SBIRS Low FDS #1	1997 -	Raytheon	>37000	3.4W @ 58K	Ongoing; no failures or anomalies
Protoflight Spacecraft Cryocooler	1999 -	AFRL-Kirtland	>27000	2.0W @ 60K	Ongoing; no failures or anomalies
Standard Spacecraft Cryocooler	1998 -	AFRL-Kirtland	>27000	1.3W @ 60K	Ongoing; no failures or anomalies
Improved SSC #1	1994-1997	Raytheon	>23600	0.8W @ 60K	Completed; no failures*
Improved SSC #2	1994-1997	Raytheon	>23900	0.6W @ 60K	Completed; no failures or anomalies

* minor, reversible gas contamination detected in ISSC #1

CRYOCOOLER INTEGRATION CHALLENGES

Passive Cryogenic Cooling Systems

One alternative to a mechanical cryocooler for an on-orbit cryogenically cooled system is a passive radiator. Radiators are a standard component of most spacecraft to reject waste heat. Cryogenic radiators, or cryoradiators, are unique in many ways. Their uniqueness arises primarily from the fourth order dependence of radiated energy to source temperature that makes the radiative rejection of heat at low temperatures an enormous challenge. High performance cryoradiators typically employ multiple cooling stages, elaborate multi-layer insulation (MLI) designs, and shields to prevent Earth view for low orbits. Additionally, there are typically operational requirements that the spacecraft be steered to preclude direct solar loading. The former three increase cost and complexity of the radiator, and the latter constrains the mission and increases cost and complexity of the spacecraft attitude control system. Cryoradiators also tend to be fairly large because the low emissive power density has to be compensated for with increased surface area. However, once deployed the radiator is reliable and imparts no vibrations to the system. There are no active components, so there is no electromagnetic interference (EMI) signature.

Stored cryogen systems are another alternative to mechanical cryocoolers. The two types of stored cryogen systems are those in which cryogenic liquid or solid is stored on the spacecraft in highly insulated containers (dewar systems) and those which expand stored high pressure gas through a Joule-Thomson orifice to create refrigeration.³ The lifetime of these systems is limited by the amount of stored cryogen or high-pressure gas. Therefore, the major drawback of the stored cryogen approach is the large size and mass of the system that arise from long-life and/or appreciable heat load requirements. The advantages are simplicity, reliability, no EMI, and vibration output limited to only that produced by moving fluid and/or boil off, which is small.

Oxford Class Mechanical Cryocoolers

The system-integration strengths and weaknesses of the mechanical cryocoolers are largely the converse of the characteristics of the passive systems. The primary advantages of the mechanical coolers are that they are compact and lightweight. Some of disadvantages arise from the necessity of utilizing moving parts to achieve these size and weight reductions. The presence of moving parts potentially limits life due to mechanical wear and imparts vibrations to the cryocooler mounting structure and cooled device.

SESSION 6- Cooling Systems

The electromagnetic motors in the cryocooler and the electronics are potential sources of EMI. The mechanical coolers require power from the spacecraft bus, and that input power must be rejected from the cryocooler system as heat. These interactions are illustrated in Figure 1 and described more fully below.

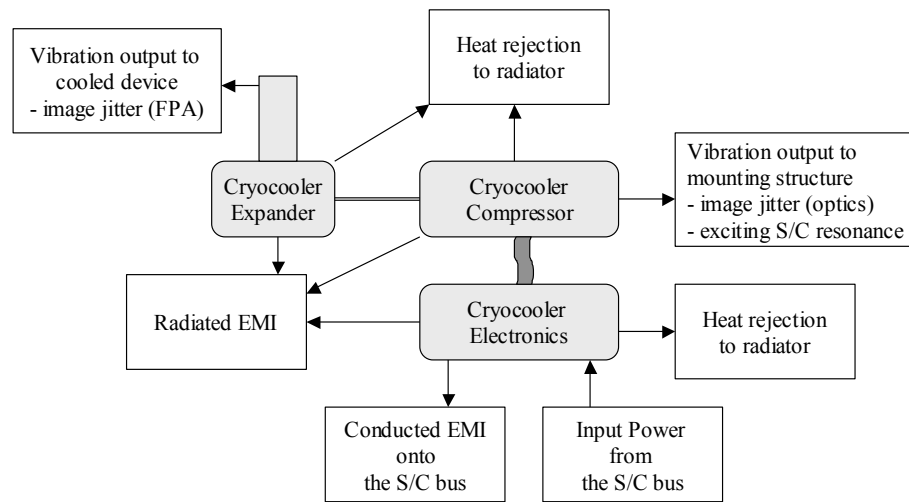


Figure 1. Cryocooler payload integration system engineering challenges

Mechanical / Thermal Interfaces: Active cryocoolers must connect to both the cryogenic temperature reservoir (cooled device) and the ambient temperature reservoir (heat rejection system). The interfaces must provide satisfactory thermal conductance and protect the thin-walled cold finger from excessively large dynamic loading during launch.

Line of Sight / Jitter Control: Active cryocoolers impart vibrations at the physical mount points. This typically necessitates the use of a highly compliant, thermally conductive cold strap at the cold end and control of the vibration output at the ambient hard mounts using a closed-loop, active vibration control system composed of measurement devices (e.g., load cells), piston position control, software, and dedicated electronic circuits.

System Reliability: Table 1 illustrates the success to date with the current generation Oxford-class cryocoolers. Nevertheless, when combined with the electronics, typical cryocooler system reliability at 10 years is calculated to be in the range of 0.95. Payload reliability requirements may necessitate the use of a second, redundant cryocooler system. This increases the load on the operational cryocooler due to parasitic load from the off cooler, and may necessitate the additional complexity of a thermal switch.

Orientation Sensitivity in 1G: Gravity driven convection forces can affect cryocooler performance during ground testing. This is more pronounced in pulse tube than Stirling coolers because the open volume of the pulse tube promotes buoyancy-driven convection cells.⁴ The problem is particularly pronounced in an off state cooler, but can also appear during operation as drive frequency and/or cold tip temperature decrease. Low-temperature, G-M systems (piston and pulse tube) exhibit orientation sensitivity, for example.

Electromagnetic Interference: Active cryocoolers output broadband magnetic and electric fields, static magnetic fields, and reflect AC current ripple onto the power bus. Each of these must be considered in actively cooled sensor design. For example, conducted EMI can be handled at the cryocooler system level through the use of either active and passive filtering circuits, or the spacecraft may dedicate power lines to the cryocooler so that low frequency AC current ripple does not interfere with other spacecraft subsystems.

CRYOCOOLER DESIGN FOR INTEGRATION

Incorporation of an active cryocooler into a payload always requires some degree of accommodation. The decision of whether that level of accommodation is warranted versus that introduced by competing passive cooling approaches is a system level decision based upon temperatures, orbit, mission, heat load, launch vehicle, etc. The best type of cryocooler, be it Stirling, pulse tube, reverse-Brayton, Joule-Thomson, etc., is also a system level decision given the competing strengths and weaknesses of the

SESSION 6- Cooling Systems

different types of cryocoolers. The following example is illustrative of how the system integrator's task can be made easier for an Oxford-class cryocooler integration by anticipating the system level challenges in the course of the cryocooler design.

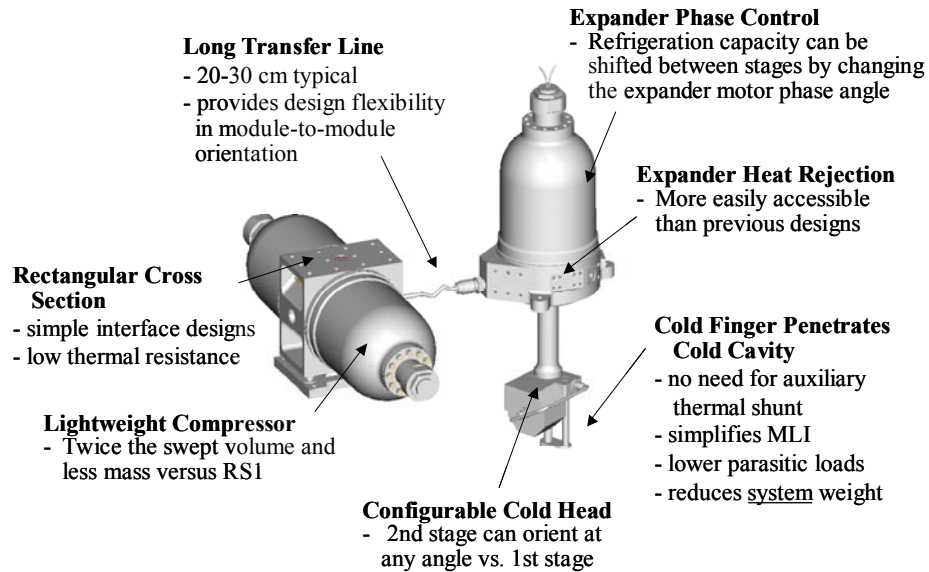


Figure 2. Raytheon Stirling Pulse Tube Two-Stage (RSP2) Cryocooler “ease of integration” features.

The Raytheon Stirling Pulse Tube Two-Stage (RSP2) Cryocooler depicted in Figure 2 embodies system-level design compatibility lessons learned over the past ten years involving the integration of mechanical cryocoolers into space-based infrared sensors. At the most basic level, the two-stage approach provides considerable advantage for applications in which a redundant cooler is required because the majority of the off-cooler parasitic can be carried at the more efficient upper stage temperature of the “on” cooler. The use of a transfer line with separate expander and compressor modules provides design flexibility, and the extension of the cold interfaces as a “finger” from the ambient temperature structure simplifies the design of the cryogenic subsystem and obviates the need for long cryogenic thermal shunts. The RSP2’s ability to shift refrigeration between stages allows for on-orbit adjustment, and when combined with a first stage triple-point thermal storage unit, provides an optimal system-level solution for duty-cycled applications. This characteristic and others of the RSP2 are discussed in more detail elsewhere.⁵

CONCLUSION

Mechanical cryocoolers for space applications, and in particular Oxford-class cryocoolers, have reached a sufficient level of maturity that they meet typical lifetime and reliability requirements of the user community. The size and mass advantages of the Oxford class cryocoolers are partially offset by the required system-level accommodation of vibration output, EMI, power draw, and heat rejection. These integration challenges are best met through a combination of features that are built into the cryocooler and proper system-level design.

SESSION 6- Cooling Systems

REFERENCES

-
- ¹ G. Davey, A.H. Orlowska, *Miniature Stirling cycle cryocooler*, Cryogenics, vol. 27, p. 148, 1987.
 - ² J.M. Wakugawa, H. Haque, K.D. Price, *Improved standard spacecraft cryocooler life test for space-based infrared surveillance*, Cryocoolers 8, p. 69, 1995.
 - ³ D.G. Gilmore, editor, Satellite Thermal Control Handbook, Aerospace Corporation Press, El Segundo, CA, p. 8-4.
 - ⁴ R.G. Ross, Jr., *AIRS pulse tube cooler system-level and in-space performance comparison*, Cryocoolers 12, p. 747, 2003.
 - ⁵ K.D. Price and C.S. Kirkconnell, *Two Stage Hybrid Cryocooler Development*, Cryocoolers 12, p. 233, 2003.

SESSION 6- Cooling Systems

PR20 *

Space Cryocoolers

Emanuel Tward (Northrop Grumman Space Technology)

Cryogenic coolers for use in space require low power and minimum weight. In this paper we describe the typical requirements and performance of a number of reliable, small, efficient, low-power, vibrationally balanced coolers designed and manufactured by NGST (formerly TRW). Eight coolers are currently in orbit on both NASA and military missions. Seven of the eight are pulse tube coolers which since launch have been continuously and successfully cooling ir focal planes to wavelengths up to 16 microns on payloads such as AIRS, Hyperion, Saber, MTI, and CX. The longest of these missions is now greater than 5 years. The eighth is a Stirling cooler that is cooling a high-temperature superconducting mux on the HTSSE payload.

The next generation of these coolers and their sophisticated control electronics are even smaller and more efficient and have been scaled over two orders of magnitude in size. Some are already integrated onto payloads and are scheduled for launch this year. Cooler capabilities are being pushed to lower temperatures (6 K), to multiple cooling stages, to higher cooling capacity and to smaller sizes. These developments will be described.

Keywords: Cryocooler, pulse tube, Stirling, space

* A PowerPoint presentation is available on the CD version of the TDW '03 proceedings.

ON-ORBIT OPERATING EXPERIENCE WITH THE NICMOS CRYOCOOLER—FIRST YEAR

Walter Swift^{1*}, Ed Cheng², Mark Zagarola¹, Frank Dolan¹

¹ Creare Incorporated, Etna Road, P.O. Box 71, Hanover, NH 03755, USA

² Conceptual Analytics LLC, 8209 Woburn Abbey Road, Glenn Dale, MD 20769, USA

ABSTRACT

A mechanical cryocooler was installed on the Hubble Space Telescope (HST) in March 2002. The turbo-Brayton cooler uses miniature high-speed rotors in gas bearings to provide vibration-free refrigeration. It is designed to re-cool the detectors on the Near Infrared Camera and Multi-Object Spectrometer (NICMOS). The cryocooler system has been operating continuously since March 19, 2002. In May 2002, the setpoint temperature was set to provide a detector temperature of 77.1 K. Detector temperatures have been maintained within ± 0.1 K by a control loop that continually adjusts compressor speed around a nominal value of 426,600 rpm. An important feature of the turbo-Brayton cryocooler is its exclusive use of self-acting gas bearings to support the miniature, low mass rotors. This approach results in extremely low vibration levels and wear-free operation. When combined with suitable decontamination procedures, the resulting hermetic system can be contamination free, resulting in un-degraded operation for periods of 5–10 years. This paper reviews the first year on-orbit operating experience with the NICMOS cryocooler and presents additional laboratory results with a version of the system ultimately designed for cooling at 6 K.

BACKGROUND

The NICMOS was installed in January 1997 during Servicing Mission 2 to the HST. Because of a thermal short in the NICMOS cryostat, the solid nitrogen that was used to cool the detectors was subliming at an accelerated rate resulting in an expected useful life of about two years rather than the three plus years originally intended. NASA approved an experimental solution to the loss of cooling in July 1997 by initiating a program to develop and install a mechanical cooling system on the HST. The NICMOS Cooling System (NCS) would interface with the NICMOS cryostat through existing vacuum-jacketed bayonet fittings that had been used in ground operations to supply cold helium for cooling the nitrogen in the cryostat.

Several factors influenced the system design. The system had to have the potential for successful operation for five years. It had to be able to provide sufficient refrigeration to restore the useful resolution of the detectors at about 77 K, yet heat loads were only approximately known. Temperature stability was to be maintained within ± 0.1 K with significant variations in thermal environment (because of orbital heat flux and changes in pointing attitude). EMI and EMC requirements for the HST had to be met, and vibration and jitter were critical. Finally, the system had to be packaged for EVA installation.

The system was designed, fabricated, and ground-tested during the next 12 months. In October 1998, the NCS was space qualified during the Hubble Orbital System Test that included ten days of nearly continuous operation on STS-95. Following the qualification flight, the system was refurbished to improve several of the system components. Additional ground tests were conducted to establish the final performance figures for the system, address control issues, and to assess vibration characteristics of the system. Nitrogen in the NICMOS cryostat was fully depleted in January 1999.

SESSION 6- Cooling Systems

Creare had been developing cryocooler technology for about 20 years prior to the NICMOS launch. One particular system had been developed to the engineering model level and had been operating in a life test for about three years. It produced 5 W of refrigeration at 65 K using a reverse Brayton refrigeration cycle. A key feature of the system was that it employs turbomachines with small, very high-speed rotors operating in gas bearings. These machines have excellent life characteristics, and are inherently low vibration because of the precision low mass rotors. The 5 W, 65 K cooler uses 215 W of input power and was an attractive candidate for the cryocooler portion of the NCS.

Nominal operating requirements were established for the NCS. They are listed in Table 1. Creare used thermodynamic models of the existing 65 K cryocooler to define the design for the NCS system. Because the system was to be installed on orbit, it was decided to use two separate loops for the cryocooler portion of the system. A hermetically sealed cryocooler would serve as the main heat pump. This was supplemented by a cryogenic circulating loop that would interface with the NICMOS dewar. In this way, the risk of neon loss over time could be minimized and controlled. The cryocooler would be launched with its neon inventory intact. The circulator loop would be launched empty and filled on orbit after connecting to the NICMOS dewar. Excess neon would be stored in supplemental tanks that could be activated to replenish the circulator loop if there was leakage at the tube interfaces.

Table 1: Nominal operating parameters for the NICMOS Cooling System (NCS)

Parameter	Value
Detector Temperature	77.1 K +/- 0.1 K
Cryostat Dome Temperature	~ 72.4 K
Cryostat Parasitic Heat Load	~ 400 mW
Neon Temperature at NICMOS Inlet	~ 65 K
Temperature at NCC Heat Rejection Interface	~ 278 K
Total Refrigeration Power	7.1 W
Radiator Temperature	- 28°C to - 10°C
NCS Power Consumption	~ 375 W

The addition of the circulator (between 0.5 and 1 W of heat at the cold end) and other interfacing characteristics resulted in an estimated cryocooler refrigeration requirement of about 7 W. This and limitations imposed by packaging raised the compressor input power from 215 W in the engineering model version to about 375 W in the NCS configuration. The hardware for the NCS was only a mild extension of technology that had already been developed and demonstrated. However, all components required space qualification.

COOLER DESCRIPTION

The NCS consists of three independent fluid loops shown in Figure 1: a cryogenic circulation loop, a closed loop cryocooler, and a capillary pumped loop. In the circulator loop, a small 72,000 rpm centrifugal circulator conveys neon at a continuous flow rate of about 0.4 g/s through tubing between the NICMOS cryostat and the cold load interface at the cold end of the cryocooler. The heat from NICMOS is rejected at the cold load interface through a series of small finned passages in a heat exchanger. In the cryocooler, a small centrifugal compressor operating at 400,000–430,000 rpm compresses neon to a pressure ratio of about 1.7. The heat of compression is rejected to the capillary pumped loop at the heat rejection interface. The neon flows through a recuperative, counterflow heat exchanger where it is cooled by a return stream from the cold end of the cryocooler. The gas expands through a turbine at the cold end removing heat from the fluid and dissipating it through an alternator at a resistive load in the electronic controller. The turbine operates at 150,000–270,000 rpm with a refrigeration capacity of 7–15 W. Temperature control and refrigeration capacity is adjusted by changes to the compressor speed, thus increasing or decreasing the turbine output. The cooled gas exiting from the turbine absorbs heat in the cold load interface and then is

SESSION 6- Cooling Systems

heated in the low-pressure side of the recuperator as it returns to the compressor inlet. Flow is steady and continuous at about 1.7 g/s in this loop. The capillary pumped loop uses ammonia that vaporizes at the heat rejection interface. At the radiator, the vapor condenses and the liquid flows back to the heat rejection interface by capillary action.

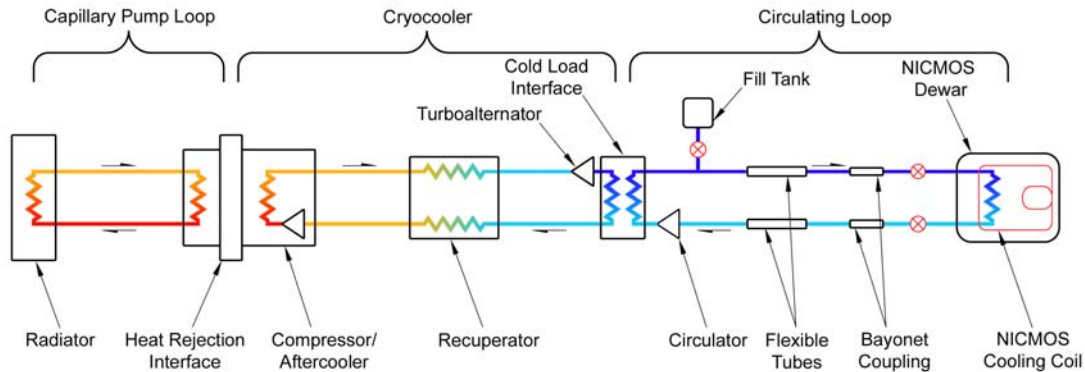


Figure 1: NICMOS Cooling System Schematic.

The three subsystems are packaged for on-orbit EVA installation. Figure 2 shows the cryocooler and circulator loop during integration. The compressor is fastened to the back plate at the bottom of the assembly. The recuperator is the tubular component with a vertical axis between the bottom of the package

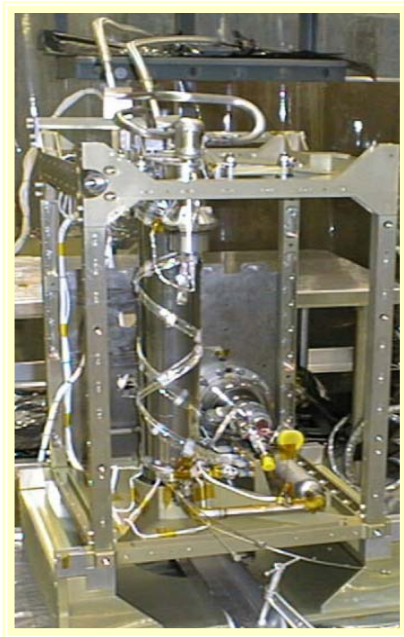


Figure 2: Cryocooler during integration.

to the top. The cold load interface is at the top of the recuperator and supports the two cold end turbomachines—the circulator (foreground) and the turboalternator (hidden). Cold end sensor leads are staked to the exterior surface of the recuperator shell. The electronics package including a DC/AC adjustable frequency inverter, the circulator drive and instrumentation electronics mount above the compressor on the back plate. The frame provides support for the cryocooler, pressure transducers, neon fill and replenishment tanks, electronics, and the heat rejection interface connecting to the capillary pumped loop. The frame footprint is about 0.5 m x 0.5 m.

Rigid tubing at the top of the frame connects to the cold load interface. Flexible tubes (approximately 1 m long) are welded to the rigid tube ends. The flexible tubes have modified bayonet ends that interface with the bayonet fittings on the NICMOS support panel.

Following the installation of the electronics, the entire cold end is wrapped in multi-layer insulation to reduce radiation heat loads. Side panels are added to prevent damage to the assembly during handling and EVA.

ON-ORBIT OPERATION

The cooldown started in mid-March, 2002. During the first 25 days, the cryocooler removed heat from the large NICMOS cryostat at a rate of about 10 W. When the control temperature reached 70 K, the machine

SESSION 6- Cooling Systems

was set to maintain that temperature. Figure 3 shows a time plot of several temperature sensors at the cold end of the system. NICMOS Outlet and NICMOS Inlet temperature sensors are attached to the tubes on the NCC assembly. NICMOS Inlet therefore is the coldest fluid exiting the cold load interface and entering the flexible tube to NICMOS. NICMOS Outlet is located just upstream of the inlet to the circulator. The difference between these two temperatures is approximately proportional to the heat load absorbed in the tubes and the NICMOS cryostat. Turbine inlet temperature is measured on the cold load interface and is only a rough approximation of the actual fluid temperature at the inlet to the machine. Control temperature is a calculated figure designed to approximately estimate the temperature at the detector cold bench in the NICMOS assembly. The approximation was derived from tests on a NICMOS simulator at GSFC.

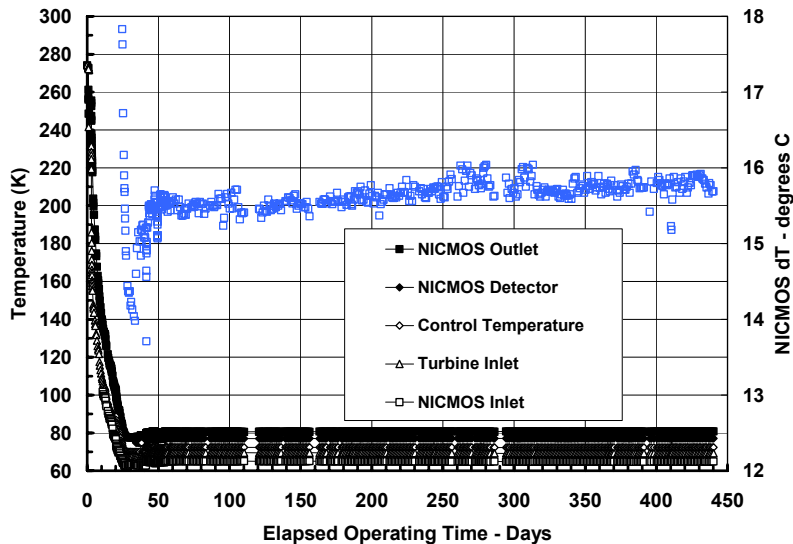


Figure 3. Operating data since cooldown.

Following the initial cooldown, the control temperature was adjusted in steps to evaluate system control response and to assess the behavior of the detectors. The control temperature was then set in order to maintain the detectors at 77.1 K. The five temperatures shown in Figure 3 are identified in the order of their value. They have remained within operating limits since the control temperature was initially set. The heat load to the circulator loop is indicated by the temperature difference between NICMOS inlet and outlet (NICMOS dT). These data indicate a small increase in heat load to the cryocooler from day 50 to present. Some of this change may be a result of the periodic change in solar flux during the year. Short period variations are due to changes in the aft shroud thermal environment primarily resulting from pointing attitude and orbit.

LOWER TEMPERATURE SYSTEMS

The operating history of the NCS has verified the reliability and attractive features of this type cooling system. Present efforts focus on extending this technology to lower temperatures and lower refrigeration capacities. This involves improved fabrication methods to further reduce the size of the basic cryocooler components. A development effort is currently underway through the Cross Enterprise Technology Development Program to produce a turbo-Brayton cooler suitable for up to 100 mW of refrigeration in the 6 K–10 K range. Two smaller compressors have been on life test in a cryogenic facility with a cold end temperature at 20 K since December 2002 supporting this effort. A subminiature turboalternator will be tested later this year in a cryogenic closed loop performance test.

Heterodyne Spectroscopy in the Thermal Infrared Region: A Window on Physics and Chemistry

Theodor Kostiuk^a,

NASA Goddard Space Flight Center, Code 693, Greenbelt MD 20771

ABSTRACT

The thermal infrared region contains molecular bands of many of the most important species in gaseous astronomical sources. True shapes and frequencies of emission and absorption spectral lines from these constituents of planetary and stellar atmospheres contain unique information on local temperature and abundance distribution, non-thermal effects, composition, local dynamics and winds. Heterodyne spectroscopy in the thermal infrared can remotely measure true line shapes in relatively cool and thin regions and enable the retrieval of detailed information about local physics and chemistry. The concept and techniques for heterodyne detection will be discussed including examples of thermal infrared photomixers and instrumentation used in studies of several astronomical sources. Use of heterodyne detection to study non-LTE phenomena, planetary aurora, minor planetary species and gas velocities (winds) will be discussed. A discussion of future technological developments and relation to space flight missions will be addressed.

INTRODUCTION

The thermal infrared region is an important region for remote studies of solar system, astrophysical and terrestrial sources. It contains spectral bands of many of the most important molecular and atomic species contained in gaseous sources. True shapes and frequencies of emission and absorption spectral lines from constituents of planetary and stellar atmospheres contain unique information on local physics and chemistry, including the temperature and abundance distribution, non-thermal effects, chemical composition, local dynamics and winds. Spectrometers capable of measuring spectra from remote thermal infrared sources require high sensitivity detectors and designs, which enable measurement of target spectra with sufficient spectral resolution to extract the desired physical and chemical parameters of the source. Infrared heterodyne spectroscopy provides the highest resolution, $\lambda/\Delta\lambda \geq 10^6$, high frequency specificity ($\geq 10^{-8}$), and sufficient sensitivity to uniquely measure gaseous constituents, non-thermal conditions, both thermal structure and species abundances, and gas velocities (winds) directly.

Infrared heterodyne detection is analogous to millimeter wave techniques. An infrared source is combined with a laser local oscillator, LO, and focused on an infrared photomixer, where the difference frequency between the source and laser frequencies is generated (Fig. 1). The resultant intermediate frequency, IF spectrum, is in the radio region of the electromagnetic spectrum and it preserves the intensity and spectral information of the infrared spectrum. It can be analyzed using radio techniques, e.g., filter banks, autocorrelators, or acousto-optic spectrometers, AOS's. These determine the absolute spectral resolution.

Heterodyne detection is a coherent technique and the detected electric field E_t is the sum of the electric fields of the source and laser local oscillator (Fig. 2). The detected power is proportional to E_t^2 . The detected power consists of a DC term and the cross product, which is at the absolute difference frequency between the two incident signals, $|\omega_s - \omega_{lo}|$. The detected heterodyne signal is thus proportional to the product of the signal and laser power. At optimum operation the noise is dominated by the shot noise generated by the laser photons in the photomixer, shot-noise-limited (SNL) operation. The noise equivalent flux is then determined by the resolving element, B, by the integration time τ , and by the efficiency of the heterodyne system, the degradation factor Δ . This technique can also be used to build interferometers, preserving the phase information $\delta\phi$, as is done in the Berkeley Infrared Spatial Interferometer (ISI) at the Mount Wilson Observatory¹.

^a E-mail: kostiuk@gsfc.nasa.gov

SESSION 7 – Heterodyne Detection

HIPWAC

Heterodyne Instrument for Planetary Wind And Composition

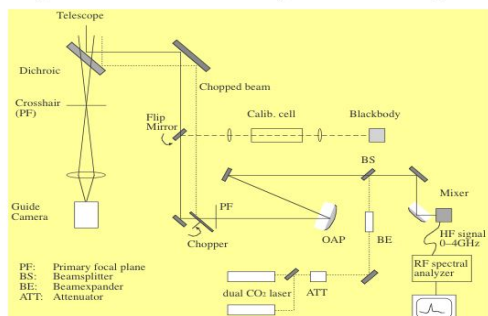


Fig.3. Schematic Layout

HIPWAC on the NASA IRTF

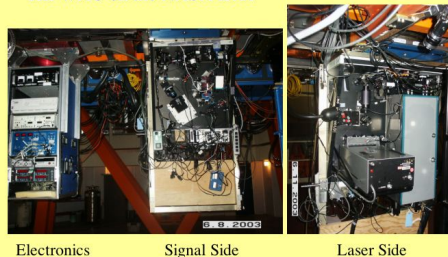


Fig. 4. HIPWAC at The IRTF

Jupiter - Comparison of spectral resolution. Figure 5 illustrates the advantage of heterodyne level spectral resolution. The bottom spectrum shows measurements of Jupiter's spectrum in the thermal infrared region with the Voyager Infrared Interferometer Spectrometer, IRIS⁵, at a spectral resolution of 0.43 cm^{-1} . A broad spectrum displaying bands of molecular constituents of Jupiter's atmosphere near the north polar region is revealed. Analysis of the band of ethane near $12 \mu\text{m}$ probes lower stratospheric altitudes, pressures higher than 10 mbar. A Fourier transform spectrometer at 0.015 cm^{-1} resolution reveals individual sub-bands of ethane and isotopic ethane. This resolution probes higher in altitude, pressures greater than a few mbar. Infrared heterodyne resolution (0.00083 cm^{-1}) measures a single line shape in a sub-band thus probes even higher, pressures ≤ 1 mbar. All spectra permit retrieval of ethane abundance, stratospheric temperature information, however, is not independently retrievable with the lower resolution spectra. Resolved individual line shapes do permit retrieval information on both ethane abundance and temperature^{6,7}.

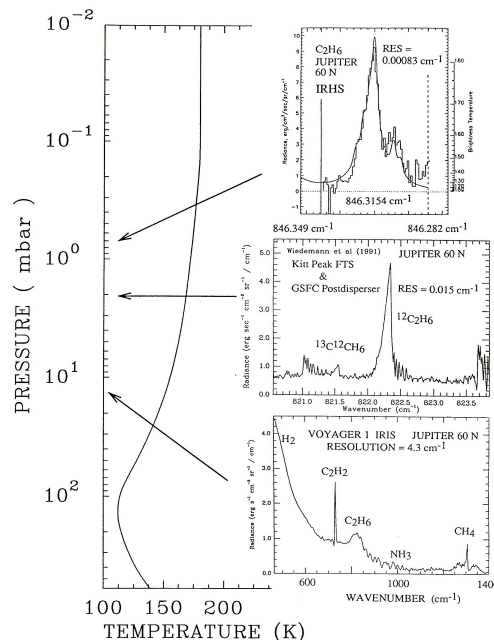


Fig. 5.

Mars CO₂ Absorption and Non-Thermal/Laser Emission: Figure 6 illustrates how infrared heterodyne spectroscopy can detect and study unique phenomena on Mars. The spectra are a measurement of atmospheric absorption and emission lines of CO₂ in the atmosphere of Mars. The left spectrum was measured by HIPWAC at 25 MHz (0.00083 cm^{-1}) resolution over a 1.6 GHz (0.053 cm^{-1}) band. It shows the CO₂ absorption line formed in the lower atmosphere, below $\sim 30 \text{ km}$ altitude, and a core emission formed in the mesosphere, 50 – 80 km altitude. The absorption line requires very high resolution to even detect it. The emission core, shown in the right spectrum in Fig. 6 at 5 MHz resolution, can only be detected and measured at heterodyne resolving powers. It is generated under non-local thermodynamic (non-LTE) equilibrium conditions, at μbar pressures under pumping by near infrared solar radiation. These lines can be bright and have a naturally occurring lasing component^{8,9}. They can be used as probes of the Mars mesosphere. Because they are formed in low-pressure regions they have Gaussian shapes. Their width measures the local kinetic temperature¹⁰ and their integrated intensity their vibrational temperature. Their measured frequencies can be used to directly measure winds, as was done on Venus¹¹.

SESSION 7 – Heterodyne Detection

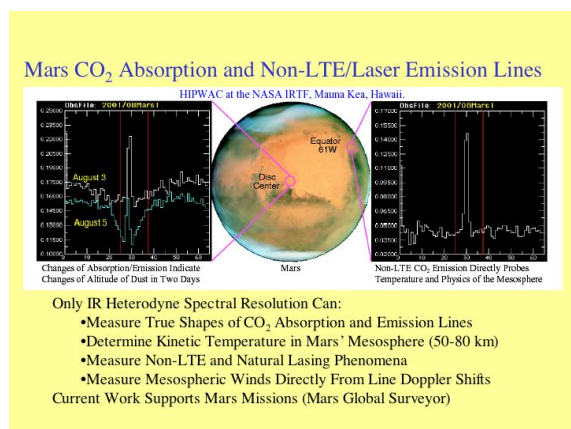


Fig. 6.

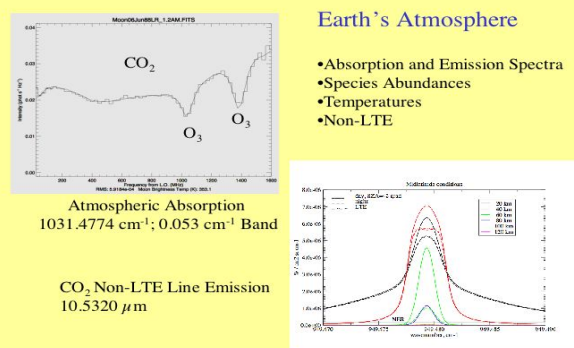


Fig. 7

Earth's Stratosphere - Constituent Abundance Profiles, Non-LTE: Figure 7 shows what can be measured in the Earth's stratosphere with thermal infrared heterodyne spectroscopy. Ozone¹², CO₂, ClO, and numerous minor constituents in the stratosphere can be measured. From Earth orbit non-LTE emission from numerous species including CO₂ (as on Mars and Venus) and ozone can be studied and the upper stratosphere and mesosphere probed. Calculations show significant non-LTE components possible as shown in the lower part of Fig. 7 (A. Kutepov, NRC/NASA GSFC, private communication, 2002).

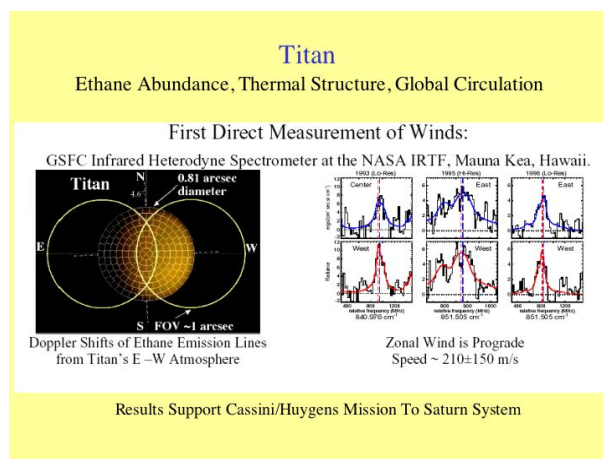


Fig. 8

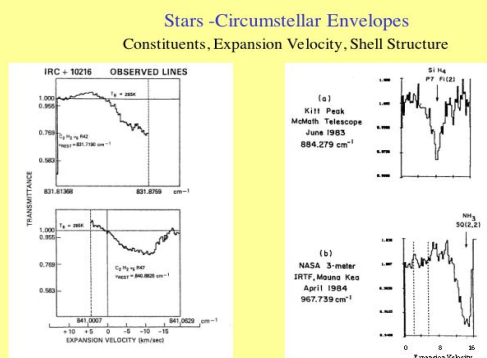


Fig. 9

Wind Measurements on Titan: Figure 8 shows results from direct measurements of the global circulation on Titan. Heterodyne resolution and high frequency determination enables direct measurement of gas velocities by measuring the Doppler shifts of individual spectral lines. This was done on Titan by measuring the difference in frequency of ethane line emission from east and west limbs of its disk¹³. The field of view of the IRHS is diffraction limited at the 3-meter IRTF, ~ 1 arcsec, and is shown in Figure 8. Resultant spectra were noisy due to the small portion of the Titan disk (~ 8.1 arcsec) that is in the measurements field-of-view. Global circulation was found to be prograde (east to west on the sky) with a speed 210 ± 150 m/s. Significant improvement in velocity uncertainty can be achieved with larger telescopes, e.g., 8-meter Subaru, whose field of view would be about 0.36 arcsec.

Circumstellar Envelopes – Composition and Shell Structure: Figure 10 illustrates species detectable with thermal infrared heterodyne techniques. Spectra of C_2H_2 , NH_3 , and SiH_4 are seen to probe different regions of the expanding shell of IRC10216. Acetylene is present throughout the stellar region and its line shape indicates shell structure, which can be compared to theoretical models.

HETERODYNE DETECTORS/PHOTOMIXERS

The key component of thermal infrared heterodyne detection is the photomixer, which determines the detection bandwidth and along with the system optical losses and laser power the system sensitivity. Conventional detectors can be photoconductors or photodiodes. Photodiodes (i.e., HgCdTe photodiodes) are the most commonly used

SESSION 7 – Heterodyne Detection

photomixers. In the conversion of incident photons to charge carriers only generation noise is present in photodiodes. In photoconductors both generation and recombination noise is present. This makes the photodiode inherently a factor of two more sensitive heterodyne detectors. However, photoconductors may have advantages in devices operating over a wider wavelength range. The principal goals of thermal infrared photomixer design are high heterodyne quantum efficiency, wide bandwidth of operation, and large wavelength coverage, particularly toward longer wavelengths ($>12\ \mu\text{m}$).

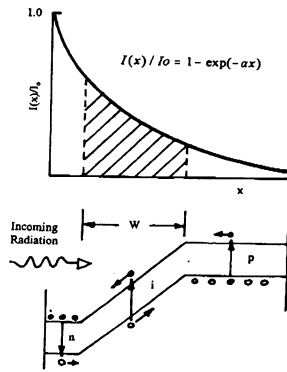


Figure 1. Energy band diagram for a conventional p-i-n photodiode. Upper part shows the incoming radiation distribution within the device.

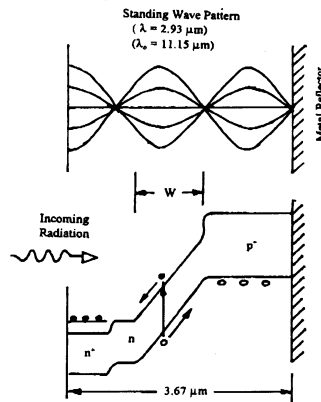


Fig. 11. Resonant optical cavity Energy levels and standing waves (Bratt, 2003)

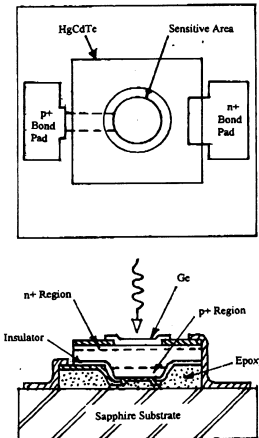


Fig. 12. ROC detector design (Bratt, 2003)

Figure 10 illustrates the energy level diagram for a conventional p-i-n photodiode (P. Bratt, Raytheon Vision Systems, private communication, 2003). Incoming radiation has only one path through the material/junction, limiting the absorption and conversion efficiency and thus the heterodyne efficiency over wide bandwidths. If a resonant optical cavity, ROC, structure is used such as shown in Figs. 11 and 12, multiple passes are possible through the junction region, enhancing absorption of incident photons and thus the heterodyne quantum efficiency over a wide bandwidth (P. Bratt, Raytheon Vision Systems, private communication, 2003). These ROC devices are only tuned to relatively narrow wavelengths (Fig. 13) and, unlike with conventional diodes, multiple devices must be used for full wavelength coverage. Figure 14 compares the relative sensitivity and bandwidth of conventional HgCdTe GOF¹⁴ and ROC photodiode mixers (Bratt, Raytheon Vision Systems, private communication, 2000).

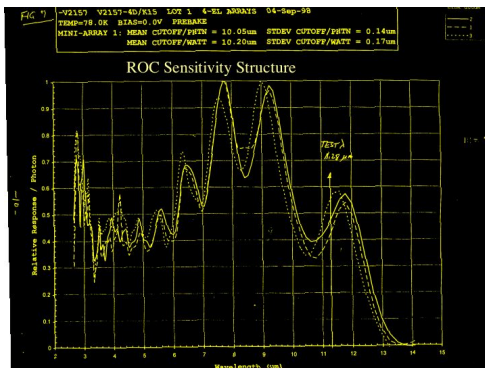


Fig. 13

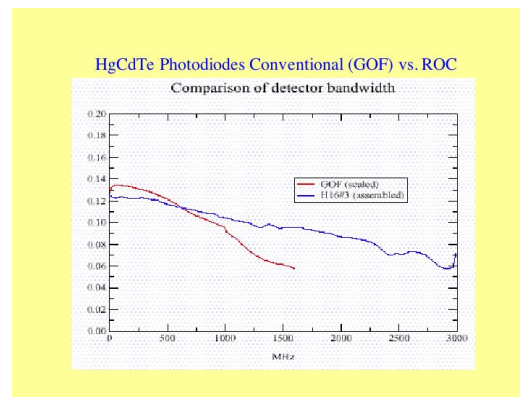


Fig. 14

Longer wavelength of operation can be achieved with photodiodes by material and doping adjustments and to a degree by cooling the device to colder temperatures, thereby reducing the energy gap, E_g . Results of such an approach by D. Spears (1987 and in Ref. 15) is shown in Fig. 15. This approach, however, limits the wavelengths to less than about $30\ \mu\text{m}$ and bandwidths to about 500 MHz.

SESSION 7 – Heterodyne Detection

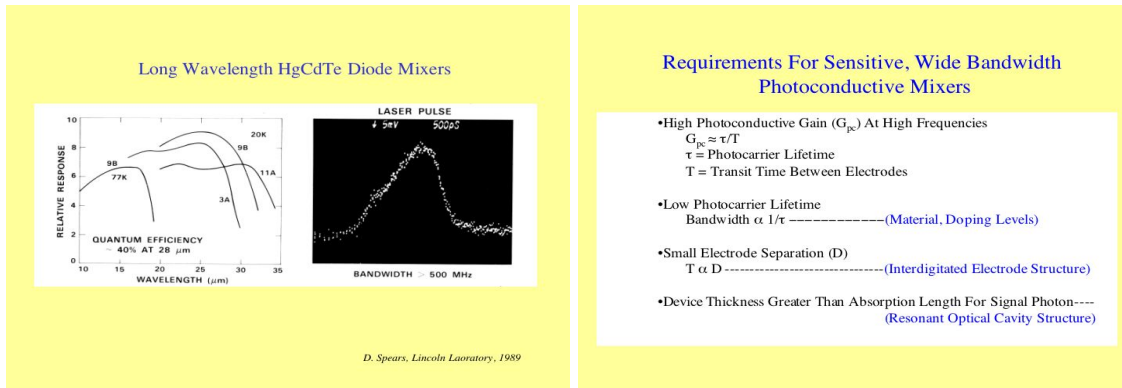


Fig. 15.

Table 1

Another approach for wide bandwidth, long wavelength photomixers which may yield devices operating to $\sim 200 \mu\text{m}$ is interdigitated electrode ROC HgCdTe photoconductors. Requirements for sensitive and wide bandwidth photoconductive mixers are presented in Table 1. Devices must have high photoconductive gain at high frequencies, which means long carrier lifetime, τ , relative to the transit time between electrodes, T . If the transit time is short enough recombination is minimized and recombination noise becomes low or insignificant, approaching that of a photodiode. For wideband (fast) operation the photocarrier lifetime must be short. This is achieved by adjusting material composition and doping levels. The transit time between electrodes can be reduced by decreasing the distance, D , between them and, with an interdigitated structure, the multiple electrodes are able to effectively “sweep up” the photocarriers. For high quantum efficiency the effective device thickness must be greater than the absorption length. For thin devices, necessary for wide bandwidths, this can be accomplished with an ROC design as described previously. Figure 16 shows an image of ROC interdigitated HgCdTe photomixers at $28 \mu\text{m}$. Figure 17 shows theoretical predictions for photodiode (dashed curve) and photoconductor (solid curve and band) long wavelength mixer performance¹⁵. Measured device performance is plotted as filled circles (photoconductor), triangles (photodiodes), and squares, GaAs Schottky diodes, for comparison to projected HgCdTe devices. ROC photoconductor mixers near $115 \mu\text{m}$ approaching the theoretical limit depicted here were fabricated¹⁶.

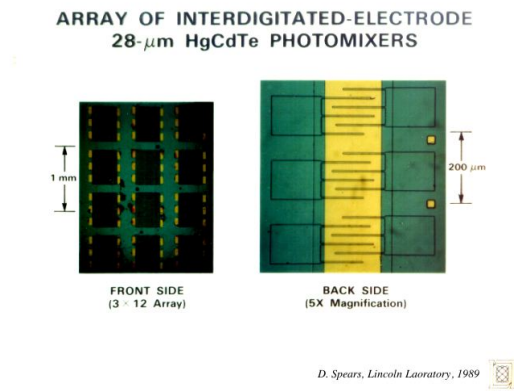


Fig.16

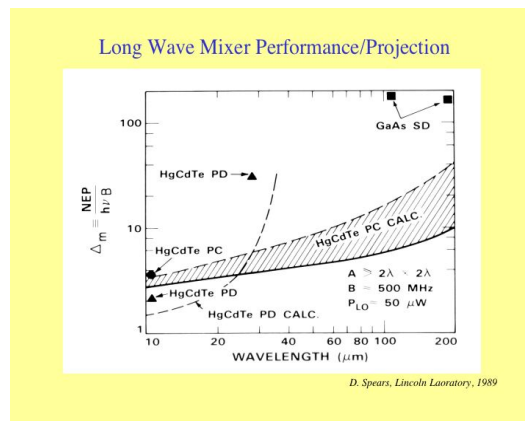


Fig. 17

FUTURE DEVELOPMENTS

Future improvements in photomixers includes development of truly operational devices in the 13-100 μm region with heterodyne quantum efficiency $>60\%$ and bandwidths $\geq 4 \text{ GHz}$. Heterodyne mixer arrays need to be developed with sensitive and uniform device performance. The ROC interdigitated devices in Fig.16 are an example. Photodiodes have also been developed in small array formats (4-12 elements) but their uniformity in performance must be addressed. Other approaches that have not been addressed adequately are, hot bolometers and quantum well infrared photodetectors, QWIP's). QWIPS show promise and initial plans are underway to test existing devices for heterodyne performance and provide data for future development with photomixer performance as the focus.

SESSION 7 – Heterodyne Detection

REFERENCES

1. D. Hale, *A Thermal Infrared Heterodyne Receiver with Applications to Astronomy*, Proc. International Workshop on Thermal Detectors-TDW, Washington DC, USA, in press, 2003
2. T. Kostiuk, and M. J. Mumma, *Remote sensing by IR heterodyne spectroscopy*, Appl. Optics 17, 2644-2654, 1983.
3. T. Kostiuk, *Physics and chemistry of upper atmospheres of planets from infrared observations*, Infrared Phys. Technol. 35, 243–266, 1994.
4. F. Schmuelling, *et al.*, *Heterodyne Instrument for Planetary Wind And Composition*, JQSRT, In Preparation, 2003.
5. R. A. Hanel, *et al.*, Science, 204, 972, 1979.
6. T. A. Livengood, T. Kostiuk, F. Espenak, and J.J. Goldstein, *Temperature and abundances in the Jovian auroral stratosphere 1. Ethane as a probe of the millibar region*. JGR 98, 18813–18823, 1993.
7. T. Kostiuk, P. Romani, F. Espenak, T.A. Livengood, J.J. Goldstein, *Temperature and Abundances in the Jovian Auroral Stratosphere 2. Ethylene as a Probe of the Microbar Region*, JGR 98, 18823–18830, 1993.
8. M. J. Mumma, D. Buhl, G. Chin, D. Deming, F. Espenak, T. Kostiuk, D. Zipoy, *Discovery of natural gain amplification in the 10-micrometer carbon dioxide laser bands on Mars - A natural laser*, Science 212, 45–49, 1981.
9. D. Deming, F. Espenak, D. Jennings, T. Kostiuk, M. Mumma, D. Zipoy, *Observations of the 10-micron natural laser emission from the mesospheres of Mars and Venus*, Icarus 55, 347–355, 1983.
10. T. Livengood, T. Kostiuk, K. Fast, J. Annen, K., G. Sonnabend, T. Hewagama, *Meridional Mapping of Mesoapheric Temperatures from CO₂ Emission Lines Along the MGS Ground Track*, BAAS 35, 913, 2003.
11. J. J Goldstein, *et al.*, *Absolute Wind Velocities in the lower thermosphere of Venus using infrared heterodyne spectroscopy*, Icarus 94, 45–63, 1991.
12. K. Fast, T. Kostiuk, g. Sonnabend, T. Livengood, F. Espenak, J. Annen, M. F. A’Hearn, T Hewagama, *Peeking Through the Picket Fence: Observing Mars Ozone from Earth*, BAAS 35, 935, 2003.
13. Kostiuk *et al.*, *Direct Measurement of Winds on Titan*, Geophys. Res. Lett. 28, 2361, 2001.
14. D.L. Spears, *Planar HgCdTe quadrantal heterodyne arrays with GHz response at 10.6 μm* , Infrared Phys 17, 5-8, 1977.
15. T. Kostiuk and D. Spears, *30 μm Heterodyne Receiver*, International Journal of Infrared and Millimeter Waves 8,1269-1279, 1987.
16. D. Spears, MIT Lincoln Laboratory, private communication, 1989.

THIS – a Next Generation Tuneable Heterodyne Infrared Spectrometer for SOFIA

Guido Sonnabend*

NASA Goddard Space Flight Center, Code 693, Greenbelt, MD 20771, USA

Daniel Wirtz, Rudolf Schieder

I. Physikalisches Institut, Universität zu Köln, Zùlpicher Str.77, 50937 Köln, Germany

ABSTRACT

A new infrared heterodyne instrument has been developed which allows the use of both tuneable diode lasers (TDL) and quantum cascade lasers (QCL) as local oscillators (LO). The current frequency tuning range of our system extends from 900 to 1100 cm^{-1} depending on the availability of lasers but is planned to be extended to 600 cm^{-1} soon. The IF-bandwidth is 1.4 GHz using an acousto-optical spectrometer (AOS). The frequency resolution and stability of the system is approximately 10^7 . Currently, mercury-cadmium-telluride (MCT) detectors are used as mixers while new devices like quantum-well-infrared-photodetectors (QWIP) and hot-electron-bolometers (HEB) are investigated. The IF-bandwidth can be extended to about 3 GHz by using a new broadband acousto-optical spectrometer presently under development. The instrument is fully transportable and can be attached to any infrared or optical telescope. The semiconductor laser is stabilized to a Fabry-Perot ring-resonator, which is also used as an efficient diplexer to superimpose the local-oscillator and the signal radiation. As a first step measurements of trace gases in Earth's atmosphere and non-LTE emission from Venus' atmosphere were carried out as well as observations of molecular features in sunspots. Further astronomical observations from ground-based telescopes and the airborne observatory SOFIA are planned for the future. Of particular interest are molecules without a permanent dipole moment like H_2 , CH_4 , C_2H_2 etc.

INTRODUCTION

In recent years IR heterodyne spectroscopy proved to be a powerful tool for astrophysical and atmospheric studies (see ^{1,2,3} and references therein). Whenever high spectral resolution is required heterodyne systems are advantageous because of their high optical throughput compared to direct detection methods like Michelson interferometry. Valuable information was gathered in the Earth's atmosphere as well as in the atmospheres of other planets of the solar system. The possible compactness of a heterodyne system is another advantage.

Gas lasers have mostly been used as LOs and the sensitivity of those systems has been shown to come close to the quantum limit whereas the restriction to the fixed laser

* Contact information for G. Sonnabend- Email: samstag@ph1.uni-koeln.de

SESSION 7- Heterodyne Detection

frequencies, which allows only about 15% of the spectral range between 9 and 12 μm be covered, is the biggest disadvantage of gas lasers.

This major limitation was overcome by TDL which are available from 1 to 34 μm . Unfortunately, the system noise temperature of advanced TDL pumped systems is worse by a factor of 3-5 compared to gas laser systems which is due to the lack of laser power, incoherent background emission, and the critical response of TDL to optical feedback. Although most of these problems were solved at an earlier stage of the development of THIS the TDL technique turned out to offer no perspective for future improvements.

At this point with the QCL a newly developed device became available. These are unipolar lasers first experimentally realized in 1994⁴ turned out to be the ideal LO for a tuneable heterodyne system. They provide sufficient optical power to reach the shot-noise detection limit and the handling is more convenient compared to TDLs. Use of QCLs brought the performance of THIS to the level of CO₂-laser based systems. THIS is widely usable at Cassegrain, Nasmyth or Coudé foci of IR or optical telescopes and is intended to be a second generation instrument for the airborne observatory SOFIA.

THE INSTRUMENTAL SETUP

Heterodyne receivers in every wavelength regime work in a common way: The broadband radiation to be analysed is superimposed with the radiation of a mono-mode LO. At present we use a QCL emitting at 9.2 μm wavelength. The power provided by these devices ranges up to a 100 mW. As mixer we use a fast MCT photovoltaic detector which is optimised for a wavelength of 10.6 μm . Through combined detection of LO and

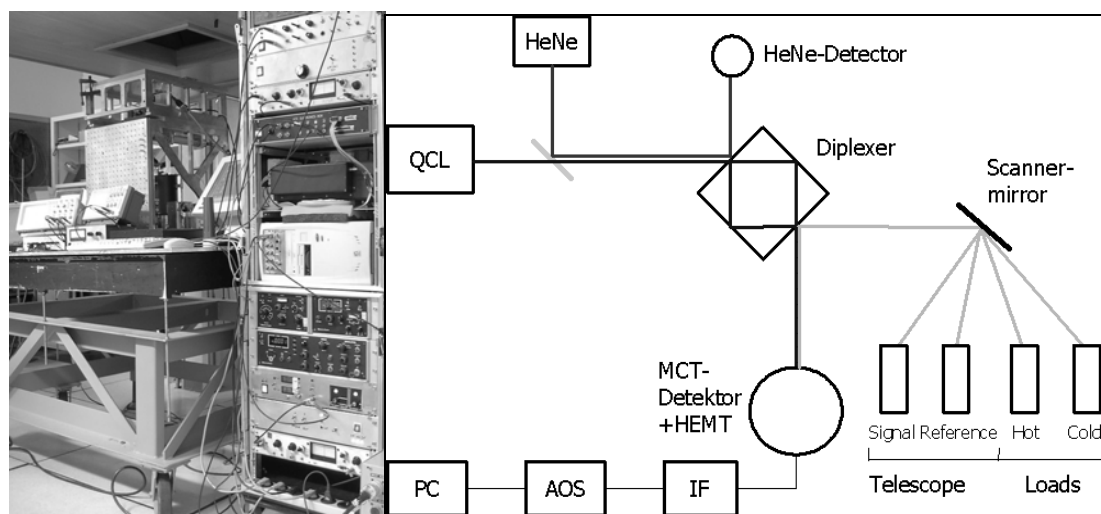


Fig. 1: left: THIS @ McMath-Pierce West Auxiliary: the optical receiver (cubic aluminum structure on the left) and back-end electronics (19"-rack on the right including the AOS) right: a schematic of the instrumental set-up showing the major components.

broadband signal the mixer generates an IF-signal that is amplified by a cooled high-electron-mobility-transistor amplifier (HEMT). Both devices are placed in a LN₂ cooled dewar. The Frequency analysis is done by a 2048 channel AOS with a total bandwidth of

SESSION 7- Heterodyne Detection

1.4 GHz.⁵ In order to avoid unnecessary losses of the LO power a confocal Fabry-Perot ring-resonator is used as diplexer to combine the LO with the broadband signal. Two focussing mirrors and two highly reflective beamsplitters make up the resonator. This device allows to superimpose about 60 % of LO power with more than 90 % of signal power.⁶

Direct calibration of the measured spectra is provided by occasionally switching between a 670 K blackbody emitter as hot load and an ambient temperature absorber as cold load. The transportable receiver (see fig. 1) consists of the optical setup (left) and the electronics (right). The optics (including the LO and the mixer) are mounted into a cubic frame made of aluminium with a size of roughly 60x60x40 cm³ and a weight of 80 kg which also allows THIS to be mounted into the focal plane of a Cassegrain telescope for example. Adaptation to different telescope focal lengths is done by a suitable off-axis parabolic mirror. Such mirrors are also used for matching the beam parameters of the LO, the mixer, and the diplexer. All electronic devices needed as well as the AOS back-end are mounted in an additional two part 19" rack. For convenient handling the receiver is remotely controlled through a personal computer that is also used for data acquisition

RESULTS

During November 2002 THIS was very successfully operated at the west auxiliary telescope of the McMath-Pierce Solar Observatory on Kitt Peak, Az. At first SiO and H₂O absorption lines in sunspots were measured. In Fig. 2 (left) one can see the rather odd line shape of this SiO absorption feature caused by contributions of different velocity components to the line.

To demonstrate the system sensitivity especially with regards to future astronomical

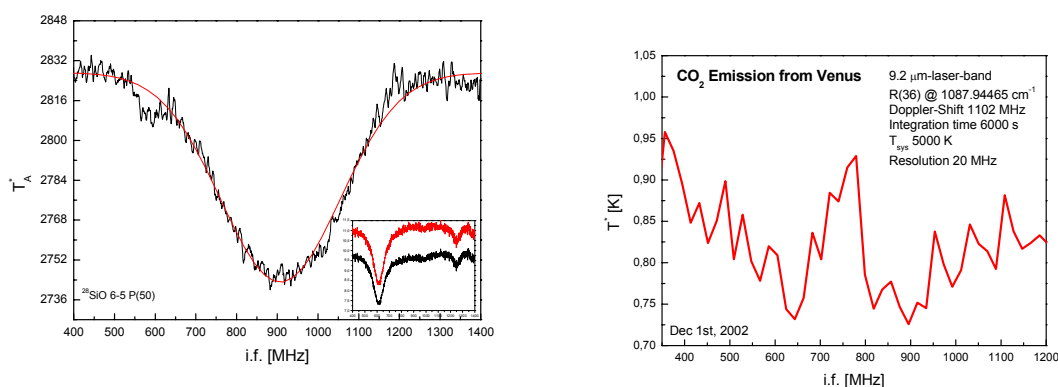


Fig. 2: left: SiO absorption feature in a sunspot. The line-profile yields a temperature of 5000 K. right: non-LTE emission from Venus. Shown is the R(36) line of the 9 μm-band of CO₂.

observations we observed non-LTE emission features in the atmosphere of Venus. It is already known since the 1970s that natural non-LTE CO₂-emission is present at the illuminated arc. We were able to detect an emission signal of the R(36) transition of the 9 μm-band of CO₂ as can be seen in fig. 2 (right), shown with a resolution of 20 MHz. Again the detected brightness temperature is plotted against the intermediate frequency.

SESSION 7- Heterodyne Detection

One can see the emission peak sitting on a broad CO₂ – absorption that stems from lower altitudes of the Venus atmosphere. The measured brightness temperature (taken in account the losses mentioned above) is about 400 mK. Further evaluation especially a comparison to a calculated atmospheric model of Venus has to be done. Having been able to detect a weak non–terrestrial signal for the first time with THIS, we are looking forward to further observing runs in 2003.

THE FUTURE

Targets for future observations are ozone absorptions on Mars, which are of great interest for understanding the Martian atmosphere. Furthermore the non-LTE CO₂ emissions observations will continue in the atmospheres of Venus, Mars, and possibly in the Earth's atmosphere. We plan also to go to longer wavelengths as soon as LOs become available, since the sensitivity improves significantly. First step might be the 13 μ m lines of Acetylene one of the most abundant hydrocarbons on Jupiter. The long–term goal is the operation of THIS on the stratospheric observatory SOFIA from roughly 2007 on. The main goal here will be the detection of cold interstellar H₂ against moderately hot IR sources at wavelengths around 17 μ m.

To reach the described goals technical developments of the laser LOs as well as the detectors are necessary. The laser development is mainly done by Alpeslasers, Switzerland. New detector technologies to be investigated are HEBs and QWIPs. HEBs are build in our institute and currently in the final test phase for infrared applications. Calculations yield good results up to 10 μ m wavelength and bandwidth of up to 8 GHz. QWIP detectors made by Fraunhofer Institut für angewandte Festkörperphysik, Germany, showed a sensitivity of about 5 % in a first test. Newly designed devices are believed to have a quantum efficiency comparable to MCT detectors while having bandwidth' up to 10 GHz. To make use of the higher bandwidth a new broadband AOS is currently under development by BAE-Systems and our Institute.

REFERENCES

1. M. M. Abbas, M. J. Mumma, T. Kostiuk, and D. Buhl, *Sensitivity limits of an infrared heterodyne spectrometer for astrophysical applications*, Applied Optics 15, 427-436, 1976.
2. T. Kostiuk and M. J. Mumma, *Remote sensing by IR heterodyne spectroscopy*, Applied Optics 22, 2644-2654, 1983.
3. G. Sonnabend, D. Wirtz, F. Schmülling, and R. Schieder, *Tunable Heterodyne Infrared Spectrometer for Atmospheric and Astronomical Studies*, Applied Optics 41, No.15, 2978-2984, 2002.
4. J. Faist, *Quantum cascade laser*, Science 264, 553-555, 1994.
5. R. Schieder, V. Tolls, and G. Winnewisser, *The Cologne acousto-optical spectrometer*, Exp. Astron. 1, 101-121, 1989.
6. F. Schmülling, B. Klumb, M. Harter, R. Schieder, B. Vowinkel, G. Winnewisser, *High sensitivity mid-infrared heterodyne spectrometer with a tunable diode laser as a local oscillator*, Applied Optics 37, 5771-5776, 1998.

LARGE FORMAT NARROW-BAND, MULTI-BAND, AND BROAD-BAND LWIR QWIP FOCAL PLANES FOR SPACE AND EARTH SCIENCE APPLICATIONS

S. D. Gunapala* and S. V. Bandara
Jet Propulsion Laboratory, Pasadena, CA 91109

ABSTRACT

A 640x512 pixel, long-wavelength cutoff, narrow-band ($\Delta\lambda/\lambda \sim 10\%$) quantum well infrared photodetector (QWIP) focal plane array (FPA), a four-band QWIP FPA in the 4-16 μm spectral region, and a broad-band ($\Delta\lambda/\lambda \sim 42\%$) QWIP FPA having 15.4 μm cutoff have been demonstrated.

I. INTRODUCTION

The QWIPs discussed in this article utilize the photoexcitation of electrons between the ground state and the first excited state in the conduction band quantum well. The quantum well structure is designed so that these photoexcited carriers can escape from the quantum well and be collected as photocurrent. These detectors afford greater flexibility than extrinsically doped semiconductor infrared detectors because the peak wavelength of the response, cutoff wavelength, and the spectral width of the response can be continuously tailored by varying layer thickness and barrier composition. There has been much interest lately¹ in large format QWIP focal plane arrays (FPAs). In this paper we discuss the design, fabrication, and test results of a 640x512 pixel narrow-band, four-band and broad-band QWIP FPAs in the 4-16 μm spectral region. These large format FPAs will be useful for many applications, such as the in-situ and remote sensing of gas molecules, thermal imaging, global atmospheric temperature profiles monitoring, cloud characteristics measurements, astronomy, tracking and identification of missiles, etc.

II. 640x512 PIXEL NARROW-BAND FOCAL PLANE ARRAY

Each period of the multi-quantum-well (MQW) structure consists of a 45 Å well of GaAs (doped $n = 5 \times 10^{17} \text{ cm}^{-3}$) and a 500 Å barrier of $\text{Al}_{0.3}\text{Ga}_{0.7}\text{As}$. Stacking many identical quantum wells together increases photon absorption. Ground state electrons are provided in the detector by doping the GaAs well layers with Si. This photosensitive MQW structure is sandwiched between 0.5 μm GaAs top and bottom contact layers doped $n = 5 \times 10^{17} \text{ cm}^{-3}$, grown on a semi-insulating GaAs substrate by molecular beam epitaxy (MBE). Then a 0.7 μm thick GaAs cap layer on top of a 300 Å $\text{Al}_{0.3}\text{Ga}_{0.7}\text{As}$ stop-etch layer was grown in-situ on top of the device structure to fabricate the light coupling optical cavity. The epitaxially grown material was processed into 200 μm diameter mesa test structures using wet chemical etching, and Au/Ge ohmic contacts were evaporated onto the top and bottom contact layers.

An experimentally measured responsivity spectrum is shown in Fig. 1. The responsivity of the detector peaks at 8.5 μm and the peak responsivity (R_p) of the detector is 83 mA/W at bias $V_B = -1.1 \text{ V}$. The spectral width and the cutoff wavelength are $\Delta\lambda/\lambda = 10\%$ and $\lambda_c = 8.9 \mu\text{m}$, respectively. The net peak quantum efficiency was 1.4% at bias $V_B = -1.1 \text{ V}$ for a 45° double pass. The lower quantum efficiency is due to the lower photoconductive gain at lower operating bias. Lower operating bias suppresses the dark current.

The photoconductive gain g was experimentally determined using¹ $g = i_n^2 / 4eI_D\Delta f + 1/(2N)$, where Δf is the measurement bandwidth, N is the number of quantum wells, and i_n is the current noise, which was measured using a spectrum analyzer. The photoconductive gain of the detector reached 0.98 at $V_B = -5 \text{ V}$. The peak detectivity is defined as $D_p^* = R_p \sqrt{A\Delta f} / i_n$, where R_p is the peak responsivity, A is the area of

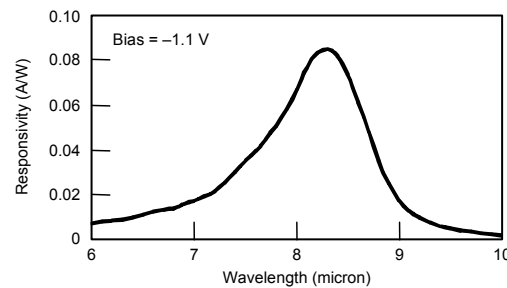


Figure 1. Responsivity spectrum of a bound-to-quasibound LWIR QWIP test structure at temperature $T = 77 \text{ K}$.

*Contact information for S. D. Gunapala: Sarath.d.Gunapala@jpl.nasa.gov, phone (818) 354-1880

SESSION 7- Heterodyne Detection

the detector and $A = 3.14 \times 10^{-4} \text{ cm}^2$. The measured peak detectivity at bias $V_B = -1.1 \text{ V}$ and temperature $T = 65 \text{ K}$ is $1 \times 10^{11} \text{ cm} \sqrt{\text{Hz}} / \text{W}$. Figure 2 shows the bias dependence of peak detectivity as a function of temperature. These detectors show BLIP at bias $V_B = -2 \text{ V}$ and temperature $T = 72 \text{ K}$ for a 300 K background with f/2 optics.

After the two-dimensional grating array was defined by the lithography and reactive ion etching, the photoconductive QWIPs of the 640x512 pixel FPAs were fabricated by dry etching through the photosensitive GaAs/ $\text{Al}_x\text{Ga}_{1-x}\text{As}$ multi-quantum well layers into the 0.5 μm thick doped GaAs bottom contact layer. The detector pixel pitch of the FPA is 25 μm and the actual pixel area is $23 \times 23 \mu\text{m}^2$. Indium bumps were then evaporated on top of the detectors for hybridization with a silicon readout integrated circuit (ROIC). QWIP FPAs were hybridized to a 640x512 pixel silicon CMOS readout and are biased at $V_B = -1.1 \text{ V}$. At temperatures below 72 K, the signal-to-noise ratio of the system is limited by array nonuniformity, readout multiplexer (i.e., ROIC) noise, and photocurrent (photon flux) noise. At temperatures above 72 K, the temporal noise due to the dark current becomes the limitation.

Figure 3 shows the measured NEDT histogram of the FPA at an operating temperature of $T = 65 \text{ K}$, 16 msec integration time, bias $V_B = -1.1 \text{ V}$ for 300 K background with f/2 optics, and the mean value is 20 mK. This agrees reasonably well with our estimated value of 10 mK based on test detector data. The net peak quantum efficiency of the FPA was 1.5%, which also agrees closely with the single element test detector results. It is worth noting that under BLIP conditions the performance of the detectors is independent of the photoconductive gain, and depends only on the absorption quantum efficiency.

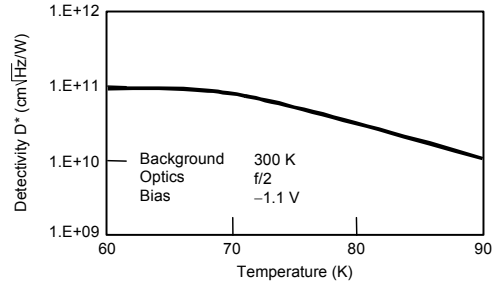


Figure 2. Detectivity as a function of temperatures at bias of -1.1 V .

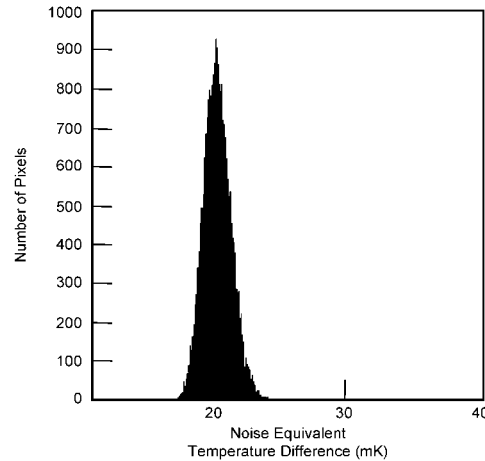


Figure 3. NEDT histogram of the 327,680 pixels of the 640x512 array showing a high uniformity of the FPA.

III. 640X512 PIXEL FOUR-COLOR SPATIALLY SEPARATED FOCAL PLANE ARRAY

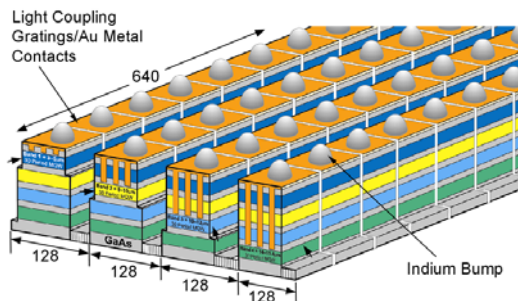


Figure 4. Layer diagram of the four-band QWIP device structure and the deep groove two-dimensional periodic grating structure. Each pixel represent a 640x128 pixel area of the four-band focal plane array.

structure is dominated by the longest wavelength portion of the device structure, the VLWIR QWIP structure has been designed to have a bound-to-quasibound intersubband absorption peak at 14.0 μm . Other QWIP device structures have been designed to have a bound-to-continuum intersubband absorption process because the photo current and dark current of these devices are relatively small compared to the VLWIR device. This whole four-band QWIP device structure was then sandwiched between 0.5 μm GaAs

This four-band vertically integrated device structure was achieved by the growth of multi-stack QWIP structures separated by heavily doped n^+ contact layers, on a GaAs substrate. Device parameters of each QWIP stack were designed to respond in different wavelength bands. Figure 4 shows the schematic device structure of a four-color QWIP FPA. A typical QWIP stack consists of a MQW structure of GaAs quantum wells separated by $\text{Al}_x\text{Ga}_{1-x}\text{As}$ barriers. The actual device structure consists of a 15 period stack of 4-5 μm QWIP structure, a 25 period stack of 8.5-10 μm QWIP structure, a 25 period stack of 10-12 μm QWIP structure and a 30 period stack of 13-15.5 μm QWIP structure. Each photosensitive MQW stack was separated by a heavily doped n^+ (thickness 0.2 to 0.8 μm) intermediate GaAs contact layer (see Fig. 4). Since the dark current of this device

SESSION 7- Heterodyne Detection

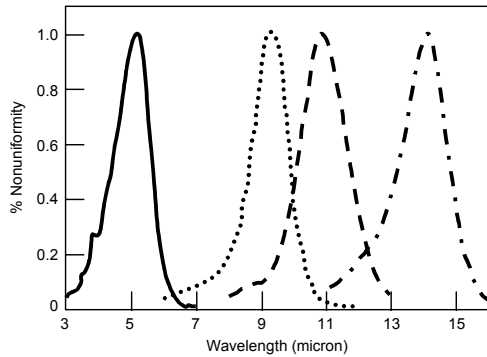
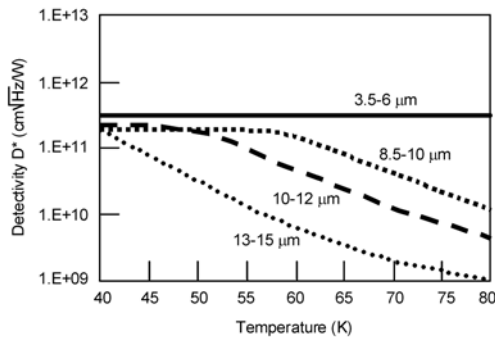


Figure 5. Normalized spectral response of the four-band QWIP FPA.



12, 10-12, and 13.5-15.5 μm spectral bands show BLIP at temperatures 40, 50, 60 and 120 K, respectively, for a 300 K background with a $f/5$ cold stop. As expected (due to BLIP), the estimated and experimentally obtained NEDT values of all spectral-bands do not change significantly below their BLIP temperatures. The experimentally measured NEDT of 4-5, 8-12, 10-12, and 13.5-15.5 μm detectors at 40 K are 21.4, 45.2, 13.5, and 44.6 mK, respectively. These experimentally measured NEDT agree reasonably well with the estimated NEDT values based on the single element test detector data¹.

IV. 640x512 PIXEL BROAD-BAND QWIP FOCAL PLANE ARRAY

The broadband QWIP device structure was designed by repeating a unit of several quantum wells with slightly different parameters such as well width and barrier height¹. The positions of ground and excited states of the quantum well are determined by the quantum well width (L_w) and the barrier height, i.e. the Al mole fraction (x) of the barrier. Since each single set of parameters for a bound-to-quasibound quantum well¹ corresponds to a spectral band pass of about 1.5 μm , three different sets of values are sufficient to cover a 10-16 μm spectral region (see Fig. 18). The MQW structure consists of many periods of these three-quantum-well units separated by thick barriers¹.

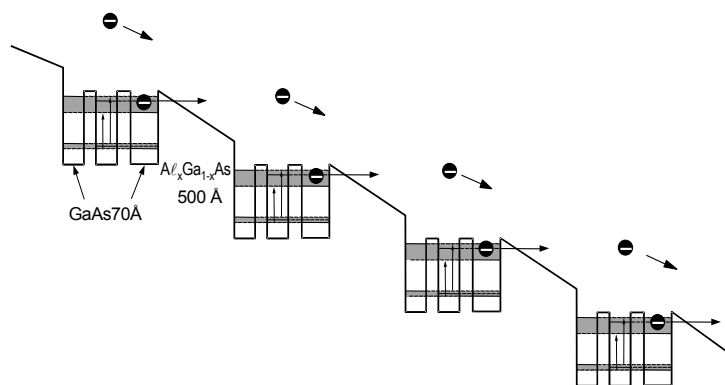


Figure 7. Broad-band MQW structure is designed by repeating a unit of several quantum wells with slightly different parameters such as well width and barrier height.

top and bottom contact layers doped with $n = 5 \times 10^{17} \text{ cm}^{-3}$ and was grown on a semi-insulating GaAs substrate by MBE.

In this section, we discuss the demonstration of the first 640x512 pixel monolithic spatially separated four-band QWIP FPA. The unique feature of this spatially separated four-band FPA is that the four infrared bands are independently and simultaneously readable on a single imaging array. This feature leads to a reduction in instrument size, weight, mechanical complexity, optical complexity and power requirements since no moving parts are needed. Furthermore, a single optical train can be employed, and the whole focal plane can operate at a single temperature.

The individual pixels of the four-color FPA were defined by photolithographic processing techniques (masking, dry etching, chemical etching, metal deposition, etc.). Four separate detector bands were defined by a deep trench etch process and the unwanted spectral bands were eliminated by a detector short-circuiting process. The unwanted top detectors were electrically shorted by gold-coated reflective two-dimensional etched gratings as shown in the Fig. 4. In addition to shorting, these gratings serve as light couplers for active QWIP stack in each detector pixel¹. Design and optimization of these two-dimensional gratings to maximize QWIP light coupling are extensively discussed elsewhere¹. The unwanted bottom QWIP stacks were electrically shorted at the end of each detector pixel row. Figure 6 shows the peak detectivities of all four spectral-bands as a function of operating temperature.

Based on this single element test detector data, the 4-5, 8-

SESSION 7- Heterodyne Detection

The device structure reported here involved 33 repeated layers of GaAs three-quantum-well units separated by $L_B \sim 575$ Å thick $\text{Al}_x\text{Ga}_{1-x}\text{As}$ barriers. The well thickness of the quantum wells of three-quantum-well units are designed to respond at peak wavelengths around 13, 14, and 15 μm, respectively. These wells are separated by $L_u \sim 75$ Å thick $\text{Al}_x\text{Ga}_{1-x}\text{As}$ barriers. The Al mole fraction (x) of barriers throughout the structure was chosen such that the $\lambda_p = 13$ μm quantum well operates under bound-to-quasibound conditions. The excited state energy level broadening has been further enhanced due to the overlap of the wavefunctions associated with excited states of quantum wells separated by thin barriers¹. Energy band calculations based on a two band model show excited state energy levels spreading about 28 meV.

In Fig. 8, the responsivity curve at $V_B = -2.5$ V bias voltage shows broadening of the spectral response up to $\Delta\lambda \sim 5.5$ μm, (i.e. the full-width at half-maximum from 10.5 – 16 μm). This broadening $\Delta\lambda/\lambda_p \sim 42\%$ is about a 400% increase compared to a typical bound-to-quasibound QWIP. The responsivity of the detector peaks at 13.5 μm and the peak responsivity (R_p) of the detector is 250 mA/W at bias $V_B = -2.5$ V. The peak quantum efficiency was 11% at bias $V_B = -2.5$ V for a 45° double pass. The calculated D^* value for the present device ($\lambda = 15.4$ μm) at $T = 55$ K and $V_B = 2.5$ V is $3 \times 10^{10} \text{ cm}^2/\text{Hz}/\text{W}$. Even with broader response, this D^* is comparable to previously reported D^* of QWIPs with narrow spectral response. Figure 9 shows the detectivity D^* as a function of the operating temperature of the device. A light coupling random reflector array was defined by the lithography and dry etching. Photoconductive QWIPs of the 640x512 pixel FPAs were then fabricated by dry etching through the photosensitive GaAs/ $\text{Al}_x\text{Ga}_{1-x}\text{As}$ MQW layers into the 0.5 μm thick doped GaAs bottom contact layer. The pixel pitch of the FPA is 25 μm and the actual pixel size is $23 \times 23 \mu\text{m}^2$. The random reflectors on top of the detectors were then covered with Au/Ge and Au for Ohmic contact and reflection. Indium bumps were then evaporated on top of the detectors for hybridization with silicon ROIC. A single QWIP FPA was chosen and hybridized to a 640x512 pixel silicon CMOS ROIC and biased at $V_B = -2.5$ V. At temperatures below 48 K, the signal to noise ratio of the system is limited by array nonuniformity, multiplexer readout noise, and photo current (photon flux) noise.

In summary, we have demonstrated the first 640x512 pixel spatially separated monolithic four-band FPA, narrow-band FPA, and the first 640x512 pixel broad-band FPA. These can be used in many ground based and space borne applications that require long-wavelength, large, uniform, reproducible, and low 1/f noise narrow-band, multi-band, and broad-band LWIR FPAs. These FPAs were back-illuminated through the flat thinned substrate membrane (thickness ≈ 2000 Å). As described elsewhere¹ this thinned GaAs FPA membrane has completely eliminated the thermal mismatch between the silicon CMOS ROIC and the GaAs based QWIP FPA, and has completely eliminated the pixel-to-pixel optical cross-talk of the FPA. This initial array gave very good images with 99.9% operability.

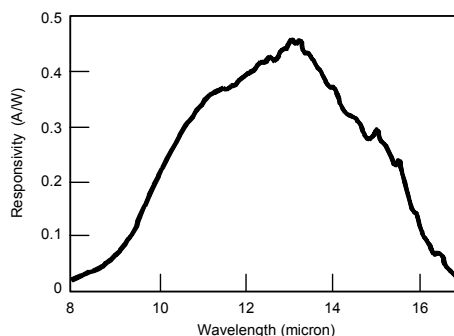
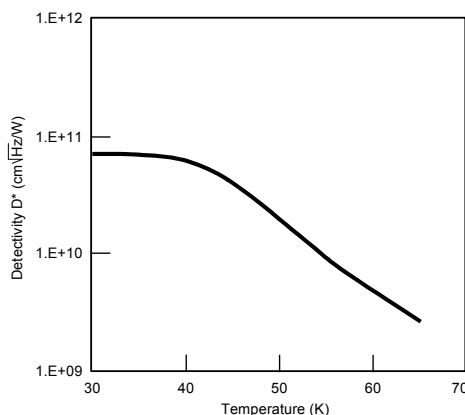


Figure 8. Responsivity spectrum of a broadband QWIP at temperature $T = 55$ K.



ACKNOWLEDGMENTS

The research described in this paper was performed by the Jet Propulsion Laboratory, California Institute of Technology, and was jointly sponsored by the Breakthrough Sensors and Instrument Component Technology Thrust of the NASA Cross-Enterprise Technology Development Program and the Advance Technology Initiative Program of the NASA Earth Science Technology Office.

REFERENCES

- 1 S. D. Gunapala and S. V. Bandara, *Quantum Well Infrared Photodetector (QWIP) Focal Plane Arrays*, Semicon. Semimet., vol. 62, H. C. Liu and F. Capasso, Ed. San Diego: Academic Press, pp. 197-282, 2000.

A Thermal Infrared Heterodyne Receiver with Applications to Astronomy

David D. Snyder Hale*

Space Sciences Laboratory, University of California at Berkeley, Berkeley, CA 94720

ABSTRACT

A method for detection of thermal infrared radiation from astronomical sources is discussed from an instrumentation point of view. This method utilizes heterodyne detection, whereby light collected by a telescope is spatially mixed with single-mode radiation from an infrared laser local oscillator onto a HgCdTe photodiode. The operating wavelength range of the receiver is adjustable from approximately 9 to 12 μm , with an intermediate frequency response of the photodiode and associated electronics spanning from 200 to 2800 MHz, or 2.6 GHz in each sideband. The instrumentation which will be discussed is currently in use by the UC Berkeley Infrared Spatial Interferometer (ISI) at the Mount Wilson Observatory. Each of the three ISI elements consists of a 1.65m telescope with complete heterodyne receiver, and is capable of operating as the front end to a variety of different instruments. The sensitivity of the receiver to measuring weak stellar sources will be discussed and contrasted with homodyne receiver performance. Actual spectroscopic and interferometric measurements of astronomical sources will be mentioned.

INTRODUCTION

In principle, heterodyne detection is a process of mixing two signals. For astronomical detection, a stellar signal is combined, or mixed with a stable, fixed-frequency signal (the "local oscillator") onto a nonlinear detector; the frequency of the local oscillator (LO) is chosen to lie at the center of the band to be detected in the source. The multiplication of these two signals produces a detector response which contains frequencies equal to the sum and difference of the two input frequencies, while preserving the amplitude and phase information contained in the original stellar signal. Typically the difference frequency between the stellar and local oscillator signal frequencies (termed the intermediate frequency) is that which is desired because of the often greater flexibility of handling a relatively lower frequency signal.

The heterodyne frequency conversion technique is particularly well-suited for detection of thermal infrared radiation, i.e. frequencies on the order of tens of THz. A mid-infrared stellar signal collected by a telescope may then be spatially mixed with radiation from a laser (which serves as the local oscillator), onto a photodiode which serves as the nonlinear (square law) detector. Intermediate frequencies on the order of GHz are typically obtained, and standard radio techniques are utilized for amplification, transmission, filtering, recording, etc.

Heterodyne receivers are typically characterized by their effective bandwidth and detection efficiency. The detectors themselves exhibit an intermediate frequency resistive-capacitive (RC) time response which is characteristic of the detector construction. Because the intermediate frequency (IF) signal is then amplified, the frequency response of electronic circuits must also be factored into the overall response of the system. The combined frequency response of detector and electronics determines the total effective bandwidth. Effective detection efficiency accounts for not only the quantum efficiency of the detector, but also other factors such as net transmission efficiency of the atmosphere and telescope optics. At present, 11 μm heterodyne receivers have (double sideband) bandwidths of nearly 6 GHz (0.2 cm^{-1}), and net efficiencies of about 30%, which accounts for quantum efficiencies of approximately 40-50% and transmission efficiencies of $\sim 60\%$ from star to detector. Larger bandwidths ($\sim 1\text{ cm}^{-1}$) and higher quantum efficiencies ($\sim 80\%$) may possibly be realized with quantum-well infrared photodetector (QWIP) devices, but these have yet to be proven in the application of astronomical heterodyne detection.

**Contact information for D.D.S. Hale - Email: david@isi.mtwilson.edu*

SESSION 7- Heterodyne Detection

INSTRUMENTATION

A heterodyne receiver designed for detection of stellar mid-infrared signals has been constructed as follows. Collection of light from an astronomical source is performed with a 1.65m aperture telescope of effective focal length $f/89$. A few centimeters beyond the focal point, the telescope beam is split into two parts by a dichroic beamsplitter which sends mid-infrared (N band) radiation on to the heterodyne detection system, and near-infrared (K band) radiation on to a camera for guiding and tip/tilt wavefront correction. Because the atmospheric index of refraction does not change significantly between the K and N bands, wavefront correction in the near-infrared is adequate to stabilize the mid-infrared signal. The mid-infrared stellar beam reflected off of the dichroic beamsplitter is then sent to a beamsplitter where it is combined with light from a CO₂ laser (which has been properly shaped by a series of lenses in order to ensure the laser and telescope beams are of the same f-number). The combined beams propagate to a mirror which reflects the beam into a signal detection dewar through an antireflection (AR) coated $f/1.5$ aspheric ZnSe lens and an AR coated ZnSe window tilted at 5° from normal incidence to the optical axis in order to prevent back-reflections. Figure 1 shows a schematic¹ of these various beams. The radiation is focused by the lens on a liquid nitrogen cooled HgCdTe photodiode, which produces the intermediate frequency (IF) signal.

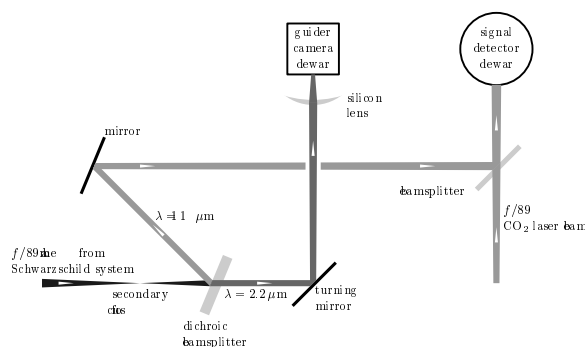


Figure 1: Schematic diagram of heterodyne mixing optics. Additional optics for chopping are not shown.

The CO₂ laser local oscillator (LO) is similar to the Freed² design, and operates with a meter-long semi-confocal cavity having a concave mirror at one end with a radius of curvature of twice the cavity length, and a grating at the other end in a Littrow configuration acting as a plane mirror where the beam waist is located. Oscillation on undesirable modes is prevented or reduced by apertures inside the cavity in front of the grating and the concave mirror. A variety of CO₂ isotopes can be used for operation on any one of a series of laser frequencies between approximately 9 and 12 μm . Different laser lines are easily selected by setting the tilt of the 80 groove/mm original ruled diffraction grating. Passive frequency stabilization is integral to the laser design. Four invar rods define the cavity length and the gas discharge operates in a sealed tube surrounded by a jacket of circulating and thermally stabilized water. Laser output power is stabilized via a computer-controlled servo loop which is able to make small adjustments to the cavity length by means of a piezoelectric element.

The IF signal from the photodiode, produced by the product of the stellar and LO signals, encompasses a wide range of frequencies within the time responsiveness of the detector. Those frequencies within the detector bandwidth above the CO₂ laser LO frequency form the upper sideband, while frequencies below the LO frequency form the lower sideband. A low-noise FET pre-amp mounted on the same cold finger in the signal dewar as the HgCdTe photodiode amplifies the IF signal before reaching a room temperature amplifier. The combined frequency response of the amplifier electronics and photodiode extends from approximately 200 to 2800 MHz, and is equalized to within a few dB over the entire 2.6 GHz passband. Since both upper and lower sidebands contribute to the IF signal equally, an instrument will have an effective infrared bandwidth of twice the IF bandpass, or 5.2 GHz ($\sim 0.17 \text{ cm}^{-1}$).

The heterodyne detection system just described has primarily been in use as the receiver for an interferometer³, but has also served as the front-end for two different spectrometers^{4,5}. These three instruments will not be described in detail here, but a few of their measurements will be mentioned in a later section on results.

SESSION 7- Heterodyne Detection

PERFORMANCE

The fundamental noise power for a heterodyne detector (which detects only one polarization, i.e. that of the LO) is equivalent to an average of one quantum per second per unit bandwidth in the same polarization as the LO. Since heterodyne detection has the ability to measure the phase of a wave, and phase is complimentary to energy or number of quanta, this noise is an inescapable result of quantum mechanics and the uncertainty principle^{6,7}. The average signal-to-noise for an ideal photodiode using heterodyne detection is thus⁸

$$\left(\frac{S}{N}\right)_{het} = \frac{P_v}{h\nu} \sqrt{\Delta\nu t} \quad (1)$$

where P_v is the signal power in a single polarization per unit bandwidth per unit time, $h\nu$ is the quantum energy, $\Delta\nu$ is the full double sideband (DSB) detector bandwidth, and t is the integration time.

An interesting comparison can be made between heterodyne and homodyne (i.e. direct) detection. For homodyne detection the fundamental noise is dominated by detector dark current and read noise only for very narrow ($\sim 0.1 \text{ cm}^{-1}$) bandwidths, and is more frequently dominated by thermal background radiation striking the detector when larger bandwidths are used. The average signal-to-noise for an ideal direct detector is

$$\left(\frac{S}{N}\right)_{hom} = \frac{P_v}{h\nu} \sqrt{2\Delta\nu t \frac{(e^{h\nu/kT} - 1)}{1 - \epsilon}} \quad (2)$$

where T is the temperature of the optics and atmosphere through which the signal is received, and ϵ is the fractional transmission of radiation reaching the telescope.

From these equations it appears that direct detection may have an advantage by a factor of ~ 45 over heterodyne detection, when comparable narrow (0.2 cm^{-1}) bandwidths are used. However, this advantage is not always realized to this extent. In practice, direct detectors may utilize bandwidths as large as 100 cm^{-1} where they are predominantly background noise limited. Present mid-infrared cameras can have 1σ detection limits of $\sim 6 \times 10^{-14} \text{ W}$ in 1 second of averaging time, about a factor of 10 below the theoretical limit given above, negating much of the expected gain from the broad bandwidth. For bandwidths as narrow as about 1 cm^{-1} , sensitivities of about $\sim 2 \times 10^{-15} \text{ W}$ can be achieved in 1 second by direct detection, roughly 1.5 times the theoretical noise of an ideal heterodyne detector with a DSB bandwidth of $\sim 5 \text{ GHz}$.

Heterodyne receivers are of course also not perfectly efficient, but with their much narrower bandwidths they are limited primarily by fundamental quantum fluctuations rather than those caused by sources such as amplifier noise; hence, they are able to achieve sensitivities much closer to their theoretical limit. The constructed heterodyne receiver is routinely able to detect about $\sim 2 \times 10^{-15} \text{ W}$ in a 1 second average, assuming a net efficiency of about 30% and 5.2 GHz DSB bandwidth, which is within a factor of ~ 1.5 of that predicted by theoretical equation (1).

RESULTS

While the heterodyne receiver described herein was designed with the versatility in mind to accept a variety of instruments, it was principally built for use with an interferometer, namely the UC Berkeley Infrared Spatial Interferometer (ISI), a more thorough description of which can be found by Hale³ *et al.* Interference fringes are obtained by multiplying the IF signal from two (or more) telescopes in an RF correlator. Since interference is carried out at the relatively narrow-band IF frequencies, delay requirements for compensating geometrical pathlength differences between the source and the receiving elements are greatly relaxed, allowing the ISI to integrate for many hours by calculating delays without fringe tracking (as a direct-detection interferometer must do). The ISI has been used primarily to study the spatial distribution of dust around late-type stars by measuring visibility curves and applying spherically symmetric radiative transfer models in order to estimate dust shell inner radii, temperature, and optical depth. The inner radii of many dust shells have been clearly resolved by the ISI, and in some cases measurements of the diameter of the central star have been obtained to 1% precision. Continual monitoring

SESSION 7- Heterodyne Detection

has identified changes in visibilities due to variations in stellar luminosity and also movements and changes in the surrounding dust.

This heterodyne receiver is also well-suited for spectral line research. A spectrometer constructed by Betz⁴ *et al.* was used with one of the ISI receivers to measure infrared emission lines of stratospheric ammonia (NH₃) produced by the collision of Comet Shoemaker-Levy 9 with Jupiter in July 1994. Lineshapes of three different NH₃ emission lines at 10.7 μm were measured with a resolving power of $\sim 10^7$; a detailed analysis of the temporal behavior and NH₃ abundance distributions has recently been made by Fast⁹ *et al.*

The ISI heterodyne receivers have also been used with a spectral filterbank, described by Monnier⁵ *et al.* Using off-the-shelf 60 MHz RF filters, spectral resolutions of $\lambda/\Delta\lambda = 27\text{THz}/60\text{MHz} = 4.5 \times 10^5$ are readily obtained, enough to resolve features arising from Doppler shifts as small as ~ 0.7 km/s. A bank of 32 such filters was used to measure the line profiles of CO₂ in absorption in the Martian atmosphere, and NH₃ in the carbon star IRC+10216. Additionally, this bank of filters may be used in conjunction with the ISI's RF correlator, allowing for interferometry on spectral lines to be carried out. Using this filterbank with the interferometer, Monnier¹⁰ *et al.* were able to locate the molecular formation regions of silane (SiH₄) and ammonia (NH₃) around the carbon stars IRC+10216 and VY Cma.

SUMMARY

A heterodyne receiver of $\sim 0.2 \text{ cm}^{-1}$ bandwidth for thermal infrared ($\sim 9 - 12 \mu\text{m}$) wavelengths has been constructed, capable of 1σ detection of $\sim 2 \times 10^{-15} \text{ W}$ from an astronomical source in 1 second of integration. To date, three different instruments have been used with the receiver for spectroscopic and interferometric observations of planetary atmospheres, late-type stars, and the dusty environment surrounding stars. While direct detection will always remain the most sensitive method of detection of mid-infrared astronomical sources for wide bandwidths, heterodyne detection can be competitive with, and for narrow bandwidths such as required for spectral line research, can even surpass direct detection.

REFERENCES

1. E.A. Lipman, *Studies of Evolved Stars with a Mid-Infrared Interferometer*, Ph.D. Dissertation, University of California at Berkeley, 1998.
2. C. Freed: *Design and Short-Term Stability of Single-Frequency CO₂ Lasers*, IEEE Journal of Quantum Electronics, vol. QE-4, no.6, 404, 1968.
3. D.D.S. Hale, M. Bester, W.C. Danchi, W. Fitelson, S. Hoss, E.A. Lipman, J.D. Monnier, P.G. Tuthill, and C.H. Townes: *The Berkeley Infrared Spatial Interferometer: A Heterodyne Stellar Interferometer for the Mid-Infrared*, Astrophysical Journal, vol. 537, 998-1012, 2000.
4. A. Betz, E.C. Sutton, and R.A. McLaren: *Infrared Heterodyne Spectroscopy in Astronomy*. In Laser Spectroscopy III, Springer Series in Optical Sciences vol.7, eds. J.L. Hall and J.L. Carlsten, 31, 1977.
5. J.D. Monnier, W. Fitelson, W.C. Danchi, and C.H. Townes: *Mid-Infrared Interferometry on Spectral Lines. I. Instrumentation*, Astrophysical Journal Supplement Series, vol. 129, 421-429, 2000.
6. R. Serber & C.H. Townes: *Quantum Electronics*, ed. C.H. Townes, Columbia Univ. Press, 1960.
7. H.J. Kimble & D.F. Wells: *Squeezed States of the Electromagnetic Field*, Journal of the Optical Society of America B, vol.4, issue 10, 1450, 1987.
8. R.H. Kingston: *Detection of Optical and Infrared Radiation*, Springer Series in Optical Sciences vol.10, ed. D.L. MacAdam, 25, 1979.
9. K. Fast, T. Kostiuik, P. Romani, F. Espenak, T. Hewagama, A. Betz, R. Boreiko, and T. Livengood: *Temporal Behavior of Stratospheric Ammonia Abundance and Temperature Following the SL9 Impacts*, Icarus, vol. 156, 485-497, 2002.
10. J.D. Monnier, W.C. Danchi, D.S. Hale, P.G. Tuthill, and C.H. Townes: *Mid-Infrared Interferometry on Spectral Lines. III. Ammonia and Silane around IRC+10216 and VY Canis Majoris*, Astrophysical Journal, vol. 543, 868-879, 2000.

ABSTRACTS—Poster Session

P1

Superconducting Electronics for Detector Readouts

Jerome Luine, Dale Durand, Larry Eaton (TRW)

Spacecraft subsystems that support thermal detector imaging arrays that operate at temperatures below 80 K can be benefited by the use of superconducting electronics (SCE). SCE can greatly simplify spacecraft complexity, thereby reducing costs, and significantly enhance the performance of science instruments and control electronics. For example, by integrating an analog signal processor and analog-to-digital converter with an imaging sensor array, cryogenic system complexity is reduced and instrument performance is increased. The number of signal wires leading from the cryogenic detector environment to higher temperature electronics is reduced thereby reducing cryogenic system complexity. Reduced signal line count not only simplifies the cryogenic package but also reduces the cryogenic heat load. Cryogenic package simplification and reduced heat load result in lower cost and increased reliability. Instrument performance is enhanced by executing as much signal processing at the sensor array as possible. Multiplexing and digitizing the signals in the very low-noise cryogenic environment increases signal-to-noise ratio. These benefits can also be used to dramatically increase the number of sensor elements thereby increasing resolution to levels that are extremely difficult or impossible to achieve with today's technology. Furthermore, materials used for SCE have been found to have orders of magnitude greater radiation hardness than any other electronics materials. SCE is ideal for cryogenic instruments as well as other spacecraft electronic systems. The status of SCE technologies for thermal detector readout and signal processing will be presented.

Keywords: Superconductor electronics, detector readout, signal processing

P2

Development of a Submillimeter/Far-infrared Radiometer for Cirrus Measurements.

Darren Hayton, Peter Ade (University of Wales at Cardiff), Frank Evans (University of Colorado), Clare Lee (University of Wales at Cardiff), Ira Nolt, Mike Vanek (NASA Langley Research Center)

We introduce a low-cost, lightweight and compact polarisation-sensitive radiometer for the measurement of Cirrus clouds in the submillimeter and far-infrared region ($10\text{--}150\text{ cm}^{-1}$). It is widely recognised that enhanced global measurements of cirrus properties are essential to the development of General Circulation and Climate Prediction Models since cirrus clouds have a strong effect on the Earth's Global Radiation Budget. The purpose of this project is to design and build a novel instrument suitable for aircraft deployment in order to measure Ice Water Path (IWP) along with cirrus particle size and shape. This airborne instrument, which is currently under development in Cardiff, will serve as a prototype for a future satellite-based radiometer. The radiometer will capitalise on the ongoing measurements of the NASA-led, Fourier Transform interferometer-based, FIRSC (Far-Infrared Sensor for Cirrus) instrument for which Cardiff has been closely associated. Data from FIRSC campaigns is being used to select optimum radiometer channels that exhibit good sensitivity to specific cirrus. This new multichannel radiometer will, however, have some key advantages over similar spectroscopic instruments, for example, portability, increased optical efficiency, a multi-angle field of view and a reduced integration period leading to an improved spatial resolution. The radiometer will benefit from the application of state-of-the-art submm/FIR polariser and solid filter technology currently being developed in Cardiff. The instrument will require a detector array that is robust enough to withstand aircraft/space deployment.

Keywords: Earth observation, far-infrared/submm, cirrus clouds, radiometer, airborne instrument, satellite prototype

ABSTRACTS–Poster Session

P3 **Thermoelectric Cooling Utilizing CeB₆ Single Crystal at Cryogenic Temperatures**

Sergey Harutyunyan, Violetta Vartanyan, Vahan Nikoghosyan,
Armen Kuzanyan (Institute for Physical Research, Ashtarak, Armenia),
Kent Wood, Armen Gulian (NRL, USA)

Thermoelectric refrigerators operating at cryogenic temperatures will considerably simplify and facilitate the problem of obtaining temperatures below 4.2 K, which is required for different types of sensitive photon detectors. The results of investigation of the cooling on the basis of the Peltier effect in a single crystal of CeB₆ grown by the floating zone method are presented. The temperature dependencies of thermopower $S(T)$, resistivity $\rho(T)$, and thermal conductivity $k(T)$ have been measured, and the parameter $ZT=TS^2/\rho k$ has been calculated in the temperature range 3.5 K–300 K. The value of 0.2 at 4.5 K has been obtained for ZT , which allows one to expect noticeable Peltier cooling in this material at that temperature. Initial measurements of thermoelectric cooling vs. electric current value were made at temperatures 3.5 K, 4.5 K, 5.5 K, 9.5 K. A single-stage prototype solid-state micro-refrigerator demonstrated a temperature drop of 0.2 K at the temperature 4.5 K.

Keywords: Thermoelectric, detector, micro-refrigerator

P4 **Antireflection Coatings for Far IR Filters** Carole Tucker, Vic Haynes, Peter Ade (University of Wales at Cardiff)

The far-infrared bandpass and blocking filters developed at Cardiff University are made from layers of a dielectric substrate. This technique makes the filters solid and robust, however, we are always left with a dielectric slab of the overall filter thickness which creates fringing in the spectrum and hence loss in transmission at certain frequencies. We present results obtained from an antireflection technique, providing near 100% transmission over a desired band of frequencies. This technology is also being developed for use on windows and lenses. Comparison with a theoretical model shows good agreement allowing us freedom to explore designs before manufacture.

Keywords: Far IR, antireflection coatings, bandpass, blocking filters

P5 **In situ Pulsed Laser Deposition of C-Axis Oriented MgB₂ Films and Their Characterization**

Sanjay Shinde (University of Maryland), Brook Lakew (NASA Goddard Space Flight Center), S.B. Ogale, V.N. Kulkarni, S.N. Kale, T. Venkatesan (University of Maryland)

The recent discovery of an intermetallic superconductor MgB₂ has renewed interest in the area of superconductivity not only because of fundamental understanding of superconductivity but also due to its potential applicability in devices such as thermal detectors. Considerable amount of research has been devoted to obtain MgB₂ films by an all in situ growth technique. We have grown MgB₂ thin films by an all in situ pulsed laser deposition process from pure B and Mg targets. Ultrathin layers of B and Mg were deposited in a multi-layer configuration. Hundreds of such Mg-B bilayers with a capping Mg layer on the top were deposited on sapphire substrate. These depositions were done in high vacuum ($\sim 10^{-7}$ Torr) and at room temperature. After deposition, such a configuration was annealed at high temperature for a short time in a forming gas (4% H₂ in Ar). The best films, obtained by this procedure, showed superconducting transition temperature ~ 30 K. These films have been characterized by x-ray diffraction, Rutherford Backscattering Spectrometry, AC susceptibility, resistivity- (with and without magnetic field) and 1/f noise-measurements. The physical properties of these films will be presented and discussed.

Acknowledgements: This work was supported by the Office of Naval Research under grant # N000149611026 and NASA Goddard Space Flight Center, DDF fund.

Keywords: MgB₂ films, pulsed laser deposition

ABSTRACTS—Poster Session

P6

Cryocoolers for Space

Peter Kittel, Jeff Feller, Pat Roach (NASA Ames Research Center),
Ali Kashani, Ben Helvensteijn (Atlas Scientific)

Many planetary and Earth science missions require cooling to increase sensitivity and reduce thermal noise of detectors, for preserving high Isp propellants, or for protecting instruments from hostile environments. For space applications, such cooling requires reliable, efficient, long-life coolers that are relatively compact, lightweight, and have low vibration. We have developed and are developing coolers that meet these requirements over a wide range of temperatures. These include pulse tube coolers cooling from 300 K to below 6 K, a magnetic cooler cooling from 10 K to 2 K, a **³He** sorption cooler cooling from 2 K to 0.3 K and a helium dilution cooler cooling from 0.3 K to 0.05 K. Details of these coolers and their advantages are presented.

Keywords: Cryocoolers, pulse tube, dilution refrigerator, ADR, sorption cooler

P7

High Aspect Ratio Hole Array Filters for a Wide Range of Wavelength

R.K. Fetting, H. Hein, J. Schulz (Institut f. Mikrostrukturtechnik)

Metal mesh filters are used as cutoff and band pass filters for radiation from the infrared to microwaves. Usually they are constructed of metal films where the thickness is much thinner than the size of the structures. In some instances films thicker than the size of the apertures are of advantage. Simple theoretical models predict that thick metal films with densely packed circular or hexagonal holes act as high pass filters. They should exhibit a sharp cutoff and an out of band rejection which is the better, the larger the aspect ratio of film thickness to hole diameter.

The cutoff wavelength is about twice the hole diameter. The LIGA process that combines E-beam or x-ray lithography with electroplating is well suited to produce filters with the favorable aspect ratios of > 2:1. With this process filters were produced for the Isophot instrument onboard ESAs' ISO satellite. The filters had hexagonal holes of 80 micron width in a 180-micron thick film.

The rejection of radiation of wavelength > 150 micron is excellent. Recently filters have been produced using E-beam lithography and electroplating with hole diameters of 1 micron in a 2.5-micron thick gold film with a similarly good rejection for wavelengths > 2 micron. With these filters the suitability of layout and processes is demonstrated for the entire range from 2 micron to the microwave region.

P8

Resonance Modes of Meshes with Rectangular and Hexagonal Structures

Oren Sternberg, J. Shah (Naval Research Lab), K.D. Moeller (New Jersey Institute of Technology), R. Fetting (FZ-Karlsruhe, Germany)

We compare simulation results of inductive cross-shaped, square, and hex-shaped meshes for different sizes and thicknesses in the far-infrared spectral region. We present the dependence of the peak transmittance, bandwidth and sidebands structures of square-shaped, round, cross, and hex structures. Experimental data and simulations are presented for meshes of hexagonal structure as well as other structures. In addition the dipole model and the TE-mode theory are compared for various meshes. An empirical formulas and cutoff frequencies are discussed.

ABSTRACTS–Poster Session

P9

Programmable 2-D Addressable Cryogenic Aperture Masks

A.S. Kutyrev, S.H. Moseley, M. Jhabvala, M. Li, D.S. Schwinger,
R.F. Silverberg, R.P. Wesenberg (Microshutter Team)

We are developing a two-dimensional array of square microshutters (programmable aperture mask) for a multi-object spectrometer for the James Webb Space Telescope (JWST). This device will provide random access selection of the areas in the field to be studied. The device is in essence a close packed array of square slits, each of which can be opened independently to select areas of the sky for detailed study. The device is produced using a 100-micron thick silicon wafer as a substrate with 0.5-micron thick silicon nitride shutters on top of it. Silicon nitride has been selected as the blade and flexure material because its stiffness allows thinner and lighter structures than single crystal Si, the chief alternative, and because of its ease of manufacture. The 100 micron silicon wafer is backetched in a high aspect ratio Deep Reactive Ion Etching (Deep RIE) to leave only a support grid for the shutters and the address electronics. The shutter actuation is done magnetically whereas addressing is electrostatic. 128x128 format microshutter arrays have been produced. Their operation has been demostarted on 32x32 subarrays. Good reliability of the fabrication process and good quality of the microshutters has been achieved. The mechanical behavior and optical performance of the fabricated arrays at cryogenic temperature are being studied.

REPORT DOCUMENTATION PAGE			Form Approved OMB No. 0704-0188	
Public reporting burden for this collection of information is estimated to average 1 hour per response, including the time for reviewing instructions, searching existing data sources, gathering and maintaining the data needed, and completing and reviewing the collection of information. Send comments regarding this burden estimate or any other aspect of this collection of information, including suggestions for reducing this burden, to Washington Headquarters Services, Directorate for Information Operations and Reports, 1215 Jefferson Davis Highway, Suite 1204, Arlington, VA 22202-4302, and to the Office of Management and Budget, Paperwork Reduction Project (0704-0188), Washington, DC 20503.				
1. AGENCY USE ONLY (Leave blank)		2. REPORT DATE February 2004		3. REPORT TYPE AND DATES COVERED Conference Publication
4. TITLE AND SUBTITLE TDW'03 International Thermal Detectors Workshop			5. FUNDING NUMBERS Code 693	
6. AUTHOR(S)				
7. PERFORMING ORGANIZATION NAME(S) AND ADDRESS (ES) Goddard Space Flight Center Greenbelt, Maryland 20771			8. PERFORMING ORGANIZATION REPORT NUMBER 2004-00980-0	
9. SPONSORING / MONITORING AGENCY NAME(S) AND ADDRESS (ES) National Aeronautics and Space Administration Washington, DC 20546-0001			10. SPONSORING / MONITORING AGENCY REPORT NUMBER CP—2004—212748	
11. SUPPLEMENTARY NOTES				
12a. DISTRIBUTION / AVAILABILITY STATEMENT Unclassified—Unlimited Subject Category: Report available from the NASA Center for AeroSpace Information, 7121 Standard Drive, Hanover, MD 21076-1320. (301) 621-0390.			12b. DISTRIBUTION CODE	
13. ABSTRACT (Maximum 200 words) NASA's future planetary and Earth Science missions will require ever more sensitive thermal detectors operating between 2K and 300 K. It is in response to this need that the International Workshop on thermal detectors (TDW03) was held. It put together space borne IR/Sub-mm and heterodyne instrument scientists and astronomers, thermal detector developers, cryocooling technologists as well as bandpass and blocking filter experts. Their varied expertise and backgrounds allowed for a fertile discussion on outstanding issues and future detector developments. In this regard TDW03 was a great success.				
14. SUBJECT TERMS Thermal detectors			15. NUMBER OF PAGES 120	
			16. PRICE CODE	
17. SECURITY CLASSIFICATION OF REPORT Unclassified	18. SECURITY CLASSIFICATION OF THIS PAGE Unclassified	19. SECURITY CLASSIFICATION OF ABSTRACT Unclassified	20. LIMITATION OF ABSTRACT UL	